Growth Dynamics, Fabrication and Operational Stability of Organic Field-Effect Transistors Based on $SnCl_2Pc$, VOPc and CuPc Molecules

A Dissertation submitted to

Indian Institute of Technology Guwahati

For the Degree of

Doctor of Philosophy

By

Sk Md Obaidulla

Department of Physics

Indian Institute of Technology Guwahati

Guwahati-781039, India

September, 2016

To my parents, Bilara, Oliullah, Muzibar Chacha and Moti Chacha

DEPARTMENT OF PHYSICS
Indian Institute of Technology Guwahati
Guwahati-781039, India

Date: Sep-27th, 2016

STATEMENT

The work contained in the thesis entitled ***"Growth Dynamics, Fabrication and Operational Stability of Organic Field-Effect Transistors Based on $SnCl_2Pc$, VOPc and CuPc Molecules"*** has been carried out by me at Indian Institute of Technology Guwahati under the supervision of **Prof. P. K. Giri**, Professor, Department of Physics, Indian Institute of Technology Guwahati. This work has not been submitted elsewhere for the award of any degree.

Sk Md Obaidulla

Roll Number-10612111
Senior Research Fellow
Department of Physics
Indian Institute of Technology Guwahati
Guwahati-781039, India

Prof. P. K. Giri
Professor
Department of Physics
Indian Institute of Technology Guwahati
Guwahati-781039, India

Phone: +91 361 2582703, Fax: +91 3612690762
Email: giri@iitg.ernet.in

Date: Sep 27th, 2016

CERTIFICATE

This is certify that the work contained in the dissertation entitled ***"Growth Dynamics, Fabrication and Operational Stability of Organic Field-Effect Transistors Based on $SnCl_2Pc$, VOPc and CuPc Molecules"*** has been carried out by Mr. Sk. Md. Obaidulla at Indian Institute of Technology Guwahati under my supervision. This work has not been submitted elsewhere for the award of any degree.

(Prof. P. K. Giri)

Thesis Supervisor

ACKNOWLEDGEMENT

At the time of writing the acknowledgement, I realize that nearly five and half years of my Ph.D. life at IIT Guwahati is finally coming to an end and I am able to submit my thesis report. The research work reported in this thesis is the results of years of hard work with patience and would not have been possible without the help, support and encouragement of a number of people. My deepest appreciation to all the people who helped me directly or indirectly to make this thesis a reality.

First and foremost, I would like to express my sincere gratitude to my thesis supervisor, Prof. P. K. Giri. I am really indebted to him for accepting me as a Ph.D. student into his research group. Nothing in this thesis could be achieved without his guidance. I have learned not only a great deal of knowledge from him, but also how to become a better researcher, a team player, and a leader. His broad vision, constant enthusiasm, hard work, excellent guidance, valuable discussion, kind-support, bright ideas and strategic guidance with his great patience at every stage in my research have set a very high bar for me. It has been truly an honor and luck for me to have the chance of being with him during my Ph.D. life. In addition, I am thankful to him for giving me complete freedom in my work and providing the necessary arrangements to collaborate with other institute laboratory facilities and supports throughout my Ph. D. work to achieve the goal. He is my inspiration now and for rest of my life.

I would also like to express my honest gratitude to my doctoral committee members, Dr. A. K. Sharma (Chairman), Prof. Perumal Alagarswamy and Prof. H. B. Nemade for regular review of my research work and their valuable suggestions.

I would like to express my gratefulness to our collaborating partners which are Prof. Y. N. Mahapatra, Mr. Subhash Singh of IIT Kanpur, for fruitful discussions and suggestions, particularly for providing facility for device fabrication. Especially, I thank Subhash for his experience and optimism, for his patience and dedication in making sure every transistor worked as best as it could. I must thank Prof. Imakita of Kobe University (Japan) for providing XPS data for $SnCl_2Pc$ thin films.

I am grateful to Indian Institute of Technology Guwahati for providing the fellowship, good accommodation in this beautiful green campus and having enjoyable working environment. I am thankful to Prof. P. Poulose, our Head of the Department of Physics, Prof. C. Y. Kodalkar, Prof S. Ghosh, Prof. T. N. Dey, Prof. G. S. Setlur and other faculty members of Physics, members of the Central Instruments Facilities and Centre for Nanotechnology for providing me a research friendly environment with up-to-date research facilities. I am also thankful to Department of Chemistry and Centre for Nano Technology to carry out the UV-Vis spectroscopy measurements and other necessary facility. A special thanks to the scientific officers and technicians, Dr. Sidananda Sharma, Madhurya Bora, Indrajit Talukdar, Kaustav Acharya, Dr. K. K. Senapati, Chandan Borgohain for their help and cooperation to complete my work. I also express my special thanks to Prof. P. K. Iyer for help to carry out the part of the work in his lab. I express my sincere thanks to seniors Dr. Arindam Pal, Dr. Bata Krusna Santra, Dr. Vipin Kumar, Dr. Zaheer Abbas Ahmed, Dr. Enamullah, Dr. Parvendra Kumar, Dr. Akhilesh Sing, Dr. Souvik Paul, and Dr. Bappaditya Pal for their help and good company.

Also, I wish to take this opportunity to extend my sincere thanks to all of my teachers from kindergarten to graduate school who have truly raised me up in the world of science, step by step and word by word.

Many wonderful colleagues have made my life at IIT Guwahati splendid. Specially, thanks to my labmates Ramesh, Gone, Sumaiya, Kamal, Joydip, Samarjit, Larionette and Ruma for a good and enjoyable company and their supports. They shared every success and problems in and out of the lab during my stay at IIT Guwahati.

I must thank my friends Bishu, Upen, Partha, Noor, Bhagaban, Kartik, Arnab, Tapas, Rahul, for their company and sharing success, problems, frustrations and, every kind of discussions throughout my stay at IIT Guwahati. I cannot repay the support and encouragement I received from Suresh, Krishna, Sanjib, Kartik, Ramiz, Kallol, Prahlad, Gyan, Shanta, Abhijit, Sourav, Sudin, Ashish, Bibhuti, Anabil, Venky, Deep, Maidul, Nawaz, Robin, Krishna, Soumya, Prativa, Nagendra, Nilajan, Samir, Akhtar, Adil, Somnathda, Camelia during my Ph.D life that helped me in various ways. I am happy to thank them.

I should acknowledge the supports received from Subratada, Anand sir, Rajesh Dwivedi, S. Kramakarm mam, Ravi and Mofizulda, Mukul, Sabana, Alimuddin, Rezwan and well-wishers. They supported me in all possible ways during my early days of study by means of inspiration, motivation, academic books, free tuitions and financial help.

On the personal side, I would like to express my deepest sense of gratitude to my parents for their endless love, blessings and constant encouragement to pursue higher studies. Their hard work and dedication in helping me to pursue higher studies is the strongest source of inspiration for me. On the personal side, I would like to thank my parents – for everything. It is through their hard work and dedication that I am in the position to complete this Ph.D thesis. I will always remember their love, care and inspiration. Especially, my parents taught me the value of, patience, hard work, and to be honest, in particular they reminded me always, "Be a great with heart through proper education, not by others". Finally, I would like to express most importantly a great thanks and praise to Allah, who always guide and support me. My deepest gratitude goes to my brother Oliullah, Muzibar Chacha for their love and support constantly. He (my brother) took care many of our family tasks, so I could focus on my career and school. They may not care for the difference between a molecule and transistor, but their inspiration and smiles made all the difference in the world when early time fabricated transistors were going badly – and organic transistors went badly sometimes. Thanks to $SnCl_2Pc$ molecules and the transistors, when they finally worked, I really tested the happiness through my heart at that moment.

Obaidulla

IIT Guwahati

भारतीय प्रौद्योगिकी संस्थान गुवाहाटी
Indian Institute of Technology Guwahati

CONTENTS

Synopsis

Thin films based on molecular semiconductor, specifically "small" conjugated organic molecules, like metal phthalocyanine (M-Pc), are finding an increasing application in a number of electronic and optoelectronic devices [1-5]. In particular, they have been exploited in organic field-effect transistors (OFET), organic light emitting diodes, photovoltaic devices, and organic sensors due to their favorable properties, e.g., thermal and chemical stability, well ordered thin film growth and wide absorption band in the optical region [1,6-10]. Further, the structure and morphology of the first organic layer in the device have a large impact on the charge carrier mobility in OFETs. For each specific material, the charge carrier mobility depends crucially on the overlap between π-orbitals of vicinal molecules, which in turn is intimately related to the microscopic structure and density of structural defects in the organic film. These molecules also exhibit a certain degree of "specific tunability" due to various metals ion (M= Sn, Cu, CO, Zn etc.) and the side groups (R= F, Cl, NH_2, $O(CH_2)_{10}OH$ etc.) that can be introduced within a broad range of composition [1,11]. The optimized transport phenomena, such as injection and recombination of charge carriers depend, among other parameters, on molecular packing, range of grain boundaries/microstructure and roughness/morphology of surfaces. Thus, in organic electronic devices, e.g. OFET, where the thin films of specific organic semiconductors serve as active layer, the controlled deposition of molecular thin films as well as understanding their growth mechanism is primarily a key requirement for the optimization of electro-optical properties [12-15]. Understanding the growth dynamics of organic thin films is one of the key issues in the field of organic electronics.

In the past two decades, a theoretical framework relating the mechanisms of thin film growth to a set of scaling exponents describing the dependence of the surface roughness on film thickness and lateral length scale has been established [16]. Much effort has been devoted to theoretically predict the scaling exponents for certain growth models, as well as to

determine them experimentally for a large variety of thin film systems. However, detailed studies for calculating *scaling exponents* of organic thin films are rare and, in particular, the deposition of small molecules based organic thin films under high vacuum conditions. Among the well-known growth modes of thin films, one can distinguish among three different growth modes, i.e. layer-by-layer, layer-plus-island, and islands due to various relevant interactions of surface and interface energies [17-22]. However, it has been found that the layer-plus-island growth mode is typically most favorable for organic semiconductor films [17,23,24].

OFETs, whose characteristics are modulated by an external electrical field, are probably the most prominent components is virtually all modern microelectronic devices. Since they were first described in 1987, enormous progress has been made on OFETs, especially in the last several years. OFETs have many advantages over conventional silicon technology: they can be fabricated at low cost, large area coverage and on flexible substrates with high durability, stretchability, bio compatibility. They are key building blocks for applications such as active matrix-display driving circuits, sensors arrays, low-cost data storage devices for smart cards and price tags [6,25].

Over the last few years, high-quality, air stable, n-type transistors based on organic semiconductors have been demonstrated with performance close to that of the best p-type materials. However, most research efforts have focused on the development of materials with high field-effect mobility; as a result the mobility of n-channel organic field-effect transistor (OFET) exceeds that of the amorphous silicon FET (a-Si FET). On the other hand, very limited studies have been performed on the bias-stress stability of n-channel OFETs, which is of utmost importance to realize the full commercial potential of OFETs, as most of the fabricated OFETs still remain on the laboratory scale and work under vacuum conditions [26-33].

This thesis presents a systematic study on the growth kinetics of organic thin films based on different metal phthalocyanine molecules ($SnCl_2Pc$, VOPc and CuPc), which are grown on various substrates. Next, a systematic study on the low operating voltage, high air stable unipolar OFET is presented, which is highly desirable for real life applications. Further, it also includes results on a thorough study of the ambipolar OFET based on

heterojunction of organic thin films. These studies are very significant and should be addressed before commercialization of the devices, specifically for biological/chemical sensors, ionization detectors etc. The complete thesis work has been organized into EIGHT chapters, as summarized below:

Chapter 1 presents a brief introduction to the growth dynamics of organic thin films. In addition, fundamental issues related to the growth mechanism and origin of superior properties of organic molecules are discussed. A brief discussion on statistical analysis of the rough surface has been included. Starting from the fundamental properties of organic semiconductors, the basic principles of OFET operation and charge transport properties, bias-stress stability are briefly discussed. The fundamental parameters related to OFET performances (e.g. mobility, threshold voltage, current on/off ratio, characteristics time constant) are pointed out. The problems and challenges related to the stability of the devices are highlighted. Finally the focus of the present thesis is presented at the end.

Chapter 2 provides a brief account of the experimental procedures for the growth of organic thin films on various substrates using thermal vacuum-deposition technique, fabrication of the unipolar and bipolar OFETs and their characterizations are presented. Salient features of the experimental techniques, e.g., TGA, AFM, XRD, XPS, UV-Vis, I-V, C-V etc. used in the present work are discussed along with their working principles. The methodology adopted and for the analysis of the raw-data extracted from the images of organic thin films acquired from different instruments is also discussed.

In Chapter 3, the results on the growth dynamics of $SnCl_2Pc$ based n-type organic thin films on different inert like substrates are presented. We addressed the structural evolution of $SnCl_2Pc$ thin films grown by thermal evaporation on Si(100) and glass substrates as a function of thickness of the film. The growth dynamics of $SnCl_2Pc$ thin films has been studied using AFM, XRD, XPS, UV-Vis and height-height correlation function (HHCF) analysis. By analyzing the scaling behavior and 2D fast Fourier transforms, it is concluded that the morphological evolution of the deposited $SnCl_2Pc$ molecules follows a mound like formation model, which suggests that the $SnCl_2Pc$ crystallites grow in the upward direction as the film thickness increases on glass substrate, which may be due to the high step-edge barrier. One of the important findings is that the growth exponent β value for

$SnCl_2Pc$ thin film on glass substrate is comparable to that predicted by the random deposition model, while for Si substrate it is very small and results in "smoothening"-a lying down geometry, which may be due to the small step-edge barrier. This study is very much important, as it reveals suitability of a particular substrate for the device fabrication.

Chapter 4 discusses the growth dynamics of VOPc based promising p-type organic thin films on different substrates as function of substrate temperature. The growth dynamics of VOPc thin films has been studied using AFM, XRD, and HHCF analyses. We specifically analyzed the scaling behavior and 2D fast Fourier transforms of the AFM images. We investigated the temperature dependence of growth front scaling characteristics for VOPc thin films vapor deposited onto SiO_2 and ITO-glass substrates in the temperature range 23°C–210°C. With increasing substrate temperature, both the rms roughness amplitude (w) and the in-plane correlation length (ξ) increase closely following an Arrhenius behavior. We also investigated the evolution of surface morphology and scaling behavior of thickness dependent VOPc thin films grown on SiO_2 and ITO-glass substrates using atomic force microscopy (AFM), XRD, and height-height correlation function analyses. The root-mean-square roughness amplitude (w) evolves with film thickness (d) as a power law, $w \propto d^{\beta}$. From the height distribution and *scaling exponents* analysis, it is concluded that the roughening mechanism follows nearly a nonlinear type of film growth model.

Chapter 5 presents results on low operating voltage and low bias stress n-channel OFETs made of vacuum deposited $SnCl_2Pc$. OFETs were fabricated on PMMA/Al_2O_3 bilayer gate dielectric and on SiO_2 gate dielectric. The devices with top contact Ag electrode exhibit excellent n-channel behavior with electron mobility values of 0.01 cm^2/Vs, low threshold voltage of 4 V, current on/off ratio 10^4 with an operating voltage of 10 V. Bias stress instability effects are investigated during long term operation using thin film devices under low vacuum. The amount of bias stress of $SnCl_2Pc$ based OFETs is extremely small with characteristic relaxation time $>10^5$ s obtained using stretched exponential model. Stressing the $SnCl_2Pc$ devices by applying 10 V to the gate for half an hour results in a decrease of the drain current, I_{DS}, by only 10%. These devices show highly stable electrical behavior under multiple scans and low threshold voltage instability under electrical dc bias stress (for 2h) even after 40 days. These findings are very important, since low power

consumption, high air stable n-channel OFETs are less reported and these can be implemented in real life application, e.g., sensors, detectors. Further, the effect of contact metals on the electrical performances and the bias-stress stability in $SnCl_2Pc$ based n-channel OFETs was studied using Ag and Al contacts and it shows improved performance and operational stability of the OFETs with Ag contact.

Chapter 6 focuses on the device performance and air stability of VOPc based p-channel OFETs. OFET devices with a hexa-methyl disilazane (HMDS) passivation layer on SiO_2 layer shows high performance and better air stability than the devices with non-treated SiO_2 layer. The devices with top contact Au electrodes exhibit excellent p-channel behavior with high hole mobility value of ~0.01 cm^2/Vs for HMDS-treated devices. Bias stress stability study shows stretchehed expoential decay behavior during the long term operation with a constant bias voltage in ambient conditions with a resulting decay of drain current by only <15% for the HMDS-treated case, while it shows a very sharp decay of constant by >70% for the devices with bare SiO_2 layer. The corresponding characterics time constant (τ) is calculated as ~10000 s for HMDS-treated case, while it is very low (480 s) for bare/non-treated devices. The poor performance of the device based on bare SiO_2 layer is believed to be due to the charge trapping by the voids created in the inter grain region of the film, while it is almost negligible for HMDS-treated SiO_2 case. This work opens up the possibility of tuning the bulk properties of OFETs using self-assembled monolayers.

Chapter 7 presents the fabrication procedure and analysis of low operating voltage and low bias-stress top-contact $SnCl_2Pc$/CuPc heterostructure-based bilayer ambipolar OFETs. Herein, a symmetrical Ag top contact-bottom gate (TC-BG) bilayer ambipolar organic field-effect transistor based on the heterojunction of vacuum-deposited small molecules, tin(IV) phthalocyanine dichloride ($SnCl_2Pc$) (n-channel) and copper phthalocyanine (CuPc) (p-channel) has been demonstrated. A hydroxyl free PMMA with Al_2O_3 bilayer dielectric exhibits low operating voltage and low bias stress (relaxation time $\tau=10^5$ s) for both n-channel and p-channel cases. The optimized $SnCl_2Pc$/CuPc heterostructure exhibits balanced carrier mobility and both types of charge carriers, electrons and holes, are facilitated by the same low work function Ag contact, depending on the bias conditions, from the TC-BG architecture. The Ag contact also exhibits Ohmic injection of

charge carriers with low contact resistance in the n-channel region under an optimal heterostructure configuration. The contact resistance for electron and hole-injection is strongly dependent on the thickness of the $SnCl_2Pc$ and CuPc layers, respectively. The bias stress stability is modeled using a stretched exponential fitting. Our results demonstrate that the ambipolar device characteristics and performance can be controlled by adjusting the thickness of the molecular layer, which is highly desirable. Such simple heterostructure engineering with utilization of organic molecular semiconductors can truly enable the development of promising low-cost and flexible organic electronics for extensive applications. This work is very much important for the development of improved organic light emitting field-effect transistors and organic inverters.

In **Chapter 8,** we summarize the important findings of the present thesis along with highlights of the new findings and its implications for the future research. Open questions and the different directions of future studies related to this thesis are presented at the end.

List of Publications:

In Peer Reviewed Journals:

1. Murali Gedda, Nimmakayala V. V. Subbarao, Sk. Md. Obaidulla and Dipak K. Goswami, "*High carrier mobility of CoPc wires based field-effect transistors using bi-layer gate dielectric"*

***AIP Advances* 3, 112123 (2013).**

2. SK Md Obaidulla, D. K. Goswami and P. K. Giri, "*Low bias stress and reduced operating voltage in $SnCl_2Pc$ based n-type organic field-effect transistors*",
***Appl. Phys. Lett.* 104, 213302 (2014).**

3. Sk. Md. Obaidulla and P. K. Giri, "*Low operating voltage and low bias stress in top-contact $SnCl_2Pc$/CuPc heterostructure-based bilayer ambipolar organic field-effect transistors*",
***J. Mater. Chem.* C 3, 7118 (2015).**

4. Sk. Md. Obaidulla and P. K. Giri, "*Surface roughening and scaling behavior of vacuum-deposited $SnCl_2Pc$ organic thin film on different substrates*",
***Appl. Phys. Lett.* 107, 221910 (2015).**

5. Sk. Md. Obaidulla, Subhash Singh, Y. N. Mohapatra and P. K. Giri**, "***Ambient condition bias stress stability of VOPc based p-channel organic field-effect transistors*", **Physics Status Solidi (under Review)**

6. Sk. Md. Obaidulla, R. Alam and P. K. Giri. "*Temperature dependent growth study of VOPc - a non-planar molecule based organic thin films*".
(***Journal of Applied Physics***, to be communicated)

7. Sk. Md. Obaidulla, Subhash Singh, Y. N. Mohapatra and P. K. Giri. "*Growth roughening and scaling behavior of VOPc based non-planar organic thin films on different substrates*".
(***Journal of Applied Physics***, to be communicated)

8. Sk Md Obaidulla, and P. K. Giri "*Effect of contact metal on the performances and the bias stress stability of $SnCl_2Pc$ based n-channel Organic Field-effect Transistors*".
(***Organic Electronics***, to be communicated).

Conference Papers:

1. Sk Md Obaidulla, Dipak K Goswami, "*Morphological and Photo physical properties of Thin Films of 3-Nitro perylene*", International Conference on Material Science (**ICMS-2013**)", organized by Department of Physics, Tripura University, Tripura, India, February 21-23, 2013.

2. Sk Md Obaidulla, Dipak K Goswami, "*Growth and Morphological properties of Thin Films of perylene derivatives*" "6th India-Singapore Joint Physics Symposium on Physics of Advance Materials (**ISJPS-2013**)", Department of Physics & Meteorology, IIT Kharagpur, India, February 25-27, 2013.

3. Sk Md Obaidulla, V suresh, Dipak K Goswami, "*High performances n-channel organic field-effect transistors based on core halogenated perylene derivatives*", 3rd International Conference on Advanced Nanomaterials and Nanotechnology (**ICANN-2013**)", Center for Nanotechnology, IIT Guwahati, Guwahati, India, Dec 8-10, 2013.

4. Sk Md Obaidulla, P. K. Giri, Dipak K Goswami, "*Tin (IV) phthalocyanine dichloride based n-type organic field-effect transistors with high operation stability*", 3rd international conference on physics at surfaces and interfaces (**PSI -2014**)"- EMSI, IOP, IIT-BBS and IACS-Kolkata, Puri, Odisha, India, Feb 24 – 28, 2014,.

5. Sk Md Obaidulla, P. K. Giri, "*Growth dynamics of SnCl2Pc/CuPc heterostructure and ambipolar organic field-effect transitors*" "1st international conference on emerging materials: characterization and applications (**EMCA-2014**)", CGCRI and NIT Durgapur, Kolkata, India, Dec 4-6, 2014.

6. Sk Md Obaidulla, P. K. Giri, "*Reliability in an n-type organic field-effect transistors*" "Research Conclave 2015", IIT Guwahati, Guwahati, India, March 23-26.

7. Sk Md Obaidulla, and P. K. Giri, "*Contact Effect on the performances and the Bias Stress in $SnCl_2Pc$ based n-channel Organic Field-effect Transistors*", 12th International Thin-Film Transistor Conference (**ITC-2016**), Hsinchu, Taiwan, Feb 25-26, 2016.

8. Sk Md Obaidulla, and P. K. Giri, "*Performances and air-stability in $SnCl_2Pc$ based n-channel Organic Field-effect Transistors*", 2nd Research Conclave 2016, organized by IIT Guwahati, Guwahati, India, March 17-20, 2016. **(*Best Poster Award)***

Conference/ Workshops Attended:

1. "2nd International Conference on Advanced Nanomaterials and Nanotechnology (**ICANN-2011**)", IIT Guwahati, Dec 8-10, 2011.
2. ***"****Quality improvement Programme – Computational Techniques in Physics", IIT Guwahati, 1-6 Aug, 2011.*
3. *"The Short course on Organic Electronics and Solar Cells (**SCDT – 2012**)" IIT Kanpur, 9–14 July, 2012.*
4. ***"INUP** Hands – on Training on 'Nano-fabrication Technologies", Centre for Nano Science and Engineering, Indian Institute of Science, Bangalore, and 18 – 28 June, 2013.*
5. *2nd National Workshop on "MEMS/NEMS and Theranostic Devices" (**NWNTD**), IIT Guwahati, 16-17March, 2015.*
6. *National Workshop on "Advanced Probing Techniques in TEM (APTTEM-2016)", IIT Guwahati, 15-16 February, 2016*
7. *2nd National Workshop on "MEMS/NEMS and Theranostic Devices" (**NWNTD**), IIT Guwahati, 21-22 March, 2016.*

Online Course Study

1. "Fundametals of Nanoelectronics: Basic concepts", *by nano-Hub,* ***Purdue university****, spring 2012.*

References:

[1] Z. Bao, J. Locklin, Organic Field-Effect Transistors, CRC Press, Boca Raton, FL, USA, 2007.

[2] H. Wang, D. Song, J. Yang, B. Yu, Y. Geng, D. Yan, Applied Physics Letters **90**, 253510 (2007).

[3] J. Cornil, J.L. Brédas, J. Zaumseil, H. Sirringhaus, Adv. Mater. **19**, 1791 (2007).

[4] D. Song, H. Wang, F. Zhu, J. Yang, H. Tian, Y. Geng, D. Yan, Adv. Mater. **20**, 2142 (2008).

[5] R.D. Yang, J. Park, C.N. Colesniuc, I.K. Schuller, J.E. Royer, W.C. Trogler, A.C. Kummel, The Journal of Chemical Physics **130**, 164703 (2009).

[6] H. Klauk, Organic Electronics: Materials, Manufacturing and Applications.

[7] G.H. Gelinck, H.E.A. Huitema, E. van Veenendaal, E. Cantatore, L. Schrijnemakers, J.B.P.H. van der Putten, T.C.T. Geuns, M. Beenhakkers, J.B. Giesbers, B.-H. Huisman, E.J. Meijer, E.M. Benito, F.J. Touwslager, A.W. Marsman, B.J.E. van Rens, D.M. de Leeuw, Nat Mater **3**, 106 (2004).

[8] J. Zaumseil, H. Sirringhaus, Chem. Rev. **107**, 1296 (2007).

[9] H. Ohta, T. Kambayashi, K. Nomura, M. Hirano, K. Ishikawa, H. Takezoe, H. Hosono, Advanced Materials **16**, 312 (2004).

[10] G.A. Chamberlain, Solar Cells **8**, 47 (1983).

[11] S. Md. Obaidulla, D.K. Goswami, P.K. Giri, Appl. Phys. Lett. **104**, 213302 (2014).

[12] A.L. Baraba´si, H.E. Stanley, Fractal Concepts in Surface Growth, Cambridge University Press, Cambridge, 1995.

[13] Y.P. Zhao, J.B. Fortin, G. Bonvallet, G.C. Wang, T.M. Lu, Phys. Rev. Lett. **85**, 3229 (2000).

[14] D. Tsamouras, G. Palasantzas, J.T.M. De Hosson, Appl. Phys. Lett. **79**, 1801 (2001).

[15] S.M. Obaidulla, P.K. Giri, J. Mater. Chem. C **3**, 7118 (2015).

[16] Y. Zhao, G.-C. Wang, T.-M. Lu, Characterization of Amorphous and Crystalline Rough Surface: Principles and Applications, Academic Press, New York, 2001.

[17] A.C. Dürr, F. Schreiber, K.A. Ritley, V. Kruppa, J. Krug, H. Dosch, B. Struth, Phys. Rev. Lett. **90**, 016104 (2003).

[18] S. Zorba, L. Yan, N.J. Watkins, Y. Gao, Appl. Phys. Lett. **81**, 5195 (2002).

[19] S. Yim, T.S. Jones, Phys. Rev. B **73**, 161305 (2006).

[20] S. Zorba, Y. Shapir, Y. Gao, Phys. Rev. B **74**, 245410 (2006).

[21] S. Yim, T.S. Jones, Appl. Phys. Lett. **94**, 021911 (2009).

[22] J. Kim, N. Lim, C.R. Park, S. Yim, Surf. Sci. **604**, 1143 (2010).

[23] G. Zhang, B.L. Weeks, M. Holtz, Surf. Sci. **605**, 463 (2011).

[24] F. Schreiber, Phys. Status Solidi (a) **201**, 1037 (2004).

[25] B.A. Jones, M.J. Ahrens, M.-H. Yoon, A. Facchetti, T.J. Marks, M.R. Wasielewski, Angewandte Chemie International Edition **43**, 6363 (2004).

[26] S.D. Wang, T. Minari, T. Miyadera, Y. Aoyagi, K. Tsukagoshi, Applied Physics Letters **92**, 063305 (2008).

[27] H. Sirringhaus, Advanced Materials **21**, 3859 (2009).

[28] B. Lee, A. Wan, D. Mastrogiovanni, J.E. Anthony, E. Garfunkel, V. Podzorov, Physical Review B **82**, 085302 (2010).

[29] J. Kim, J. Jang, K. Kim, H. Kim, S.H. Kim, C.E. Park, Advanced Materials **26**, 7241 (2014).
[30] W.H. Lee, H.H. Choi, D.H. Kim, K. Cho, Advanced Materials **26**, 1660 (2014).
[31] L. Wang, H. Qin, W. Zhang, L. Zhang, D. Yan, Thin Solid Films **545**, 514 (2013).
[32] P.F. Baude, D.A. Ender, M.A. Haase, T.W. Kelley, D.V. Muyres, S.D. Theiss, Applied Physics Letters **82**, 3964 (2003).
[33] M.M. El-Nahass, K.F. Abd-El-Rahman, A.A. Al-Ghamdi, A.M. Asiri, Physica B: Condensed Matter **344**, 398 (2004).

भारतीय प्रौद्योगिकी संस्थान गुवाहाटी • Indian Institute of Technology Guwahati •

भारतीय प्रौद्योगिकी संस्थान गुवाहाटी
Indian Institute of Technology Guwahati

List of Symbols and Abbreviations

Abbreviations	Description
AFM	Atomic Force Microscopy
XRD	X-ray Diffraction
TGA	Thermogravometric analysis
Al_2O_3	Aluminum oxide
OFET	Organic Field-Effect Transistors
Å	Angstrom
$SnCl_2Pc$	Tin (IV) phthalocyanine dichloride
CuPc	Copper (II) Phthalocyanine
VOPc	Vanadium (IV) oxide phthalocynaine
-OH	Hydroxyl group
HMDS	Hexamethyl disilazane
Ag	Silver
PMMA	Polymethyl methacrylate
PS	Polystyrene
PVA	Poly vinyl phenol
OMVD	Organic Molecular Beam Deposition
HOMO	Highest Occupied Molecular Orbital
LUMO	Lowest Unoccupied Molecular Orbital
HHCF	Height-height Correlation Function
ACF	Auto Correlation Function
2D FFT	2D-fast Fourier Transform
ξ	Correlation Length
α	Growth Exponent

Abbreviations	Description
β	Roughness Exponent
$1/z$	Dynamic Exponent
Au	Gold
Al	Aluminum
BS	Bias stress
C_i	Capacitance
k	Dielectric Constant
W/L	Channel Width/Channel Length
V_{th}	Threshold Voltage
I_{DS}	Drain-Source Current
I_{DS}/I_0	Normalized Drain Current
μ_{sat}	Saturation Mobility
S	Source Electrode
D	Drain Electrode
G	Gate Electrode
SS	Subthreshold Slope
β	Dispersion Parameter
τ	Characteristics Time Constant
HV	High Vacuum
SiO_2	Silicon di-oxide
TC	Top-contact
BG	Bottom gate
SAM	Self-assembled monolayer

Chapter 1

Introduction

This chapter provides a brief introduction to organic semiconductors-small molecules/monomers, polymers, and few specific molecules: $SnCl_2Pc$, VOPc, and CuPc. The growth study of organic thin films, and charge transport mechanism in organic semiconductors have been discussed. Thereafter, the fundamentals of organic field-effect transistors including working principles, hysteresis, and the device reliability are briefly addressed. The lacunae and challenges of growth dynamics of organic thin films and fabrication of low operating voltage, highly stable organic field-effect transistors and the focus of the present thesis and organization of the thesis are presented at the end.

1.1 Organic Semiconductors

Organic semiconductor refers to organic (non-metallic) materials that exhibit semiconducting properties. Semiconductivity in these materials occurs for single molecules, short chains of molecules and long polymer chains depending on the material. Small molecule semiconductor includes pentacene, rubrene, anthracene, metal phthalocyanine etc. The first study of electronic properties of the dark and photo conductivity on anthracene organic crystals dates back to the early 20^{th} century [1,2]. After the discovery of electroluminescence in the 1960s [3], molecular crystals were intensely investigated by many researchers. These investigations established the basic processes involved in the charge carrier types as well as charge carrier transport. The first application of organic semiconductor started only in the 1980s, on both small molecules and doped conjugated polymers [4-7]. The development and the application of the organic molecules in their various forms (small molecules, polymer chains) are, now the object of the study of a new discipline, called Organic Electronics, that uses organic molecules instead of the classical inorganic semiconductors normally used for the production of electronic and optoelectronic devices, such as organic field-transistors (OFET) [8,9], organic light emitting field-effect transistors (OLFET) [10,11], light emitting diode (LED), lighting products, radio frequency identification tags (RFIDs) [12], etc. In the

meantime, major advances in the synthesis of new forms of conducting and semiconducting organic materials and polymers have enabled the fabrication of high-performance devices using inexpensive techniques, such as thermal evaporation, spin-coating, ink-jet printing, and screen-printing, compatibility with different substrates, low processing temperature. However, many aspects of the device reliability need to be overcome (i.e. environmental stability, lifetime, etc.), before commercialization of this alternative technology becomes a reality. Device reliability lies on a good understanding of their electrical properties.

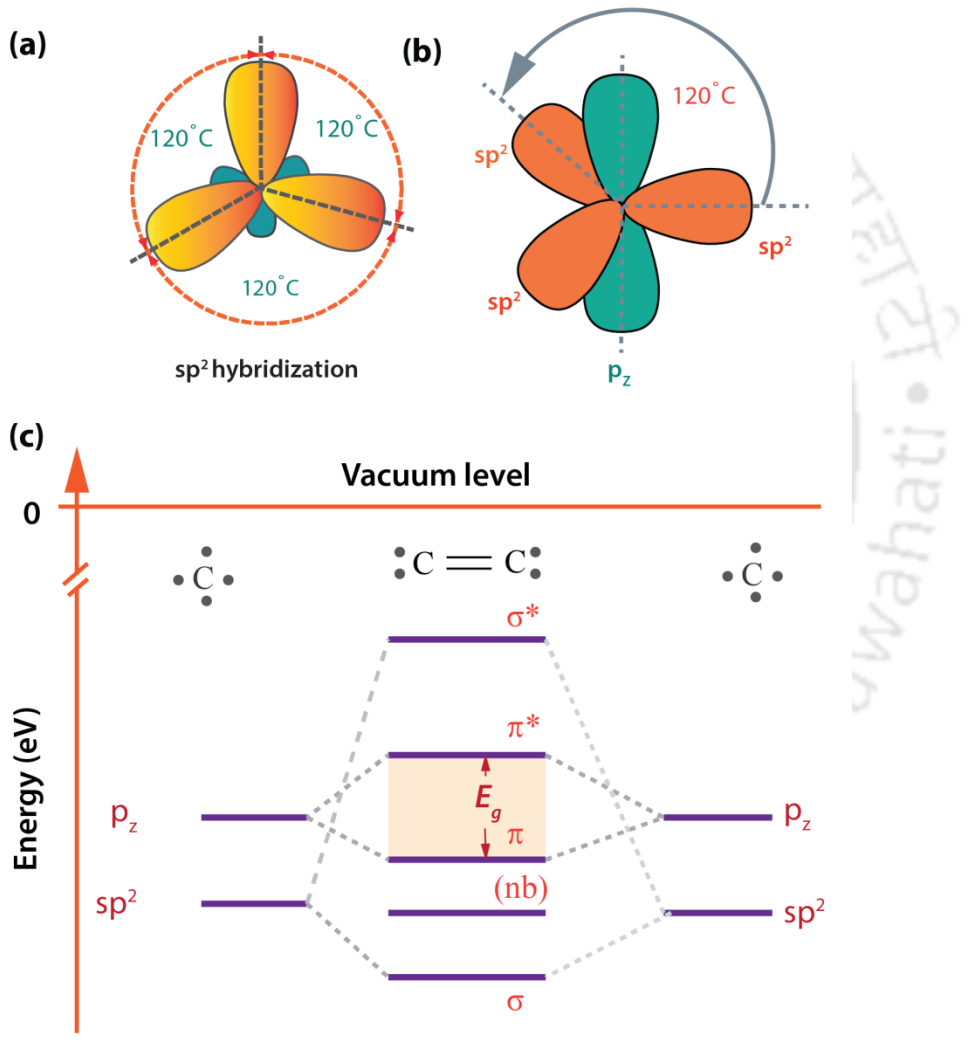

Figure 1.1: (a) A schematic of sp^2 hybridization of a carbon atom, (b) hybridization of sp^2 and p_z atomic orbitals. (c) Energy level diagram of two interacting carbon atoms and of two individual carbon atoms combined to form π, σ and nonbonding molecular orbitals [13].

Organic semiconductors consist of organic materials which exhibit semiconducting properties. The shape and the size of these molecules can vary drastically from relatively small molecules over larger molecules like phthalocyanine molecules, which are studied extensively in this thesis. Phthalocyanines are very large and complex molecules. A common feature of all organic semiconductors is the presence of a conjugated π-electron system. The formation of this system can be explained by the electronic configuration of the binding carbon atoms. The electronic configuration of a free carbon atom is $1s^2 2s^2 2p^2$, i.e. the *1s*, *2s* and 2*p* orbitals are occupied by two electrons. When two carbon atoms are bound via a double bond, an sp^2-hybridization is formed (see **Fig. 1.1(a)**) [14]. One *s*- and two *p*-orbitals (p_x and p_y) form three coplanar degenerated orbitals. Thus, an σ-bond between two neighboring carbon atoms is formed. The two p_z-orbitals remain perpendicular to this plane. Two neighboring p_z-orbitals are overlapping and the so-called π-bond is generated, as depicted in **Fig. 1.1(b)**. The electrons in this orbital are delocalized. Due to the interaction with the unpaired electron of the neighboring carbon atom, a splitting of the energy level takes place and a bonding π and an antibonding π* orbital are formed, which are referred to as highest occupied molecular orbital (HOMO, π) and lowest unoccupied molecular orbital (LUMO, π*), respectively. This effect is depicted in **Fig. 1.1(c)**. After filling the levels from low to high (using Hund's Rules for the spins) it can be recognized that four electrons (two from each carbon atom) are used in bonding, two in σ-molecular orbitals, and two in π molecular orbitals. The remaining four electrons are in nonbonding (nb) orbitals and are still available for bonding to the rest of the chain and the ligands. Thus the formation of a chain of single and double bonds thus causes an energy structure with a HOMO and a LUMO level, with a splitting ('band gap', E_g) in the range of semiconductors [13]. So, it is clear that a material with only single σ bonds, like polyethylene, will have a much wider band gap and will not easily fall in to the category of semiconductors. The same goes for polyallenes with only double bonds. To result in a semiconductor material, conjugation is essential. Generally speaking, the larger the conjugated network is on a molecule, the smaller the HOMO-LUMO gap [15]. Thus, molecular solids with delocalized π-electron systems show electronic excitation energies in the range of one to several eV. This corresponds to the transition of an electron from the HOMO to the LUMO. So, it can be noted that σ-bonds are responsible to form the backbone of the molecule, while π-orbitals are involved in the charge carrier

transport, as schematically shown in **Fig. 1.2**. In practice, most organic semiconductors conduct better via holes because of a higher efficiency of trapping (immobilizing) of electrons.

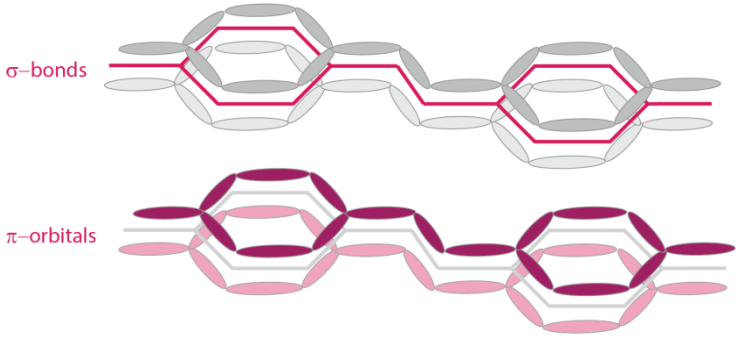

Figure 1.2: A schematic of coupled C-atoms in conjugated double bond structure.

The active layer in most organic electronic devices consists of one or more thin films of organic semiconductors. These films can be amorphous or polycrystalline. Apart from thin films, also highly pure single-crystals of organic semiconductors are under intensive research. In this case, band-like transport behavior has been observed HOMO and LUMO can be seen as analogs to valence and conduction band in inorganic semiconductors, respectively. However, an important difference to inorganic semiconductors is the fact that HOMO and LUMO do not form extended band.

1.2 Organic Semiconducting Molecules

The immensely broad spectrum of organic semiconducting molecules can be classified into two major groups: polymers, and small weight molecules or oligomers [16]. Small weight molecules have a well-defined molecular weight and can be found with high purity. On the contrary, polymers are long-chain molecules formed by the repetition of molecular units. The number of repetition units is indeterminate, thus leading to a variable molecular mass. From the point of view, the electronic and optical properties are highly reproducible for the case of small molecules, while it can vary batch to batch for polymer case. The polymers are generally processed from solution, e.g. by spin-coating method and results in poor performances due to irregular grain distribution. On the contrary, small molecules/monomers and oligomers are generally deposited by vacuum deposition method. Their major advantage

with respect to the polymers is that they can be grown in films of high purity and crystalline order, two important requirements to obtain high charge carrier mobility. Devices properties are highly reproducible due to the inherent properties. Some of the very common small molecules and polymers are schematically shown in **Fig. 1.3**. In this thesis, we have extensively studied the growth kinetics of thin films formed by phthalocyanine based small molecules.

One of the most widely studied classes of organic semiconductors is the metallophthalocyanine (MPc) family of molecules [17]. They are used in organic photovolataic devices (OPVs) devices, organic light emitting diodes (OLEDs), organic sensors due to their ease of synthesis, chemical stability and compatibility with vacuum evaporation. They also exhibit a certain degree of "specific tunability" due to various metals ion (M = Sn, Cu, CO, H_2, Zn, etc.) and the side groups (R=F, Cl, NH_2, $O(CH_2)_{10}OH$, etc.) that can be introduced within a broad range of composition [8].

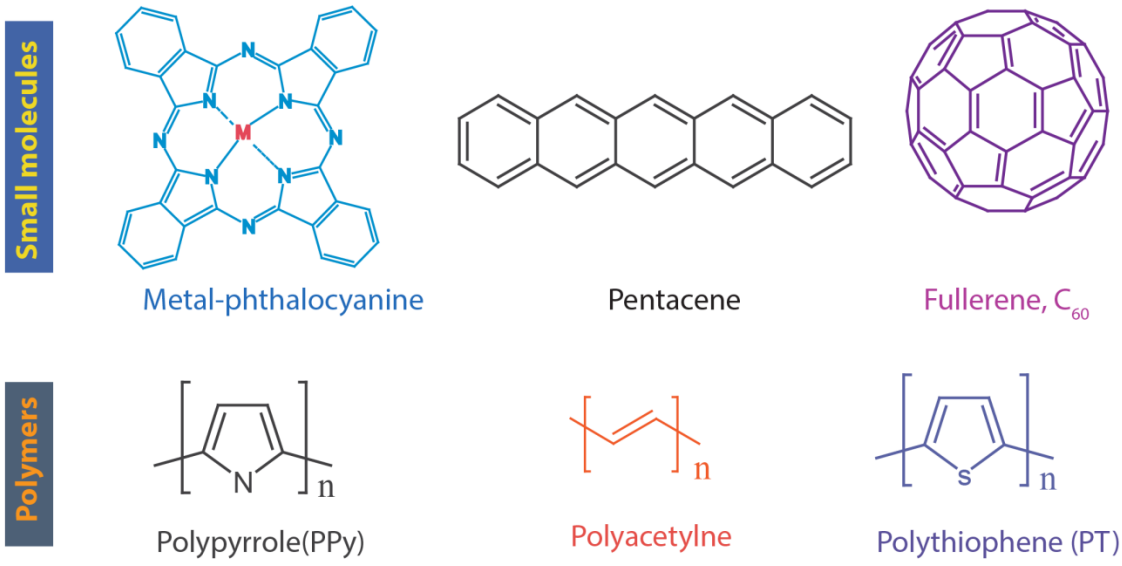

Figure 1.3: Molecular structure of a few common small molecules: Metal phthalocyanine, pentacene, fullerene (upper panel) and polymers: polypyrrole, polyacetylene, polythiophene (lower panel).

1.2.1 Tin (IV) Phthalocyanine Dichloride ($SnCl_2Pc$)

Among the different phthalocyanines, for the present study, we have chosen for our studies tin (IV) phthalocyanine dichloride [$SnCl_2Pc$: $Sn(C_{32}H_{16}N_8)Cl_2$, n-type], a sky blue dye, which is schematically represented in **Fig. 1.4 (a)**. It is a non-planar disc-like molecule belonging to the group of the metal-phthalocyanines, in which Cl- atoms are 'stick-out' top and bottom pyramidacally both side from the molecular plane where Sn metal atom resides in the molecular center. In the triclinic forms $SnCl_2Pc$, the Pc macrocycles are not staggered but slipped. A view of the $SnCl_2Pc$ molecular packing in the unit cell is shown in **Fig. 1.4 (b)**. By simply changing the side group, a large number of similar sister phthalocyanines with different optoelectronic properties can be synthesized. The solubility of the $SnCl_2Pc$ complex in polar solvents, such as water, methanol and ethanol, is insignificant, but the complexes are slightly soluble in pyridine, dimethylformamide, dimethyl sulfoxide, tetrahydrofuran and high-boiling aromatic solvents, such as chloronaphthalene or quinoline [18]. The chlorine (Cl) ions increase the electron affinity of the molecules and favor an efficient electron injection into the empty LUMO states. As a consequence, the preferential n-type semiconducting behavior is observed for $SnCl_2Pc$ when combined with typical contact materials, such as Ag, Al. The electric properties of $SnCl_2Pc$ are reasonably stable upon air-exposure. Since there are only few air-stable n-type organic semiconductors, this makes

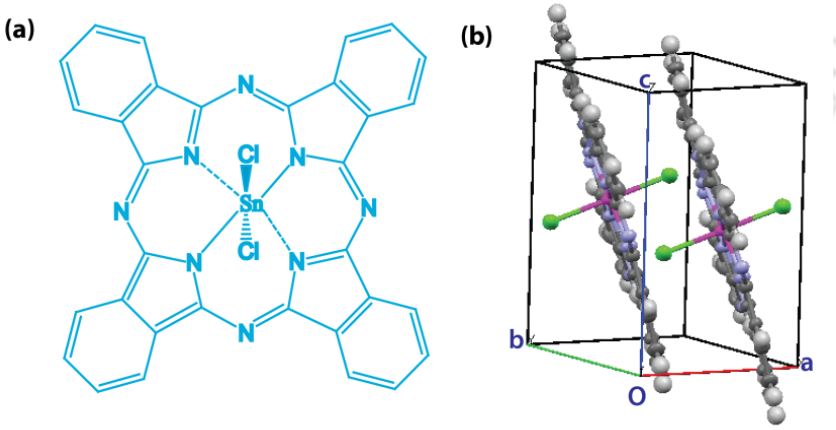

Figure 1.4: (a) The molecular structure and dimension of $SnCl_2Pc$. (b) The molecular arrangement within a thin film unit cell [18].

$SnCl_2Pc$ an interesting candidate for all those applications in which both n-type and p-type semiconductors are needed, such as organic solar cells, ambipolar transistors or OLEDs, organic light emitting filed-effect transistors. There are a few studies focused on the bulk-structure of various phthalocyanines, including a recent study devoted to the characterization of $SnCl_2Pc$ by X-ray powder diffraction, for which the obtained cell parameters, volume and number of molecules per unit cell are shown in **Table 1.1**.

Table 1.1: Summary of the cell parameters reported for the bulk structure of $SnCl_2Pc$ [18].

$SnCl_2Pc$	**Triclinic, spacegroup $P\bar{1}$**
a	7.363 Å
b	8.676 Å
c	11.048 Å
α	74.21°
β	80.33°
γ	85.47°
V	669.1 $Å^3$
M	702.12

1.2.2 Vanadium (IV) Oxide Phthalocyanine (VOPc)

Vanadium (IV) oxide phthalocyanine [VOPc: $VO(C_{32}H_{16}N_8)$, p-type**]** is a deep blue dye and shows p-type semiconducting behavior in combination with gold (Au) contacts. Vanadyl phthalocyanine (VOPc, schematically shown in **Fig. 1.5 (a)**, which is different from the planar phthalocyanines, and show a nonplanar, pyramid-like molecular geometry. The V–O axis lies perpendicular to the plane of the molecule, leading the vanadyl oxygen atom to 'stick out' of the overall molecular plane. VOPc molecule is also the building block of other molecules, as it can be doped at side groups. A view of the VOPc molecular packing in the unit cell is shown in **Fig. 1.5(b)** [19,20]. In general VOPc molecules preferentially follow with an "edge-on" direction on the substrates [21]. Non-planar metal phthalocyanines exhibit some unique advantages over their planar counterparts, including broader optical absorption

profiles and shifted frontier energy level positions. These properties have led to their use in efficient organic photo voltaic cells (OPVs) and organic filed-effect transistor (OFET) devices. There are several studies focused on the bulk-structure of vanadium oxide phthalocyanines, by X-ray powder diffraction, for which the obtained cell parameters, volume and number of molecules per unit cell are shown in **Table 1.2.**

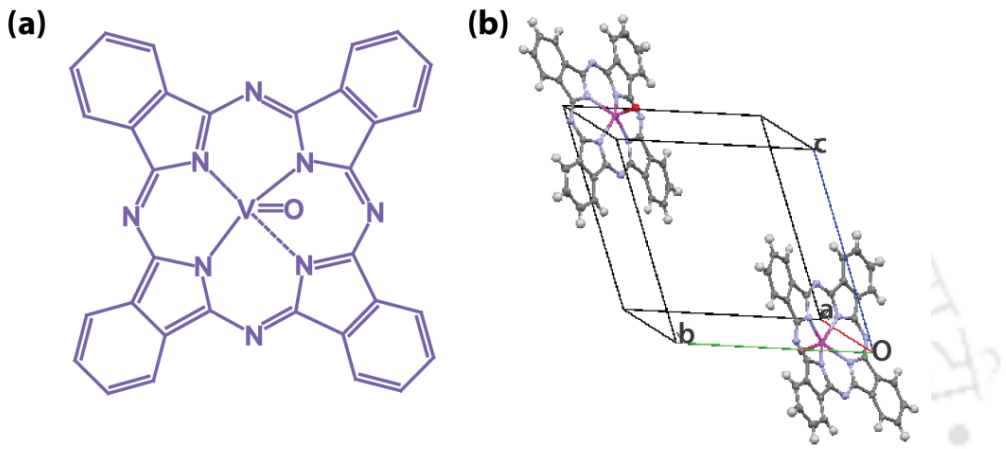

Figure 1.5: (a) The molecular structure and dimension of VOPc. (b) The molecular arrangement within a thin film unit cell [20].

Table 1.2: Summary of the cell parameters reported for the bulk structure of VOPc molecules [20].

VOPc	**Triclinic spacegroup($P\bar{1}$)**
a	12.027 Å
b	12.58Å
c	8.71Å
α	96.15°
β	94.88°
γ	68.16°
V	1 212Å^3
M	579.5

1.2.3 Copper (II) Phthalocyanine (CuPc)

Copper phthalocyanine [CuPc: $Cu(C_{32}H_{16}N_8)$**, p-type]** is a blue dye. In a Scottish dye factory, a reaction vessel cracked and exposed the Pc-reagents to the outer steel piping, leading to the creation of a green–blue material. This material was CuPc, a Pc ligand with Cu ion in the center. The possible use of CuPc in general, as dye pigments became immediately apparent and industrial production started in 1935 due to their intense coloring properties and they can also be employed as a building block for the construction of new molecular materials for optoelectronic applications. These phthalocyanines are planar molecules. The molecule has a completely conjugated structure that exhibits exceptional stability apart from the semiconducting properties [8]. From the planar structure of the molecule one can see how effectively the metal atom is protected within the interior of the molecule. The central metal atom is covalently bonded with two nitrogens of the porphine ring and also has co-ordinate linkage with two other nitrogens of the same ring (see **Fig. 1.6(a)**). The other factors that contribute to the stability of phthalocyanines are the symmetry of the molecule and the lack of any dipole moment. There are several copper phthalocyanine analogues that have been reported, in which the isoindole unit has been replaced with various other heterocyclic rings.

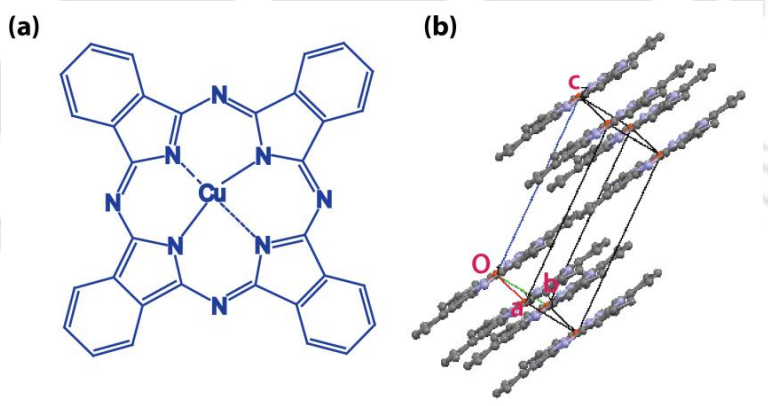

Figure 1.6: (a) The molecular structure and dimension of CuPc. (b) The molecular arrangement within a thin film unit cell [19,22].

It has a triclinic unit cell containing one molecule; A view of the VOPc molecular packing in the unit cell is shown in **Fig. 1.6(b)** [19]. From the crystallographic information, four different polymorphs were identified: phases α, β, γ and x. The two most common structures in CuPc are the β phase and the metastable α phase and this compound has no toxicity and

carcinogenic effects. Those phases can be distinguished by the overlap of their neighboring molecules. Their structural properties are summarized in **Table 1.3** [19].

Table 1.3: Summary of the cell parameters reported for the bulk structure of CuPc (β-phase) molecules [19].

CuPc	**Triclinic space group ($P\bar{1}$)**
a	12.886 ± 0.002 Å
b	3.769 ± 0.003 Å
c	12.061 ± 0.003 Å
α	96.22 ± 0.07°
β	90.62 ± 0.04°
γ	90.32 ± 0.08°
V	582.3 ± 0.5 Å3
M	12.886 ± 0.002 Å

1.3 Growth Kinetics of Thin Films

We briefly discuss general issues related to growth physics of thin films, including epitaxial relations, surface and interface energies, growth modes, correlation functions, dynamic scaling, and growth exponents. We also point out the general features that distinguish organic systems from inorganic systems, such as the different interaction potentials and the internal degrees of freedom of organic molecules. **Figure 1.7** schematically represents the processes relevant in organic thin film growth, such as adsorption (as a result of a certain impingement rate), desorption, intra-layer diffusion (on a terrace), interlayer diffusion (across steps), nucleation and growth of islands [23].

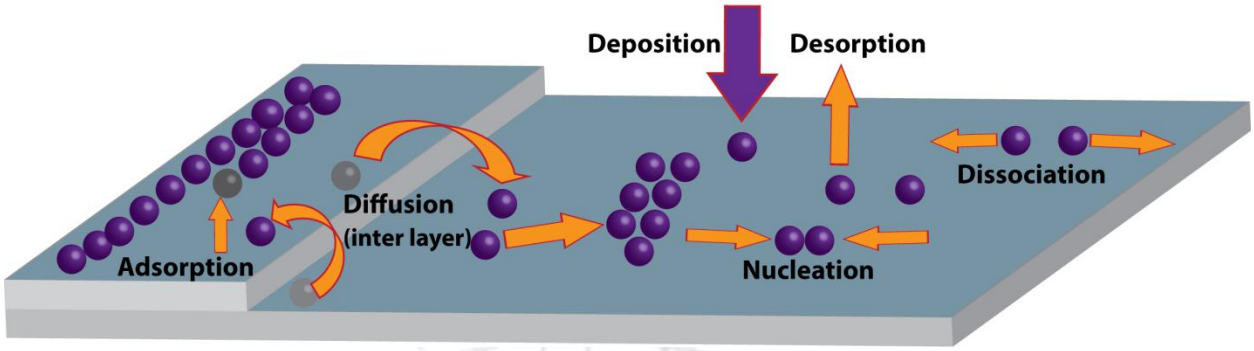

Figure 1.7: Schematic of processes of organic thin film growth, such as adsorption, desorption, intra-layer diffusion, interlayer diffusion, nucleation and growth of islands [23].

1.3.1 Quantitative Analysis of Rough Surface

Mathematically rough surfaces can be described by a surface height profile $h(\boldsymbol{r},t)$, where h denotes surface height with respect to the substrate at a position $\boldsymbol{r}$ on the surface at the time t. The functional form of $h(\boldsymbol{r},t)$ implies that there is only one surface height at a particular $\boldsymbol{r}$, which means $h(\boldsymbol{r},t)$ should be single valued function. Surface growth is commonly referred as "$d+1$" dimensions, which means that the substrate is d-dimensional, and the growth takes place in one extra dimension. Growth in "2+1" dimensions is the most common experimentally, as depositions usually occur on a planar substrate. **Figure 1.8** shows the

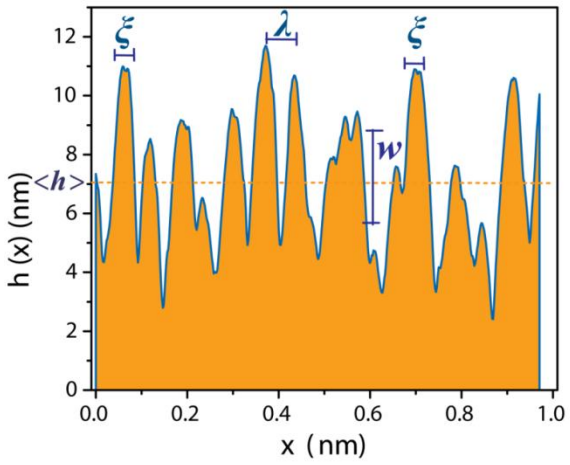

Figure 1.8: A schematic of statistical parameters used to describe the rough surface of a thin film. Here the mean height is $\langle h \rangle$, interface width is $\boldsymbol{w}$, lateral correlation length is $\boldsymbol{\xi}$, and wavelength is $\boldsymbol{\lambda}$.

schematic of surface height profile along with mean height $\langle h \rangle$, interface width w, lateral correlation length ξ, and wavelength λ [24].

Mean Height:

The mean surface height $\langle h \rangle$ of a surface profile is defined as

$$\langle h \rangle \equiv \langle h(r,t) \rangle .$$

It is very common to redefine the surface height profile such that $\langle h \rangle = 0$, by choosing a suitable reference height. This is helpful when concentrating on surface height fluctuations because any artificial effect introduced by the mean height is removed. If the deposition rate is constant, then the average height increases linearly with time i.e. $\langle h \rangle \sim t$.

Interface width/ RMS Roughness (W):

The most common statistics used to describe the roughness of a surface is the standard deviation W of the surface heights, also called the interface width or root-mean-square (RMS) roughness. The interface width w is defined as

$$w(t) \equiv \sqrt{\left(\langle h(r,t)^2 \rangle - \langle h(r,t) \rangle^2 \right)} \tag{1.1}$$

Larger values of the interface width indicate a rougher surface. It is common to observe a power law behavior for the interface width with deposition time,

$$w(t) \sim t^{\beta} \tag{1.2}$$

Where β is referred to as the *growth exponent* and it is widely used to describe the dynamic properties of thin films. It has also been seen that the saturation value of w increases with increasing L (system size) and its follows the power law,

$$w_{sat} \sim L^{\alpha} \tag{1.3}$$

where α ($0 \leq \alpha \leq 1$) *is* the *roughness exponent*, and it describes the surface fractility [25].

Lateral Correlation Length ξ:

After certain deposition time, the surface height saturates, which means in growth the process correlation develops along the surfaces, which implying that the different sites of the surface are not completely independent, but depend upon the heights of neighboring sites. The

typical distance, over which the heights "know about" each other/the characteristics distance over which they are correlated – is called correlation length, and it is denoted by ξ**.** It has been found that $\boldsymbol{\xi}$ is related with deposition time as

$$\xi \sim t^{1/z} \tag{1.4}$$

where **z** is called the *dynamic scaling exponent*. For some systems, scaling exponents are related by $1/z \approx \beta/\alpha$ [23].

ξ can also be determined from the autocorrelation function, $R \equiv {}^{1}/_{w^2}\,\langle h(r,t)h(r+r',t)\rangle$, and it can be found out from the following equation for the self-affine surface [26],

$$g(r) = 2w^2\left[1 - exp\left\{-\left(\frac{r}{\xi}\right)^{2\alpha}\right\}\right]$$

Height-height Correlation Function:

The scaling theory of growth-induced surface roughness is based on the behavior of height-height correlation function (HHCF) , which is defined as the mean square of height difference,

$$g(r,t) = \left\langle \left[h(x,y) - h(x',y')\right]^2 \right\rangle, \tag{1.5}$$

here $r = \sqrt{(x-x')^2 - (y-y')^2}$ is the lateral distance between two mounds. The relative magnitudes of *r* and the correlation length ξ can divide the HHCF into two distinct behaviors: (i) $r \ll \xi$, $g(r) \propto r^{2\alpha}$ and (ii) $r \gg \xi$, $g(r) = 2w^2$. A typical HHCF plot is schematically shown in **Fig. 1.9**. The above concepts are used to understand the growth dynamics of $SnCl_2Pc$ and VOPc organic thin films on various substrates.

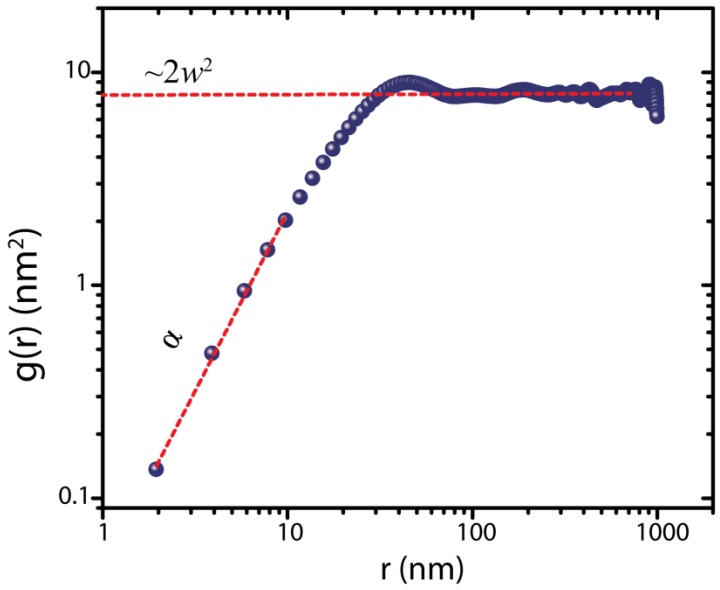

Figure 1.9: A plot of height-height correlation function (HHCF) for rough surfaces.

It is worth noting that sometimes beyond the lateral correlation length, surface heights are not correlated, and they may exhibit a periodic behavior on a length scale larger than the lateral correlation length. So, in order to calculate long range behavior, the power spectral density function (PSD) is used, which can be derived from Fourier transform (FT) of the surface height in reciprocal space.

1.4 Charge Transport Mechanism in Organic Semiconductors

Semiconductors are divided into two types: intrinsic and extrinsic ones. An intrinsic semiconductor is an insulator at very low temperature, but the band gap is small enough that the conduction band can partly be populated at room temperature. (**Figure 1.10** shows the energy band diagram).

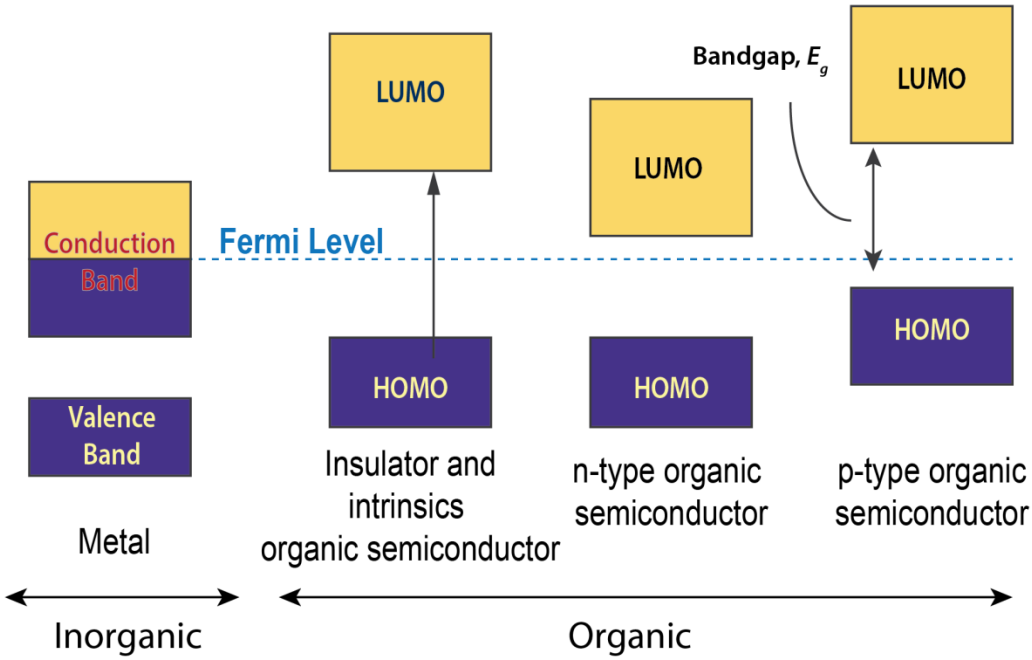

Figure 1.10: Energy band diagram of a metal, an insulator, and an extrinsic organic semiconductor [27].

In metal, the valence band and conduction band come very close to each other or even they overlap with each other, in insulators they have large band gap (>4 eV) and the electrical conductivity is almost zero, while in semiconductor (whether it is organic or inorganic), they have a finite 'band gap, E_g' separated by HOMO (conventionally 'valence band') and LUMO (conventionally 'conduction band') (<4 eV). The representative energy band diagrams are shown schematically in **Fig. 1.10**. Doping of intrinsic organic semiconductors induces localized energy levels close to the conduction (n-type) or valence (p-type) band edge (**Fig. 1.10**, extrinsic semiconductors). By this technique, the energy for the introduction of an electron or a hole in the material is tremendously lowered, and the compound becomes more suitable for the fabrication of the devices. It has been shown that the most organic semiconductors used for device fabrication are contaminated with relatively high amounts of both kinds (p- and n-type) of impurities. So, by doping organic semiconductors properties can be tuned to an n-type and p-type. It is worth noting that organic semiconductors are intrinsically ambipolar depending upon the processing, their properties can be controlled.

1.4.1 Charge Injection and Transport Across Metal-Semiconductor Junction

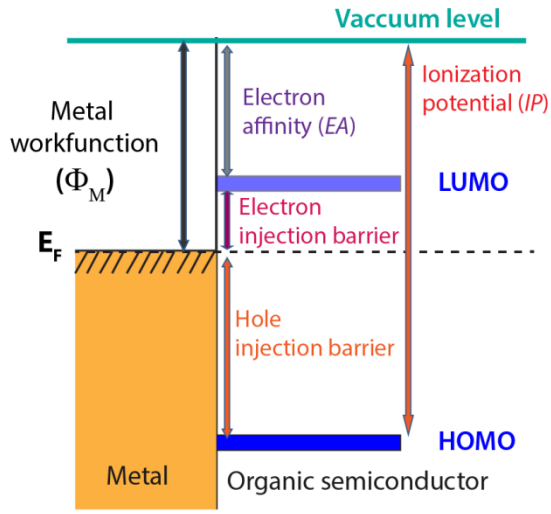

Figure 1.11: Energy level diagram of metal/organic semiconductor junction [28].

From the practical point of view, charge injection from a metallic electrode into a semiconductor is a very important issue. The interface between the source/drain contact and organic semiconductor requires low contact resistance, which is a function of both parasitic resistance and the energy barrier at the contact/semiconductor interface. Low energy barrier necessitate matching the electrode work function (Φ_M) with the semiconductor ionization potential (*IP*s). **Figure 1.11** shows a schematic of the energy band diagram at the metal/semiconductor interface. Contact material should be selected such that the barrier of hole injection (φ_B=*IPs*-Φ_M) is minimized (for p-type OFET), to allow for high charge injection efficiency at the contacts. In addition to energetic matching at the interface, the contact material must possess high conductivity for optimal OFET performance. Most metal/organic semiconductor junction form a *Schottky* contact, indicating the presence of an injection barrier [16,29]. The barrier arises as a consequence of a different morphology of organic semiconductors at the contacts, quality of the contact and lowering of the effective work function of contacts due to formation of interfacial dipole. Therefore, extensive efforts have been devoted to find a way to improve contacts in organic devices.

Usually an *Ohmic* contact is desirable, which requires the work function of the contact metal to match with the HOMO of the organic semiconductor in the case of a p-type OFET, and with the LUMO in the case of an n-type OFET. This requires a high work function metal for p-type OFET and a low work function metal for an n-type OFET. The work function of various common metals is listed in **Table 1.4**. Glold (Au) and platinum (Pt) are favorable choices for their high work function, which has good electrical compatibility with the p-type OFET. They

Table 1.4: Work function (Φ_M) of some selected metals [30]:

Work Function	**Ag**	**Al**	**Au**	**Cu**	**Pt**	**ITO**
Φ_M **(eV)**	4.26	4.28	5.1	4.65	5.65	4.8-5.2

have environmentally stable nature at the contact/semiconductor interface. In contrast, silver (Ag) and aluminum (Al) are generally used for their low work function, which has good electrical compatibility with n-type OFET. However, these require protection from ambient atmosphere, otherwise, they would rapidly degrade. The simplified energy level diagrams of **Fig. 1.12(a)** and **1.12(b)** illustrate the carrier injection into the semiconductor in an organic thin-film transistor (OTFT) for an n-channel and p-channel, respectively.

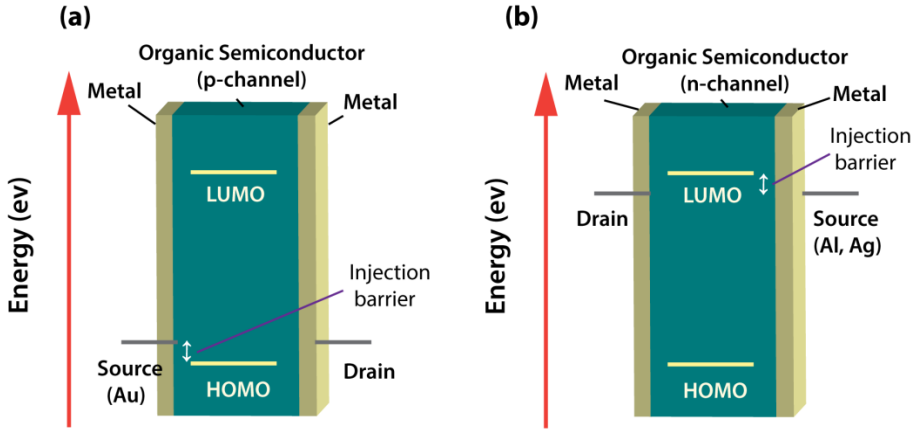

Figure 1.12: Energy level diagram of an organic semiconductor and the work functions of source and drain metal electrodes for (a) p-channel and (b) n-channel, respectively. Note that in transistors, there is no injection from the drain.

1.4.2 Charge Carrier Transport in Organic Materials

The charge transport mechanism in molecular organic solids differs significantly from that of inorganic semiconductors, because in organic materials normally ionic molecular states, i.e. radical cations and anions, are involved. In molecular solids, electrons or holes have to move from one molecule to another and these ionic states are stabilized by polarization energies in the crystal. Due to the exciton binding energy, the optical gap is significantly smaller than the single molecule gap to create an uncorrelated electron-hole pair. Furthermore, the active layer in most OFETs is not single crystalline and the energy levels of valence and conduction bands of polycrystalline or amorphous layers are less discrete, due to varying polarization energies of different molecular environments. The contribution of different defects or trapping states on the hopping transport was described by Bässler et al. with a Gaussian distribution [31]. The spatial and energetic disorder in the semiconducting layer is proportional to the bandwidth of the Gaussian density of states.

Band Transport Model:

The band transport model, as it can be used to describe carrier transport in silicon (Si), Germanium (Ge)-based devices, can only be applied for highly ordered organic single crystals at low temperatures. Compared to inorganic materials, the bandwidth of organic crystals is still very small and the measured charge carrier mobilities range from 1 to ~35 cm^2/Vs, which is comparable to the mobility in amorphous silicon. In these materials, charge transport is limited by scattering of the carriers, mainly on phonons, i.e, thermally induced lattice deformations. This model is no longer valid for low conductivity materials such as organic semiconductors. The main difference between the two cases is that in an inorganic semiconductor, charge transport is limited by phonon scattering, whereas in the organic case, it is phonon assisted. As regards to high purity crystals, different measurement techniques showed increasing mobilities with decreasing temperatures, suggesting band transport instead of hopping [16,32]. This inverse temperature dependence of the charge carrier mobility μ can be expressed by equation $\mu \propto T^{-n}$ (In most practical cases, n is positive, so the mobility increases when temperature decreases).

Contrary to organic crystals, disordered organic materials do not form energy bands, due to low molecular interactions among the molecules based on Van-der-Waals forces. Some models have been developed to explain theoretically the temperature and electric-field dependencies of charge carrier drift mobility, however the exact nature of charge transport in these crystals is still unresolved for the time being.

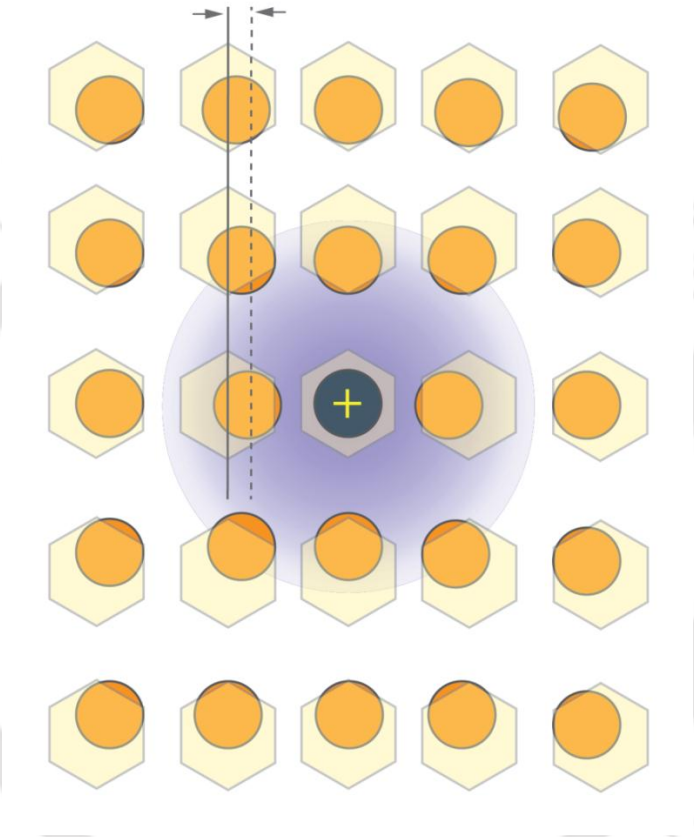

Figure 1.13: A schematic representation of the formation of a polaron when a positive charge is placed on a molecule in a conjugated organic solid. The hexagons symbolize the core of the nuclei, while the circles represent the delocalized π-electrons [16].

Polaron Transport:

The main reason why the band model is unable to account for charge transport in organic semiconductors is that it fails to account for a crucial phenomenon in these materials: polarization. The occurrence of polarization in organic solids has been analyzed in detail by

Silinsh and Cápek [33]. The principle is the following. A charge carrier residing on a molecular site tends to polarize its neighboring region. As the resulting polarization cloud moves with the charge, the traveling entity is no longer a naked charge, but a "dressed" charge, and the formed species is called a *polaron*. In conjugated solids, the main polarization effect is that on the clouds formed by the π-electrons. The principle is illustrated in **Fig. 1.13**, where the conjugated molecules are symbolized by benzene rings; the hexagons represent the (fixed) core of the six carbon atoms, while the circles stand for the delocalized π-electrons. Under the effect of the positive charge on the central molecule, the π-electron rings tend to move towards the central molecule, thus creating an electric dipole, the magnitude of which is greater as the molecule is closer to the center. It is worth noting that in polaronic charge transport, not only the charge moves under an applied electric field but also the lattice deformation moves with it.

Hopping Transport:

The absence of an ideal 3D periodic lattice in disordered organic semiconductors does not allow to describe charge carrier transport in terms of band conduction. In this case, charges must move between these localized states and overcome the energy difference between them, emitting or adsorbing phonons during intra-chain or inter-chain transitions (see **Fig. 1.14 (a)**). Hopping models have proved useful in rationalizing charge transport in disordered materials, such as polymers. Time of flight (TOF) measurements have revealed that the carrier mobility in these organic materials is thermally activated. Another ubiquitous feature relates to the field dependence of μ obeying a law, $\ln(\mu) \propto \sqrt{F}$, where F is the magnitude of the electric field [34]. The current practice is to interpret this behavior in terms of Gill's [16,35] or Poole–Frenkel (PF)-like equation,

$$\mu = \mu_0 e^{-\left(E_0 - \beta\sqrt{F}\right)/kT_{eff}} \tag{1.6}$$

Where $T_{eff}=T^{-1}-T_0^{-1}$, E_0 = activation energy in the absence of electric field, β = the Poole-Frenkel coefficient, F = magnitude electric field, k = Boltzmann constant, T_0 = temperature at which the extrapolated data of Arrhenius plots for various electric fields intersect with one

another, μ_0 = mobility at T_0. The problem with **Eq. (1.6)** is that it presents several physical inconsistencies, among which are the lack of physical meaning for the effective temperature and the fact that the actual values of the PF factor are far from that predicted by the conventional PF theory.

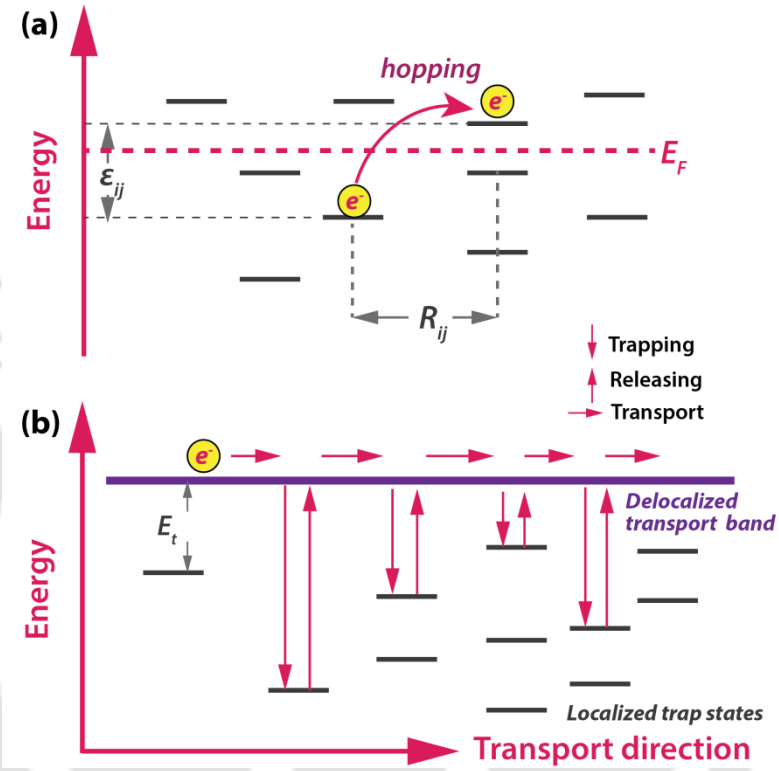

Figure 1.14: A schematic of charge-transport mechanisms in organic semiconductors: (a) hopping model assumes a transport mechanism driven by thermal energy and/or tunneling between the discrete states. (b) The multiple trapping and release model assumes a transport mechanism driven by thermal activation of charge carriers into extended states followed by a trapping in discrete states. However, the charge carriers are frequently trapped in states with depth E_t, from which they are thermally excited back into the band.

The disorder model developed by Bässler [16,31] relies on the following assumptions: (1) Because of the randomness of the intermolecular interactions, the electronic polarization energy of a charge carrier located on a molecule is subject to fluctuations; (2) transport is described in terms of *hopping* among localized states; in analogy to optical absorption profiles, the DOS is described by a Gaussian distribution of variance ; (3) charge transport is a random walk described by a generalized master equation of the Miller–Abrahams form [36]:

$$\gamma = \gamma_0 e^{-2\gamma\Delta R_{ij}} e^{-\frac{\varepsilon_{ij}}{kT}}, \tag{1.7}$$

where $\Delta R_{ij}$is the intersite distance and $\varepsilon_{ij}$the energy difference of the sites. Depending on the structural and energetic disorder of the system, it may be possible that a charge carrier finds more favorable to hop over a larger distance with lower activation energy than over a shorter distance with high activation energy. However the activation energy depends on the molecular order and on the charge carrier density. If the charge carrier density is increased the lower trap level are filled, the activation energy decreases and the mobility increases. Since the energy-dependent transition is thermally-activated, the optimal hopping distance will depend on temperature. This mechanism of hopping conduction is called variable-range hopping (VRH) [37]. This model was introduced by Vissemberg and Matters, and describes the temperature and gate voltage dependence in OFETs introducing a percolation model based on VRH in an exponential density of states. The VRH model has been used to describe the charge-transport mechanism in amorphous materials with a maximum mobility of $\sim 10^{-3}$ cm^2/Vs.

Multiple Trapping and Release (MTR) Model:

The MTR model applies to well-ordered materials, prototypes of which are vacuum grown small molecules based organic semiconductor, where thermally activated mobility is often observed. This model was introduced to explain charge transport in amorphous silicon devices and was used by Horowitz *et al.* to interpret the data obtained on poly-crystalline sexithiophene-a small molecule based OFETs [9]. The basic assumption of the model is a distribution of localized energy levels located in the vicinity of the transport band edge. During their transit in the delocalized band, the charge carriers interact with the localized levels through trapping and thermal release. **Figure 1.14(b)** schematically represents the MTR model for charge transport mechanism for disordered organic semiconductors. Impurities, defects, and grain boundaries can scatter charge carriers back into localized states. For this model, some interactions are postulated: (i) Carriers arriving at a defect are trapped with a very high probability near to one, and (ii) the release of the carriers is thermally controlled. The resulting effective mobility μ_{eff} is related to the mobility μ_0 in the

undisturbed mobility in the band by an **Eq. (1.8)** [38]. This model is widely used to explain charge transport in amorphous silicon.

$$\mu = \mu_0 \alpha e^{-(E_C - E_t)/kT}, \quad (1.8)$$

where E_t is the "depth" of the traps, the energy difference between the band edge and the trap levels, and E_c the conduction band edge. α is the ratio of the trap density of state (DOS) to the effective density of states at transport band edge. In all circumstances, whichever the actual energy distribution of traps, the main feature predicted by the MTR model is thermally activated mobility. An important outcome of the MTR model is that in the case of energy distributed DOS, mobility is gate voltage dependent.

1.5 Organic Field-Effect Transistors (OFETs)

Field-effect transistor is an electronic device that relies on the electric field to control a current through the 'conductive channel' made of a semiconducting material. When the active layer is fabricated from organic semiconductors (OSCs), the device is referred to as an organic field-effect transistor (OFET). The most common configuration of an OFET is the organic thin film transistor (OTFT). OTFTs are usually applied for two goals: first, investigation of the OSC properties (e.g. field-effect mobility, light-induced modifications, degradation effects after prolonged operation, etc.); second, OTFTs can be used as switching or sensing devices in organic electronic applications.

1.5.1 Basic Design and Operating Principle of OFETs

The basic idea that guides the insulated-gate field-effect transistor (FET) traces back to the mid-1920s , but it was not triggered until 1960 that this early concept could be successfully demonstrated, with the invention of the metal-oxide-semiconductor FET (MOSFET). Organic field-effect measurements on copper phthalocyanine (CuPc) films were reported as early as 1964. However, the organic field-effect transistors, came into applications in the late 1980s [39].

Figure 1.15 shows a three-dimensional view of an organic thin-film transistor. It is a three terminal device: (1) source (*S*), (2) drain (*D*) and (3) gate electrode (*G*). The active part of the device is constituted of an organic semiconductor thin film equipped with two electrodes: the source and the drain. The distance between the source and the drain is called the channel length *L*; the transverse dimension of the structure is the channel width *W*. A third electrode, the gate, is laid out along the channel between source and drain; this electrode is electrically isolated from the semiconductor film by a thin insulating film called dielectric material, hence forming a metal-insulator-semiconductor (MIS) structure. By applying a voltage between source and gate, one induces the formation of an accumulation layer at the semiconductor–insulator interface, thus forming a conducting channel between these two electrodes. So, the gate turn the device on and off with an applied voltage, and thus controls the current flow (I_{DS}) in the semiconductor between the source and drain electrodes [16].

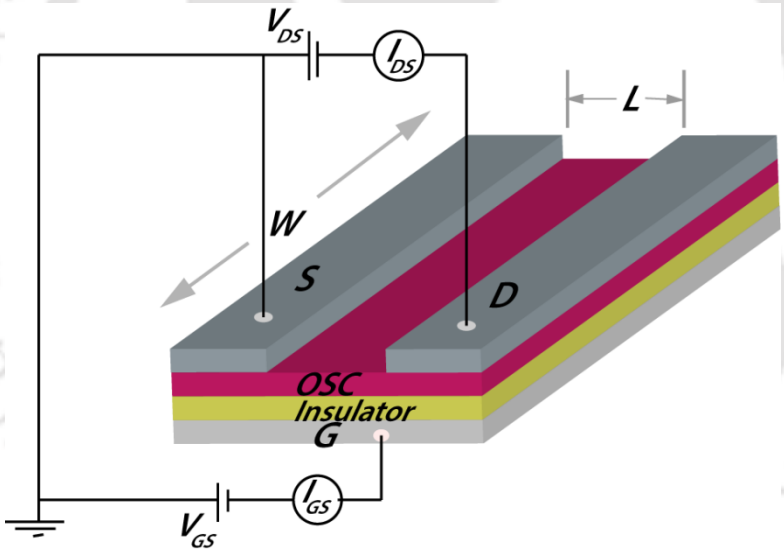

Figure 1.15: A schematic of top contact organic field-effect transistors (OFET): V_{DS}: drain voltage; I_{DS}: drain current; *L*: channel length; *W*: channel width; *S*: source electrode; *D*: drain electrode; *G*: gate electrode; V_{GS} : gate voltage; I_{GS} : gate current, OSC: organic semiconductor [40].

As shown in **Fig. 1.16**, OFETs are commonly used in three main device configurations combining the basic components (electrodes, channel and insulator). Specifically, in bottom gate-bottom contact (BGBC) configuration the organic layer is deposited on the gate insulator, after the source and drain contact is realized on gate insulator. On the contrary, the device structure in which source and drain contacts are pre-patterned on the gate insulator

and the organic material is deposited on their top is known as bottom gate top contact (BG TC) geometry. Finally, in the bottom contact-top gate (BCTG) structure, the gate insulator is deposited on the organic channel and the device fabrication is completed with the gate electrode.

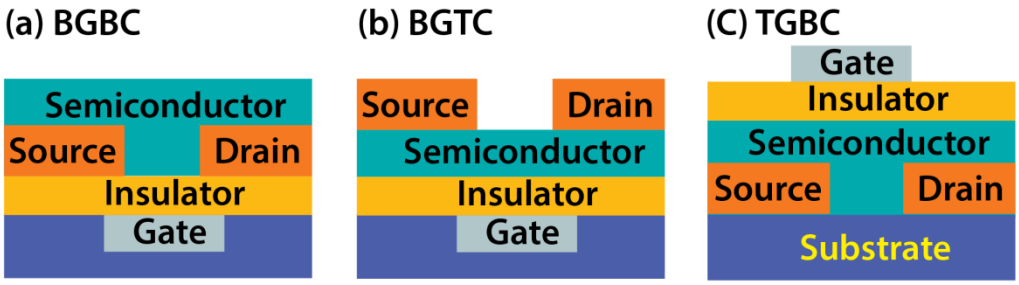

Figure 1.16: A schematic of commonly used field-effect transistor configurations: a) bottom gate-bottom contact (BGBC), b) bottom gate- top contact (BGTC), c) bottom contact- top gate (BCTG) [41].

However, it has been found that the small contact area tends to generate large contact resistance of the bottom contact OFETs. In contrast, top-contact OFETs usually have relatively large areas for carrier injection at the contact/semiconductor interface, resulting in smaller contact resistance [30,41]. In this work, a top-contact configuration was employed to the OFETs due to its lower contact resistance compared to that of OFETs with a bottom-contact configuration. As discussed earlier, the lower contact resistance in a top-contact configuration is associated with the increased effective contact area. On the other hand, the bottom-contact configuration is limited by the nonlinear film morphology near the contacts.

A unique feature of OFETs is that, unlike diodes, these devices are two dimensional. That is, they are governed by two independent voltages perpendicular to each other. The role of the gate voltage is to induce charges in the conducting channel, while the drain voltage drives these charges from source to drain. The most popular equations to describe the current-voltage curves of an FET are very simple, but this simplicity hides several assumptions: (1) the transverse electric field induced by the gate voltage is largely higher than the longitudinal field induced by the gate bias (so-called gradual channel approximation); (2) the mobility is constant all over the channel. In short, I–V characteristics can be drawn by either varying the drain voltage at a constant gate voltage (output characteristics I_{DS}-V_{DS}) or changing the gate voltage at a fixed drain voltage (transfer characteristics I_{DS}-V_{GS}). In the former case, the

curves are divided into a linear regime at low V_{DS} ($V_{DS} \ll V_{GS}$) that convert into the saturation regime when $V_{DS} > V_{GS}$. The current in both regimes is given by eqns. (1.9) and (1.10) [16,42]:

$$I_{DS\,lin} = \frac{W}{L}\mu C_i\left[\left(V_{GS} - V_{Th}\right)V_{DS} - \frac{V_{DS}^{\ 2}}{2}\right], \qquad \text{for } |V_{DS}| \le |V_{GS} - V_{Th}| \tag{1.9}$$

$$I_{DS\,sat} = \frac{W}{2L}\mu C_i\left(V_{GS} - V_{Th}\right)^2, \qquad \text{for } |V_{DS}| \ge |V_{GS} - V_{Th}| \tag{1.10}$$

Here, $C_i = \frac{\epsilon_0 kA}{d}$ is the capacitance of the insulator, μ is the mobility in the semiconductor, and V_{Th} is the threshold voltage.

The mobility μ_{lin} in the linear regime can be extracted from the Eq. (1.9) by taking the first derivative of the I_{DS} with respect to V_{GS} at constant V_{DS}:

$$\mu_{lin} = \frac{L}{WC_iV_{DS}}\left(\frac{\partial I_{DS}}{\partial V_{GS}}\right)_{V_{DS}=const} \tag{1.11}$$

Similarly, the saturation mobility μ of the OFET is calculated using the following formula, which is derived from the eqn. (1.10):

$$\mu_{sat} = \frac{2L}{WC_i}\left(\frac{\partial\sqrt{I_{DS}}}{\partial V_{GS}}\right)^2_{V_{DS}=const} \tag{1.12}$$

where the slope $\frac{\partial\sqrt{I_{DS}}}{\partial V_{GS}}$ can be calculate from the linear extrapolation of the $\sqrt{|I_{DS}|}$ vs. V_{GS} plot (see **Figure 1.17(b)**).

In the linear regime, the total resistance R_{total} of an OFET can be expressed as the sum of R_{ch} and R_C as below $R_{total} = R_{ch} + R_C$.

Where R_C and R_{ch} $(= \frac{L}{wc_i(V_{GS}-V_{Th})\mu})$ are the contact resistance and the channel resistance, respectively.

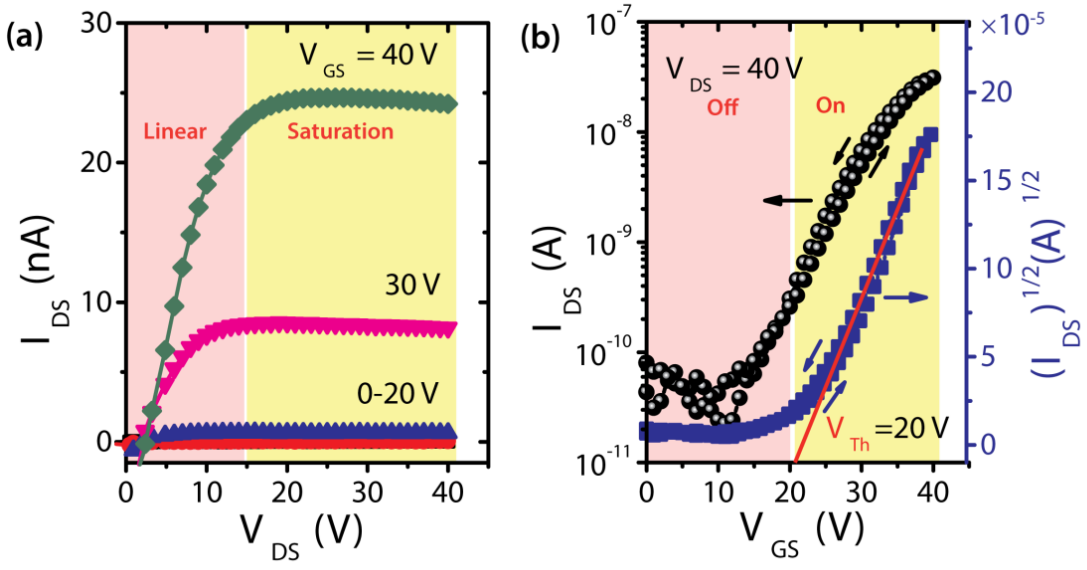

Figure 1.17: **(a)** I_{DS} vs. V_{DS} output characteristics of a top-contact OFET for different V_{GS} biases. **(b)** $|I_{DS}|$ vs.V_{GS} and $\sqrt{|I_{DS}|}$ vs.V_{GS} transfer characteristics of OFETs [43].

Figure 1.17 shows typical output characteristics I_{DS}-V_{DS} and transfer curves I_{DS}-V_{GS} (**Fig. 1.17(b)**), respectively for a top-contact OFET. In the output characteristics, the linear regime at low V_{DS} and the saturation regime at high V_{DS} are clearly visible. So, the I–V curves are used to extract its basic parameter, primarily the mobility and threshold voltage. It is noteworthy to outline that the V_{Th} strongly depends on the specific device structure and in particular on the combination of dielectric and semiconductor.

Apart from showing the performance of the device, I–V curves are used to extract its basic parameter, primarily the mobility and the threshold voltage. A widely used method for parameter extraction consists of plotting the square root of the saturation current as a function of the gate voltage. As seen in **Eq. (1.10)**, this is supposed to give a straight line, the slope of which gives the mobility while its extrapolation to the axis corresponds to the threshold voltage.

The performances of OFETs can be characterized by several key parameters including, on/off current ratio (I_{ON}/I_{OFF}), field-effect mobility (μ), subthreshold slope (S), threshold

voltage and so on. Reliable and reproducible extractions of the parameters from the transfer curve or the output curve of a transistor are prerequisites for a comparison between the performances of devices. Here, the basic requirements for proper parameter extraction are defined. The sub-threshold slope is obtained from the saturated transfer characteristics and is defined as the inverse slope of the log($|I_{DS}|$) vs. V_{GS} curve at large constant V_{DS}, as indicated in **Fig. 1.17(a)**. The sub-threshold slope is related to the device switching speed: the smaller the sub-threshold slope, the faster the transition between the ON and the OFF states. I_{ON}/I_{OFF} ratio is defined as the ratio between the maximum drain current in the ON state (I_{ON}) and the minimum drain current in the cut-off regime (I_{OFF}). It is evaluated from the saturated transfer characteristics at large constant V_{DS}, as shown in **Fig. 1.17(b)**. In terms of technical applications, this ratio should be as large as possible. Typical values for the on/off current ratio are six to seven orders of magnitude.

In addition, these devices under biasing conditions $V_{GS}>V^{e}_{Th}$ and $V_{GS}-V_{DS}<V^{h}_{Th}$, electron and hole accumulation layers are simultaneously present in different portions of the channel, extending from the source and drain contacts into the channel, so called *ambipolar organic field effect* transistors. So, in ideal ambipolar or bipolar transistors are transistors in which both holes and electrons are mobile inside the conducting channel. Ambipolar organic field-effect transistors have the potential to be the next generation of light-emitting devices [29,42,44,45].

1.5.2 Subthreshold Slope and Charge Traps

Below the threshold voltage, there is a subthreshold (S) region in which the drain current depends exponentially on the gate-source voltage. In the subthreshold region, the drain current is induced by the carriers that have sufficient thermal energy to overcome gate-voltage-controlled energy barrier. The subthreshold slope S, also called subthreshold swing, can be described quantitatively by

$$S = \frac{\partial V_{GS}}{\partial\left(\log_{10} I_{DS}\right)} \tag{1.13}$$

At room temperature $S = \frac{kT}{q}\ln(10) \approx 57$ mV/dec. Conceptually, subthreshold voltage slope can be used to estimate the density of the trapped charge carriers at the interface by [46],

$$N_t^{\max} \approx \left[\frac{qS\log(e)}{k_B T} - 1\right]\frac{C_i}{q} \tag{1.14}$$

where q is electronic charge, N_t^{max} is the upper limit of the trapped charges, and k_B is Boltzman's constant. Obviously lower trapped charge density will result in lower subthreshold slope.

1.5.3 Hysteresis

Organic field-effect transistors often exhibit a current hysteresis (difference between the forward and the reverse sweeps). Moreover, we often have a persistent shift of the transfer characteristic when a gate bias is applied for a prolonged time. These phenomena are known as electrical instability. Electrical instability is most likely caused by the trapping of charge in long-lived trap states. The term "long-lived" refers to a trapping, and release time which is long compared to the time needed to measure a transfer characteristic (e.g. 1 min.). The shift of the transistor characteristic (threshold voltage shift) ΔV_{th} can be related to the density of the interface-traps (N_t), which can be estimated by the following equation according to [47],

$$N_t = \frac{C_i \Delta V_{th}}{e} \tag{1.15}$$

The long-lived states may be extrinsic in nature (e.g. certain chemical groups on the surface of the gate dielectric). They may also be located within the semiconductor in regions with increased structural disorder, i.e. may result from structural defects. Furthermore, a reversible electrochemical reaction of adsorbed water with the organic semiconductor or with chemical groups on the surface of the gate dielectric may play a role as well. It has also been suggested that gate bias stress effect is an intrinsic phenomenon and is due to the formation of hole bipolarons, which is a tightly bound state with a very low mobility. Impurity states might even catalyze the formation of bipolarons. Other marginal causes of electrical instability of

an organic field-effect transistor include the transfer of charge from the semiconductor to the gate dielectric, or the movement of charged ions within the gate dielectric.

1.5.4 Electrical Stability of OFETs: Bias Stress Model

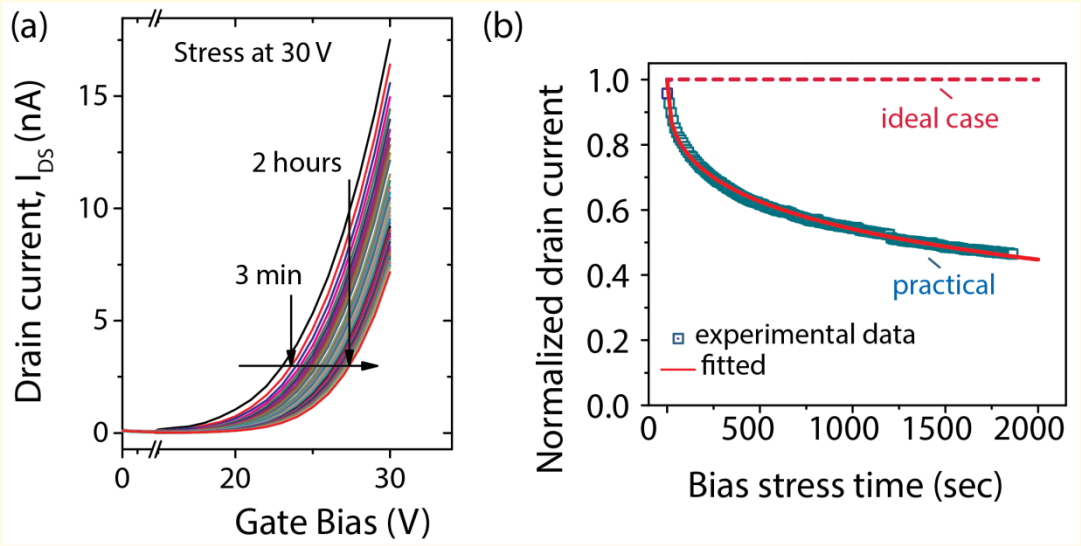

Figure 1.18: (a) Transfer curves of an OFET for different stressing times: The gate bias voltage during the stressing is 30 V [43]. **(b)** Alternative gate bias stress measurement by normalized drain current when bias voltages are constant.

Transistors should provide a stable current under applied bias. It is a fundamental requirement for practical applications of OFETs. At the moment, the commercialization of organic transistors is hampered by their operational instability for which the origin is basically unknown and there is an ongoing debate in the literature. V_{Th} stability is a important figure of merit as well as the field-effect mobility, because it is related to the operational and lifetime. The stability of OFETs mainly has two aspects. One is the air stability that is a well-known problem for organic semiconductor materials. The other limit is a characteristic of threshold voltage shift (ΔV_{Th}) after prolonged gate-bias stress that results from the operation of the OFETs. However it is generally believed that the electronic trap states in the semiconductor or at the interface between the semiconductor and the dielectric or in the dielectric layer can cause instabilities of the threshold voltage of OFETs.

Physics of Stretched Exponential decay of Drain Current:

Upon applying a gate bias, the bias-stress effect results from trapping of mobile carriers that can be described with the change in the free carrier density (N_f), given as [48,49]

$$\frac{d}{dt}\Delta N_f = -AD\Delta N_f \tag{1.16}$$

where t is time, A is a proportionality constant that is proportional to a capture cross-section for the charge carriers and D is the diffusivity. In OFET, D is the time-dependent diffusion coefficient for the carriers relaxing in the mobile state and it is inversely proportional to an average time for a carrier to find a deep trap. In addition, D follows a power law universal to virtually all the disordered systems exhibiting dispersive transport: $D(t) = D_0\,(\omega t)^{\beta-1}$, where D_0 is the diffusion constant, ω is a hopping frequency between charge trap states, and β is a dispersion parameter. The solution to this differential equation is given by a stretched exponential function.

$$N_f(t) = N_f(0)\exp\left[-\left(\frac{t}{\tau}\right)^{\beta}\right] \tag{1.17}$$

where $N_f(0)$ is the initial free carrier density, τ is a characteristic time constant. Assuming that the threshold voltage shift (ΔV_{th}) of an OFET at a given time is given by $\Delta V_{th}(\text{t}) = eN_{tr}(t)/C$, where e is the elementary charge, $N_{tr}(t)$ is the trapped charge density that is assumed as $N_f(0) - N_f(t)$, and C is the capacitance of the gate-dielectric. The corresponding normalized threshold voltage shift (over the threshold voltage shift at $t=\infty$) can be given as

$$\Delta V_{Th}(\text{t}) = \left\{V_{Th}(\text{t}=\infty) - V_{Th}(\text{t}=0)\right\}\exp\left[-\left(\frac{t}{\tau}\right)^{\beta}\right] \tag{1.18}$$

Usually the threshold voltage shift $\Delta V_{th}(t)$ is analyzed by measuring transfer curves at various times, with a gate bias applied in between. This straightforward measurement has some drawbacks, however. Firstly, it is slow, therefore, information about the first few, or even fraction of seconds is not accessible. Secondly, some devices, especially OFETs do not show a linear regime and thus deriving a threshold voltage is not straightforward, even as the

transfer curve clearly shifts. Therefore, we use a different method to measure the gate bias stress influence over time. Instead of measuring a full transfer curve, the evolution of the drain current $I_{DS}(t)$ is measured at a certain applied gate voltage V_{GS} and source drain voltage V_{DS}. The decrease of $I_{DS}(t)$ over time can be translated into a shift of the transfer curve (and, therefore, V_{th}) and it can be derived from **Eq. (1.18)** [48,50],

$$I_{DS}(\mathrm{t}) = I_{DS}(0)\exp\left[-\left(\frac{t}{\tau}\right)^{\beta}\right] \tag{1.19}$$

where τ is the time constant, and β is the stretching parameter ($0 < \beta \leq 1$). A stretching parameter close to 1 indicates a narrow distribution of time constants (the limit $\beta = 1$ being the exponential function with a single time constant), while a smaller stretching parameter ($\beta < 1$) implies a broader distribution of time constants [51]. Although this expression was originally developed to describe the bias-stress effect in amorphous silicon transistors considering the time-dependent evolution of trap states due to hydrogen migration, we employ similar mathematical formulation to describe the dispersive trapping process in OFETs.

1.6 Advances in Organic Field-Effect Transistor Performance

Organic field-effect transistors (OFETs) have received immense attention since the invention of the first OFETs in 1986 by Tsumura and coworkers [52]. They have the potential in integrated circuits for large area, flexible, and low-cost electronics for active matrix displays, radio frequency identifications tags, organic light emitting transistors and organic light emitting diodes and so on [53]. A large numbers of molecule were designed and synthesized for electron transporting (n-type), hole transporting (p-type) and ambipolar organic semiconductors or combinations of n-type and p-type to make ambipolarity with improved performance and stability [54]. **Table 1.1** summarizes the OFET performance parameters of various molecular semiconductors. Compared to the inorganic semiconductors, molecules of organic semiconductor can be tuned and modified such as charge transport, energy level etc. can be optimized. Synthesis of organic semiconductors can be relatively easily scaled up and can be yielded in high purity. These advantages are not only important for commercialization, but also allow us scientifically to explore the relationships between

structures and properties. Over the past decades, the performance of OFETs has surpassed our expectations, with OFET mobility in some cases exceeding those of amorphous silicon FETs (~1.0 $cm^2V^{-1}s^{-1}$) [55-58]. However, the overall improvement of n-type organic semiconductors still falls behind the p-type organic semiconductors in terms of mobility, air stability, operational stability etc. However, most well-known p-type organic semiconductors such as pentacene, P3HT etc. suffer air stability. Considering n-type, p-type, and/or their combinations in ambipolar organic semiconductors playing significant roles in ambipolar transistors and complementary circuits, development of novel n-type and ambipolar semiconducting materials with high performance is still a critical focus in organic electronics and organic optoelectronic applications. Apart from high charge carrier mobility, large on/off ratio, and low threshold voltage, high air stability is essential for real life applications, which is one of the key property for organic semiconductor devices. To achieve these requirements, the development of new organic semiconductors is highly desirable. The recent advances in the device performance of n-type, p-type and ambipolar organic semiconductor devices are summarized in Table 1.1.

Table 1.1: Summary of the OFET device performance reported for n-type, p-type and the combination of small molecule organic semiconductors (Note that the mobilities for most of the semiconductors are p-type).

Semiconductors	**Gate-dielectric**	μ (cm^2/Vs)	V_{op} (V)	V_{th} (V)	τ (s)	β	**Ref.**
$SnCl_2Pc$	PMMA-Al_2O_3	0.01	10	3-4	10^5 (air)	0.32	This work [43]
	P6p-SiO_2	0.3	100	27	…	…	[59]
Perylene derivative	SiO_2	0.02-0.03	50	…	7.5×10^3	0.32	[60]
	SiO_2	…	50	...	3.8×10^4	0.41	[60]
	SiO_2	1.7	150	-	…	…	[61]
Napthalene diimide derivative	OTS-SiO2,	0.7	80	25-26	2.8×104	0.59	[62]
		0.62	60	21	….	….	[63]
	HMDS-SiO_2	0.1-0.7	80	10-18	1.2×10^4	0.56	[63]
Diindenopyrazinediones derivatives	HMDS-SiO_2	0.001	100	27	…	…	[64]
Quinone	HMDS-SiO_2	0.15	100	17	….	…	[65]
Pentacenequinones	OTMS	0.1	70	34	….	….	[66]
TriF-IF-dione	PS	0.1	90	9.2	9.3×10^2	…	[67]
C60	PMMMA-SiO_2	1.1	30	2.1	……	…	[68]
Pentacene	HMDS-SiO_2,	0.1-0.2	40	2.1	7.1×10^5	0.45	[69,70]
	PS-SiO_2	0.7	60	27.5	3.2×10^5	0.55	
TES-ADT	HMDS-SiO_2	0.16	40	0.4	…	….	[71]
P3HT	HMDS-SiO_2,	…	80	…	4×10^7,	…,	[48,72]
	ODTS-SiO_2				1.5×10^4	0.4	
TIPS-PEN (single-crystal)	Parylene	0.05	80	…	1.8×10^5	0.37	[73]
Tetracene (single-crystal)	…	…	…	…	3.1×10^4	0.37	[69]
C8-BTBT	PMMA	3.1	40	…	4.9×10^3	0.40	[74]
Thiophene-derivative	f-PVP-SiO_2,	1.7	80	..,	..	..	[75,76]
	IDTO	1.9	3	44	10^5	..,	
TIPS-TAP	SAM-AlOx-SiO_2	6.8	50	18–22	…	…	[77]
VOPc	HMDS-SiO_2,	0.01	40	20	10^4 (air)	0.67	This work
	P6p-SiO_2	0.55	40	…	10^7(vac.)	0.38	[78]
NT FBII/Pentacene	HMDS-SiO_2	μ_p=0.23, μ_n=0.09	40	$V_{th,p}$=11 $V_{th,n}$=6	…	…	[79]
$SnCl_2Pc$/CuPc	PMMA-Al_2O_3	$\mu_p=2.1\times10^{-4}$ $\mu_n=1.8\times10^{-4}$	10	$V_{th,p}$=6.84 $V_{th,n}$=2.53	10^5	0.57	This work [80]
Pentacene/C60	Olefin-Si_3N_4-SiO_2	μ_p=0.28 μ_n=0.18	40	…	…	…	[81]
P13/CuPc	PMMA-SiO_2	$\mu_p=5.5\times10^{-3}$ $\mu_n=3.1\times10^{-2}$	60	$V_{th,p}$=10.2 $V_{th,n}$=25.3	…	…	[82]

1.7 Lacunae and Challenges

Despite successful synthesis of organic molecules with high purity, limited research has been carried out on the systematic growth of organic molecular thin films by tuning various growth parameters those are responsible for crystallization and resultant thin film morphology [83-104]. Among the different explored materials, small aromatic molecules particularly phthalocynanine molecules have emerged as promising candidates because they can be grown in films with thermal and chemical stability, high crystalline order, and wide absorption band at the optical region [16,23,89,102,105-111]. Only recently, few groups have determined the structure and packing of stabilized organic thin film phases on various substrates [112]. Although, a few experimental as well as theoretical efforts have been made to establish a molecular level understanding of the growth of organic thin films, however the physics related to morphological evolution is still an on ongoing debate for the growth of organic thin films [86,113,114].

For inorganic materials, scaling concepts are quite successfully implemented to describe and predict the statistical features of the morphology of growing surfaces and interfaces which is grown far from equilibrium conditions [25,26,115-121]. So, the scaling theory can be applied to quantify the statistical properties of the surface morphology of organic thin films and to formulate theoretical models of growth modes for small molecules based thin films. The height-height correlation function of the thin film can be established to relate physical growth mechanisms from the set of scaling exponents [110]. These exponents can be used to quantify the interface features, and the morphological evolution of thin film and of the lateral correlation length of the surface, specifically they lead to the universality class for particular organic thin film systems. However, most of the organic molecular thin films does not belong to any known universality classes. Hence, in order to understand the details of surface evolution of these complex materials, a new class of growth model/universality class may be needed.

There are currently small number of studies reported on the growth behavior of molecular films, which usually have very different characteristics compared to that commonly observed for inorganic and metallic thin films [122]. However, a number of promising organic molecules/compounds have found applications in various high performance devices. So, it is

very much essential to investigate the growth dynamics of promising organic molecules which are used as active layer for optoelectronic applications. There are specific issues for growth of organic molecular thin film which can lead to quantitatively and qualitatively different growth behavior [23], such as:

(a) *Internal degrees of freedom:* Organic molecules are large-'extended objects' as compared to the inorganic atoms and thus have internal degrees of freedom. This is probably the most fundamental difference between growth of atomic layers in inorganic systems and growth of organic films. The *orientational degrees of freedom,* which is not included in conventional growth models can give rise to qualitatively new phenomena, such as the change of the molecular orientation during film growth, such as 'lying-down' and 'standing-up' geometry. Also, the *vibrational degrees of freedom* can have an impact on the interaction with the surface as well as the thermalisation upon adsorption and the diffusion behavior. These intrinsic anisotropy will lead the extra diffusion barrier during the growth of thinfilms on various substrates.

(b) *Interaction potential*: The interaction potential between molecule and molecule and molecule and substrate is generally different from the case of atomic adsorbates, and hence, van-der-Waals (vdW) interactions are also important. So, the interaction vdW potential also contributes to the step-edge barrier during the thin film deposition.

(c) *Molecule size*: The size of the molecules and its unit cells are typically greater than that of the typical inorganic substrates, which leads to lattice mismatches. Organics thin films frequently crystallize in low-symmetry structures on to inorganic substrates, which again can lead to multiple domains and it results in extra energy barrier or Schwoebel type barrier/step-edge barrier.

Generally, most of the above issues directly or indirectly have impacts on the thin film surface morphology and the molecules experience a barriers during the diffusion. Thus, the growth dynamics exhibit substrate induced differences and exhibits significant differences with that of the inorganic systems.

Thin films of organic semiconductors have attracted significant interest due to their promising organic electronics applications. They have potential applications in various

optoelectronic devices, most notably in organic field-effect transistors (OFETs), organic light emitting diodes (OLEDs), and organic photovoltaics (OPVs), organic sensors, organic displays, radio frequency identification tags (RFIDs) etc. The advantages of organic electronics in comparison to silicon-based technology are manifold. Properties such as low-cost fabrication, material flexibility (leads to different choices for device fabrication), large-scale fabrication by roll-to-roll printing process, even possibly biocompatiblity and biodegradiblity of the electronic material scientifically and technologically are most attractive [12,59,123-133].

The solution deposition and vacuum deposition are two basic methods for fabricating organic semiconductor thin films. The former is suitable for processing soluble organic small-molecule or polymer materials, while the latter is suitable for processing insoluble organic small-molecule materials. Vacuum deposition is primarily used to fabricate small molecule based organic semiconductor thin films. It allows a very precise control in fabrication and tailoring of the properties of the organic thin films, which is of utmost necessity for detailed study of growth mechanism. Its main advantages are the easy control of the thickness and purity of the film, and the fact that highly ordered films can be obtained by tuning deposition parameters, such as the molecule deposition rate and the substrate temperature [9].

From the view of device perspective, the manufacturing of high quality organic field-effect transistors (OFETs) is necessary, since it is a key component for various optoelectronic devices. Here, the organic semiconductor is only not the component, and it is also very important to incorporate a suitable gate insulator. Again, the crucial parameters is not only the dielectric constant, but also its thickness. The insulator should be ideally pin-hole or void free to achieve the high device performance. The major motivation to search for alternatives to SiO_2 gate insulator is to significantly reduce the OFET operating voltage. In fact, while the carrier mobilities of organic semiconductors have now approached those of amorphous Si, this has generally been achieved at very large drain-source voltage or gate-source voltages, typically greater than 30-50 V. OFET operation employing such large biases will require excessive power consumption, which is a hinderance for real life applications. Furthermore, in such devices, the semiconductor carrier mobility is gate bias dependent. So, the issues related to SiO_2 gate dielectric can be stated as: (a) high operating voltage, (b) low dielectric

constant, (c) cost-effective process, (c) high leakage current, (d) high temperature processing, and (d) limited choice of substrates. In contrast to SiO_2, PMMA/Al_2O_3, SAM modified Al_2O_3, $SrTiO_3$, $BaTiO_3$ have several advantages such as (a) low leakage current density (b) low operating voltage, (c) room temperature processable, (d) low-cost, (e) un-limited choice of substrates [8,16,134-137]. So, OFET gate insulators can fulfill demands specific to organic electronics such as low-cost manufacturing by using high k-gate dielectric, such as PMMA/Al_2O_3 as compared to that of SiO_2 gate dielectric. In addition, over the last few years, high-quality, n-type transistors based on organic semiconductors has been demonstrated with performance close to that of the best p-type materials. However, most research effort has focused on the development of materials with high field-effect mobility and good environmental stability; as a result the mobility of n-channel/p-channel organic field-effect transistor (OFET) exceeds that of the amorphous silicon FET (a-Si FET). Further, very limited studies have been performed on the bias-stress stability of n-channel/p-channel OFETs, though this is of paramount importance to realize the full commercial potential of OFETs. Furthermore, after low operating voltage and high air stable unipolar OFET (n-channel or p-channel), there is an urgent demand for low power consumping, high air stable ambipolar organic field-effect transistors, which allows both electrons and holes to be injected and transported in the same devices, i.e., devices can operate in unipolar mode as well as in an ambipolar mode. There are several challenges to acieve ambipolarity, such as: (a) circuit complexity, (b) active material selection, (c) choice of contact electrode, (d) choice of proper gate dielectric, (e) low operating voltage, (f) high operation stability in ambient condition etc. Bilayer heterojunction structures appear to be one of the very promising approaches for device fabrication, as they are readily deposited on the same substrate without breaking the vacuum.

1.8 Focus of the Present Thesis

Understanding of the film morphology and growth model of organic molecular semiconductors is quite limited. Organic thin films reveal a good variety of growth mechanisms, from single crystal growth to rough granular growth, which makes it really difficult to generalize to model the organic growth using one simple independent model. Despite of substantial success, there are several challenges for the fabrication of high quality

unipolar and ambipolar organic field-effect transistors with reproducible device properties for their applications in various areas of electronic and optoelectronics applications. The main focus of the present thesis is as follows:

- The influence of the molecule-substrate (organic-inorganic) interation on the growth process and the substrate dependent structure and morphology of organic thin film.
- The influence of thickness and substrate temperature on organic thin film evolution.
- Possible growth scenario and underlying physics of $SnCl_2Pc$ and VOPc thin films using height-height correlation function (HHCF), scaling exponents and 2D-fast Fourier transform analysis.
- Fabrication of low operating voltage organic field-effect transistors (OFET) and study of effect of different gate dielectric SiO_2, $PMMA/Al_2O_3$ on top-contact $SnCl_2Pc$ based n-channel OFET devices performances.
- Bias stress stability study using stretched exponential decay function.
- Effect of contact electrodes Al and Ag on the device performances and bias stress stability of $SnCl_2Pc$ based OFET.
- Fabrication of top contact VOPc based promising p-channel OFET and studies of effect of self-assembled mono layer HMDS treated and non-treated SiO_2 gate dielectric on the device performances. Microscopic understanding of VOPc thin films on HMDS treated and non-treated substrates.
- Ambient condition reliability study for HMDS treated and non-treated on VOPc p-channel OFET using stretched exponential model and plausible explanations for device stability.
- Fabrication of low operating voltage top-contact $SnCl_2Pc/CuPc$ heterostructure ambipolar OFET using $PMMA/Al_2O_3$ bilayer gate dielectric.
- Study of effect of active layer thickness variation on contact resistance and relation between thickness variation and device performance.
- Bias stress stability study using stretched exponential model for both p-channel and n-channel ambipolar OFET and possible mechanism of device instability.
- Cyclic bias stress stability of ambipolar OFET as devices often need ‘on’ and ‘off’ operation mode.

1.9 Organization of the Thesis

This thesis presents a systematic study on the growth mechanism, growth dynamics of organic thin films and device performances of organic unipolar and ambipolar field-effect transistors based on phthalocyanine molecules. The complete thesis work has been organized into eight chapters. The present chapter, i.e., ***Chapter 1*** introduced a brief account of the organic semiconductors, particularly small molecule based $SnCl_2Pc$, VOPc, CuPc molecules. This chapter also included brief discussion on the study of growth kinetics of thin films, charge transport, electrical parameters of OFETs, and its bias stress stability. ***Chapter 2*** provides a brief description of the experimental techniques used for the present work along with the working principles of some characterization tools. In ***Chapter 3,*** we present the results the evolution of surface morphology and scaling behavior of non-planar $SnCl_2Pc$ thin films grown on Si(100) and glass substrates. Our results imply the superiority of glass substrate over the Si substrate for the growth of device quality $SnCl_2Pc$ thin film. The systematic study of substrate dependent growth behavior and possible growth model is described elaborately in this chapter. In ***Chapter 4,*** we present the systematic study of the surface evolution and growth dynamics of non-planar VOPc molecular thin film on SiO_2 and ITO-glass substrate, substrate temperature dependent growth behavior and particularly provide some insights on the role of molecular-substrate interface. It includes discussion on the substrate induced growth scenario from the AFM, height-height correlation function (HHCF) and two dimensional fast Fourier transform (2D FFT) analyses. ***Chapter 5*** provides a quantitative analysis of the electrical performances and stability of vacuum-deposited thin film based n-channel organic field-effect transistors with $SnCl_2Pc$ in top contact bottom gate configuration using Ag source/drain electrodes and PMMA/Al_2O_3 as a bilayer gate dielectric as well as SiO_2 gate dielectric. Furthermore, we demonstrate the effect of contact electrodes Al and Ag on the performance and stability of $SnCl_2Pc$ based n-channel OFET. In ***Chapter 6,*** we address the VOPc based p-channel OFET performance in an ambient condition and its operational stability using HMDS treated SiO_2 and non-treated SiO_2 gate dielectric layer. We demonstrate that HMDS treated devices shows high performances and better air stability than the devices with non-treated SiO_2 layer**.** In ***Chapter 7,*** we explore a bilayer ambipolar OFET based on the heterojunction of low band gap $SnCl_2Pc$ and CuPc small molecules and Ag top contact, which exhibit ambipolar conduction in heterostructure configuration. The change in

the active layer thickness resulted in the evolution of the field-effect mobility values and it is also found that the optimized thickness of $SnCl_2Pc$/CuPc heterostructure yielded balanced carrier mobility. We also study the device stability for optimized thickness of the $SnCl_2Pc$/CuPc layers. Finally, in ***Chapter 8,*** we provide a summary and outlook of the present thesis. In particular, the highlights of the major contributions of the thesis, important conclusions of the present work and scope for future studies on phthalocyanine based organic molecules and its application as organic field - effect transistors are presented.

References

[1] J. Kim, J. Jang, K. Kim, H. Kim, S.H. Kim, C.E. Park, The Origin of Excellent Gate-Bias Stress Stability in Organic Field-Effect Transistors Employing Fluorinated-Polymer Gate Dielectrics. *Adv. Mater.* **26**, 7241 (2014).

[2] K.S. J. Koenigsberger, General subject of conduction in metallic salts. *Ann. Physik* **32**, 179 (1910).

[3] M. Pope, H.P. Kallmann, P. Magnante, Electroluminescence in Organic Crystals. *J. Chem. Phys.* **38**, 2042 (1963).

[4] G. Horowitz, D. Fichou, X. Peng, Z. Xu, F. Garnier, A field-effect transistor based on conjugated alpha-sexithienyl. *Solid State Communications* **72**, 381 (1989).

[5] G. Horowitz, X. Peng, D. Fichou, F. Garnier, The oligothiophene-based field-effect transistor: How it works and how to improve it. *J. Appl. Phys.* **67**, 528 (1990).

[6] A. Tsumura, H. Koezuka, T. Ando, Macromolecular electronic device: Field-effect transistor with a polythiophene thin film. *Appl. Phys. Lett.* **49**, 1210 (1986).

[7] A. Tsumura, H. Koezuka, T. Ando, Polythiophene field-effect transistor: Its characteristics and operation mechanism. *Synthetic Metals* **25**, 11 (1988).

[8] H. Ohta, T. Kambayashi, K. Nomura, M. Hirano, K. Ishikawa, H. Takezoe, H. Hosono, Transparent Organic Thin-Film Transistor with a Laterally Grown Non-Planar Phthalocyanine Channel. *Adv. Mater.* **16**, 312 (2004).

[9] G. Horowitz, Organic Field-Effect Transistors. *Adv. Mater.* **10**, 365 (1998).

[10] F. Dinelli, R. Capelli, M.A. Loi, M. Murgia, M. Muccini, A. Facchetti, T.J. Marks, High-Mobility Ambipolar Transport in Organic Light-Emitting Transistors. *Adv. Mater.* **18**, 1416 (2006).

[11] J. Zaumseil, R.H. Friend, H. Sirringhaus, Spatial control of the recombination zone in an ambipolar light-emitting organic transistor. *Nat. Mater.* **5**, 69 (2006).

[12] D. Tobjörk, R. Österbacka, Paper Electronics. *Adv. Mater.* **23**, 1935 (2011).

[13] P. Stallinga, *Electrical Characterization of Organic Electronic Materials and Devices*, John Wiley & Sons, (2009).

[14] Y. Liang, H.-C. Chang, P. Paul Ruden, C. Daniel Frisbie, Examination of Au, Cu, and Al contacts in organic field-effect transistors via displacement current measurements. *J. Appl. Phys.* **110**, 064514 (2011).

[15] I. Kymissis, Org*anic Field Effect Transistors:Theory, Fabrication and Characterization*, Springer, (2009).

[16] Z. Bao, J. Locklin, *Organic Field-Effect Transistors*, CRC Press, Taylor & Francis Group, (2007).

[17] S.G.J. Mathijssen, M. Kemerink, A. Sharma, M. Cölle, P.A. Bobbert, R.A.J. Janssen, D.M. de Leeuw, Charge Trapping at the Dielectric of Organic Transistors Visualized in Real Time and Space. *Adv. Mater.* **20**, 975 (2008).

[18] J. Janczak, R. Kubiak, Two isomorphous complexes: dichloro[phthalocyaninato(2-)]tin(IV) and dichloro[phthalocyaninato(2-)]germanium(IV). *Acta Cryst. C* **59**, m237 (2003).

[19] R.F. Ziolo, C.H. Griffiths, J.M. Troup, Crystal structure of vanadyl phthalocyanine, phase II. *J. Am. Chem. Soc, Dalton Transactions*, 2300 (1980).

[20] C.H. Griffiths, M.S. Walker, P. Goldstein, Polymorphism in Vanadyl Phthalocyanine. *Mol. Cryst. Liq. Cryst.* **33**, 149 (1976).

[21] L. Li, Q. Tang, H. Li, W. Hu, Molecular Orientation and Interface Compatibility for High Performance Organic Thin Film Transistor Based on Vanadyl Phthalocyanine. *J. Phys. Chem. B* **112**, 10405 (2008).
[22] A. Hoshino, Y. Takenaka, H. Miyaji, Redetermination of the crystal structure of [alpha]-copper phthalocyanine grown on KCl. *Acta Cryst. B* **59**, 393 (2003).
[23] F. Schreiber, Organic molecular beam deposition: Growth studies beyond the first monolayer. *Phys. Status Solidi (a)* **201**, 1037 (2004).
[24] M. Pelliccione, T.-M. Lu, *Evolution of Thin Film Morphology: Modeling and Simulations* (2008).
[25] A.-L. Barabasi, H.E. Stanley, *Fractal concepts in surface growth*, (1995).
[26] T.-M.L. Matthew Pelliccione, *Evolution of Thin Film Morphology: Modeling and Simulations* Springer (2008).
[27] H. Klauk, Organic Electronics: Materials, Manufacturing and Applications, (2006).
[28] W. Brütting, *Physics of Organic Semiconductors*, 2005.
[29] J. Cornil, J.L. Brédas, J. Zaumseil, H. Sirringhaus, Ambipolar Transport in Organic Conjugated Materials. *Adv. Mater.* **19**, 1791 (2007).
[30] Flora M. Li, A. Nathan, Y Wu, B.S. Ong, *Organic Thin Film Transistor Integration: A Hybrid Approach*, Wiley, (2011).
[31] H. Bässler, Charge Transport in Disordered Organic Photoconductors a Monte Carlo Simulation Study. *Phys. Status Solidi (b)* **175**, 15 (1993).
[32] N. Karl, J. Marktanner, R. Stehle, W. Warta, Proceedings of the international conference on science and technology of synthetic metals High-field saturation of charge carrier drift velocities in ultrapurified organic photoconductors. *Synthetic Metals* **42**, 2473 (1991).
[33] E.A. Silinsh, V. Cápek, *Organic molecular crystals: Interaction, localization, and transport phenomena*, AIP Press, New York, (1994).
[34] P.W.M. Blom, M.J.M. de Jong, M.G. van Munster, Electric-field and temperature dependence of the hole mobility in poly(p-phenylene vinylene). *Phys. Rev. B* **55**, R656 (1997).
[35] W.D. Gill, Drift mobilities in amorphous charge-transfer complexes of trinitrofluorenone and poly-n-vinylcarbazole. *J. Appl. Phys.* **43**, 5033 (1972).
[36] A. Miller, E. Abrahams, Impurity Conduction at Low Concentrations. *Phys. Rev.* **120**, 745 (1960).
[37] M.C.J.M. Vissenberg, M. Matters, Theory of the field-effect mobility in amorphous organic transistors. *Phys. Rev. B* **57**, 12964 (1998).
[38] P.G. Le Comber, W.E. Spear, Electronic Transport in Amorphous Silicon Films. *Phys. Rev. Lett.* **25**, 509 (1970).
[39] C.J. Schramm, R.P. Scaringe, D.R. Stojakovic, B.M. Hoffman, J.A. Ibers, T.J. Marks, Chemical, spectral, structural, and charge transport properties of the "molecular metals" produced by iodination of nickel phthalocyanine. *J. Am. Chem. Soc* **102**, 6702 (1980).
[40] S. Allard, M. Forster, B. Souharce, H. Thiem, U. Scherf, Organic Semiconductors for Solution-Processable Field-Effect Transistors (OFETs). *Angew. Chem. Int. Ed.* **47**, 4070 (2008).

[41] D. Natali, M. Caironi, Charge Injection in Solution-Processed Organic Field-Effect Transistors: Physics, Models and Characterization Methods. *Adv. Mater.* **24**, 1357 (2012).
[42] J. Zaumseil, H. Sirringhaus, Electron and Ambipolar Transport in Organic Field-Effect Transistors. *Chem. Rev.* **107**, 1296 (2007).
[43] S. Md. Obaidulla, D.K. Goswami, P.K. Giri, Low bias stress and reduced operating voltage in SnCl2Pc based n-type organic field-effect transistors. *Appl. Phys. Lett.* **104**, 213302 (2014).
[44] M.S. Kang, C.D. Frisbie, A Pedagogical Perspective on Ambipolar FETs. *ChemPhysChem* **14**, 1547 (2013).
[45] S.Z. Bisri, C. Piliego, J. Gao, M.A. Loi, Outlook and Emerging Semiconducting Materials for Ambipolar Transistors. *Adv. Mater.* **26**, 1176 (2014).
[46] S.J. Kang, G.-H. Lee, Y.-J. Yu, Y. Zhao, B. Kim, K. Watanabe, T. Taniguchi, J. Hone, P. Kim, C. Nuckolls, Organic Field Effect Transistors Based on Graphene and Hexagonal Boron Nitride Heterostructures. *Adv. Funct. Mater.* **24**, 5157 (2014).
[47] J. Zhou, R. Chen, A low voltage and small hysteresis C 60 thin film transistor. *Journal of Semiconductors* **32**, 024006 (2011).
[48] H.H. Choi, M.S. Kang, M. Kim, H. Kim, J.H. Cho, K. Cho, Decoupling the Bias-Stress-Induced Charge Trapping in Semiconductors and Gate-Dielectrics of Organic Transistors Using a Double Stretched-Exponential Formula. *Adv. Funct. Mater.* **23**, 690 (2013).
[49] H. Sirringhaus, Reliability of Organic Field-Effect Transistors. *Adv. Mater.* **21**, 3859 (2009).
[50] X.-H. Zhang, S.P. Tiwari, B. Kippelen, Pentacene organic field-effect transistors with polymeric dielectric interfaces: Performance and stability. *Organic Electronics* **10**, 1133 (2009).
[51] U. Zschieschang, R.T. Weitz, K. Kern, H. Klauk, Bias stress effect in low-voltage organic thin-film transistors. *Applied Physics A* **95**, 139 (2009).
[52] A. Tsumura, H. Koezuka, T. Ando, Macromolecular electronic device: Field-effect transistor with a polythiophene thin film. *J. Appl. Phys.* **49**, 1210 (1986).
[53] H. Sirringhaus, 25th Anniversary Article: Organic Field-Effect Transistors: The Path Beyond Amorphous Silicon. *Adv. Mater.* **26**, 1319 (2014).
[54] Y. Zhao, Y. Guo, Y. Liu, 25th Anniversary Article: Recent Advances in n-Type and Ambipolar Organic Field-Effect Transistors. *Advanced Materials* **25**, 5372 (2013).
[55] T. Sekitani, U. Zschieschang, H. Klauk, T. Someya, Flexible organic transistors and circuits with extreme bending stability. *Nat Mater* **9**, 1015 (2010).
[56] T. Kamiya, H. Hosono, Material characteristics and applications of transparent amorphous oxide semiconductors. *NPG Asia Mater* **2**, 15 (2010).
[57] H. Sirringhaus, N. Tessler, R.H. Friend, Integrated Optoelectronic Devices Based on Conjugated Polymers. *Science* **280**, 1741 (1998).
[58] A. Nathan, G.R. Chaji, S.J. Ashtiani, Driving schemes for a-Si and LTPS AMOLED displays. *Journal of Display Technology* **1**, 267 (2005).
[59] D. Song, H. Wang, F. Zhu, J. Yang, H. Tian, Y. Geng, D. Yan, Phthalocyanato Tin(IV) Dichloride: An Air-Stable, High-Performance, n-Type Organic Semiconductor with a High Field-Effect Electron Mobility. *Adv. Mater.* **20**, 2142 (2008).

[60] M. Barra, F.V.D. Girolamo, F. Chiarella, M. Salluzzo, Z. Chen, A. Facchetti, L. Anderson, A. Cassinese, Transport Property and Charge Trap Comparison for N-Channel Perylene Diimide Transistors with Different Air-Stability. *J. Phys. Chem. C* **114**, 20387 (2010).

[61] R.J. Chesterfield, J.C. McKeen, C.R. Newman, P.C. Ewbank, D.A. da Silva Filho, J.-L. Brédas, L.L. Miller, K.R. Mann, C.D. Frisbie, Organic Thin Film Transistors Based on N-Alkyl Perylene Diimides: Charge Transport Kinetics as a Function of Gate Voltage and Temperature. *J. Phys. Chem. B* **108**, 19281 (2004).

[62] D. Zhang, L. Zhao, Y. Zhu, A. Li, C. He, H. Yu, Y. He, C. Yan, O. Goto, H. Meng, Effects of p-(Trifluoromethoxy)benzyl and p-(Trifluoromethoxy)phenyl Molecular Architecture on the Performance of Naphthalene Tetracarboxylic Diimide-Based Air-Stable n-Type Semiconductors. *ACS Appl. Mater. Interfaces* **8**, 18277 (2016).

[63] B.J. Jung, K. Lee, J. Sun, A.G. Andreou, H.E. Katz, Air-Operable, High-Mobility Organic Transistors with Semifluorinated Side Chains and Unsubstituted Naphthalenetetracarboxylic Diimide Cores: High Mobility and Environmental and Bias Stress Stability from the Perfluorooctylpropyl Side Chain. *Adv. Funct. Mater.* **20**, 2930 (2010).

[64] J.-i. Nishida, H. Deno, S. Ichimura, T. Nakagawa, Y. Yamashita, Preparation, physical properties and n-type FET characteristics of substituted diindenopyrazinediones and bis(dicyanomethylene) derivatives. *J. Phys. Chem.* **22**, 4483 (2012).

[65] M. Mamada, D. Kumaki, J.-i. Nishida, S. Tokito, Y. Yamashita, Novel Semiconducting Quinone for Air-Stable n-Type Organic Field-Effect Transistors. *ACS Appl. Mater. Interfaces* **2**, 1303 (2010).

[66] Z. Liang, Q. Tang, J. Liu, J. Li, F. Yan, Q. Miao, N-Type Organic Semiconductors Based on π-Deficient Pentacenequinones: Synthesis, Electronic Structures, Molecular Packing, and Thin Film Transistors. *Chem. Mater.* **22**, 6438 (2010).

[67] Y.-I. Park, J.S. Lee, B.J. Kim, B. Kim, J. Lee, D.H. Kim, S.-Y. Oh, J.H. Cho, J.-W. Park, High-Performance Stable n-Type Indenofluorenedione Field-Effect Transistors. *Chem. Mater.* **23**, 4038 (2011).

[68] X.-H. Zhang, B. Domercq, B. Kippelen, High-performance and electrically stable C60 organic field-effect transistors. *J. Appl. Phys.* **91**, 092114 (2007).

[69] W.H. Lee, H.H. Choi, D.H. Kim, K. Cho, 25th Anniversary Article: Microstructure Dependent Bias Stability of Organic Transistors. *Adv. Mater.* **26**, 1660 (2014).

[70] H.H. Choi, W.H. Lee, K. Cho, Bias-Stress-Induced Charge Trapping at Polymer Chain Ends of Polymer Gate-Dielectrics in Organic Transistors. *Adv. Funct. Mater.* **22**, 4833 (2012).

[71] K. Park, S.H. Park, E. Kim, J.-D. Kim, S.-Y. An, H.S. Lim, H.H. Lee, D.H. Kim, D.Y. Ryu, D.R. Lee, J.H. Cho, Polymer Brush As a Facile Dielectric Surface Treatment for High-Performance, Stable, Soluble Acene-Based Transistors. *Chem. Mater.* **22**, 5377 (2010).

[72] S.G.J. Mathijssen, M. Cölle, H. Gomes, E.C.P. Smits, B. de Boer, I. McCulloch, P.A. Bobbert, D.M. de Leeuw, Dynamics of Threshold Voltage Shifts in Organic and Amorphous Silicon Field-Effect Transistors. *Adv. Mater.* **19**, 2785 (2007).

[73] B. Lee, A. Wan, D. Mastrogiovanni, J.E. Anthony, E. Garfunkel, V. Podzorov, Origin of the bias stress instability in single-crystal organic field-effect transistors. *Phys. Rev. B* **82**, 085302 (2010).

[74] C. Liu, Y. Xu, Y. Li, W. Scheideler, T. Minari, Critical Impact of Gate Dielectric Interfaces on the Contact Resistance of High-Performance Organic Field-Effect Transistors. *J. Phys. Chem. C* **117**, 12337 (2013).

[75] H. Kim, M. Rajeshkumar Reddy, G. Kwon, D. Choi, C. Kim, S. Seo, Synthesis and characterization of 2,7-diethynyl-benzo[b]benzo[4,5]thieno[2,3-d]thiophene derivative as organic semiconductors for organic thin-film transistors. *Synthetic Metals* **220**, 599 (2016).

[76] S. Bisoyi, U. Zschieschang, M.J. Kang, K. Takimiya, H. Klauk, S.P. Tiwari, Bias-stress stability of low-voltage p-channel and n-channel organic thin-film transistors on flexible plastic substrates. *Organic Electronics* **15**, 3173 (2014).

[77] X. Xu, Y. Yao, B. Shan, X. Gu, D. Liu, J. Liu, J. Xu, N. Zhao, W. Hu, Q. Miao, Electron Mobility Exceeding 10 cm2 V−1 s−1 and Band-Like Charge Transport in Solution-Processed n-Channel Organic Thin-Film Transistors. *Adv. Mater.* **28**, 5276 (2016).

[78] L. Wang, G. Liu, F. Zhu, F. Pan, D. Yan, Electrical instability in vanadyl-phthalocyanine thin-film transistors. *J. Appl. Phys.* **93**, 173303 (2008).

[79] Y. Yan, Q.-J. Sun, X. Gao, P. Deng, Q. Zhang, S.-D. Wang, Probing bias stress effect and contact resistance in bilayer ambipolar organic field-effect transistors. *J. Appl. Phys.* **103**, 073303 (2013).

[80] S.M. Obaidulla, P.K. Giri, Low operating voltage and low bias stress in top-contact SnCl2Pc/CuPc heterostructure-based bilayer ambipolar organic field-effect transistors. *J. Phys. Chem. C* **3**, 7118 (2015).

[81] S.J. Noever, S. Fischer, B. Nickel, Dual Channel Operation Upon n-Channel Percolation in a Pentacene-C60 Ambipolar Organic Thin Film Transistor. *Adv. Mater.* **25**, 2147 (2013).

[82] D.-K. Kim, J.-D. Oh, E.-S. Shin, H.-S. Seo, J.-H. Choi, Study on copper phthalocyanine and perylene-based ambipolar organic light-emitting field-effect transistors produced using neutral beam deposition method. *J. Appl. Phys.* **115**, 164503 (2014).

[83] M.A. Loi, E. da Como, F. Dinelli, M. Murgia, R. Zamboni, F. Biscarini, M. Muccini, Supramolecular organization in ultra-thin films of [alpha]-sexithiophene on silicon dioxide. *Nat. Mater.* **4**, 81 (2005).

[84] A.C. Mayer, A. Kazimirov, G.G. Malliaras, Dynamics of Bimodal Growth in Pentacene Thin Films. *Phys. Rev. Lett.* **97**, 105503 (2006).

[85] J. Yang, T. Wang, H. Wang, F. Zhu, G. Li, D. Yan, Ultrathin-Film Growth of para-Sexiphenyl (I): Submonolayer Thin-Film Growth as a Function of the Substrate Temperature. *J. Phys. Chem. B* **112**, 7816 (2008).

[86] A.C. Dürr, F. Schreiber, K.A. Ritley, V. Kruppa, J. Krug, H. Dosch, B. Struth, Rapid Roughening in Thin Film Growth of an Organic Semiconductor (Diindenoperylene). *Phys. Rev. Lett.* **90**, 016104 (2003).

[87] G. Hlawacek, P. Puschnig, P. Frank, A. Winkler, C. Ambrosch-Draxl, C. Teichert, Characterization of Step-Edge Barriers in Organic Thin-Film Growth. *Science* **321**, 108 (2008).

[88] D.G. de Oteyza, E. Barrena, J.O. Ossó, S. Sellner, H. Dosch, Thickness-Dependent Structural Transitions in Fluorinated Copper-phthalocyanine (F16CuPc) Films. *J. Am. Chem. Soc* **128**, 15052 (2006).

[89] J. Yang, D. Yan, T.S. Jones, Molecular Template Growth and Its Applications in Organic Electronics and Optoelectronics. *Chem. Rev.* **115**, 5570 (2015).

[90] G. Zhang, B.L. Weeks, M. Holtz, Application of dynamic scaling to the surface properties of organic thin films: Energetic materials. *Surface Science* **605**, 463 (2011).

[91] S. Kowarik, A. Gerlach, S. Sellner, F. Schreiber, J. Pflaum, L. Cavalcanti, O. Konovalov, Anomalous roughness evolution of rubrene thin films observed in real time during growth. *Phys. Chem. Chem. Phys.* **8**, 1834 (2006).

[92] S. Kowarik, A. Gerlach, F. Schreiber, Organic molecular beam deposition: fundamentals, growth dynamics, and in situ studies. *J. Phys. Condens. Matter.* **20**, 184005 (2008).

[93] S. Bommel, N. Kleppmann, C. Weber, H. Spranger, P. Schäfer, J. Novak, S.V. Roth, F. Schreiber, S.H.L. Klapp, S. Kowarik, Unravelling the multilayer growth of the fullerene C60 in real time. *Nat. Commun.* **5** (2014).

[94] J. Yang, S. Yim, T.S. Jones, Molecular-Orientation-Induced Rapid Roughening and Morphology Transition in Organic Semiconductor Thin-Film Growth. *Scientific Reports* **5**, 9441 (2015).

[95] A. Winkler, On the nucleation and initial film growth of rod-like organic molecules. *Surface Science* **652**, 367 (2016).

[96] T.N. Krauss, E. Barrena, X.N. Zhang, D.G. de Oteyza, J. Major, V. Dehm, F. Würthner, L.P. Cavalcanti, H. Dosch, Three-Dimensional Molecular Packing of Thin Organic Films of PTCDI-C8 Determined by Surface X-ray Diffraction. *Langmuir* **24**, 12742 (2008).

[97] X. Zeng, L. Wang, L. Duan, Y. Qiu, Homoepitaxy Growth of Well-Ordered Rubrene Thin Films. *Crystal Growth & Design* **8**, 1617 (2008).

[98] T.V. Desai, A.R. Woll, F. Schreiber, J.R. Engstrom, Nucleation and Growth of Perfluoropentacene on Self-Assembled Monolayers: Significant Changes in Island Density and Shape with Surface Termination. *J. Phys. Chem. C* **114**, 20120 (2010).

[99] M. Naboka, S. Soubatch, A. Nefedov, F.S. Tautz, C. Wöll, Direct Evidence of the Temperature-Induced Molecular Reorientation in Tetracene Thin Films on AlOx/Ni3Al(111). *J. Phys. Chem. C* **118**, 22678 (2014).

[100] K. Vasseur, C. Rolin, S. Vandezande, K. Temst, L. Froyen, P. Heremans, A Growth and Morphology Study of Organic Vapor Phase Deposited Perylene Diimide Thin Films for Transistor Applications. *J. Phys. Chem. C* **114**, 2730 (2010).

[101] H. Peisert, T. Schwieger, J.M. Auerhammer, M. Knupfer, M.S. Golden, J. Fink, P.R. Bressler, M. Mast, Order on disorder: Copper phthalocyanine thin films on technical substrates. *J. Appl. Phys.* **90**, 466 (2001).

[102] T.V. Basova, V.G. Kiselev, I.S. Dubkov, F. Latteyer, S.A. Gromilov, H. Peisert, T. Chassè, Optical Spectroscopy and XRD Study of Molecular Orientation, Polymorphism, and Phase Transitions in Fluorinated Vanadyl Phthalocyanine Thin Films. *J. Phys. Chem. C* **117**, 7097 (2013).

[103] M. Yilmaz, M. Ozdemir, H. Erdogan, U. Tamer, U. Sen, A. Facchetti, H. Usta, G. Demirel, Micro-/Nanostructured Highly Crystalline Organic Semiconductor Films for

Surface-Enhanced Raman Spectroscopy Applications. *Adv. Funct. Mater.* **25**, 5669 (2015).

[104] D.M. DeLongchamp, R.J. Kline, D.A. Fischer, L.J. Richter, M.F. Toney, Molecular Characterization of Organic Electronic Films. *Adv. Mater.* **23**, 319 (2011).

[105] S. Heutz, S.M. Bayliss, R.L. Middleton, G. Rumbles, T.S. Jones, Polymorphism in Phthalocyanine Thin Films: Mechanism of the α → β Transition. *J. Phys. Chem. B* **104**, 7124 (2000).

[106] Y. Li, S. Chen, Q. Liu, Y. Li, Y. Shi, X. Wang, J. Ma, Z. Hu, Influence of Deposition Pressure on the Film Morphologies, Structures, and Mobilities for Different-Shaped Organic Semiconductors. *J. Phys. Chem. C* **118**, 14218 (2014).

[107] D. Hong, Y.R. Do, H.T. Kwak, S. Yim, Structural templating and growth behavior of copper phthalocyanine thin films deposited on a polycrystalline perylenetetracarboxylic dianhydride layer. *J. Appl. Phys.* **109**, 063507 (2011).

[108] D. Roy, N.M. Das, P.S. Gupta, Effect of annealing on the growth dynamics of ZnPc LB thin film and its surface morphology. *AIP Advances* **4**, 077126 (2014).

[109] H. Peisert, I. Biswas, M. Knupfer, T. Chassé, Orientation and electronic properties of phthalocyanines on polycrystalline substrates. *Phys. Status Solidi (b)* **246**, 1529 (2009).

[110] Y. Zhang, E. Barrena, X. Zhang, A. Turak, F. Maye, H. Dosch, New Insight into the Role of the Interfacial Molecular Structure on Growth and Scaling in Organic Heterostructures. *J. Phys. Chem. C* **114**, 13752 (2010).

[111] Z. Wang, T. Miyadera, T. Yamanari, Y. Yoshida, Templating Effects in Molecular Growth of Blended Films for Efficient Small-Molecule Photovoltaics. *ACS Appl. Mater. Interfaces* **6**, 6369 (2014).

[112] M. Petit, R. Hayakawa, Y. Wakayama, T. Chikyow, Early Stage of Growth of a Perylene Diimide Derivative Thin Film Growth on Various Si(001) Substrates. *J. Phys. Chem. C* **111**, 12747 (2007).

[113] C. Frank, J. Novák, R. Banerjee, A. Gerlach, F. Schreiber, A. Vorobiev, S. Kowarik, Island size evolution and molecular diffusion during growth of organic thin films followed by time-resolved specular and off-specular scattering. *Phys. Rev. B* **90**, 045410 (2014).

[114] X. Zhang, E. Barrena, D. Goswami, D.G. de Oteyza, C. Weis, H. Dosch, Evidence for a Layer-Dependent Ehrlich-Schwobel Barrier in Organic Thin Film Growth. *Phys. Rev. Lett.* **103**, 136101 (2009).

[115] J.H. Jeffries, J.K. Zuo, M.M. Craig, Instability of Kinetic Roughening in Sputter-Deposition Growth of Pt on Glass. *Phys. Rev. Lett.* **76**, 4931 (1996).

[116] G.-C.W. Yiping Zhao, and Toh-Ming Lu, *Characterization of Amorphous and Crystalline Rough Surface: Principles and Applications*, ACADEMIC PRESS, (2001).

[117] J.T. Drotar, Y.P. Zhao, T.M. Lu, G.C. Wang, Surface roughening in shadowing growth and etching in 2+1 dimensions. *Phys. Rev. B* **62**, 2118 (2000).

[118] A. Pal, R. Ghosh, P.K. Giri, Early stages of growth of Si nanowires by metal assisted chemical etching: A scaling study. *Appl. Phys. Lett.* **107**, 072104 (2015).

[119] S. Chen, J. Liang, Y. Mo, D. Luo, S. Jiang, Onset of shadowing-dominated growth of Ag films in glancing angle deposition: Kinetic Monte Carlo simulation. *Appl. Surf. Sci.* **264**, 552 (2013).

[120] D. Bonamy, L. Ponson, S. Prades, E. Bouchaud, C. Guillot, Scaling Exponents for Fracture Surfaces in Homogeneous Glass and Glassy Ceramics. *Phys. Rev. Lett.* **97**, 135504 (2006).
[121] L. Ponson, D. Bonamy, E. Bouchaud, Two-Dimensional Scaling Properties of Experimental Fracture Surfaces. *Phys. Rev. Lett.* **96**, 035506 (2006).
[122] S. Yim, T.S. Jones, Growth dynamics of C60 thin films: Effect of molecular structure. *Appl. Phys. Lett.* **94**, 021911 (2009).
[123] R.A. Street, Thin-Film Transistors. *Adv. Mater.* **21**, 2007 (2009).
[124] M. Mas-Torrent, C. Rovira, Novel small molecules for organic field-effect transistors: towards processability and high performance. *Chem. Soc. Rev.* **37**, 827 (2008).
[125] H. Klauk, Organic thin-film transistors. *Chem. Soc. Rev.* **39**, 2643 (2010).
[126] M. Irimia-Vladu, P.A. Troshin, M. Reisinger, G. Schwabegger, M. Ullah, R. Schwoediauer, A. Mumyatov, M. Bodea, J.W. Fergus, V.F. Razumov, H. Sitter, S. Bauer, N.S. Sariciftci, Environmentally sustainable organic field effect transistors. *Organic Electronics* **11**, 1974 (2010).
[127] L. Schmidt-Mende, M. Watson, K. Müllen, R.H. Friend, Organic Thin Film Photovoltaic Devices from Discotic Materials. *Molecular Crystals and Liquid Crystals* **396**, 73 (2003).
[128] X.J. Yu, J.B. Xu, W.Y. Cheung, N. Ke, Optimizing the growth of vanadyl-phthalocyanine thin films for high-mobility organic thin-film transistors. *J. Appl. Phys.* **102**, 103711 (2007).
[129] L. Li, Q. Tang, H. Li, W. Hu, X. Yang, Z. Shuai, Y. Liu, D. Zhu, Organic thin-film transistors of phthalocyanines, Pure and Applied Chemistry, 2008, p. 2231.
[130] M.T. Hussein, I.S. Naji, A.F. Abdulameer, E.K. Hassen, M.S. Badri, Capacitive-resistive measurements of cobalt-phthalocyanine organic humidity sensors. *Photonic Sensors* **5**, 257 (2015).
[131] P. Lutsyk, J. Misiewicz, A. Podhorodecki, Y. Vertsimakha, Photovoltaic properties of SnCl2Pc films and SnCl2Pc/pentacene heterostructures. *Sol. Energ. Mat. Sol. Cells* **91**, 47 (2007).
[132] B.P. Rand, J. Xue, F. Yang, S.R. Forrest, Organic solar cells with sensitivity extending into the near infrared. *Appl. Phys. Lett.* **87**, 233508 (2005).
[133] L. Zuo, X. Jiang, M. Xu, L. Yang, Y. Nan, Q. Yan, H. Chen, Enhancement of short current density in polymer solar cells with phthalocyanine tin (IV) dichloride as interfacial layer. *Sol. Energ. Mat. Sol. Cells* **95**, 2664 (2011).
[134] L.A. Majewski, R. Schroeder, M. Grell, P.A. Glarvey, M.L. Turner, High capacitance organic field-effect transistors with modified gate insulator surface. *J. Appl. Phys.* **96**, 5781 (2004).
[135] A. Facchetti, M.H. Yoon, T.J. Marks, Gate Dielectrics for Organic Field-Effect Transistors: New Opportunities for Organic Electronics. *Adv. Mater.* **17**, 1705 (2005).
[136] A.F. Rocı´o Ponce Ortiz, and Tobin J. Marks, High-k Organic, Inorganic, and Hybrid Dielectrics for Low-Voltage Organic Field-Effect Transistors. *Chem. Rev.* **110**, 205 (2010).
[137] S.O. Janos Veres, Giles Lloyd, and Dago de Leeuw, Gate Insulators in Organic Field-Effect Transistors. *Chem. Mater.* **16**, 4543 (2004).

This Page is Left Blank Intentionally

Chapter 2

Experimental Techniques

In this chapter, we have provided a brief outline of the various experimental techniques used for the preparation of samples, systematic growth of organic thin films and fabrication for OFET devices. The techniques related to the fabrication of organic field-effect transistors are elaborated in details. Organic molecular beam deposition (OMBD) that works under high vacuum condition and anodization techniques for thin film growth are discussed in this thesis. For the characterization of both thin film and thin film-based devices, several standard analytical, optical, electrical characterization tools are used, which are discussed in this chapter. The methodology adopted to analyze the data from various spectroscopic tools is also discussed in brief.

For the present thesis, we use atomic force microscopy (AFM), X-ray diffraction (XRD), Thermogravimetric analysis (TGA), X-ray Photoelectron Spectroscopy (XPS), and UV-visible absorption spectroscopy. While AFM gives information on the surface morphology of the substrate, organic layer, polymer dielectric layer and 2D planar structure at the nanometer to micrometer scale, XRD probes the crystalline structure of the layers in a macroscopic scale. TGA analysis reveals the structural stability of the molecules. Furthermore, XPS analysis yields the chemical composition of thin film surface and/or surface-interfaces. UV-vis absorption spectroscopy measurement provides the information on the electronic transitions and the quantification of the anisotropy of the layers, which are related to the degree of structural order present. Semiconductor parameter analyzer provides information on different electrical parameters including the mobility of the carriers in the materials. The combination of all these different techniques allows a better understanding of the properties of the organic layers. With the inter disciplinary approach, we aim to develop a better understanding of the interaction between the structural, optical and electrical properties of the organic layers and OFET devices.

We now present an overview of the materials and methods that were employed for our experimental work. More specific experimental details can be found in ***Chapter 4*** through ***Chapter 7***, where we describe the relevant details of each system.

2.1 Thin Film Growth Techniques

Physical vapor deposition involves the deposition of molecules/metal atom from the vapor phase to the solid phase onto a desired substrate. Thin films can be grown by the basic techniques of vacuum evaporation, which are elaborated below:

2.1.1 Organic Molecular Beam Deposition

Nowadays, a variety of techniques are available for depositing organic thin films, such as liquid deposition (e.g. drop-cast, spin-coating, blade coating), direct printing (e.g. contact stamp printing). However, for molecule that are low soluble or partially soluble in the common solvent, the organic molecular beam deposition is a typical method, which is being increasingly used for small molecule based organic semiconductor thin-film preparation [1]. The organic small molecules, such as acenes, phthalocynanine sublime at relatively low sublimation temperature (generally lower than <400 °C in high vacuum) [2-4] and can easily be deposited by thermal evaporation. However, here the control of temperature is much more critical compared to inorganic materials, as they can be destroyed easily at high temperature. Therefore, evaporation is done at temperatures below the melting point by sublimation for particular molecule. In this thesis, all the organic thin films are grown by vacuum deposition. The substrate temperature is another key parameter in thin film growth. Higher substrate temperature provides more kinetic energy to the condensing molecules, such that they have enough energy to move to a site of lower surface potential and form a preferred structure [5]. It has been generally found that the thin film growth is improved by keeping the substrate at elevated temperature, though it may vary due to substrate variation [6]. We have assembled an OMBD system, which works under high vacuum (base pressure ~ 10^{-7} mbar) using two type of vacuum pumps (rotary and turbo). The high vacuum serves the following specific purposes: (a) to eliminate the scattering by residual gas molecules, and (b) to provide high purity films together with the possibility of an improved molecular ordering. A highly pure organic thin film is desirable for a particular device

application without contamination (in-situ), which may occur at low vacuum (10^{-3}-10^{-4} mbar) and that is why very high pressure is needed for the molecular deposition. Typical evaporation rates of molecules were 0.2-0.4 nm Å/s. The microstructure of an evaporated thin film depends on the evaporation rate, substrate temperature, and chemical and physical nature of the substrate surface. The size of the grains in a polycrystalline film will generally be larger for high substrate temperature. The physical nature of evaporated films can also be changed by post-deposition heat treatment (annealing).

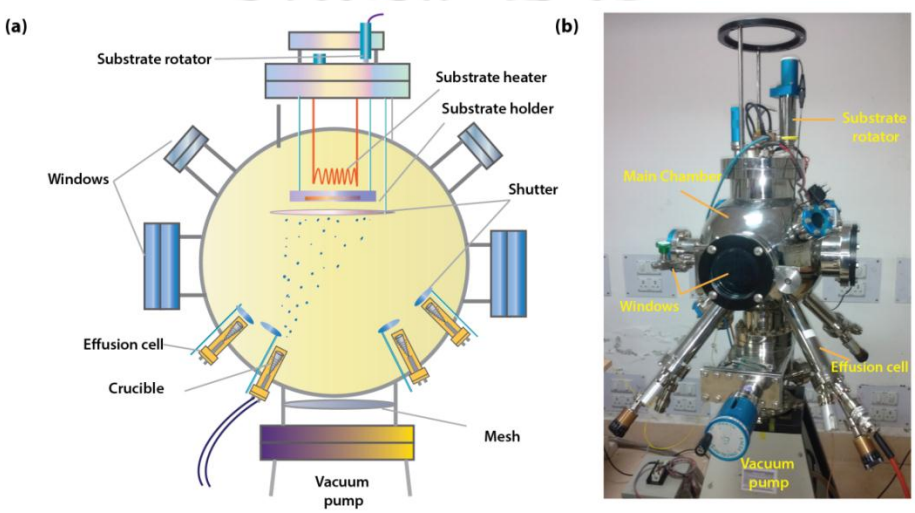

Figure 2.1 (a) Schematic representation of physical evaporation chamber and **(b)** photograph of actual OMBD chamber used for the present work.

Figure 2.1(a) shows a schematic of the design of the OMBD chamber and **Fig. 2.1(b)** shows the actual photograph of the designed chamber. This chamber has been designed in such a way that one can performed co-evaporation of four different compounds simultaneously with the help of four Knudsen-cells (MBE-Komponenten GmbH) assembled at four different positions of the chamber. Each Knudsen-cell contains one quartz crucible, which is used to load the organic compound and these crucibles are surrounded with heating coil for uniform heating. This set-up is adopted for the deposition of the phthalocyanine molecules. Each source has its own shutter in the proximity and a common quartz crystal microbalance (QCM) for monitoring deposition rate and thickness of the deposition film. The thickness of film is sometime verified by profilometer (Dektak), since as after several depositions, the DTM can give error.

2.1.2 Vacuum Thermal Evaporation

Solid materials vaporize when they are heated to a sufficiently high temperature into the vacuum evaporation chamber [7]. Thin film deposition then occurs as atoms are removed from a solid (generation of the depositing species) and then travel over some distance in a vacuum chamber (transport of species from source to substrate) and impinge on the substrate (film growth on the substrate). Even in a vacuum chamber, the molecules travel at high velocities making frequent collisions with residual gas molecules such as N_2, O_2, H_2O and CO_2. From kinetic theory, the mean free path (λ) of gas can be approximated as [8],

$$\lambda \sim \frac{1}{p} \tag{2.1}$$

where p is the pressure (mbar). Thus it is necessary to use low pressures, which lead to straight line paths between the source and the substrate. In air and at room temperature, a typical mean free path is 65nm. In the pressure range of 10^{-6} mbar, the mean free path is very large (of the order of *km*) compared to the source-to-substrate distance. Important features of thin film growth are the evaporation rate, substrate temperature and the chemical and physical natures of the substrate surface. Residual gas molecules in the chamber also have an effect − the more residual gas molecules, the more likely it is for some of these to be trapped in the film or for chemical reactions between residual gas molecules and evaporated molecules to occur. A schematic diagram of a thermal evaporation system is shown in **Fig. 2.2(a)**.

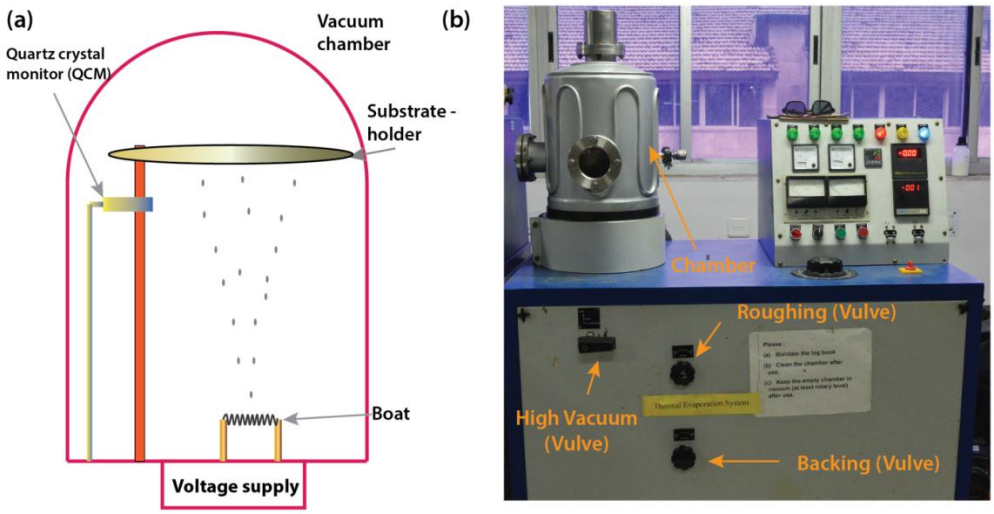

Figure 2.2 (a) Schematic diagram representation of the thermal evaporation chamber, and **(b)** photograph of actual evaporation systems (VT vacuum, Bangalore) used for the present work.

Here we have used the thermal evaporation system for metal deposition, was Ag and Al film for OFET contact electrodes. Al was deposited using a wire helix/wire basket boat, while Ag deposited using a dimple boat. Heating boats were made of high melting point tungsten and molybdenum boats. Thermal evaporation is the simplest way of depositing materials onto a substrate. During heating, some evaporants (especially reactive metals) will react with gases which are in the chamber. A clear indication of evaporation is the reduction in the chamber vacuum while the material is being evaporated.

2.1.3 Anodization Process for Al_2O_3 Layer Growth

For the gate insulator, aluminum oxide (Al_2O_3) was electrochemically grown on the aluminum surface by the galvanostatic anodization in 0.01 mol/l citric acid (anhydrate). This technique is one of the cheapest, as it is solution based. The whole process can be done under ambient conditions and at room temperature. We have used a glass substrate with size 1.5 cm×2.5 cm to fabricate devices onto it and we have cleaned by piranha solution before depositing aluminam of thickness ~150-200 nm. The dimensions of aluminam patterned strips were 1 mm×20 mm. The glass substrate with the aluminum layer was immersed in the electrolyte solution, together with a platinum counter electrode (see **Figure 2.3**). The electrolyte solution was stirred during the whole anodization process [9-11].

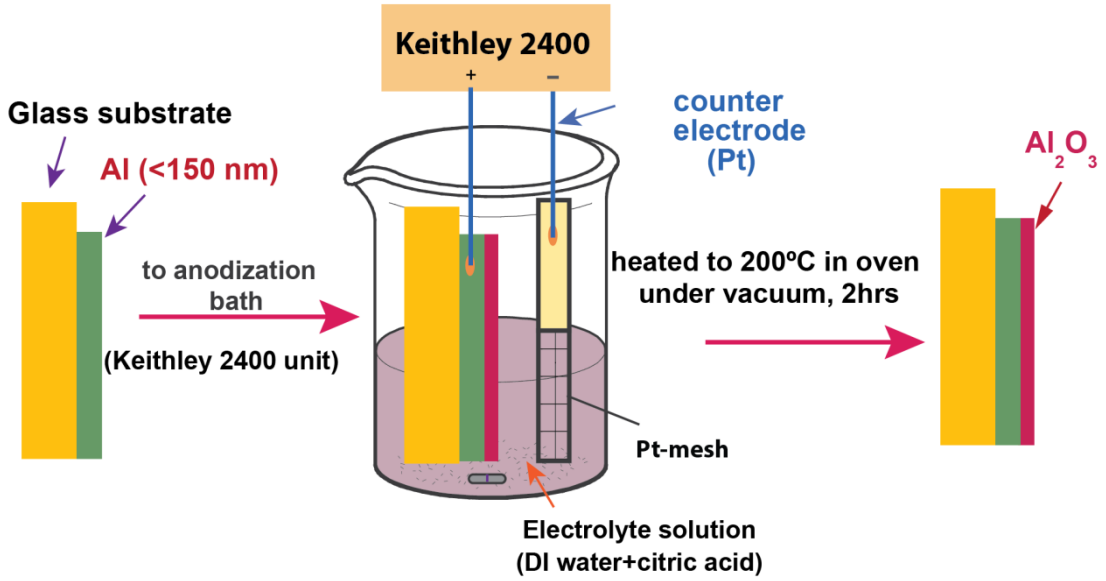

Figure 2.3: Schematic of the anodization setup, with the aluminum deposited on a glass substrate as a working electrode and a platinum foil as a counter electrode.

The oxidation process of aluminum is given by,

Anode reaction: $2Al+3H_2O \rightarrow Al_2O_3+6e^-+6H^+$

Cathode reaction: $6H^+ + 6e^- \rightarrow 3H_2$

A constant current density of 0.6 mA cm^{-2} was applied through Keithley 2400 source meter and the oxide thickness is directly proportional to the anodization time. We obtained an Al_2O_3 layer of thicknesses ~15 nm, corresponding to anodization time of 10 minutes. Following the anodization, the sample is kept in an ultrasonic bath of deionized water at 80°C for several minutes, where the oxide swells up due to water uptake and pinholes are reduced. Afterwards the sample is heated up to 200°C in an oven under reduced pressure for several hours to get rid of all water residues. This galvanostatic anodization process is the simplest method, where the anodization is performed by "ramping up the voltage up to a limiting anodisation voltage V_A", and the final thickness of the film is determined by the "anodisation ratio" $c_{Al} \approx 1.3$ nm/V [9]. It can be noted that direct Al_2O_3 substrates are not used for the device application due to its high roughness. A PMMA based

organic dielectric layer is passivized on to Al_2O_3 to get smoother layer as shown in **Fig. 2.4 (a)** and **2.4(b)**.

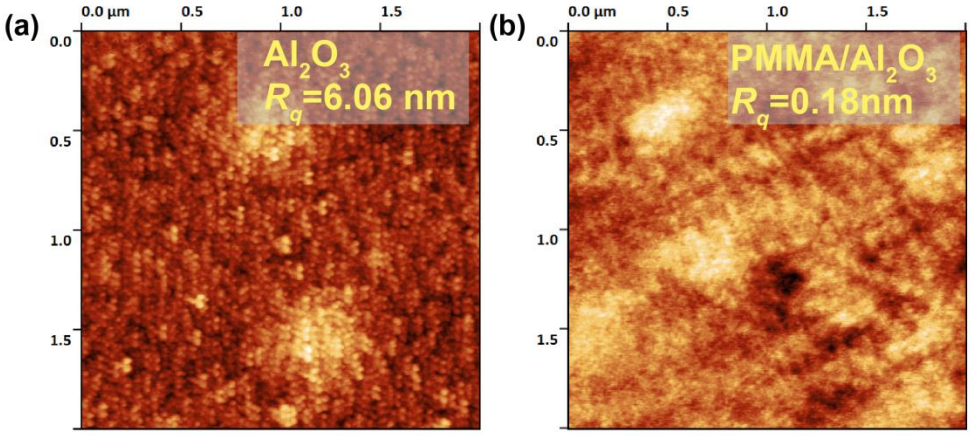

Figure 2.4: AFM topographies (2 μm × 2μm) taken of (a) 13 nm deposited aluminum oxide film on glass, and (b) PMMA coated Al_2O_3. (RMS roughness R_q is indicated for each cases).

Use of Al_2O_3 as a gate dielectric provides several advantages. Aluminum is a cheap starting material, and can be applied to any substrate (glass, plastic etc.) by simple evaporation techniques. The Al_2O_3 prepared by the above method is pinhole-free, has a very low leakage current and a high breakdown yield strength.

2.1.4 Spin Coating and Thickness Measurement

A. Thin Film Coating: Spin coating is a fast and easy method to generate thin and homogeneous organic films out of solutions. Spin coating is a procedure used to apply for uniform thin films on to flat substrates. In short, an excess amount of a solution is placed on the substrate (here glass substrate) holder, which is then rotated at high speed (typically around 3000 rpm) in order to spread the fluid by centrifugal force. A machine used for spin coating is called a spin coater. This method was first described by Emslie *et al.* (1958) and Meyerhofer et al. (1978) using several simplifications. **Figure 2.5(a)** shows a photograph of the spin-coater was used in this thesis. The spin coating process is shown schematically in **Fig. 2.5(b)**. In general, the thickness of a spin coated film is

proportional to the inverse of the square root of spin speed squared as in the below equation, where *d* is the thickness and *w* is the angular velocity:

$$d \propto \frac{1}{\sqrt{w}} \tag{2.2}$$

However, to get a homogeneous polymer films, several factors are important and have to be considered: (i) evaporation rate of the solvent (ii) viscosity of the fluid (iii) concentration of the solution (iv) angular velocity (rotating speed), and (v) spinning time.

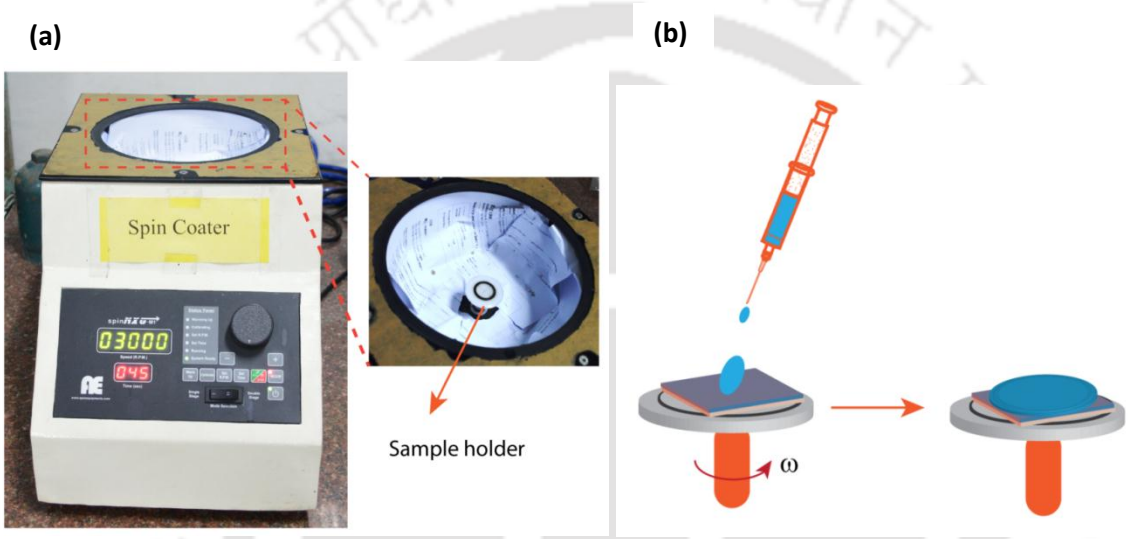

Figure 2.5: (a) Photograph of l the spin–coater (Apex. Spin NXG-M1), and (b) Schematic representation of spin-coating process.

B. Annealing: After spin-coating of polymer dielectric film (like PMMA), we annealed it under low vacuum condition (1 mbar) to evaporate the solvent. It should be noted that annealed temperature of solvent should be less than the glass transition temperature of particular polymer dielectric, otherwise it will be decomposed and desired properties will not be achieved.

C. Thickness Measurement: We measured the thickness of spin-coated film using thickness profilometer. The profilometry is a method to measure surface height profiles. Here, we have used a Vecco Dektak 5000 profilometer in this thesis. A diamond tip is moved to the sample until it touches the surface. Then a defined pressure is applied and the diamond tip is

drawn horizontally over the sample to record the height profile. This could lead to changes in the surface topography. To define film thickness, an edge is needed, where the surface of the substrate is not covered with the film; otherwise it should be scratched by a sharp tweezer, one or two perpendicular to the scan direction such that it can touch the substrate.

Using a profilometer, both types of thin film thickness can be measured whether it is organic/ polymer or polymer dielectric films. Generally quartz crystal monitor (QCM) gives the organic thin film thickness during deposition, but it is not reliable for organic molecule as the parameters are well defined for inorganic cases. So, it is often necessary to calibrate the organic film-thickness by a profilometer.

2.1.5 Molecular Self Assembled Monolayers on SiO_2

Molecular Self-Assembled Monolayers (SAMs) have drawn a growing interest in the field of organic electronics due to their ability to spontaneously form highly organized organic structures over the most commonly used dielectric surfaces, such as SiO_2 or aluminum oxide (Al_2O_3) [12,13].

SAMs provide an easy method to turn an inorganic surface into organic and to significantly change its properties. For instance, hexamethyldisilazane (HMDS), as a result of their favorable attachment to hydroxidized or oxidized surfaces, allow to significantly lower the surface energy of SiO_2 and to change its behavior from *polar* to *non-polar* [14]. Moreover, they reduce the density of hydroxyl groups, which are known to behave as electronic trap states limiting electron transport in the overgrown organic semiconductor. It has been reported that the chemical structure of the molecules of HMDS together with the SAMs result in the covalent bond of their head-groups with the siloxanes and silanols present on the substrate surface. However, there are several SAMs that can be used, namely trichloro(octyl) silane (OTS), trichloro (octadecyl) silane (ODTS) etc. for surface treatment of inorganic dielectric SiO_2. In this thesis, we have used a HMDS monolayer for its availability in high purity (due to short channel length), and easy processing. Details of the deposition process is elaborated in ***Chapter7***. **Figure 2.**6 shows the HMDS deposition process onto SiO_2 substrate.

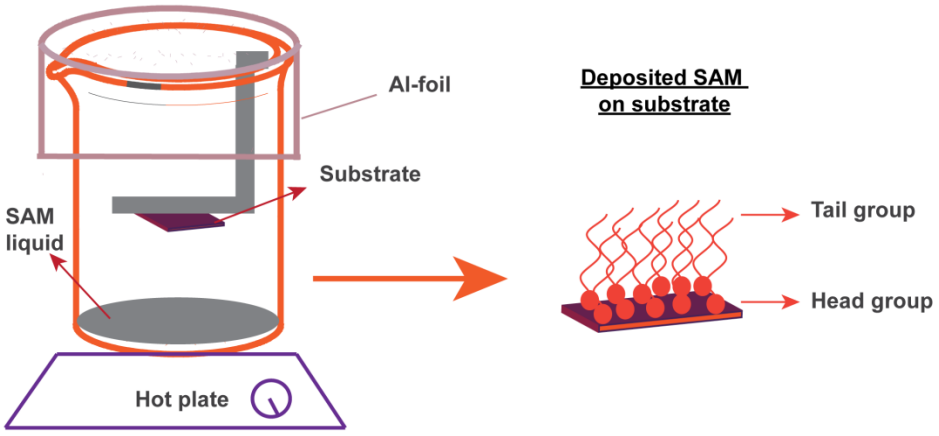

Figure 2.6: Schematic of the deposition process of HMDS.

The application of SAMs to OFETs is the use of insulating high quality SAMs as gate dielectrics. Because SAMs are only one molecule thick and self-limiting, it is possible to create almost perfect, low leakage insulators with high capacitance through careful engineering of the surface. This high gate capacitance makes it possible to achieve very low leakage under very mild conditions of gate dielectric deposition.

2.2 Device Fabrication

A. Substrate Cleaning

All the works related to the molecule growth done in this thesis are based on (a) microscopic glass, (ii) ITO-glass, (iii) Si(100), and (iv) SiO2 substrates. All the organic transistors shown in this thesis are built on substrates based on (i) glass substrate, and (ii) SiO_2/Si substrates. The SiO_2, Si substrates were cleaned thoroughly in deionized water (de ionized water 18.2 MΩ-cm), acetone and finally in 2-propanol, 15 minute each and subsequently dried using a N_2 gas. We used SiO_2 substrates bare/without surface modification and sometimes with surface treated. It should be noted that the final device performances crucially depend on cleaning as well as surface treating procedure, which changes the growth morphology of molecular thin film and corresponding change the bulk properties. Glass substrates and ITO-glass substrate are firstly cleaned by piranha solution (3:1, concentrated sulfuric acid and hydrogen peroxide solution) for an hour and after that we sonicated the glass substrates by

DI-water repeatedly to clean the residue from the substrates. After a proper cleaning, all the substrates are dried in in oven at 110°C to remove the rest of solvent.

B. Passivation by SAM

In this thesis, we have used a HMDS-monolayer for passivating inorganic SiO_2 dielectric layer to fabricate organic field-effect transistor. There are several methods that can be used to deposit by HMDS namely (i) vapor exposing, (ii) dip coating and (iii) spin coating. Out of these, we have used the HMDS vaporization method for its safety as well as its ease of use to passivate the substrate. HMDS reacts with the oxide surface forming a strong bond, as shown in **Fig. 2.7.**

Figure 2.7 Schematic diagram of HMDS modification process on inorganic SiO_2 dielectric layer.

C. Coating of Polymer Dielectric

PMMA is one of the common transparent plastic materials in electronics and initially it was developed for e-beam lithography. Its solubility in many common solvents and accompanying excellent processability have made PMMA a standard organic polymer in the field. It is the only standard polymer dielectric which does not form *pore* at below glass transition temperature (~120°C) and it is also a hydroxyl (-OH)-free polymer, which yields the substrate more hydrophobic in nature. On the other hand, PVA, PVP, PS forms pore and particularly PVA and PVP show hydrophilic nature due to containing –OH group. Again, PMMA's transparency is also an advantage for display backplane applications. **Figure 2.8** shows structure of some of the commonly used polymer layers for different applications [15].

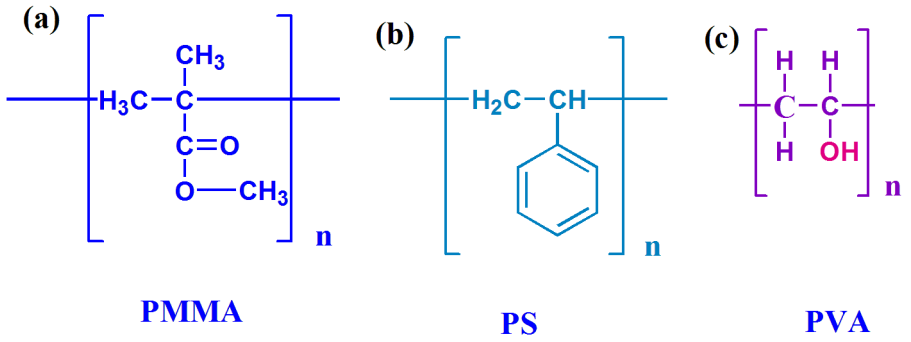

Figure 2.8: Molecular structures of (a) PMMA, (b) PS, and (c) PVA.

In this study, PMMA (M_w≈550 000 kg/mol, Sigma Aldrich) is used for the gate dielectric layer in OFETs. As described in the preceding section, PMMA can be used as trap passivation layer on Al_2O_3. For this purpose, purified PMMA is dissolved in anisole to a 2.5 wt. % solution. The latter is stirred overnight on a hotplate at 50°C. PMMA layers are fabricated by spin-coating with a rotation speed of 3000 rpm for duration of 60 s. Thereafter, the substrates are dried on a hotplate at 50°C for several minutes at low vacuum. This procedure results in ~100 nm-thick, smooth transparent PMMA layers. In **Table 2.1**, we listed some commonly used polymer dielectric materials with their dielectric constant (k), and glass transition tempaerature (T_g).

Table 2.1: List of common polymer dielectric materials [15].

Polymer dielectric	PMMA	PS	PVA	PVP
k	3.2	2.6	7.8	5
***T_g*(°C)**	105	95-107	85	130-185

***k**=dielectric constant, **T_g**=glass transition temperature.*

In this study, poly(methyl methacrylate) (PMMA) gate dielectric layers (anisole as solvent) were deposited by spin-coating. The initial spin speed was 3000 rpm for 60 seconds for 2.5 wt% solution dispersal to reduce the PMMA to the thickness of 100 nm. The substrate was then baked at 80 °C on a hot plate for 30-60 minutes to cure the PMMA. Concentrations of the spin-coated solutions are given in the relevant chapters.

2.3 Physical Characterization Techniques

2.3.1 Atomic Force Microscopy (AFM)

Atomic Force Microscopy (AFM) is a widespread technique to analyze the topography of surfaces in a spatial range from few angstroms to several microns. It can detect height differences in the nanometer range. It has been developed in 1986 by Binnig et al. [16] few years after the invention of Scanning Tunneling Microscopy (STM) for which G. Binning and H. Rohrer were awarded of the Nobel Prize in Physics in 1986. The basic principle of an AFM is the interaction between a small tip mounted on a cantilever and the sample surface. A systematic sketch of an AFM is given in **Fig. 2.9**. The idea is to use a tip attached to the end of a cantilever with elastic constant *k*, and measure the tip-sample forces by the cantilever deflection, which are related, according to Hooks law, by

$$F_x = -k_x \Delta x \qquad (2.3)$$

The same relation applies for the z direction if the force on the tip has also a component along the surface plane. AFM is extremely popular since its use is not limited to a specific

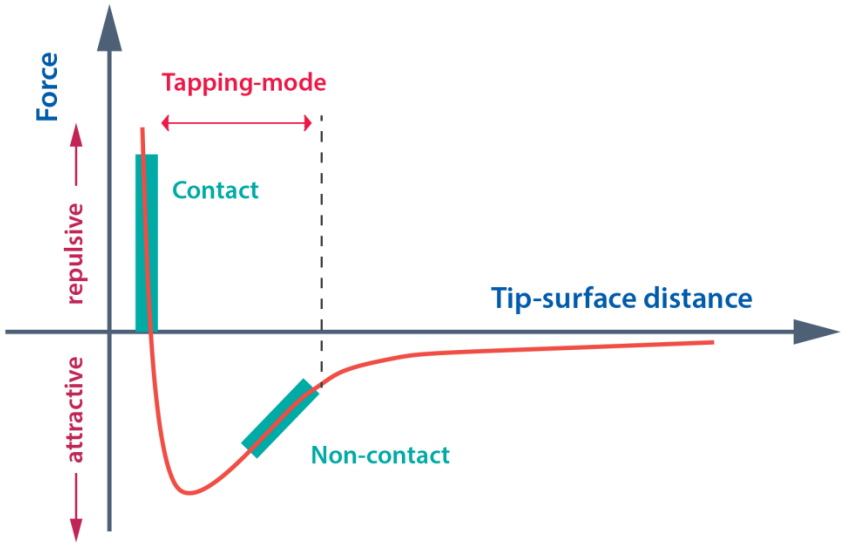

Figure 2.9: Schematic representation of the general behavior of tip-sample forces versus distance and illustrating the force regimes under which each of the three most common AFM imaging modes operate.

type of specimen such that it can be employed on metals, semiconductors, and insulators, without any special specimen preparation. Moreover, it can be employed in ambient air or even in liquids.

In AFM, a sharp tip – usually a few microns long and with a radius of curvature of less than 10 nm – is micro fabricated at the free end of a cantilever. Commercially manufactured probes and cantilevers are predominantly of silicon nitride (Si_3N_4) or silicon (Si). Typically the upper surface of the cantilever, opposite to the tip, is coated with a thin reflective surface, usually of either gold (Au) or aluminum (Al) [17].The interatomic forces occurring between the tip and sample induce a cantilever deflection proportional to their strength. The deflection is recorded as the tip is scanned across the sample, yielding a topographical map of the surface. Often, as shown in **Fig. 2.10(a)**, the small cantilever deflection is measured by means of a laser beam directed to the back of the cantilever and reflected off to a position-sensitive photodiode. If each section of the detector is labeled A to D as shown in **Fig. 2.10(a)**, then the deflection signal is calculated by the difference in signal detected by the A+B versus C+D quadrants. Comparison of the signal strength detected by A+C versus B+D will allow detection of lateral or torsional bending of the lever. **Figure 2.10(b)** shows the actual photograph of the AFM instrument (Agilent 5500).

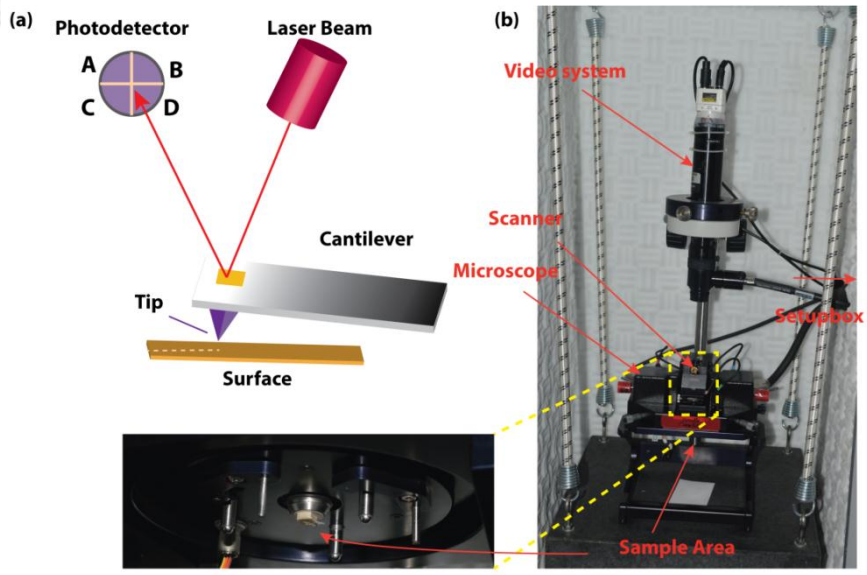

Figure 2.10: (a) Schematic sketch of an AFM. The height profile of a sample can be obtained by measuring the interaction between the tip and the atoms on the surface of the specimen. **(b)** Photo of actual AFM instrument (Agilent 5500) used in this thesis.

There are three primary modes of use of an AFM: (i) *contact*, (ii) *tapping* and (iii) *non-contact mode* [17]. In *contact mode* AFM, the tip contacts the sample surface during the scanning. A feedback loop maintains a constant deflection between the cantilever and the sample by vertically moving the scanner and thus the force between the tip and the sample remains constant. There are several drawbacks in *contact mode*. Lateral forces can occur when the probe traverses steep edges on the sample, which may cause damage to the probe or the sample, or also result from adhesive or frictional forces between the probe and the sample. In order to overcome the limitations of contact mode imaging as mentioned earlier, the intermittent or *tapping mode* of imaging was developed. For *tapping mode* AFM, the cantilever is oscillated at or slightly below its resonant frequency with amplitude ranging typically from 20 nm to 100 nm and it is usually chosen for soft organic materials . The tip lightly taps on the sample surface during scanning, contacting the surface at the bottom of its swing. A feedback loop maintains constant oscillation amplitude by maintaining a constant RMS of the oscillation signal and thus a constant tip-sample interaction is maintained during scanning. On the other hand, for *non-contact mode* AFM, the cantilever is oscillated at a frequency which is slightly above the cantilevers resonant frequency, typically with an amplitude of a few nanometers (<10 nm). The tip does not contact the sample surface, but oscillates above the sample surface during scanning. On the other hand, for *non-contact mode* AFM, the cantilever is oscillated at a frequency which is slightly above the cantilevers resonant frequency, typically with 51 an amplitude of a few nanometers (<10 nm). The tip does not contact the sample surface, but oscillates above the sample surface during scanning. This information can be used by a regulation circuit to construct a two-dimensional height profile with the help of measurement software. The root-mean-square roughness R_q is often used to characterize a given surface. R_q is defined as the standard deviation of the average surface height ($\bar{h}$).

Additionally, since charge carrier transport is limited to the first few nanometers of the organic semiconductor in OFETs, the roughness is not a crucial parameter for the transport as long as the films are closed but the roughness of the dielectric surface is a key limiting factor to charge carrier transport as will be seen in the respective chapters.

In the context of this work, the AFM imaging of the organic polymer gate dielectrics and phthalocyanine based thin films was performed using the *tapping mode*. *Tapping mode* AFM is suitable for organic thin film and soft surfaces that are easily damaged, because the tip is not dragged over the surface when it is in contact mode. Different scanning-area dimensions were considered, ranging from 10 $\mu m \times 10\ \mu m$ to 1 $\mu m \times 1\ \mu m$. For each sample, several images were taken in different distinct locations of the sample. The width, length and area of the grains are calculated and used to generate suitable plots to aid in the analysis of film topology. A deeper analysis of the film topology and a comparison between the different films is presented in ***Chapter 3*** and ***Chapter 4***.

The acquisition/processing of the images and the roughness analysis were performed by the software Gwyddion 4.0, WSxM 8.0. The elaboration of the AFM data concerning the nucleation and the growth of phthalocyanine, was conducted by means of the software.

The R_q roughness of an AFM image, constituted by $M \times N$ pixels (usually 512×512), is given in the following equation:

$$R_q = \sqrt{\frac{1}{N}\sum_{j=1}^{N} h_j^{\,2}} \tag{2.4}$$

Where $R_a = \frac{1}{N}\sum_{j=1}^{N} h_j$. In the following formulas we assume the mean value of h_j as zero,

$$h_j = z_j - \bar{z} \equiv z_j$$

From AFM analysis, we usually evaluate auto correlation function (ACF) and height-height correlation function (HHCF) based only on profiles along the fast scanning axis. It can therefore be evaluated from the discrete AFM data values (assumed1D) as,

ACF:

$$R(r) = \frac{1}{N(M-m)}\sum_{l=1}^{N}\sum_{k=1}^{N-m} h_{k+m}h_{k,l} \tag{2.5}$$

HHCF:

$$g(r) = \frac{1}{N(M-m)} \sum_{l=1}^{N} \sum_{n=1}^{M-m} \left(h_{n+m,l} - h_{n,l} \right)^2 \quad (2.6)$$

2.3.2 X-ray Diffraction (XRD)

X-ray diffraction experiment provides information about the crystalline phase of thin films in the reciprocal space. X-ray diffraction is applied to bulk material, thin films, and powders to yield information on crystalline structure and orientation, crystalline perfection, composition, thin film thickness and uniformity, as well as strain. X-ray related techniques are most popular because they are compatible with insulating substrates, are nondestructive, and do not require vacuum or special sample preparation. Moreover, the information obtained is not limited to the surface of the films but can probe the entire thickness of the layer. X-ray related methods are extremely powerful in determining the degree of crystallinity, average domain size, and film orientation. That is why X-ray diffraction (XRD) is used for this purpose. XRD is a common technique to analyze the structural properties of all kinds of specimens, inorganic or organic. A schematic drawing of an XRD setup is shown in **Fig. 2.11(a)**. In the **Fig. 2.11 (b),** we show the photograph of XRD instrument (Rigaku). The X-ray tube is mounted on one side of the setup, the turnable sample holder at the center and the detector, which can be moved along a circle around the sample holder, is on the opposite side. Monochromatic X-rays hit the sample at the scattering angle/Bragg angle θ. In case of a crystalline sample the radiation can be reflected if the Bragg condition [18],

$$2d_{hkl}.Sin\theta = n\lambda \text{ (n=1,2,3,…..)} \quad (2.7)$$

is fulfilled. Electromagnetic waves with a wavelength comparable to interatomic distances are scattered at lattice planes with Miller indices (hkl) and spacing d_{hkl} . Here, d_{hkl} denotes the distance between the lattice planes in crystals, and λ (= 1.54056 Å) is the wavelength of

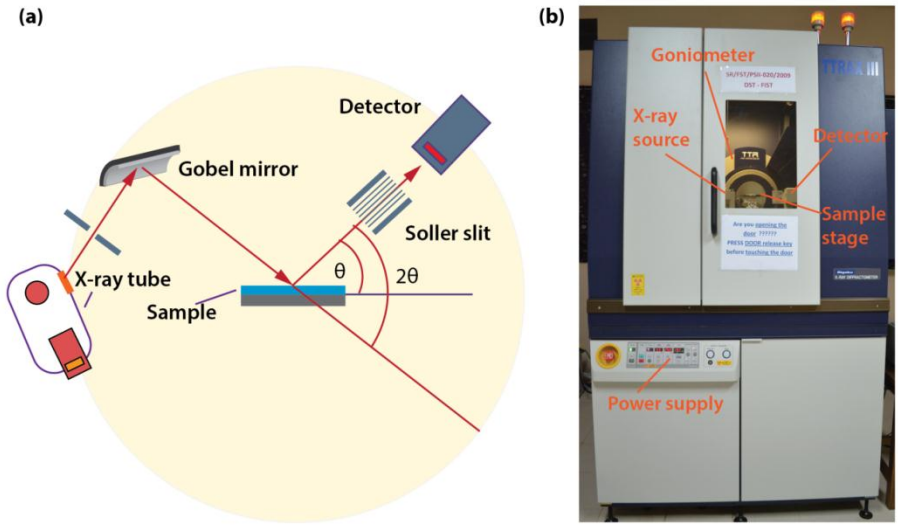

Figure 2.11: **(a)** Schematic drawing of an XRD setup, **(b)** Photograph of 18kW X-Ray Diffractometer (Rigaku) at IIT Guwahati for the present study.

the incident X-ray beam**. Figure 2.12** shows the scattering geometry for a crystal where (*hkl*) is the lattice planes with respect to the surface. The reflected radiation can be measured if the detector is located at 2θ relative to the incident beam. d_{hkl} can be determined by the angular positions of the

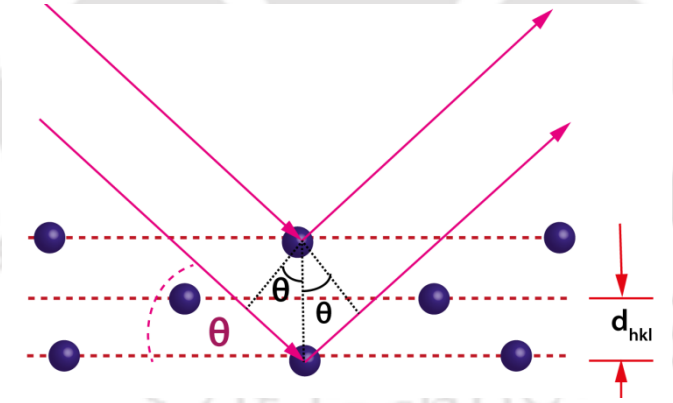

Figure 2.12: The incoming X-rays with wave vectors are scattered by lattice planes with inter-planar distance d_{hkl} [18].

maxima of the spectrum. Our evaporated organic thin films, such as tin (IV) phthalocyanine dichloride films, often have a polycrystalline structure as measured by XRD thin film mode. Thin film phase is identified from the peak positions of the diffractogram. However, it is observed that XRD measurements give reasonable information if the film thickness is more than 30-nm. All the XRD measurements presented in this thesis were taken using

commercially available on a X-RAY DIFFRACTOMETER (TTRAX III, RIGAKU 2500). In this case, Cu-K_α radiation with λ=1.54056 Å is used.

2.3.3 Ultraviolet-Visible Absorption

Ultraviolet–visible spectroscopy or **ultraviolet-visible spectrophotometry** (**UV-Vis**) refers to absorption spectroscopy or reflectance spectroscopy in the ultraviolet-visible spectral region. The absorption or reflectance in the visible range directly affects the perceived color of the chemicals involved. In this region of the electromagnetic spectrum, atoms and molecules undergo electronic transitions. Absorption measures transitions from the ground state to the excited state. Molecules containing π-electrons or non-bonding electrons (n-electrons) can absorb the energy in the form of light (ultraviolet or visible) to excite these electrons to higher anti-bonding (π*) molecular orbitals. The more easily the electrons are excited (i.e. lower energy gap between the HOMO and the LUMO), the longer the wavelength of light it can absorb [19].

The electronic absorption of atoms and molecules generally lies in the ultraviolet or visible region; hence, it is often referred to as "UV-visible absorption". Because of the involvement of vibrational energy levels, different absorption bands may be observed. Practically, the wavelength range denominated by UV-vis and measureable in air (due to atmospheric absorption) starts around 185 nm and extends up to 850 nm. Absorption of ultraviolet and visible radiation by an atomic or molecular species can be attributed to the excitation of electrons, generally from bonding orbitals and thereby creating a so-called 'excited state'. The energy of the absorbed radiation can therefore be correlated with the types of bonds present in the studied species and help to identify the functional groups in a molecule.

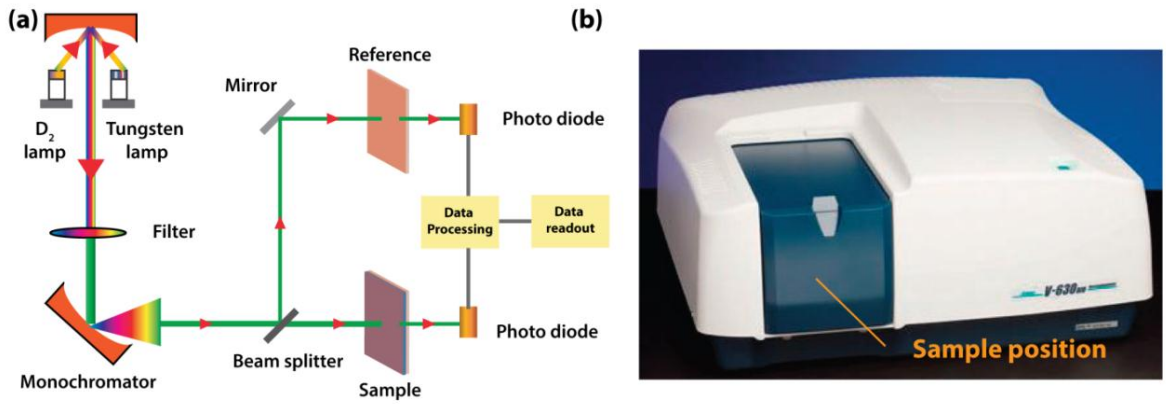

Figure 2.13: (a) Working principle of UV-Vis spectroscopy. **(b)** Photograph of the actual spectrophotometer (JASCO).

The electronic absorption of a substance at certain light wavelength follows the Lambert–Beer law [20]:

$$\log\left(\frac{I}{I_0}\right) = -\varepsilon c l \tag{2.8}$$

where I_0 and I are the intensity of the incident light and the transmitted light, respectively, ε is the molar extinction coefficient, C is the molar concentration of the molecule, and l is the distance that the light travels through the material. **Equation (2.8)** is frequently used for solutions, where l is the thickness of the solution in the light path. For molecular crystals and for thin films consisting of one compound, the concentration C is a constant that depends on the density of the material and the molecular mass. In such cases, the product of ε and C can be replaced by constant k and the equation can be rewritten as, $I = I_0 e^{-kl}$, where l is the thickness of the crystal or film [20].

The absorption spectrum can be monitored by recording the absorbance as a function of the wavelength (or frequency) of the incident light. The instrument used in this thesis is a double-beam spectrophotometer **JASCO, V-630**. The working principles of UV-vis is schematically presented in **Fig. 2.13(a)** and the photograph of the instrument is depicted in **Fig. 2.13(b).**

2.3.4 Thermogravimetric Analysis (TGA)

Thermogravimetry deals with the change in the mass of a substance or so called weight loss, continuously monitored as a function of temperature or time, when it is heated or cooled at a predetermined rate. The sample and the reference are exposed to the heating ramp via symmetric placement of ceramic crucible within the furnace. The reference material is a substance which has the same thermal mass as the sample and donot undergo any phase transformations during the heating. The difference between the sample and reference is measured by a "differential thermocouple" in which one junction is in contact with the underside of the sample crucible, and other junction is in contact with the underside of the reference crucible. It provides information on the thermal stability of the sample (organic/inorganic) at different temperatures and pressures of the environmental gases.

From the results of TGA, it is possible it to note the temperature up to which the material does not loose weight. For metal phthalocyanine molecules, we have found that weight the loss started close to 450°C. It is also possible to know the temperature at which material starts decomposing, whether the decomposition occurs in one or more stages. Here the thermogravimetric analyses (TGA) of sample has been carried out by using a Netzsch, Germany made TGA in an argon gas environment. The local environment inside the TGA is purged with an inert argon (Ar) gas such that it prevents the unwanted reaction with oxygen atmosphere. **Figure 2.14 (a)** shows the schematic of TGA setup and **Fig.2.14 (b)** shows the photograph of TGA instrument used for this study. In general, the derivative of the TGA weight loss gives the information about the apparent weight loss for a particular species. It can be noted that for polymer, graphene oxide, reduced graphene oxide, gives multiple peak points for different functional groups. For metal phthalocyanine it shows a single peak.

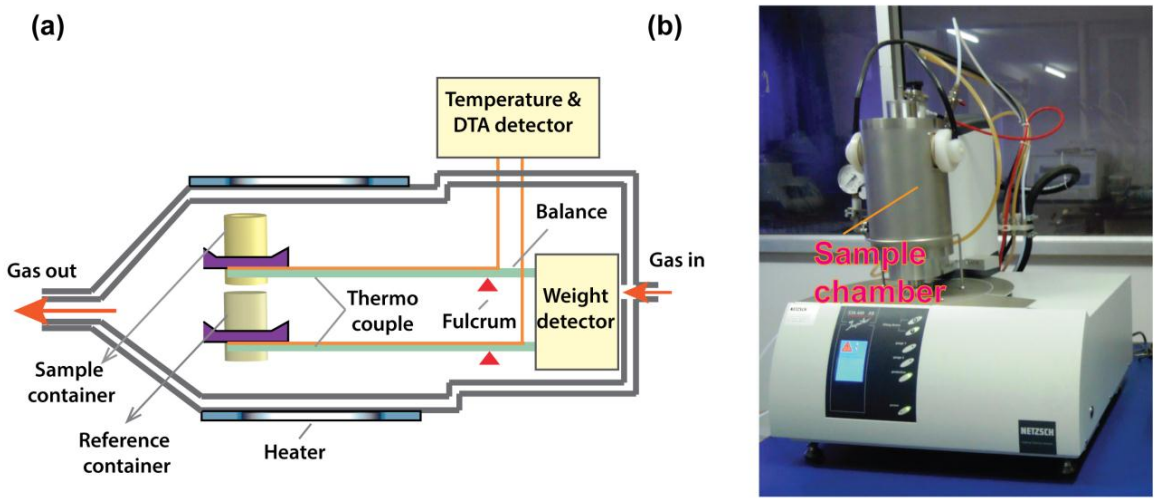

Figure 2.14: (a) Working principle of TGA. **(b)** A photograph of the TGA equipment (NETZSH, GERMANY).

The Specifications of the equipment are:

Temperature Range: Ambient to 1000º C

Sensitivity: 0.1m gm (0.0001mg)

Atmosphere: Ar

2.3.5 X-ray Photoelectron Spectroscopy (XPS)

XPS is a key surface characterization tool which combines surface sensitivity with the ability to quantitatively obtain both elemental and chemical state information for each element detected through the chemical shift. It is widely used for studies of surface defects and chemical environment, because of its high sensitivity to surface (i.e., up to 10 nm from the sample surface). It also provides useful information about the depth profile (i.e., an evaluation of the variation of composition with depth) and the surface impurities present in the sample. The principle of XPS is based on the photoelectric effect outlined by Einstein in 1905 was developed by Siegbahn and his research group [21], where the concept of the photon was used to describe the ejection of electrons from a sample surface when photons

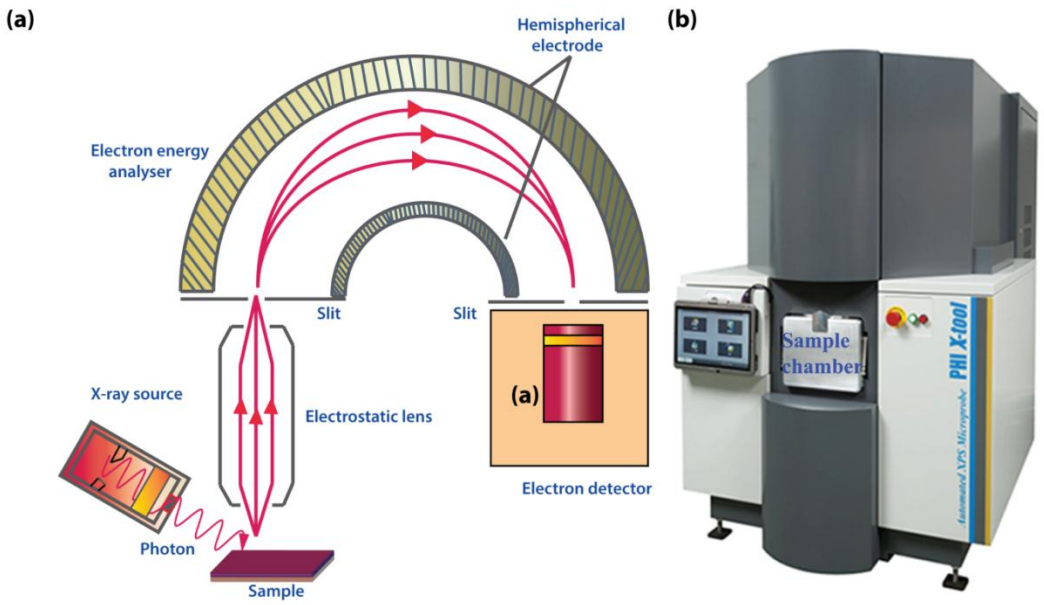

Figure 2.15: (a) Schematic drawing of an XPS setup, **(b)** Photograph of actual XPS system used (PHI X-Tool).

impinge upon it. This process can be expressed by the following equation [22]:

$$BE = h\nu - KE - \varphi \tag{2.9}$$

where *BE* is the binding energy of the electron in the atom, *hν* is the photon energy of x-ray source, KE is the kinetic energy of the emitted electron that is measured in the XPS spectrometer and φ is the spectrometer work function. For XPS, Al Kα (1486.6 eV) or Mg Kα (1253.6 eV) is generally used as the source of x-rays. The photon is absorbed by an atom of the sample, leading to emission of a core (inner shell) electron. The energy of the photoelectrons leaving the sample is determined using an appropriate electron energy analyzer and this gives a spectrum with a series of photoelectron peaks. For each and every element, there will be a characteristic binding energy associated with each core atomic orbital, i.e., each element will give rise to a characteristic set of peaks in the photoelectron spectrum at kinetic energies determined by the photon energy and the respective binding energies. The peak intensities measure how much of a material is at the surface, while the peak positions indicate the elemental and chemical composition. Other values, such as the

full width at half maximum (FWHM) are useful indicators of chemical state changes and physical influences.

In this study, XPS measurements were carried out with a PHI X-Tool automated photoelectron spectrometer (ULVAC-PHI Inc.) using *Al* K_α X-ray beam (1486.6 eV) with a beam current of 20 mA. Some of the samples were characterized with ESCALAB 3400 (Shimadzu, Japan) instrument using Mg Kα X-ray beam (1253.6 eV). Carbon *1s* spectrum was used for the calibration of the XPS spectra recorded for various samples. In case of Si substrate, XPS shows Si^{4+}, Si^{3+}, and Si^{+} oxidation states corresponding to different suboxides of Si, which are due to the native oxides. For organic thin films, it shows different oxygen concentrations**. Fig. 2.15(a)** shows a schematic representation of a XPS instrument and **Fig. 2.15(b)** shows a photograph of the XPS instrument used for this study. The broad peaks with shoulders are fitted with Gaussian line shape using the origin8.5 Peak Fit software.

2.4 Electrical Characterization Techniques

2.4.1 Semiconductor Parameter Analysis

The OFET current, *I*, versus voltage, *V*, characteristics were measured in an electrically screened chamber under low vacuum (10^{-2} mbar) conditions using a Keithley 4200 semiconductor characterization systems (SCS) and sometimes by a Keithley 2602 double channel source meter. **Figure 2.16** shows a photograph of Keithley 4200 SCS semiconductor parameter analyzer. Tungsten probes were used for connections to the sample. To measure the output characteristics of the OFETs, a DC voltage was applied to the gate while the value of the drain-source voltage (V_{DS}) was swept in forward and reverse directions. During this sweep, the drain current (I_{DS}) was measured as function of voltage (V_{DS}). This loop was performed several times with different gate voltages. To measure the transfer characteristics of OFETs, a DC voltage was applied to the drain and the drain current was measured at each point of a defined gate voltage sweep for both forward and reverse directions. For bias stress stability measurements, a constant bias voltage was applied to the drain and source contacts. The *I-V* measurements for both output and transfer characteristics

of OFETs were made using three probes. We have performed the device characterization and the reliability checking under low vacuum or in air ambient condition using a probe station.

In order to measure the leakage current density, the bias voltage were supplied by a Keithley 4200 SCS source meter and two probes were used for the measurement of the leakage current density.

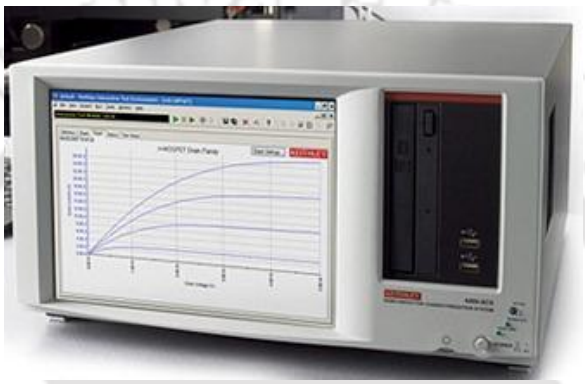

Figure 2.16: A photograph of Keithley 4200SCS semiconductor characterization system used here.

2.4.2 Electrical Probe Station

The model CRX-EM-HF Lake-Shore probe station was used in this thesis work. It is a cryogen-free closed cycle refrigerant probe station with a ±0.6 T horizontal, in-plane electromagnet. All standard CV, IV, microwave, and electro-optical probing, plus in-plane horizontal field electromagnetic measurements can be performed on this versatile probe station. One can use the CRX-EM-HF for testing magneto-transport parameters. A 360° sample stage rotation option allows measurement of angular-dependent and anisotropic magneto-transport properties. From all features, we have extensively used electrical measurement and parametric analyses of all devices. The fabricated devices are measured within the probe station.

2.4.3 Leakage Current and Capacitance Measurements

Leakage current and capacitance measurements were carried out to further characterize the gate insulator. These measurements were done in an ambient condition using Keithley 4200-SCS high resistance meter. For practical use, the on/off ratio of an OFET should be maximized [8,15]. Typically, current on and off ratio in an OFET is the leakage current through the gate dielectric. As a result, reducing leakage current is one method to increase the on/off ratio. In addition, a high leakage current can induce a degradation of organic semiconductor material at the interface of an OFET. Therefore, minimizing the leakage current of a gate dielectric is critical. From the electric measurement, we infer that the anodized aluminum oxide with PMMA layer yields very low leakage current density (~10^{-9} A/cm^2). A self-assembled monolayer treatment on inorganic dielectric layer results in low leakage current density as compared to non-treated gate dielectric layer.

References

[1] T.U. Kampen, Low Molecular Weight Organic Semiconductors, Wiley-VCH Verlag (2010).

[2] S.M. Obaidulla, P.K. Giri, Surface roughening and scaling behavior of vacuum-deposited SnCl2Pc organic thin films on different substrates. *Applied Physics Letters* **107**, 221910 (2015).

[3] K.P. Gentry, T. Gredig, I.K. Schuller, Asymmetric grain distribution in phthalocyanine thin films. *Physical Review B* **80**, 174118 (2009).

[4] R. Ruiz, D. Choudhary, B. Nickel, T. Toccoli, K.-C. Chang, A.C. Mayer, P. Clancy, J.M. Blakely, R.L. Headrick, S. Iannotta, G.G. Malliaras, Pentacene Thin Film Growth. *Chemistry of Materials* **16**, 4497 (2004).

[5] Albert-Laszlo Barabasi, H.E. Stanley, Fractal concepts in surface growth. (1995).

[6] S. Md. Obaidulla, D.K. Goswami, P.K. Giri, Low bias stress and reduced operating voltage in SnCl2Pc based n-type organic field-effect transistors. *Applied Physics Letters* **104**, 213302 (2014).

[7] M. Ohring, *Materials Science of Thin Films (Second Edition): Deposition and Structure*, Elsevier, (2002).

[8] Ioannis_Kymissis, *Organic Field Effect Transistors:Theory, Fabrication and Characterization*, Springer, (2009).

[9] L.A. Majewski, R. Schroeder, M. Grell, Flexible high capacitance gate insulators for organic field effect transistors. *Journal of Physics D: Applied Physics* **37**, 21 (2004).

[10] L.A. Majewski, R. Schroeder, M. Voigt, M. Grell, High performance organic transistors on cheap, commercial substrates. *Journal of Physics D: Applied Physics* **37**, 3367 (2004).

[11] Y. Qin, D.H. Turkenburg, I. Barbu, W.T.T. Smaal, K. Myny, W.-Y. Lin, G.H. Gelinck, P. Heremans, J. Liu, E.R. Meinders, Organic Thin-Film Transistors with Anodized Gate Dielectric Patterned by Self-Aligned Embossing on Flexible Substrates. *Advanced Functional Materials* **22**, 1209 (2012).

[12] S.G.J. Mathijssen, M. Cölle, H. Gomes, E.C.P. Smits, B. de Boer, I. McCulloch, P.A. Bobbert, D.M. de Leeuw, Dynamics of Threshold Voltage Shifts in Organic and Amorphous Silicon Field-Effect Transistors. *Advanced Materials* **19**, 2785 (2007).

[13] S.A. DiBenedetto, A. Facchetti, M.A. Ratner, T.J. Marks, Molecular Self-Assembled Monolayers and Multilayers for Organic and Unconventional Inorganic Thin-Film Transistor Applications. *Advanced Materials* **21**, 1407 (2009).

[14] J. Veres, S. Ogier, G. Lloyd, D. de Leeuw, Gate Insulators in Organic Field-Effect Transistors. *Chemistry of Materials* **16**, 4543 (2004).

[15] Zhenan Bao, J. Locklin, Organic Field-Effect Transistors, CRC Press Taylor & Francis Group, (2007).

[16] G. Binnig, C.F. Quate, C. Gerber, *Atomic Force Microscope*, American Physical Society, (1986).

[17] W.R. Bowen, N. Hilal, *Atomic Force Microscopy*, (2009).

[18] C. kittel, Introduction to solid state physics. (2005).

[19] W. Brütting, *Physics of Organic Semiconductors*, Wiley-VCH Verlag, (2005).

[20] F. Schreiber, Organic molecular beam deposition: Growth studies beyond the first monolayer. *Phys. Status Solidi (a)* **201**, 1037 (2004).

[21] C.N. K. Siegbahn, A. Fahlman, R. Nordberg, K. Hamrin, J. Hedman, G., T.B. Johansson, S. E. Kerlsson, I. Lindgren and B.Lindberg, *Nova Acta Regiae Soc. Sci., Ser IV* **20** (1967).

[22] L. Li, Q. Tang, H. Li, W. Hu, Molecular Orientation and Interface Compatibility for High Performance Organic Thin Film Transistor Based on Vanadyl Phthalocyanine. *J. Phys. Chem. B* **112**, 10405 (2008).

भारतीय प्रौद्योगिकी संस्थान गुवाहाटी • Indian Institute of Technology Guwahati •

Chapter 3

Surface Roughening and Scaling Behavior of Vacuum-Deposited $SnCl_2Pc$ Organic Thin Films on Different Substrates

In this chapter, we studied the evolution of surface morphology and scaling behavior of tin (IV) phthalocyanine dichloride ($SnCl_2Pc$) thin films grown on Si (100) and glass substrates have been studied using atomic force microscopy (AFM) and height-height correlation function analysis. X-ray diffraction measurement confirms the crystalline nature of the $SnCl_2Pc$ thin film on glass substrate, while no crystallographic ordering is present for film grown on Si substrate. The growth exponent β is found to be much larger for growth on glass substrate (0.48±0.07) as compared to that of Si substrate (0.21±0.08), which may be due to the high step-edge barrier, so called Ehrlich- Schwöbel barrier, resulting in the upward dominant growth on glass substrate. From the 2D first Fourier transform of AFM images and derived scaling exponents, we conclude that the surface evolution follows a mound like growth. These results imply the superiority of glass substrate over the Si substrate for the growth of device quality $SnCl_2Pc$ thin film.

3.1 Introduction

Thin films based on molecular semiconductor, specifically 'small' molecules like phthalocyanine are finding an increasing application in a number of optoelectronic devices. In particular, they have been exploited in organic light emitting diodes [1], photovoltaic devices [2,3], organic field-effect transistors, and organic sensors [4] due to their favorable properties, e.g., thermal and chemical stability, well ordered thin film growth and wide absorption band at the optical region. They also exhibit a certain degree of 'specific tunability', due to various metals ion (M= Sn, Cu, CO, H_2, Zn etc.) and the side groups (R= F, Cl, NH_2, $O(CH_2)_{10}OH$ etc.) that can be introduced within a broad range composition[5]. The optimized transport phenomenon like injection and recombination of charge carriers, depend among other parameters, on molecular packing, range of grain boundaries/microstructure, and roughness/morphology of surfaces. Therefore the controlled deposition of molecular thin films is primarily a key requirement for the optimization of electro-optical properties in organic-based devices in which the optimized film

thickness with desired properties are essential. In this regard, the $SnCl_2Pc$ is particularly attractive, since it is considered as a good candidate as an n-type organic material and the device based on this molecule is relatively more stable [6,7]. So, understanding the growth dynamics of organic thin films is one of the key issues in the field of organic electronics. In case of heterostructures between different organic layers, organic-organic [8,9] (for organic diode), organic-inorganic [10] (for electrode/contacts) hetero structures, the knowledge of growth kinetics is of utmost importance, since the change in their interfacial structure can play a critical role on the scaling properties of growth dynamics. However, there has been no report on the scaling behavior and growth dynamics of $SnCl_2Pc$ on different substrates that are most relevant for the device applications.

The scaling theory can be implemented to quantify the statistical properties of the surface morphology of thin films and to formulate theoretical models of growth modes of different inorganic materials, such as metals [11,12], semiconductors [13,14], as well as for organics like polymers [15], and small molecules [16,17]. In this chapter, we elucidate the change of surface morphology with variation of thickness and we address the effect of surface of substrates on the roughness scaling behavior. From height–height correlation function (HHCF) and theoretical formalism of scaling theory, we have calculated the growth exponents and these exponents describe the growth dynamics and morphological features of $SnCl_2Pc$ organic thin films.

3.2 Experimental Details

$SnCl_2Pc$ (n-type) thin films were grown in a high vacuum organic thermal evaporation chamber with a base pressure of $\sim 10^{-6}$ mbar. Commercially available $SnCl_2Pc$ (Alfa Aesar, 97%) molecules sublimed from an effusion cell were deposited onto well cleaned Si(100) and glass substrates at room temperature under identical conditions. The substrates were first cleaned separately by deionized water (18.2 MΩ-cm), Acetone, 2-propanol with sonication for 15 min each. The cleaned substrates were preheated to >300°C and subsequently cooled slowly to room temperature. During the vacuum deposition, the cell temperature was maintained at ~350±2°C, and molecules condensed on the Si and glass substrates. The average growth rate (~0.2- 0.3 Å/s) of the film was optimized by a thickness monitor during the growth. $SnCl_2Pc$ thin films with different thicknesses (8–87 nm) were deposited for different time duration and characterized ex-

situ by atomic force microscopy (AFM) (Agilent-5500), high power X-ray diffractometer (XRD) (Rigaku), X-ray photo electron spectroscopy (XPS) (ULVAC-PHI) analysis, UV-Visible spectroscopy (UV-Vis) (JASCO, V-630). Thermogravimetric analysis (TGA) (NETZSCH) was carried out in Ar gas up to 1000°C.

3.3 Results and Discussion

3.3.1 Molecule Stability and Morphological Analysis

TGA shows (see **Fig. 3.1**) that the $SnCl_2Pc$ molecules are stable up to a temperature of 450°C. As the sublimed temperature here is~350°C, the molecules are not fragmented during the deposition on various substrates.

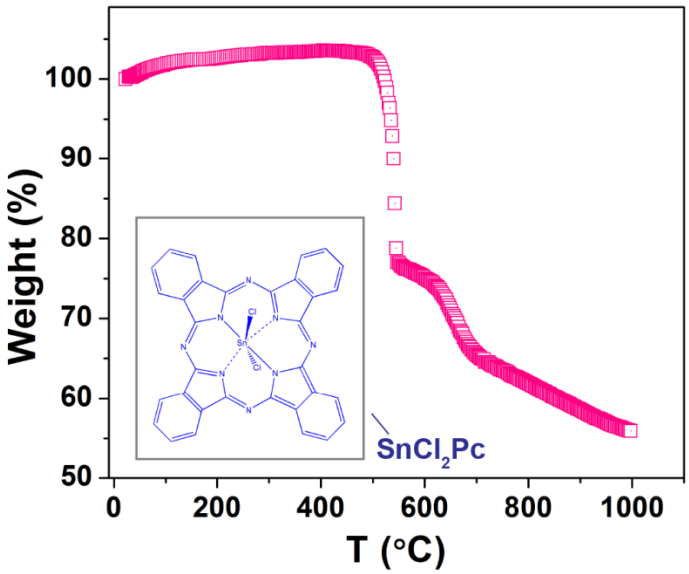

Figure 3.1: TGA plot for the $SnCl_2Pc$ molecule (heating rate: 10°C/min). The inset shows the chemical structure of $SnCl_2Pc$ small-molecule.

The surface morphology was analyzed by AFM measurement in tapping mode (size: 512×512 pixel) to avoid damage to the film. Repeated measurements were carried out at different locations of a sample in order to ensure that any changes that may occurred due to tip-sample interaction is averaged out

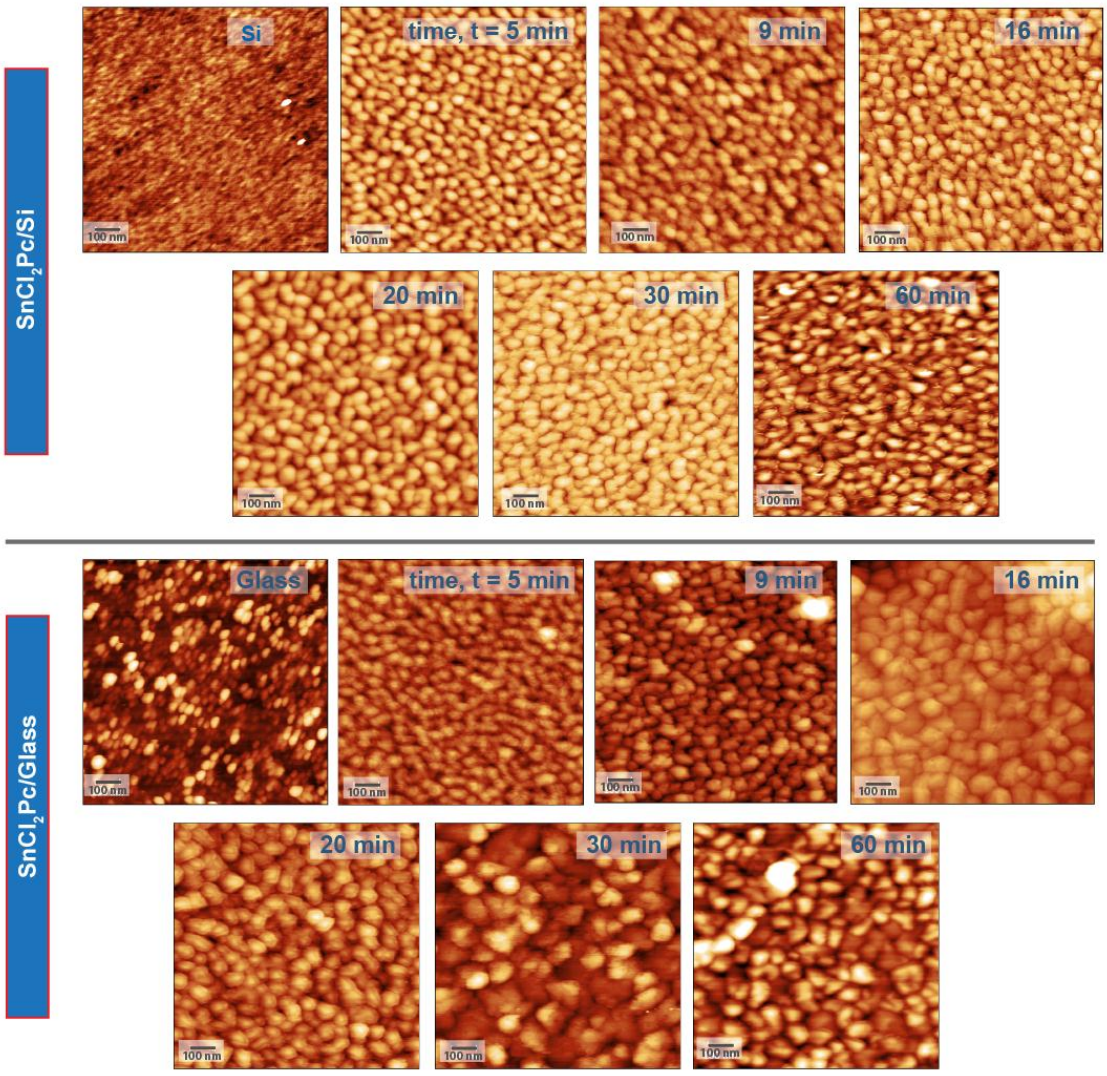

Figure 3.2: Representative AFM topography images (scan size: 1 μm×1 μm) of $SnCl_2Pc$ thin films for different deposition times 5, 9, 16, 20, 30, and 60 min on Si(100) substrate (top panel) and glass substrate (bottom panel) (thickness ~8, 16, 27, 35, 51, and 87 nm, respectively).

Representative AFM images (scan size: 1μm×1μm) taken at various stages of growth of $SnCl_2Pc$ thin film are shown in **Fig. 3.2**. The upper panel shows the morphology for $SnCl_2Pc$ thin film grown on Si (100) substrate and the lower one on glass substrate for growth duration t= 5, 9, 16, 20, 30 and 60 min. Initially, the deposited $SnCl_2Pc$ forms nearly spherical grains on both Si as well as on glass substrates. The surface features enlarge with increasing growth time. As the thickness of $SnCl_2Pc$ films increases, the grains are nucleated on the both substrates similar to other phthalocyanine based thin films. At higher thickness, the average grain size (~15 nm) is bigger for $SnCl_2Pc$ on Si case compared to that of glass substrate (~9 nm), as measured from the

AFM images. As the thickness of $SnCl_2Pc$ thin films increases, the grains are nucleated on the both substrates similar to other phthalocyanine based thin films. The nearly spherical shape of the islands (spherical crystallite) indicates negligible anisotropy, which is a common characteristic morphology for phthalocyanine derivatives [18].

3.3.2 Surface Statistical Analysis: Height-height Correlation Function and Scaling Exponents

In order to understand the dynamic scaling behavior and detailed insight into the growth processes, we have calculated the scaling exponents and root mean square (RMS) local slope of the mounds. These quantities can be obtained by calculating the height-height correlation function (HHCF), $g(r,t)$ which is defined as the mean square of height difference between two surface positions separated by a lateral distances r $(=\sqrt{(x-x')^2-(y-y')^2})$. If scaling exists, it is of the form [19,20],

$$g(r,t) = \langle [h(r+r',t) - h(r',t)]^2 \rangle = 2w(t)^2 g\left(\frac{r}{\xi(t)}\right), \tag{3.1}$$

where spatial averaging is done over r' variable of the planar sample surface. HHCF can be evaluated from real space images by spatial averaging over one or several regions, which should be much larger than r to avoid edge effects. The relative magnitudes of r and the correlation length ξ (beyond which surface heights are uncorrelated on the average) can divide the HHCF into two distinct behaviors: (i) $r \ll \xi$, $g(r) \propto r^{2\alpha}$, where α $(0 \leq \alpha \leq 1)$ is the roughness scaling exponent, which describes the surface fractility, and (ii) $r \gg \xi$, $g(r) = 2w^2$, where $w=\langle (h-\langle h \rangle)^2 \rangle^{1/2}$ is the standard deviation of the surface height/RMS roughness. The parameters ξ and w are dependent on the deposition time, t, and fit the power laws as [21]

$$\left.\begin{aligned} w &\propto t^{\beta} \\ \xi &\propto t^{1/z} \end{aligned}\right\}, \tag{3.2}$$

where β and z are growth and dynamic scaling exponents, respectively, and in many systems [11,12], they are related to $1/z \cong \beta/\alpha$. The ξ, at each thickness is determined by fitting the HHCF, where the two regime $r \ll \xi$ and $r \gg \xi$ are connected to a function for self-affine surface, which manifest anisotropic scale invariance [22], is given by

$$g(r) = 2w^2\left[1 - exp\left\{-\left(\frac{r}{\xi}\right)^{2\alpha}\right\}\right] \quad . \tag{3.3}$$

For Self-affine surface, the roughness scaling follows simple power laws with a growth exponent β and scaling exponent α, which unambiguously distinguish the growth universality classes.

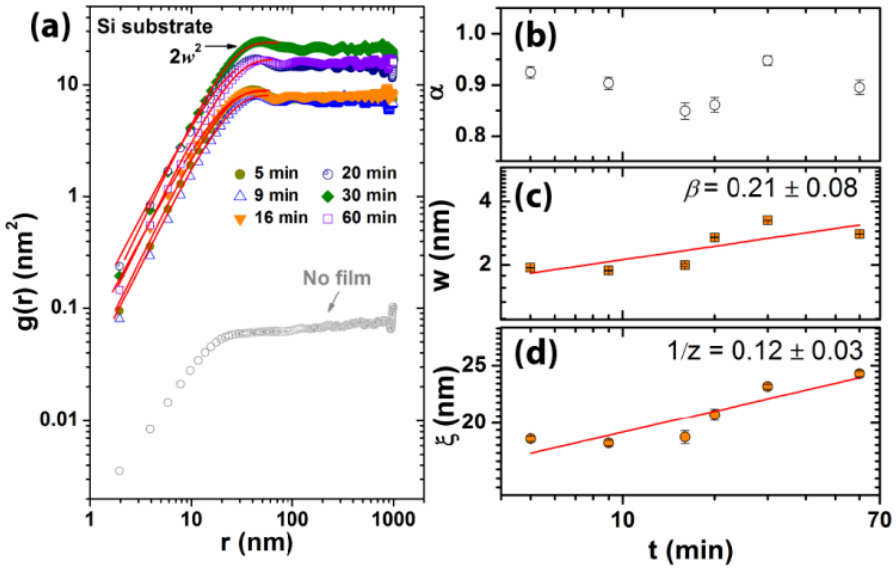

Figure 3.3: (a) HHCF $g(r)$ as a function of distance r with best fitted theoretical curve for representative $SnCl_2Pc$ thin films on Si substrate with different deposition times. The symbols are experimental data and the solid lines are fit to **Eqn. (3.2)**. **(b)** α, **(c)** w, and **(d)** ξ as a function of deposition time, t. The solid lines in (c) and (d) show the linear fit to the experimental data (symbols).

From **Fig. 3.3(a)**, it is perceptible that HHCF *g(r, t)* increases linearly at small r and saturates at large r, with the asymptotic behavior predicted by **Eq. (3.3)**. The lateral position corresponding to the grains point is equal to ξ, which is a measure of the average island size. It is clear from **Figs. 3.3(a)** and **3.4(a)** that *g(r, t)* shifts upward as growth time progresses or $SnCl_2Pc$ film thickness increases, which is similar with other organic thin film growth [16,18]. From HHCF function for the films [see **Figs 3.3(b)** and **3.4(b)**], the calculated average roughness exponent, α is ~0.90 for both Si and glass substrates.

Next, we measured the growth exponent β ($w \propto t^{\beta}$) of the $SnCl_2Pc$ films. At initial stage of growth, β is nonzero for both cases. From **Figs. 3.3(c)** and **3.4(c)**, we measured β=0.21±0.08 and

0.48±0.07 for $SnCl_2Pc$ on Si and glass substrates, respectively. Thus a large β value (0.48±0.07) is observed for the growth on glass substrate, in contrast to the small β value for Si substrate. The large β value of $SnCl_2Pc$ on glass substrate suggest that growth front is roughening and it implies

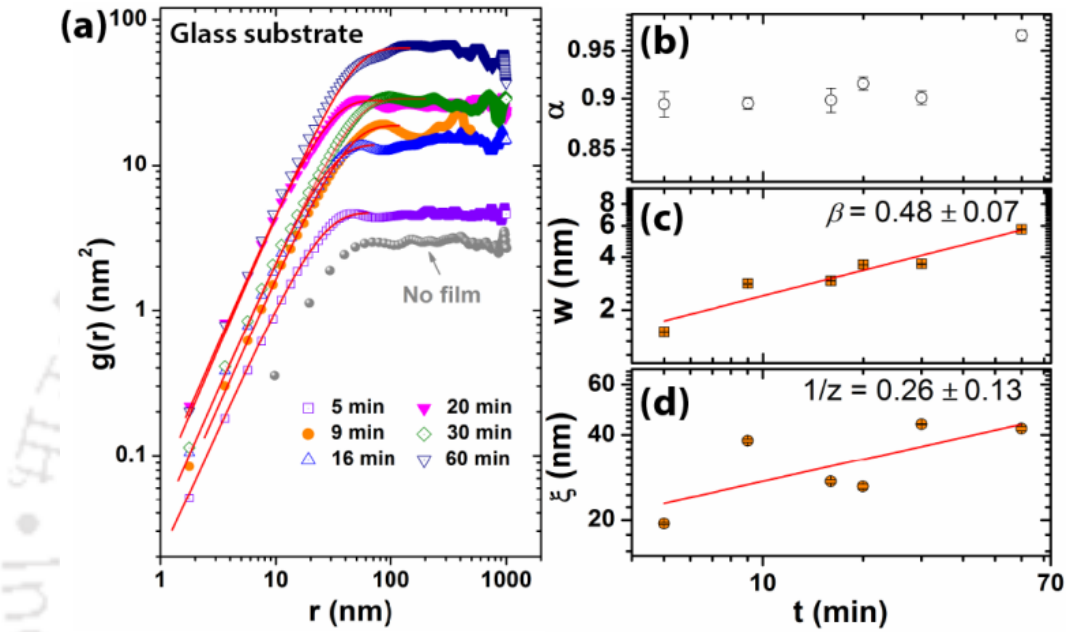

Figure 3.4: (a) HHCF $g(r)$ vs. distance r with best fitted theoretical curve (solid line) for representative $SnCl_2Pc$ thin films on glass substrate with different deposition times. **(b)** α, **(c)** w, and **(d)** ξ as a function of deposition time, t.

a large step-edge barrier or Ehrlich-Schwöbel (ES) barrier, that does not allow molecules to diffuse over the edge of step on the surface, resulting in the uphill current of diffusive particle [23], and deep grain boundaries between neighboring domains with different molecular orientations or different plane of stacking directions between the domains, which comes from the intrinsic anisotropy of the molecular structures and their crystallographic ordering. The influence of deep grain boundaries on the growth exponent is described using (1+1)–dimensional surface growth-model proposed by Yim and Jones [16] and this may contribute to the high β value due to tilted upward orientation of slip-stacked $SnCl_2Pc$ molecules on the glass substrate. High β value (>0.5) is common to growth situations where unusually rapid roughening take place, as expected for random deposition in 'hit-and-stick' model, which could arise from non-local effects such as shadowing effect or bulk diffusion [20,24-26]. The anomalous large $\beta > 0.5$

values have been reported for several organic-molecular crystalline thin film system, e.g., free-base H2Pc on glass (β=1.02±0.08) [27], ZnPc on glass substrate (β=0.62±0.04) [18], di-indeno perylene on SiO_2 (β=0.75) [28], and F16CuPc (β ~3.089) [29].These values are higher than that predicted for the random deposition model [20]. On the other hand, small β value for Si substrate may be attributed to small ES barrier at edge of the molecular layer. A decrease in the crystallographic ordering of the films may also lead to reduced step-edge barriers, although several studies have reported significant differences in the β values obtained for amorphous and crystalline films [30]. It is believed that phthalocyanines tend to grow in a standing–up configuration in thicker film on chemically 'inert' glass substrate as compared to the single crystalline Si substrate. This different growth modes observed on two different substrates can be understood in terms of molecule-substrate interactions, since molecule-molecule interaction strength is nearly the same for all investigated films. Here the molecule-substrate interaction strength may be stronger for Si substrate than the glass substrate. So the adsorption of the molecule occurs in a lying geometry of $SnCl_2Pc$ molecules on Si substrate[31]. Our XPS analysis on 5 nm thin $SnCl_2Pc$ film on Si and

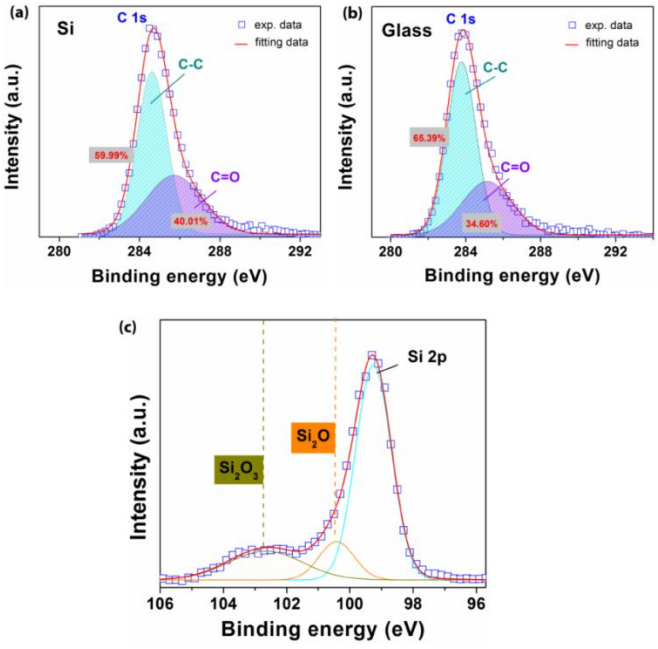

Figure 3.5: C1s XPS spectra of the $SnCl_2Pc$ organic thin film of thickness 5 nm on **(a)** Si(100) and **(b)** glass substrate. **(c)** Si 2p XPS spectrum of the Si substrate showing peaks corresponding to different oxidation states of Si.

glass substrate is presented in **Figs. 3.5(a)** and **(b)**. It shows different oxygen concentrations in the film. In **Fig. 3.5(c)**, the Si 2p spectrum of the Si substrate and Si 2p spectrum shows Si^{4+}, Si^{3+}, and Si^{+} oxidations states corresponding to different suboxides of Si, which are due to the native oxides. Thus the nature of molecular interactions in two different substrates are likely to be different, giving rise to different molecular structures. The inverse scaling exponents $1/z \sim 0.12\pm0.03$ and 0.26 ± 0.13 have been observed for $SnCl_2Pc$ thin films on Si and glass substrate, respectively (see **Figs. 3.2(d)** and **3.3(d)**). This indicates that the molecules grow in upward direction rather than lateral direction on glass substrate in comparison to Si substrate and higher density of grains is formed on glass than Si within the same scan area ($1\mu m \times 1\mu m$). Thus, during the growth the $SnCl_2Pc$ molecule, which is intrinsically anisotropic, can change its orientation (standing-up or lying-down). The anisotropic interactions with surface of the substrates (inert or reactive) may play a significant role upon the scaling relations predicted by growth dynamic theories. This information would be important in order to understand the mechanism by which molecular thin films grow and to control interfacial properties [32].

3.3.3 2D-Fast Fourier Transform Analysis

Interestingly, the calculated exponents (α, β, $1/z$) are quite close to the exponents predicted by the model of mound formation, which is reported for organic and inorganic materials. Although the asymptotic value of roughness exponent $\alpha = 1$ for mound formation, in practice a lower value can be obtained [14], in our case it is ~0.9. We have plotted 2D fast Fourier

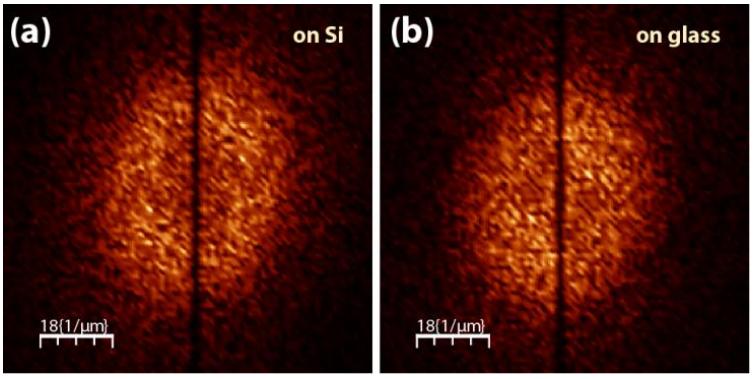

Figure 3.6: 2D FFT of the AFM images of $SnCl_2Pc$ thin film of thickness ~ 8 nm (deposited for 5 min) on: **(a)** Si, and **(b)** glass substrate. The vertical dark line in the center of images is due to the AFM fast scan direction.

transform of the surfaces from the representative AFM images on Si and glass substrates, as shown in **Figs. 3.6(a)** and **3.6(b)**, respectively. It clearly shows a ring like behavior, which supports the mound growth morphology [8,33]. Further, the HHCF is oscillatory in nature for mounded surfaces, which is clearly visible at large *r* in **Figs. 3.2(a)** and **3.3(a)**. The formation of mound on surface can be attributed to different growth effects, like step-edge barrier diffusion effect, shadowing, reemission etc., and the mound formation may be local or non-local in nature [33,34].

Further, it is found that the height distribution *p(h)* function is skewed negatively (*S*=-0.10) and positively (*S*=0.18) on Si and glass substrates respectively, which are shown in **Figs 3.7(a)** and **(b)**) where the skewness can be written as,

$$S = \frac{\langle [h-\langle h \rangle]^3 \rangle}{w^3} \tag{3.4}$$

which indicates the violation of the $h \rightarrow -h$ symmetry and thus the presence of a nonlinearity ($(\nabla h)^2$) associated with growth dependence on

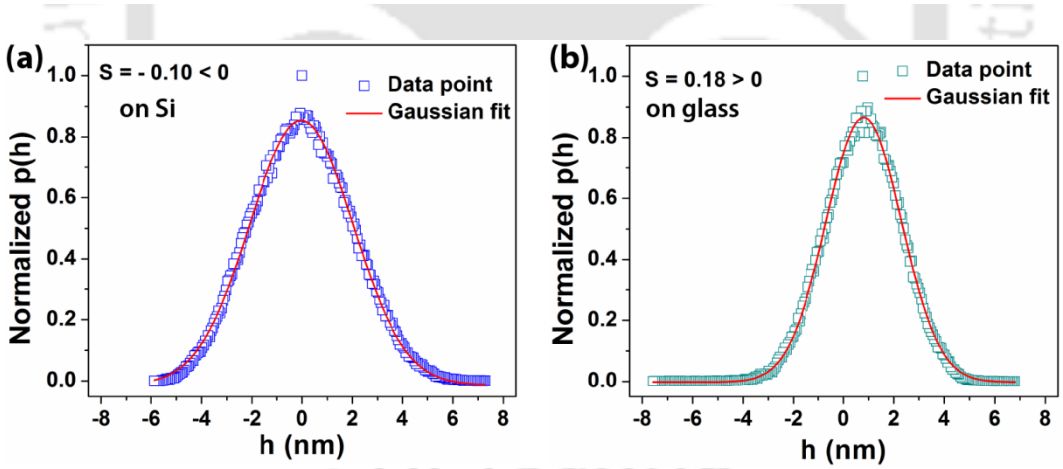

Figure 3.7: Height distribution *p(h)*obtained from the AFM images of $SnCl_2Pc$ for deposition time 5 min (~8 nm) on **(a)** Si and **(b)** glass substrates. Skewness, *S*, is negative for Si substrate, while it is positive for glass substrate.

the local surface inclination [35]. However, the calculated exponents do not match with the reported Kardar-Parisi-Zhang (KPZ) growth model,

$$\frac{\partial h}{\partial t} = v\nabla^2 h + b(\nabla h)^2 + \eta, \tag{3.5}$$

where $v\nabla^2 h$ appears due to surface relaxation and η represents random Gaussian during deposition [36,37]. Interestingly, the scaling exponents (α, β, and $1/z$) of $SnCl_2Pc$ thin films are not consistent with any of the universality classes described by the conserved growth equations for kinetic growth developed for inorganic materials. Note that the β value for $SnCl_2Pc$ on Si is quite comparable with that of copper hexadecafluro phthalocyanine ($F_{16}CuPc$) on ITO-coated glass [38].

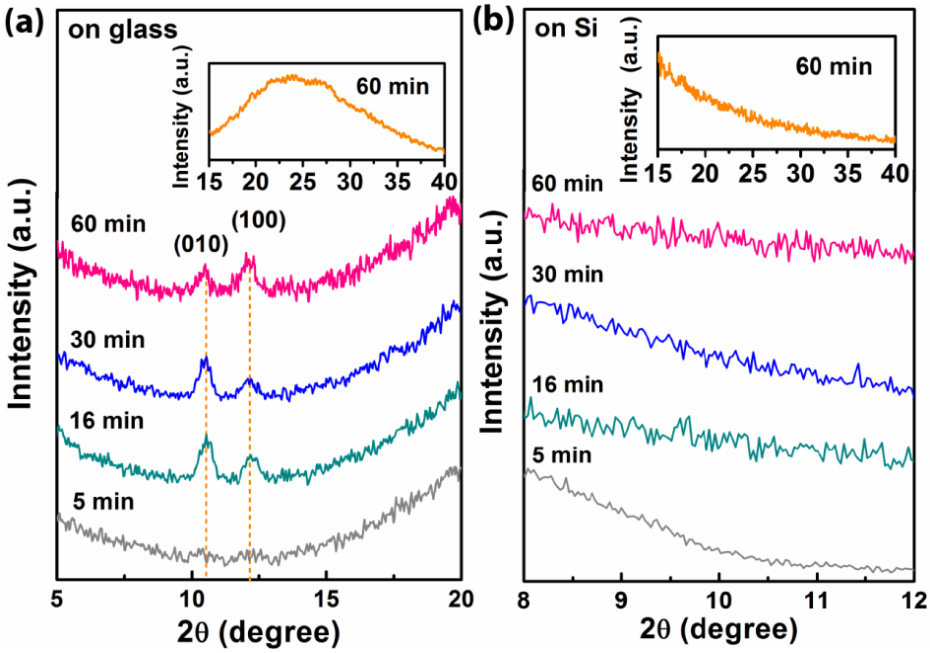

Figure 3.8: XRD patterns of $SnCl_2Pc$ thin films gown on **(a)** glass, and (**b)** Si substrate for different deposition times.

3.3.4 Structural Analysis

The structural quality of the organic film has been deduced from the XRD analysis. **Figure 3.8(a)** and **3.8(b)** show the XRD pattern of different $SnCl_2Pc$ thin films grown on glass and Si substrates, respectively. For the films on glass (**Fig. 3.8(a)**), the intensity of peak at 2θ~10° and ~12° are prominent for film thickness above ~8 nm. The inset shows the XRD pattern in extended range of 2θ=15°-40° in each case. The film on the glass substrate shows a broad peak centered at ~25° arising from the glass substrate, while no such peak was observed for the case of Si substrate. The $SnCl_2Pc$ thin films deposited on glass substrate is identified as triclinic crystallites (a=0.7363 nm, b=0.8676 nm, c=1.1048 nm, α=74.21°, β=80.33°, γ=85.47°) [39],

while the film on Si substrate is amorphous, as evidenced by the absence of any diffraction peaks for Si case, even for ~87 nm thick film. The XRD measurements with different grazing angle (ω= 0.5, 1.0 and 1.5 degree) have also been carried out for thin film on Si and glass substrate. The films on glass substrate shows the similar peak positions at different ω values while the film on Si substrate do not show any peak in the entire 2θ range (including no peak in the range 25-32°), as evident from **Fig. 3.9(a)-(b)**.

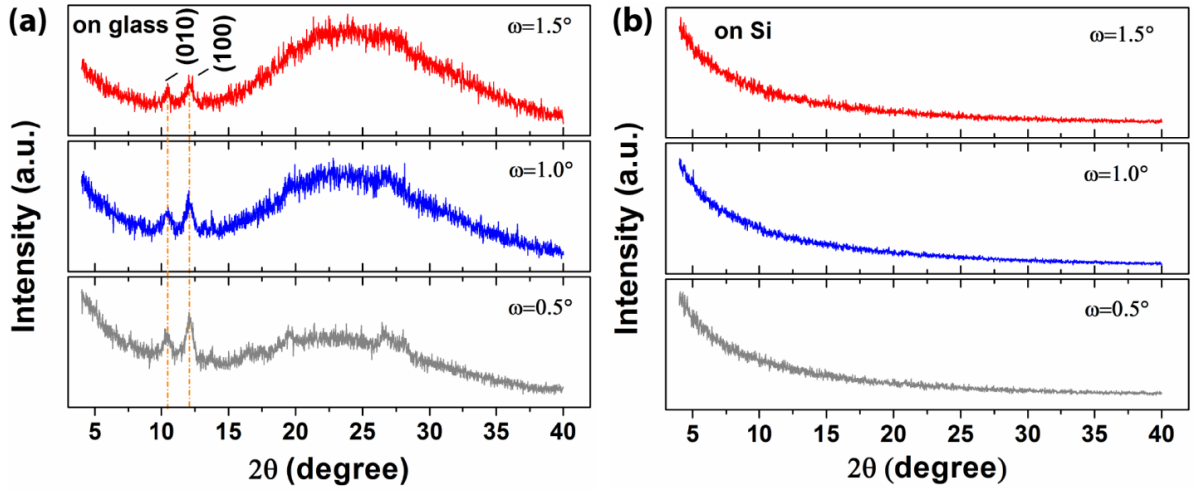

Figure 3.9: XRD patterns of ~87 nm-thick $SnCl_2Pc$ thin films gown on **(a)** glass, and **(b)** Si substrate at different grazing angle ω= 0.5 to 1.5 degree.

The peaks corresponding to inter-planar spacing, $d_{(010)}$ and $d_{(100)}$, of 8.46 Å, and 7.29 Å are due to the diffraction from the (010), and (100) plane of the $SnCl_2Pc$ crystallites and it is due to the two different kinds of slip-stacked molecular packing formed on glass substrate, which implies that the intermolecular π-π direction is parallel to the glass substrate, and it is useful for the fabrication of optoelectronic devices [6,40]. In contrast, for $SnCl_2Pc$ films on Si, no predominant peak was observed for the range of the different thicknesses studied (see **Fig. 3.8(b)**) and it confirms the amorphous nature of $SnCl_2Pc$ film on Si substrate. These interpretations for both cases (Si and glass) are schematically presented in **Fig. 3.10**. A possible reason for the lying–down molecular geometry of $SnCl_2Pc$ without any ordered molecular arrangement is its tetragonal-bipyramidal (non-planar disk like) and it would prevent it from crystallizing on the Si substrate with diamond structure. The amorphous characteristic of $SnCl_2Pc$ thin films leads to very small extra energy barrier at the step edge when the molecules move down to the lower layer. The small β value of

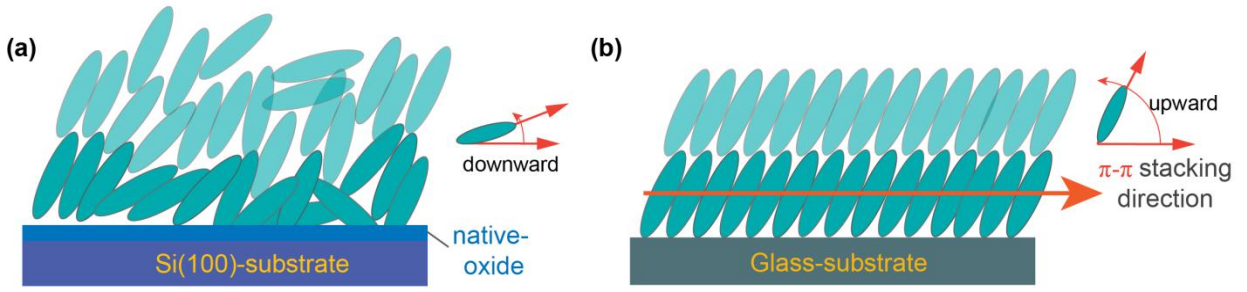

Figure 3.10: Schematic of $SnCl_2Pc$ molecule packing arrangement on different substrates: (a) Si(100) - amorphous like and (b) glass substrate - crystalline like.

$SnCl_2Pc$ films on Si can be rationalized by this amorphous characteristic and consequent small step-edge barrier. Note that no peak was observed for the $SnCl_2Pc$ films with the thickness below 8 nm on both the substrates. Although the XRD patterns is dependent on film thickness, there is no significant shift in the Q-band peak position in the UV-Vis spectra for different thickness film as shown in **Fig. 3.11** [41], which is consistent with an earlier report [42].

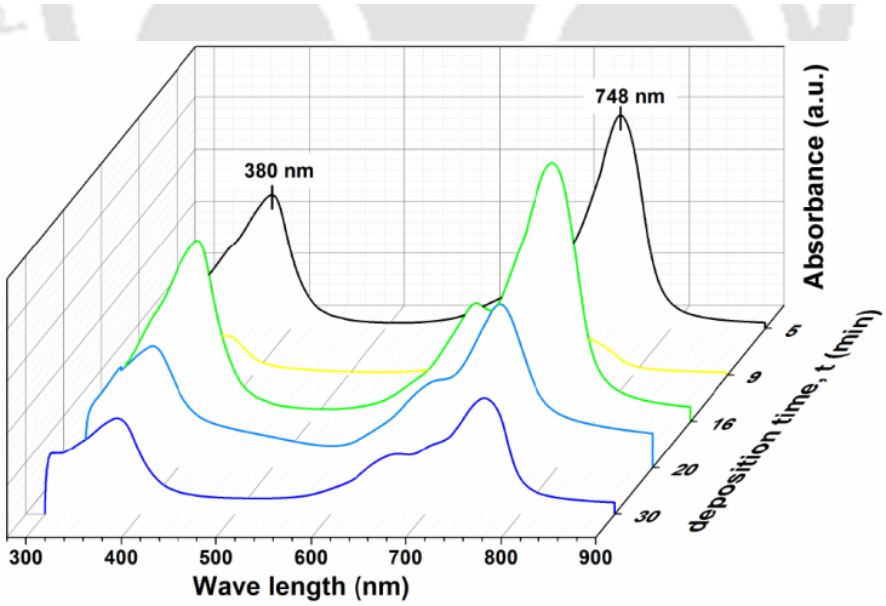

Figure 3.11: UV-Vis absorption spectra of $SnCl_2Pc$ thin films for different deposition times.

3.4 Conclusions

In conclusion, we addressed the structural evolution of $SnCl_2Pc$ thin films grown by thermal evaporation techniques on Si and glass substrates. The growth dynamics of $SnCl_2Pc$ thin films has been studied using AFM and HHCF analysis. By analyzing the scaling behavior and 2D fast Fourier transforms, it is concluded that the morphological evolution of the deposited $SnCl_2Pc$ molecules follows mound like formation, which suggests that the $SnCl_2Pc$ crystallites grow in the upward direction as the film thickness increases on glass substrate, which may be due to the high potential barrier or step-edge barrier. One of the important findings is that the β value for $SnCl_2Pc$ thin film on glass substrate is higher than random deposition model, while for Si substrate it is very small and results in "smoothening"- a lying down geometry, which may be due to the small step-edge barrier. $SnCl_2Pc$ films grown here on glass substrate exhibited crystalline behavior, which is suitable for device fabrication.

References

[1] T.C. Rosenow, K. Walzer, K. Leo, Near-infrared organic light emitting diodes based on heavy metal phthalocyanines. *J. Appl. Phys.* **103**, 043105 (2008).

[2] F. Yang, M. Shtein, S.R. Forrest, Controlled growth of a molecular bulk heterojunction photovoltaic cell. *Nat. Mater.* **4**, 37 (2005).

[3] T. Zhuang, Z. Su, Y. Liu, B. Chu, W. Li, J. Wang, F. Jin, X. Yan, B. Zhao, F. Zhang, D. Fan, Improvement of both efficiency and working lifetime in organic photovoltaic devices by using bathophenanthroline/tin(IV) phthalocyanine dichloride as bilayer exciton blocking layers. *Appl. Phys. Lett.* **100**, 243902 (2012).

[4] F.I. Bohrer, C.N. Colesniuc, J. Park, M.E. Ruidiaz, I.K. Schuller, A.C. Kummel, W.C. Trogler, Comparative Gas Sensing in Cobalt, Nickel, Copper, Zinc, and Metal-Free Phthalocyanine Chemiresistors. *J. Am. Chem. Soc.* **131**, 478 (2009).

[5] Z. Bao, J. Locklin, Organic Field-Effect Transistors, CRC Press, Boca Raton, FL, USA, (2007).

[6] D. Song, H. Wang, F. Zhu, J. Yang, H. Tian, Y. Geng, D. Yan, Phthalocyanato Tin(IV) Dichloride: An Air-Stable, High-Performance, n-Type Organic Semiconductor with a High Field-Effect Electron Mobility. *Adv. Mater.* **20**, 2142 (2008).

[7] S. Md. Obaidulla, D.K. Goswami, P.K. Giri, Low bias stress and reduced operating voltage in SnCl2Pc based n-type organic field-effect transistors. *Appl. Phys. Lett.* **104**, 213302 (2014).

[8] Y. Zhang, E. Barrena, X. Zhang, A. Turak, F. Maye, H. Dosch, New Insight into the Role of the Interfacial Molecular Structure on Growth and Scaling in Organic Heterostructures. *J. Phys. Chem. C* **114**, 13752 (2010).

[9] D. Hong, Y.R. Do, H.T. Kwak, S. Yim, Structural templating and growth behavior of copper phthalocyanine thin films deposited on a polycrystalline perylenetetracarboxylic dianhydride layer. *J. Appl. Phys.* **109**, 063507 (2011).

[10] S. Zorba, L. Yan, N.J. Watkins, Y. Gao, Kinetic roughening study of perylene on glass and Au substrates. *Appl. Phys. Lett.* **81**, 5195 (2002).

[11] J.H. Jeffries, J.K. Zuo, M.M. Craig, Instability of Kinetic Roughening in Sputter-Deposition Growth of Pt on Glass. *Phys. Rev. Lett.* **76**, 4931 (1996).

[12] G. Palasantzas, J. Krim, Scanning Tunneling Microscopy Study of the Thick Film Limit of Kinetic Roughening. *Phys. Rev. Lett.* **73**, 3564 (1994).

[13] M. Pelliccione, T. Karabacak, C. Gaire, G.C. Wang, T.M. Lu, Mound formation in surface growth under shadowing. *Phys. Rev. B* **74**, 125420 (2006).

[14] G. Lengel, R.J. Phaneuf, E.D. Williams, S. Das Sarma, W. Beard, F.G. Johnson, Nonuniversality in mound formation during semiconductor growth. *Phys. Rev. B* **60**, R8469 (1999).

[15] Y.P. Zhao, J.B. Fortin, G. Bonvallet, G.C. Wang, T.M. Lu, Kinetic Roughening in Polymer Film Growth by Vapor Deposition. *Phys. Rev. Lett.* **85**, 3229 (2000).

[16] S. Yim, T.S. Jones, Growth dynamics of C60 thin films: Effect of molecular structure. *Appl. Phys. Lett.* **94**, 021911 (2009).

[17] S. Zorba, Y. Shapir, Y. Gao, Fractal-mound growth of pentacene thin films. *Phys. Rev. B* **74**, 245410 (2006).

[18] J. Kim, N. Lim, C.R. Park, S. Yim, Growth dynamics of ZnPc and TiOPc thin films: Effect of crystallinity on anomalous scaling behavior. *Surface Science* **604**, 1143 (2010).
[19] F. Dinelli, R. Capelli, M.A. Loi, M. Murgia, M. Muccini, A. Facchetti, T.J. Marks, High-Mobility Ambipolar Transport in Organic Light-Emitting Transistors. *Adv. Mater.* **18**, 1416 (2006).
[20] M. Bronner, A. Opitz, W. Brütting, Ambipolar charge carrier transport in organic semiconductor blends of phthalocyanine and fullerene. *phys. stat. sol. (a)* **205**, 549 (2008).
[21] Matthew Pelliccione, T.-M. Lu, Evolution of Thin Film Morphology: Modeling and Simulations (2008).
[22] S.K. Sinha, E.B. Sirota, S. Garoff, H.B. Stanley, X-ray and neutron scattering from rough surfaces. *Phys. Rev. B* **38**, 2297 (1988).
[23] S. Yim, K.i. Kim, T.S. Jones, Growth Morphology of Perylene-3,4,9,10-tetracarboxylic Dianhydride (PTCDA) Thin Films: Influence of Intermolecular Interactions and Step-Edge Barriers. *J. Phys. Chem. C* **111**, 10993 (2007).
[24] G. Zhang, B.L. Weeks, M. Holtz, Application of dynamic scaling to the surface properties of organic thin films: Energetic materials. *Surface Science* **605**, 463 (2011).
[25] S. Kowarik, A. Gerlach, F. Schreiber, Organic molecular beam deposition: fundamentals, growth dynamics, and in situ studies. *J. Phys.: Condens. Matter* **20**, 184005 (2008).
[26] L. Vázquez, J.M. Albella, R.C. Salvarezza, A.J. Arvia, R.A. Levy, D. Perese, Roughening kinetics of chemical vapor deposited copper films on Si(100). *Appl. Phys. Lett.* **68**, 1285 (1996).
[27] S. Yim, T.S. Jones, Anomalous scaling behavior and surface roughening in molecular thin-film deposition. *Phys. Rev. B* **73**, 161305 (2006).
[28] A.C. Dürr, F. Schreiber, K.A. Ritley, V. Kruppa, J. Krug, H. Dosch, B. Struth, Rapid Roughening in Thin Film Growth of an Organic Semiconductor (Diindenoperylene). *Phys. Rev. Lett.* **90**, 016104 (2003).
[29] J.L. Yang, S. Schumann, T.S. Jones, Morphology and Structure Transitions of Copper Hexadecafluorophthalocyanine (F16CuPc) Thin Films. *The Journal of Physical Chemistry C* **114**, 1057 (2010).
[30] S. Kowarik, A. Gerlach, S. Sellner, F. Schreiber, J. Pflaum, L. Cavalcanti, O. Konovalov, Anomalous roughness evolution of rubrene thin films observed in real time during growth. *Phys. Chem. Chem. Phys.* **8**, 1834 (2006).
[31] H. Peisert, T. Schwieger, J.M. Auerhammer, M. Knupfer, M.S. Golden, J. Fink, P.R. Bressler, M. Mast, Order on disorder: Copper phthalocyanine thin films on technical substrates. *J. Appl. Phys.* **90**, 466 (2001).
[32] F. Schreiber, Organic molecular beam deposition: Growth studies beyond the first monolayer. *Phys. Status Solidi (a)* **201**, 1037 (2004).
[33] Y.X. Chuan Liu, and Yong-Young Noh, Contact engineering in organic field-effect transistors. *Materials Today* **00**, 00 (2014).
[34] G. Hlawacek, P. Puschnig, P. Frank, A. Winkler, C. Ambrosch-Draxl, C. Teichert, Characterization of Step-Edge Barriers in Organic Thin-Film Growth. *Science* **321**, 108 (2008).
[35] J.T. Drotar, Y.P. Zhao, T.M. Lu, G.C. Wang, Numerical analysis of the noisy Kuramoto-Sivashinsky equation in 2+1 dimensions. *Phys. Rev. E* **59**, 177 (1999).

[36] D. Tsamouras, G. Palasantzas, J.T.M. De Hosson, Growth front roughening of room-temperature deposited oligomer films. *Appl. Phys. Lett.* **79**, 1801 (2001).

[37] B.M. Forrest, L.-H. Tang, Surface roughening in a hypercube-stacking model. *Phys. Rev. Lett.* **64**, 1405 (1990).

[38] J. Yang, S. Yim, T.S. Jones, Molecular-Orientation-Induced Rapid Roughening and Morphology Transition in Organic Semiconductor Thin-Film Growth. *Scientific Reports* **5**, 9441 (2015).

[39] J. Janczak, R. Kubiak, Two isomorphous complexes: dichloro[phthalocyaninato(2-)]tin(IV) and dichloro[phthalocyaninato(2-)]germanium(IV). *Acta Cryst. C* **59**, m237 (2003).

[40] S.M. Obaidulla, P.K. Giri, Low operating voltage and low bias stress in top-contact SnCl2Pc/CuPc heterostructure-based bilayer ambipolar organic field-effect transistors. *J. Mater. Chem. C* **3**, 7118 (2015).

[41] T.J. Richards, H. Sirringhaus, Analysis of the contact resistance in staggered, top-gate organic field-effect transistors. *J. Appl. Phys.* **102**, 094510 (2007).

[42] M.M. El-Nahass, K.F. Abd-El-Rahman, A.A. Al-Ghamdi, A.M. Asiri, Optical properties of thermally evaporated tin-phthalocyanine dichloride thin films, SnPcCl2. *Physica B: Condensed Matter* **344**, 398 (2004).

This Page is Left Blank Intentionally

Chapter 4

Growth Dynamics of VOPc Organic Thin Films on Various Substrates: Substrate Temperature Dependence

In this chapter, we have studied the evolution of surface morphology and scaling behavior of vanadium oxide (IV) phthalocyanine (VOPc) thin films grown on SiO_2/Si(100) and indium tin oxide (ITO)-glass substrates using atomic force microscopy (AFM) and height-height correlation function analysis. X-ray diffraction measurement confirms the crystalline nature of the VOPc thin film grown on both substrates: SiO_2 and ITO-glass at different temperatures. The growth exponent β is found to be much larger for the film on SiO_2 substrate (0.56±0.13) as compared to that on ITO-glass substrate (0.32±0.08), which may be due to the high step-edge barrier resulting in the upward dominant growth with rapid roughening on SiO_2 substrate. From the 2D fast Fourier transform of AFM images and derived scaling exponents, it is concluded that the surface evolution follows a mound like growth.

4.1 Introduction

Thin films based on metal phthalocyanine molecular semiconductors are finding extensive applications in a number of optoelectronic devices, such as organic light emitting diodes, organic photovoltaic devices, and organic field-effect transistors, organic sensors due to their favorable properties, e.g., high thermal and chemical stability, well ordered thin film growth and wide absorption band at the optical region. They exhibit high photoconductivities and unusual nonlinear optical properties [1,2]. Specifically, they are low-cost to synthesize, can be easily commercialized for various optoelectronic applications. The optoelectronic device often needs single layer or multilayer thin films. So systematic growth study is needed for the optimized carrier transport, which depend on parameters, such as molecular packing, range of grain boundaries/microstructure and roughness/morphology of surfaces [3-6]. Therefore, the controlled deposition of molecular thin films is primarily a key requirement for the optimization of electro-optical properties in organic based devices in which the optimized film thickness with desired properties are

essential [7]. In this regard, VOPc, an organic-organic hybrid dye molecule, is receiving increasing attention, since it is considered as a good candidate for p-type organic material and the device based on this molecule exhibit high operation stability [8,9], [10]. In contrast to other planar phthalocyanine, VOPc is a non-planar polar molecule with vanadyl group arranged perpendicular to macrocycle (detailed can be found in **Chapter 1**, section 1.2.2) [11,12]. Therefore, VOPc molecules of the crystalline lattice results in two dimensional π-π stacking, which results in shorter intermolecular distances as compared to other planar phthalocyanine molecules [13]. So, the investigation of growth dynamics and ordering arrangement of organic thin films has become a topic of high interest in both fundamental and applied research. However, there has been no report on the scaling behavior and growth dynamics of VOPc on different substrates that are most relevant for device applications. We have tuned the film thickness and substrate temperature, and studied the corresponding growth modes and the evolution of the surface morphology.

It is worth noting that molecular level understanding of growth dynamics of organic thin films is still in underlying as more complex growth scenarios emerge for organic molecules due to intrinsic anisotropy [14,15]. In this chapter, we elucidate the change of surface morphology of VOPc with the variation of film thickness as well as substrate temperature. We address the substrate induced roughness scaling behavior. From the height–height correlation function (HHCF) and theoretical formalism of scaling theory, we calculate the growth exponents, and these exponents describe the morphological and statistical features of VOPc thin films on various substrates.

4.2 Experimental Details

VOPc (p-type) thin films were grown in a high vacuum organic thermal evaporation chamber with a base pressure of 10^{-6} mbar at deposition rate 0.2-0.4 Å/s measured by digital thickness meter. Commercially procured VOPc (Alfa Aesar, 97%) molecules were sublimed onto well cleaned SiO_2 (thickness~300 nm) and indium tin oxide (ITO)-glass substrates at different substrate temperature (T_d) and different thicknesses (d) under identical conditions. Silicon wafers are among the most common substrates for thin film growth. They are stable in air with their oxidized surface layer, the thickness of which can be 'tuned' by thermal oxidation. Also, they are very flat and relatively easy to clean. In the context of organic electronics, they are very popular as a substrate for thin-film transistors, since the oxide can serve as the insulating layer between the silicon as the bottom contact (gate) and the active organic semiconductor on top [15]. It should also be noted that oxidized silicon surfaces are suitable for surface modification using self-assembled monolayers (SAMs). ITO-glass is another substrate transparent electrode we have employed for growth study, as they have potential applications such as liquid crystal displays, organic light emitting diodes and photovoltaic cells [16]. The substrates were first cleaned separately by deionized water (18.2 MΩcm), acetone, and 2-propanol with sonication for 15 min each. The cleaned substrates were preheated to >120 °C and subsequently cooled slowly to room temperature. During the vacuum deposition, the cell temperature was maintained at ~350 °C, and molecules were condensed on the SiO_2 and ITO-glass substrates. The average growth rate was (0.2–0.4 Å/s) and film thickness was measured by a digital thickness monitor during the growth. VOPc thin films with different thicknesses (5–120 nm) and different substrate temperature (23-210°C) were deposited and characterized (*ex situ)* for morphology and structural information by atomic force microscopy (AFM) (Agilent-5500), and high power X-ray diffractometer (XRD) (Rigaku). Thermogravimetric analysis (TGA) (NETZSCH) was used to deduce the molecule structural stability, which was carried out in Ar gas up to 1000 °C.

4.3 Results and Discussion

4.3.1 Molecule Stability and Morphological Analysis

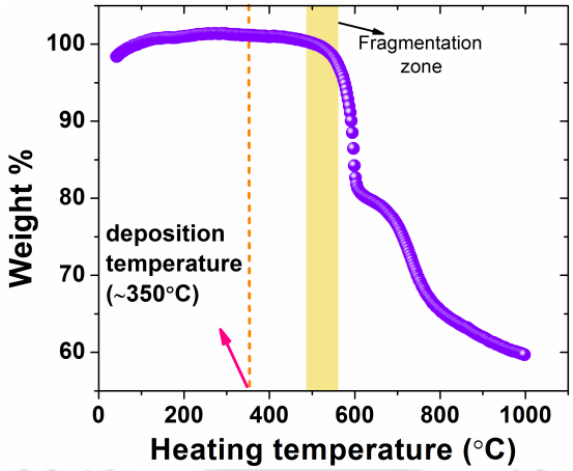

Figure 4.1: TGA plot for vanadium (IV) oxide phthalocyanine (VOPc) molecule (heating rate: 10°C/min).

TGA analysis shows (see **Fig. 4.1**) that the VOPc molecules are stable up to a temperature of ~450 °C and above the temperature, the weight loss starts. As the sublimed temperature here is ~350 °C, the molecules are not fragmented during the deposition on various substrates.

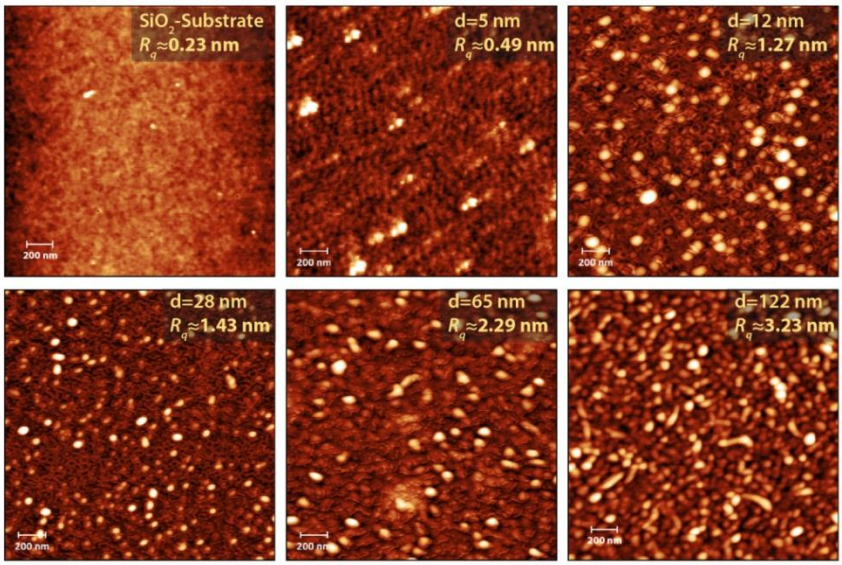

Figure 4.2: Representative AFM topography images (scan size: $2\mu m \times 2\mu m$) of VOPc thin films for different thickness: 0, 5, 12, 28, 65, and 122 nm on SiO_2/Si(100) substrate. The rms roughness is indicated in each case.

The surface morphology was analyzed by AFM measurements in the tapping mode (size: 512×512 pixel) to avoid any damage to the film. The details about the instrument, was

discussed in ***Chapter 2***. Repeated measurements were carried out at different locations of a sample in order to obtain statistical average of the film. Representative AFM images (2 μm×2 μm) taken at various stages of the growth of VOPc thin film grown on to SiO_2 substrate at room temperature (25°) with film thickness ***d***= 5, 12, 28, 65 and 122 nm, respectively, are shown in **Fig. 4.2**. In **Fig. 4.3** shows the AFM images of 65-nm-thick film at various substrate temperatures T_d=25, 80, 120, 170 and 210°C, respectively. Initially, VOPc forms nearly spherical grains on the SiO_2 substrate. The grain size elongates laterally (~10 to 16 nm) with film thickness variation 5 -122 nm and while grain size changes from ~9 to 18 nm due to increasing of substrate temperature 25 to 210°C. The nearly spherical shape of the islands (spherical crystallites) indicates negligible anisotropy and the grains enlarge in an almost regular manner with increasing thickness. For thick-film (~122nm), less irregular with relatively elongated grains can be noticeable from AFM images (see **Fig. 4.2**), which is a characteristic morphology for

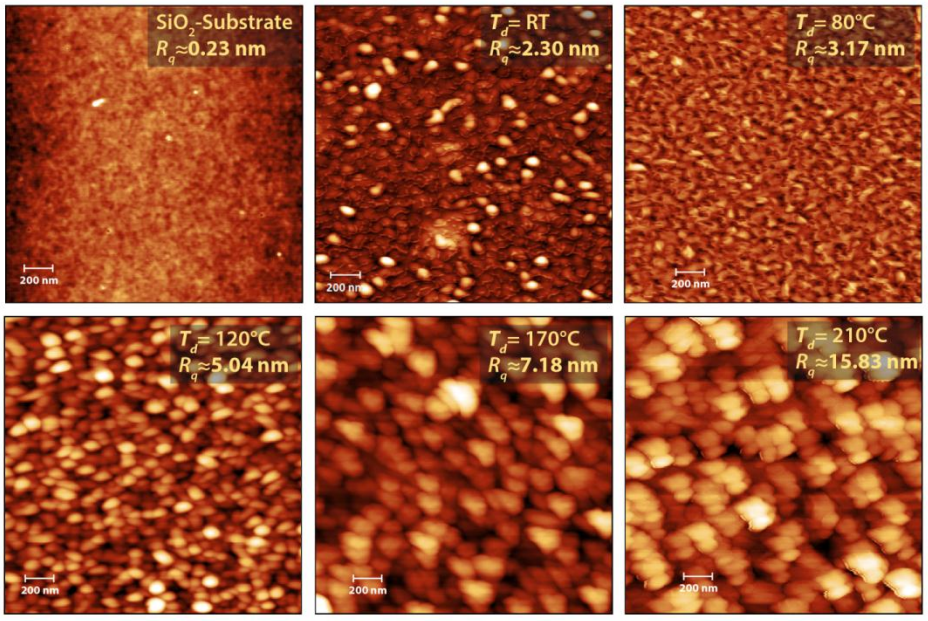

Figure 4.3: Representative AFM topography images (scan size: 2μm×2 μm) of a 65-nm VOPc thin film at different substrate temperatures: 23 (RT), 80, 120, 170 and 210 °C, respectively on SiO_2/Si(100) substrate. The rms roughness (R_q) is indicated in each case.

phthalocyanine derivatives. On the other hand, with increasing substrate temperature, crystallite shape changes from spherical to anisotropic shape and form a larger grains (~9 to

18 nm). The reason is that by diffusion process, the small grains coalescence to another grains and results into relatively extended size. The VOPc thin film morphology starts to evolve particularly at 120°C. So, it is evident that size of grains of VOPc film is larger at higher T_d (see **Fig. 4.4**).

To compare the growth dynamics and scaling behavior, we have grown VOPc films on ITO-glass under identical condition. Representative AFM images (2 μm×2 μm) are taken at various stages of the growth of VOPc thin film grown on to ITO-glass substrate at 25° substrate temperature with film thickness d= 5, 12, 28, 65 and 122 nm, respectively as shown in **Fig. 4.4**. **Figure 4.5** shows the AFM images of 65-nm-thick film at different substrate temperature (T_d) with RT (25), 80, 120, 170 and 210°C, respectively. Initially, VOPc forms

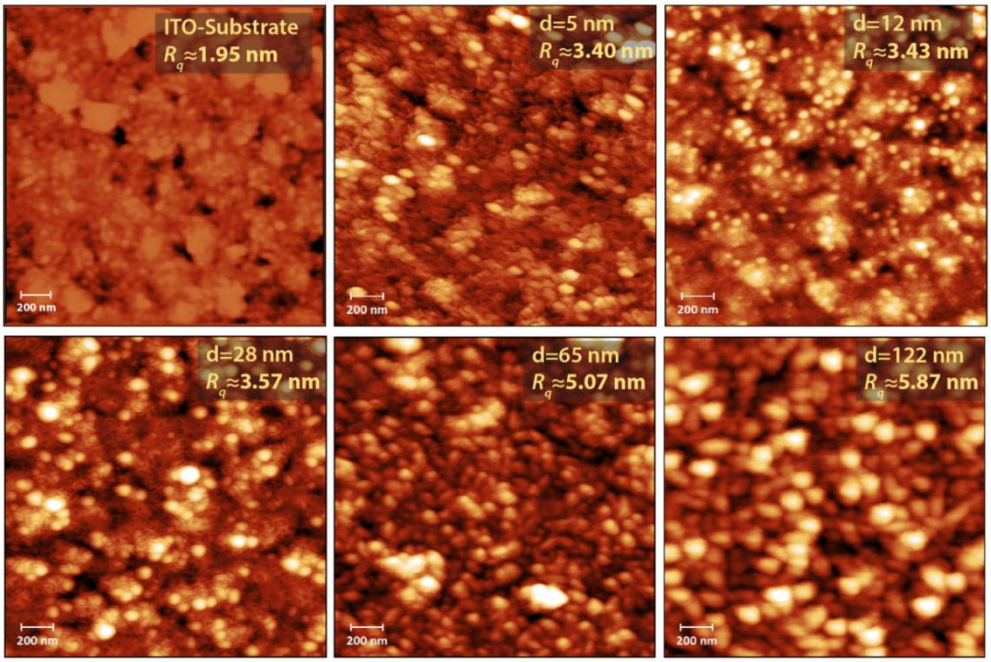

Figure 4.4: Representative AFM topography images (scan size: 2μm×2μm) of VOPc thin films for different thicknesses: 0, 5, 12, 28, 65, and 122 nm on ITO-glass substrate. The rms roughness (R_q) is indicated in each case.

nearly spherical grains on ITO-glass substrates. The surface feature enlarges with bigger circular grains from ~10 to 16 nm as the thickness increases. The nearly spherical shape of the islands (spherical crystallites) indicates negligible anisotropy. With the increases of

substrate temperature (T_d) from 25 to 210 °C, crystallite shape changes from small round grains to highly anisotropic shape (see **Fig. 4.5**) and formed a larger grain due to small grains coalescence to bigger grain, which means nucleation occurs between grains and results into the elongated terraces. So, the size of grain of VOPc film is large when $\boldsymbol{T_d}$ high, as more nucleation occurs at higher substrate temperature. So, the substrate temperature has a significant role on the evolution of VOPc thin film morphology.

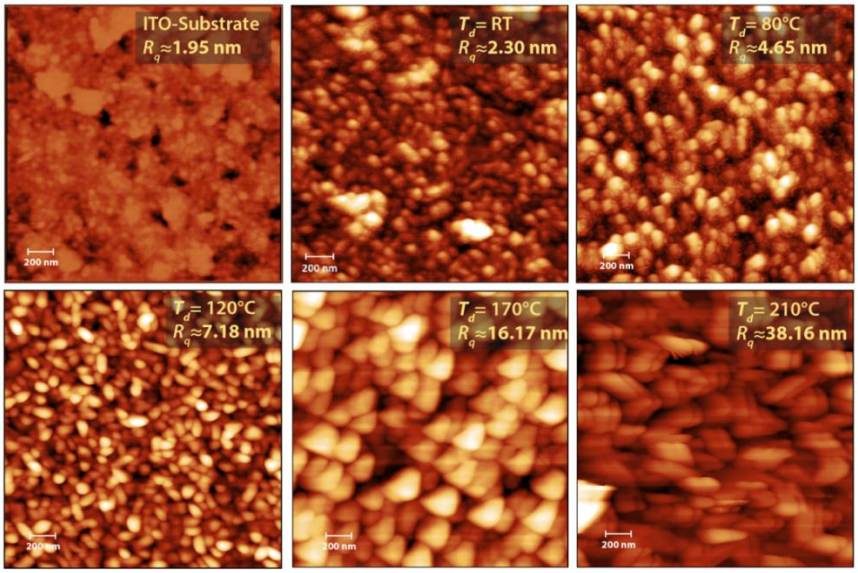

Figure 4.5: Representative AFM topography images (scan size: $2\mu m \times 2\mu m$) of 65-nm VOPc thin films grown at different substrate temperature (T_d): 23 (RT), 80, 120, 170 and 210°C on ITO-glass substrate. The rms roughness (R_q) is indicated in each case.

4.3.2 Surface Statistical Analysis: Height-height Correlation Function and Scaling Exponents

In order to understand the dynamic scaling behavior and to gain a detailed insight into the growth processes, we have calculated the scaling exponents and root mean square (RMS) local slope of the mounds. These quantities can be obtained by calculating the HHCF, g(r), which is defined as the mean square of height difference between two surface positions separated by a lateral distance $r(=\sqrt{(x-x')^2-(y-y')^2})$. It is of the form, $g(r) = \langle[h(r+r',t)-h(r',t)]^2\rangle$, where spatial averaging is done over r' variable of the planar sample surface [17,18]. HHCF can be evaluated from real space images by spatial averaging over one or several regions, which should be much larger than r to avoid edge effects. The

relative magnitudes of r and the correlation length ξ (beyond which surface heights are uncorrelated on the average) can divide the HHCF into two distinct behaviors: (i) $r \ll \xi$, $g(r) \propto r^{2\alpha}$; where α ($0 \leq \alpha \leq 1$) is the roughness scaling exponent, which describes the surface fractility (smoothness of local surface profile), and (ii) $r \gg \xi$, $g(r) = 2w^2$, where $w = \langle (h - \langle h \rangle)^2 \rangle^{1/2}$ is the standard deviation of the surface height/root-mean-square (RMS) roughness [15]. It is common to redefine the surface height profile as $\langle h \rangle = 0$, by choosing a suitable reference height. The parameters ξ and w are dependent on the thickness and fit by the power laws as $w \propto t^{\beta}$ and $\xi \propto t^{1/z}$, where β and $1/z$ are growth and dynamic scaling exponents, respectively, and in ideal system, they are related to $1/z = \beta/\alpha$ [19-21]. The ξ, at each thickness is determined by fitting the HHCF, where the two regime $r \ll \xi$ and $r \gg \xi$ are connected to a function for self-affine surface proposed by Sinha *et al.*[22], which manifest anisotropic scale invariance, is given by

$$g(r) = 2w^2 \left[1 - \exp\left\{ -\left(\frac{r}{\xi} \right)^{2\alpha} \right\} \right] \tag{4.1}$$

For self-affine surface, the roughness scaling follows a simple power law with a growth exponent α, roughness exponent β, and dynamic scaling exponents 1/z which unambiguously distinguish the growth universality classes. This height correlation function works for both two dimensionals (2D) and 3Ds. From **Eq. (4.1),** we can derived two district behavior for $r \ll \xi$ and $r \gg \xi$, as we have discussed for height-height correlation function. **Figure 4.6(a)** and **4.6(b)** shows the height-height correlation function plot for VOPc thin films grown on SiO_2 substrate for different film thickness (5 nm to 122 nm) as well as different substrate temperature increases ($\boldsymbol{T_d}$=25 to 210°C). It is perceptible from HHCF that *g*(r) increases linearly with *r* at small *r* and saturates at large *r*, with the asymptotic behavior predicted by **Eq. (4.1)**. **Figure 4.7(a)** and **4.7(b)** shows the HHCF plot for VOPc film grown on ITO-glass when thickness increases from ***d***=5 nm to 122 nm and $\boldsymbol{T_d}$ increases from 25 to 210°C, which is consistent with the results of other organic thin films. It is noticeable that *g(r)* shifts

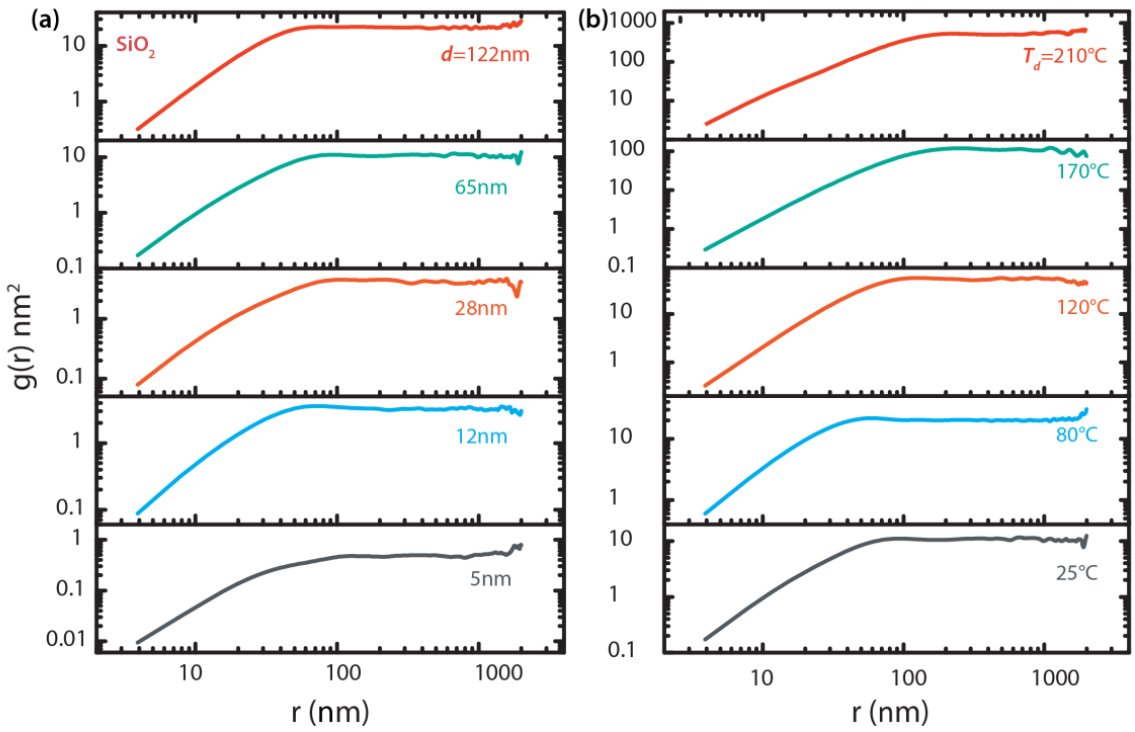

Figure 4.6: (a) HHCF $g(r)$ as a function of distance r for representative VOPc thin films on SiO_2/Si substrate with different (a) thickness (***d***=5 -122 nm) and **(b)** substrate temperature (***T_d*** = 25 - 210°C).

upward as growth time progresses or thickness increases similar to the growth on SiO_2 substrate. So, in HHCF plot, the local slope is changing with thickness for small r with VOPc film on both substrates SiO_2 and ITO glass. In case of film thickness variation, from HHCF function analysis (see **Fig. 4.6(a)** and **Fig. 4.7(a)**), the calculated average roughness exponent, α is 0.81±0.01 for SiO_2 and for ITO-glass it is 0.89±0.02. The exponent α is obtained by least-squares fitting to the linear slope, which gives 2α, of $g(r)$, at small r <30 nm in **Fig. 4.6** and **4.7**. The roughness exponent α is slightly larger for ITO glass as compared to that of SiO_2, which implies that the surface morphology formed smoother local surface in ITO-glass as compared to the growth on SiO_2 (smaller value of α implies a rougher local surface) [22,23]. It can be explained on the basis of local surface diffusion effect. This means that the local structure is changing with thickness and deposition temperature for both sets of films.

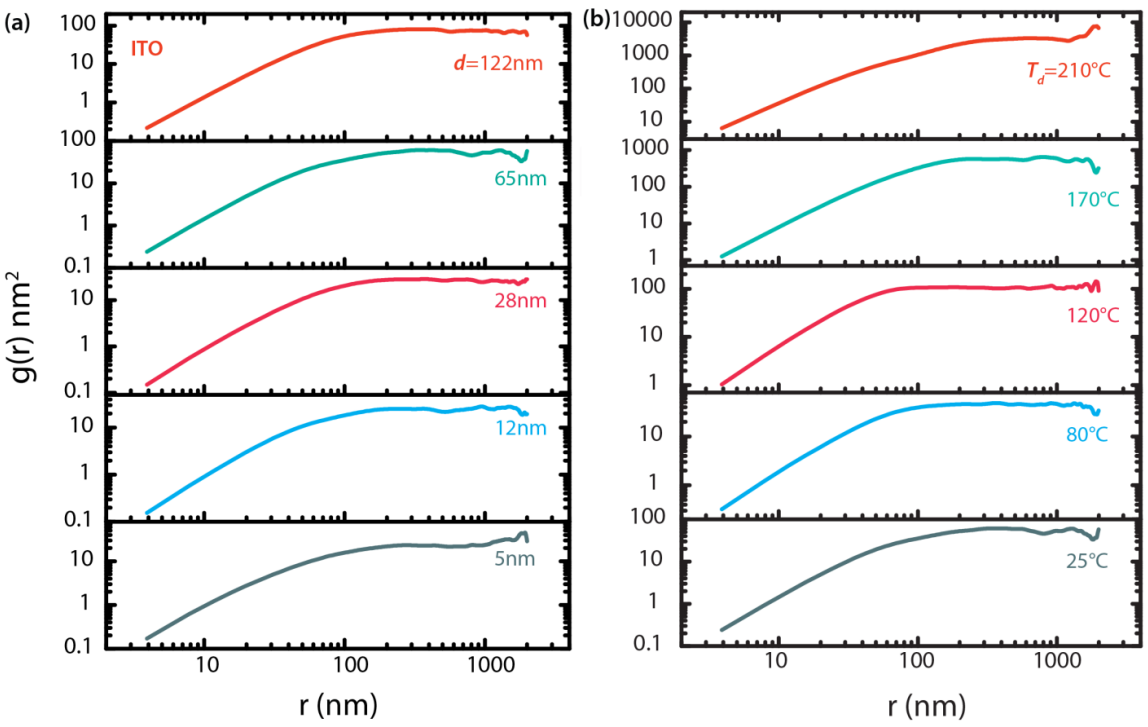

Figure 4.7: (a) HHCF $g(r)$ as a function of lateral distance r for representative VOPc thin films on ITO-glass substrate at different (a) thickness, $\boldsymbol{d}$ = 5 -122 nm (at room temperature) and **(b)** substrate temperature, $\boldsymbol{T_d}$ = 25-120°C (for 65-nm thick film).

Next, we calculated the growth exponent β ($w \propto d^{\beta}$) and scaling exponent $1/z$ ($\xi \propto d^{1/z}$) of the VOPc films in order to isolate the exact growth process in our system. At the initial stage of growth, β is nonzero for both cases. From the linear fit of in log-log plot **Figs. 4.8(a)** and **(b)**, we measured β=0.56±0.13 and $1/z$=0.10±0.05 for VOPc film on SiO_2. In case of VOPc films on ITO-glass substrate, **Figs. 4.9(a)** and **4.9(b)** yields the β value 0.32±0.05, and 1/z=0.12±0.04. These derived scaling exponents are summarized in **Table 4.1**. The large β and small $1/z$ values resulting larger the anomality for case VOPc films on SiO_2 as compared to that of ITO. Note that our computed scaling exponents are not consistent with

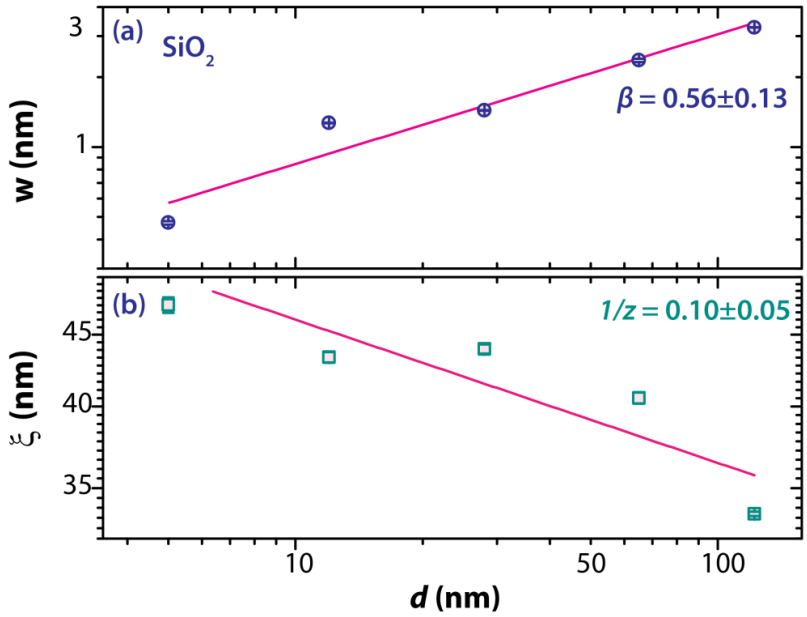

Figure 4.8: (a) *w*, and **(b)** ξ as a function of film thickness, ***d*** for representative VOPc thin film images on SiO_2/Si substrate with different deposition times. The symbols are experimental data and the solid lines are fitted data.

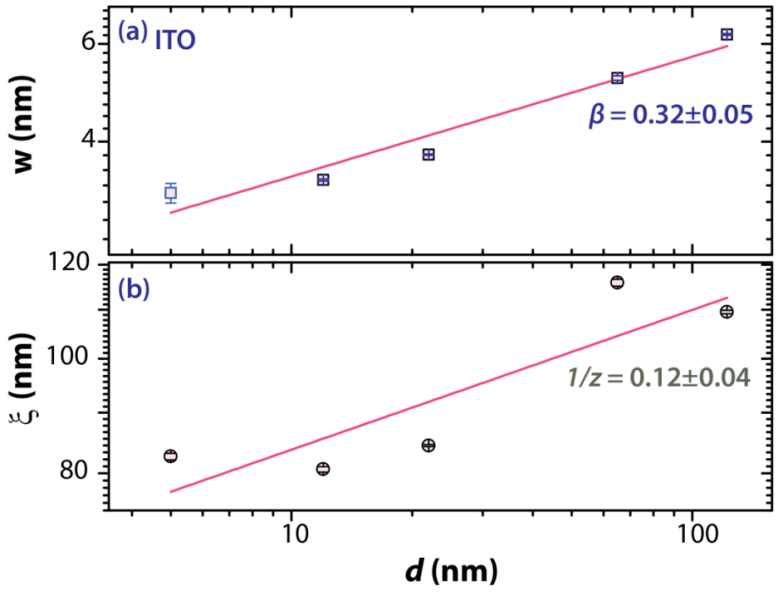

Figure 4.9: (a) *w*, and **(b)** ξ as a function of film thickness, ***d*** = 5 to 122 nm for representative VOPc thin film images on ITO-glass substrate with different deposition times. The symbols are experimental data and the solid lines are fitted data.

those based on Kardar-Parisi-Zhang (KPZ) model, $\frac{\partial h}{\partial t} = v\nabla^2 h + b(\nabla h)^2 + \eta$, where $v\nabla^2 h$ appears due to surface relaxation and η represents random Gaussian during deposition [18]. In KPZ model, α=0.5, β ~ 0.2, and *1/z* ~0.6 [18]; while in our case, α =0.8, β~0.6, and *1/z* =0.1 for SiO_2 and α ~0.9, β=0.3, and 1/z ~0.1 for ITO. In our case the dynamic scaling exponents (*1/z*) are smaller while roughness exponents (α) are higher than the KPZ predictions.

Table 4.1: Summary of the scaling exponents for VOPc films on different substrates.

Substrate	α	β	*1/z*	β/α
SiO_2	0.81±0.01	0.56±0.13	0.10±0.05	0.69±0.16
ITO	0.89±0.02	0.32±0.05	0.12±0.04	0.36±0.06

The large β value (0.56±0.13) for VOPc film on SiO_2 substrate suggests that the growth front is roughening and it implies a large additional step-edge barrier or Ehrlich-Schwöebel (ES) barrier experienced by the molecules and that does not allow molecules to diffuse over the edge of step on the surface of the same layer, resulting in the uphill current of diffused molecules. However, the strength of the step-edge barrier controls the amount of mass transport between different crystalline layers. The intrinsic anisotropy and internal degree of freedom (orientational: lying-down/standing-up, vibrational) of the molecules invokes a series of activation barriers for crossing the step-edge and results upward dominant growth leading to island formation [15,24]. It can be noted that this analogy clearly gives the indication for the mound growth. There is considerable indirect evidence that points to the presence of the step-edge barrier for other organic semiconductor molecules like F16CuPc, H2Pc, Pentacene [25-27] etc. High β value (>0.5) is common to growth situations where unusually rapid roughening takes place, as expected for random deposition in "hit-and-stick" model, which could arise from non-local effects, such as shadowing effect or bulk diffusion [22]. The diffusion barrier occurs may be due to tilt domains of the films results in rapid roughening, observed in many organic thin film growth studies, so it can explain the frequent observation of mound growth in organic growth studies [21,26,27].The anomalous large β >0.5 values have been reported for other organic-molecular crystalline thin film systems,

which are displayed in **Table 4.2,** including VOPc molecules. On the other hand, small β value (0.32±0.05) for ITO substrate may be attributed to small ES barrier at edge of the molecular layer. The low β value 0.25±0.03 reported for poly(p-xylene) was interpreted the result of monomer bulk diffusion [28]. In addition, thickness-dependent structural changes might also imply a thermodynamic driving force for roughening due to different chemical potential for different layers.

The dynamic scaling exponents are derived from the linear fitting in **Fig. 4.8(b)** and **4.9(b),** which yields $1/z$ =0.10±0.05 for SiO_2 and 0.12± 0.04 for ITO substrate, respectively. It can be concluded

Table 4.2: A summary of experimentally determined scaling exponents for several organic thin film systems, including this work: VOPc/SiO_2 and VOPc/ ITO-glass.

Thin film system	β	$1/z$	Ref.
VOPc/SiO_2	0.56±0.01	0.12±0.05	This work
VOPc/ITO	0.32±0.13	0.12±0.05	This work
H_2Pc/glass	1.02±0.08	0.72±0.13	[26]
ZnPc/glass	0.62±0.04	0.49±0.06	[29]
TiOPc/glass	0.27±0.04	0.38±0.08	[29]
DIP/SiO_2	0.74±0.05	……..	[21]
F_{16}CuPc/ITO-glass	3.08±0.04	……..	[30]

that the molecules grow faster in an upward direction than lateral direction on SiO_2 substrate and higher density of grains is formed on SiO_2 than ITO within the same scan area (2 μm×2 μm), as confirmed from AFM analysis. Thus, during the growth, the VOPc molecule, which is intrinsically anisotropic (pyramidal), can change its orientation (perpendicular or tilted on to the substrate) due to its orientational degrees of freedom [15]. The anisotropic interactions with the surface of the substrates (inert or conductive) may also play a significant role upon the scaling relations predicted by growth dynamic theories [31,32]. It is observed that for molecules growth on non-ordered poly crystalline substrate such as SiO_2 or ITO-glass, CuPc (planar molecules) grows in an ordered "standing geometry" for thicker film. A possible explanation may be that when the substrate roughness is larger than the molecules size, it

causes a weakened substrate-molecule interaction and results in the 'standing' geometry [32,33]. This information would be important to understand the growth mechanism of molecular thin films and to control the interfacial properties of the films.

In order to understand the degree of discrepancy from the conventional scaling laws for different organic molecular thin films, one can predict the growth behavior from the ratio of β/α and 1/z [29]. For SiO_2, the obtained value β/α =0.69±0.16 is ~7 times larger than the 1/z value and in case of ITO, β/α =0.36±0.06 is 3 times larger than *1/z* value. It signifies that growth of VOPc film favored more vertical growth even with faster characteristics on SiO_2 compared to ITO glass substrate. However, this discrepancy between β/α and *1/z* has been reported for several molecular thin-film systems. For example, β/α is ~2.4 times and ~3.0 times larger than the *1/z* values for H_2Pc and PTCDA (planar molecules) based thin films, respectively [26,34]. It has also been suggested that due to the existence of a high potential energy barrier/step-edge barrier as discussed earlier, prevents the upcoming fresh molecules moving to lower layer. So, it can concluded that the large ES barrier is more pronounced for thin film systems on SiO_2 as compared to the ITO-glass substrates (see **Figs. 4.2** and **4.4**). Here, for VOPc film growth, mound can be formed due to the limited diffusion which hinder growth kinetics and also due to step-edge barrier effect as observed for other organic molecules [14].

4.3.3 Temperature Dependent Growth Kinetics

In order to understand the origin of the roughening in the growth, more information can be obtained from the analysis of VOPc film grown at different substrate temperatures which is directly related to the molecular activation energy. However, due to application of substrate temperature during the film growth, thermodynamic driving forces may also be responsible for the overall evolution of morphology. So, the substrate treatment is another option to play with the energetics of the adsorbate-substrate interaction. Activation barriers calculated from the variation of surface interface width *w* with substrate temperature T_d, are associated with rotational and translational barriers of the molecular diffusion [35,36]. It is noticeable that with the increase of substrate temperature $\boldsymbol{T_d}$, the rms roughness (*w*) amplitude increase and it closely follows an Arrhenius behavior given by [35]

$$w \propto \exp\left(-\frac{E_a}{K_B T}\right), \tag{4.2}$$

Where E_a is the activation energy, T is the substrate temperature and K_B (1.381×10^{-23} m^2 kg s^{-2} K^{-1}) is Boltzmann constant. E_a proportionality constant, and deposition rate determine the orientation of the molecules with respect to the surface [37]. Understanding the effects of these experimental parameters is crucial to engineer high-quality thin films for organic electronic devices. The activation energy E_a calculated from the slope of $\ln(w)\ vs.\ 1/T$ plot as shown in **Fig. 4.10**, 0.23±0.04 eV, 0.18±0.03 eV for SiO_2 and ITO-glass substrate, respectively.

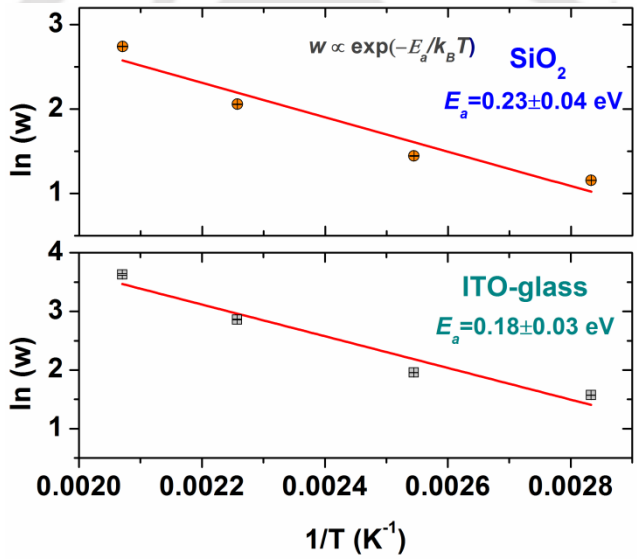

Figure 4.10: A plot of ln(w) vs. $1/T_d$ for representative VOPc thin film on (a) SiO_2/Si and (b) ITO-glass substrate, respectively. The symbols are experimental data and the solid lines are best fitted data.

So, the diffusion can be expected to be higher for VOPc film grown on ITO glass due to low activation energy (0.18 eV) as compared to that of the SiO_2 (0.23 eV). **Figure 4.11(a)** and **4.11(b)** shows a schematic of the surface profile of VOPc films are grown on SiO_2 and ITO, respectively, at certain elevated temperature (170°C). It depicts the island growth mode of VOPc films on SiO_2 substrate and the layer-by-layer plus island growth mode on ITO glass. The corresponding AFM images are shown in **Fig. 4.11(c)** and **4.11(d).** This relatively large step-edge barrier implies that the VOPc molecules on SiO_2 prefer to diffuse within the same layer rather than move down to a lower layer, providing upward three dimensional (3D)

island growth. One can notice deep and narrow crevices at the edge of islands on height profile in case of SiO_2, while shallow crevices are visible for ITO case. Molecules grow fast upwardly and create deep crevices [27]. In case growth on ITO, molecules diffuse to lower layer due to the *energetically favorable position*, resulting in layer-by-layer with island growth at elevated substrate temperature (170°C). It is possible that at high substrate temperature, the molecules are diffused along the local

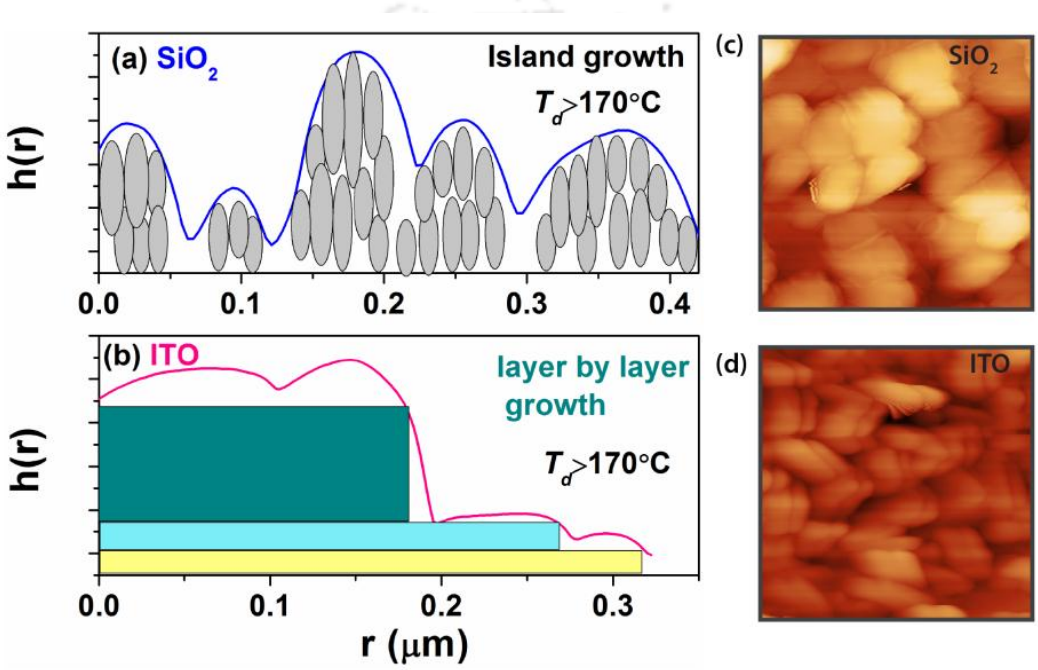

Figure 4.11: A schematic of the height profile with lateral length for VOPc films at substrate temperature more than 170°C: on (a) SiO_2 and (b) ITO glass. The corresponding AFM images are shown in (c) and (d), respectively.

surface and lateral by growth on the molecular terraces after searching for *most energetically stable position* [18]. The probability to fill the lower layer by VOPc molecules is much lower in case of ITO compared to that of the SiO_2 substrate. However, at low substrate temperature, similar type 3D island growth morphology occurs for both systems.

The calculated exponents (α, β, $1/z$) are quite close to the exponents predicted by the model of mound formation, which is reported for both organic and inorganic materials.

Although the asymptotic value of roughness exponent α=1 indicates mound formation, in practice, a

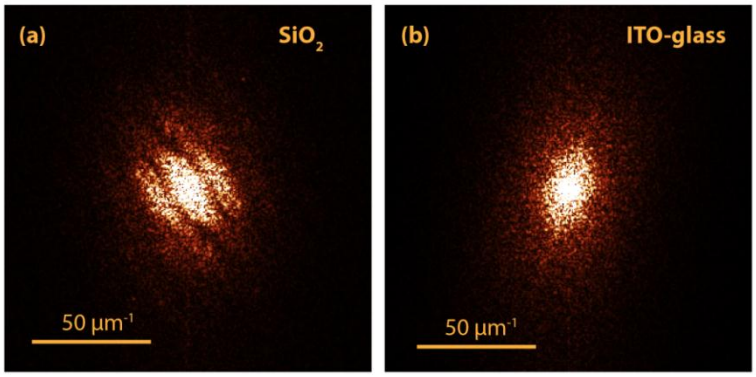

Figure 4.12: 2D FFT image of the AFM images of VOPc thin film of thickness ~5 nm on: **(a)** SiO_2/Si, and **(b)** ITO-glass substrate.

lower value can be obtained (in our case, α ~0.9 for ITO and α ~0.8 for SiO_2). Again roughness exponent β is not well-defined in case of 'mounds' formation as mounds are not stable in nature [18]. Their lateral and vertical size increases as the local slope increase, which is clearly shown in **Figs. 4.6** and **4.7**. For further confirmation about the argument on mound growth, we have plotted two dimensional fast Fourier transform (2D FFT) of the surfaces from the representative AFM images of ~5nm thick-film on SiO_2 and ITO-glass substrates, as shown in **Figs. 4.12(a)** and **4.12(b)**, which clearly shows a ring like behavior. It is one of the indications of *mound* growth morphology [19,38]. Further, the HHCF is oscillatory in nature ($r > \xi$) for mounded surfaces, which is noticeably visible at large r from **Figs. 4.6(a)** and **4.7(a)**. The formation of mound on surface can be attributed to different growth effects, such as step-edge barrier, diffusion effect, shadowing, and reemission, and it may be local or non-local in nature [22].

Further, it is found that the height distribution function $p(h)$ is positively skewed. The skewness S=3.15 for SiO_2 and S=1.65 for ITO-glass, substrate as shown in **Fig. 4.13(a)** and **4.13(b)**, where the *skewness S* ($= \frac{\langle [h-\langle h \rangle]^3 \rangle}{w^3}$) is compared with a Gaussian distribution (S=0). It clearly indicates the violation of the $h \rightarrow -h$ symmetry and thus the presence of a nonlinearity ($(\nabla h)^2$) associated with growth dependence on the local surface inclination.

However, the calculated exponents do not match with the reported Kardar-Parisi-Zhang (KPZ) growth model [18], as observed in other molecules [31,39]. Interestingly, the scaling exponents (*α, β,* and *1/z*) of organic VOPc thin films grown on SiO_2 and ITO substrates is not consistent with any of the known universality classes of self-affine surfaces described by the conserved growth equations for kinetic growth developed for inorganic materials. We believe that the morphology of VOPc thin film on SiO_2 and ITO glass is decided primarily by the surface diffusion and step-edge barrier effects. However, other parameters related to VOPc film growth can also play some role. Therefore, the mound formation model proposed is the most acceptable scenario in the present case [38].

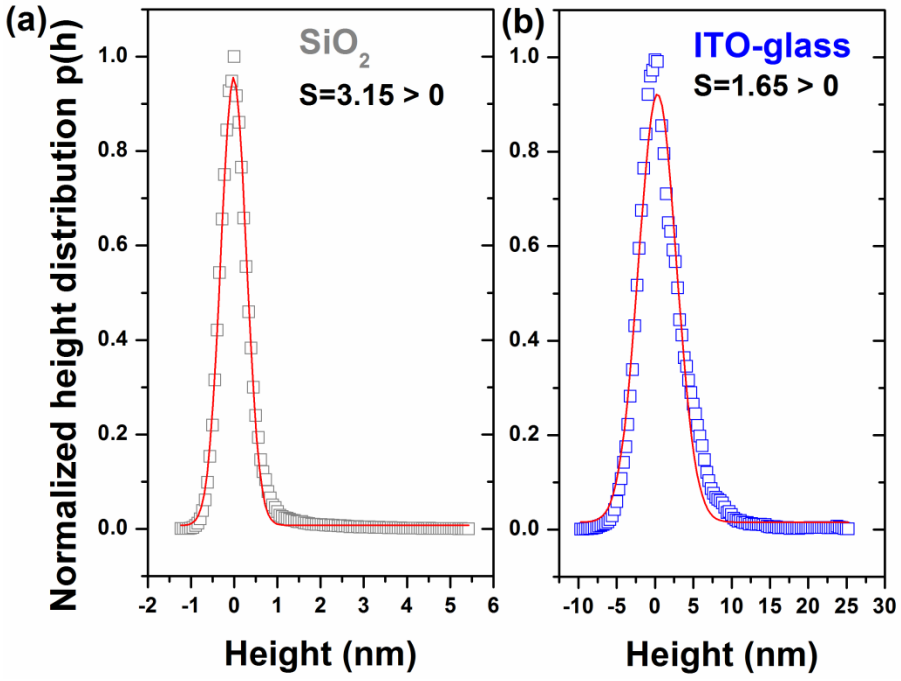

Figure 4.13: Height distribution function *p(h)* obtained from the AFM images of ~5 nm-thick film VOPc film on: (a) SiO_2 and (b) ITO- glass substrates. The solid line shows the Gaussian fitting. Skewness, *S* is positive for both Si substrate and glass substrate.

4.3.4 Structural Analysis

The structural quality of the VOPc films has been evaluated from the XRD measurements. Figures **4.14(a)** and **4.14(b)** show the XRD pattern of VOPc thin films grown on SiO_2 substrates, for different thickness as (5 to 120nm) and at different substrate temperature ($\boldsymbol{T_d}$= 25 to 210°C), respectively. VOPc film shows crystalline signature on both SiO_2 and ITO glass. The x-ray diffraction peaks arising at 2θ=7.5° is prominent for the film thickness above 12 nm and it is from the (010) plane correspond to inter planar spacing d_{hkl} =11.77 Å [40]. The film shows a broad peak centered at ~23° arising due to SiO_2 substrate (see **Fig. 4.14(a)**). The VOPc thin film deposited on SiO_2 substrate is identified as triclinic crystallites (phaseII, triclinic, spacegroup

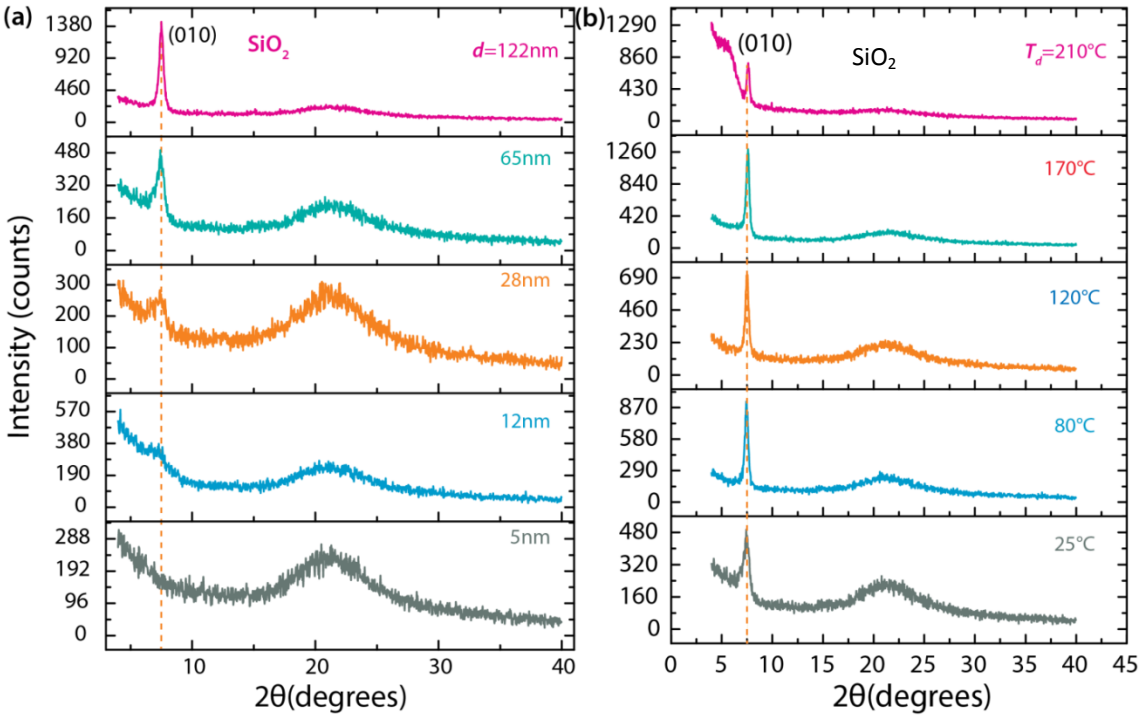

Figure 4.14: XRD pattern of VOPc thin-films grown on SiO_2/Si (100) substrate: **(a)** at different thickness ***d***, and **(b)** 65-nm thick films at different substrate temperature $\boldsymbol{T_d}$.

P$\bar{1}$, a =12.027 Å, b=12.571 Å, c=8.690 Å, α=96.04°, β=94.80°, and γ=68.20°) [41]. The deposition of VOPc films at elevated substrate temperature (>120°C) led to the change of morphology and size of crystallites, as shown in **Fig. 4.3** and **Fig. 4.5**. However, no

measurable shift in peak position is observed in the XRD pattern indicating no change in inter planar spacing in both cases (see Fig. **4.14(a)** and **4.14(b)**). The diffraction peak from (010) plane arises due to the 'edge-on' molecular orientation formed on the SiO_2 substrate, which implies that the intermolecular π-π stacking direction is parallel to the substrate and larger π–π stacking overlap results in high mobility of charge carriers [3,41,42]. In contrast, for VOPc films on ITO-glass for different film thickness $\boldsymbol{d}$= 5 to 122 nm and at different substrate temperature $\boldsymbol{T_d}$=25 to 210°C, XRD peak at 2θ=7.5° from (010) plane, corresponding to inter planar spacing d_{hkl} =11.77 Å is observed as shown in **Fig. 4.15(a)-(b)**.

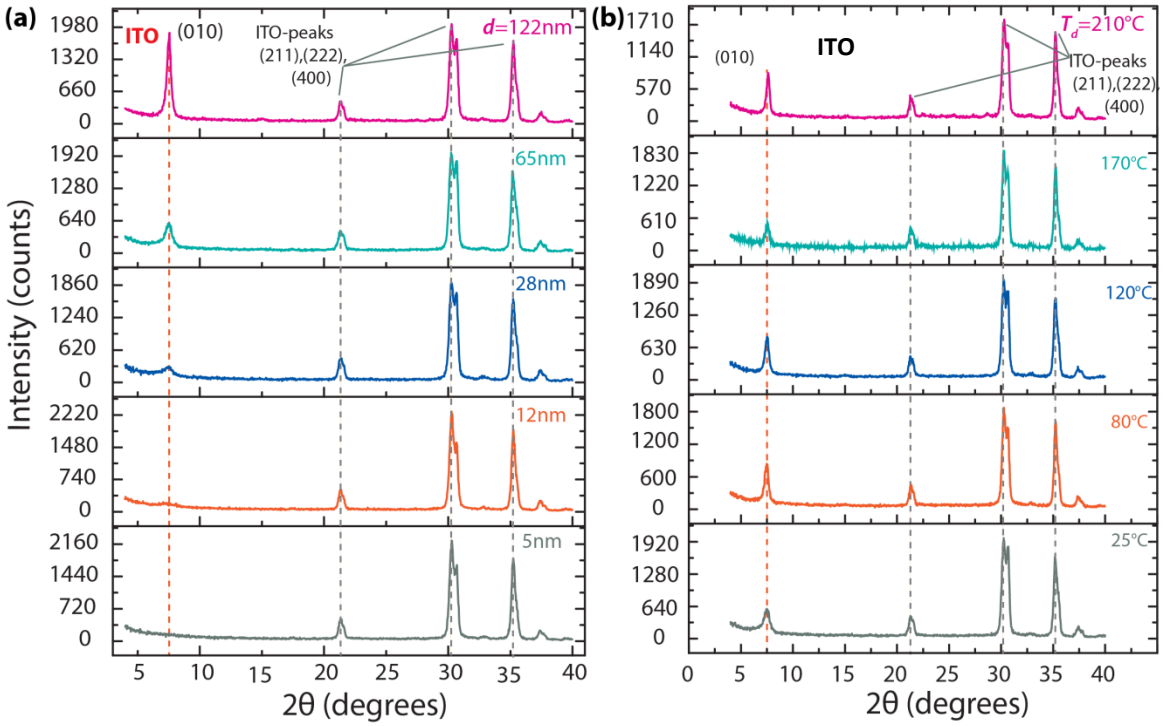

Figure 4.15: XRD patterns of VOPc thin-films grown on ITO-glass: **(a)** at different thickness $\boldsymbol{d}$, and **(b)** at different substrate temperature $\boldsymbol{T_d}$ (film thickness ~65 nm).

The (010) plane indicates 'edge-on' orientation similar to the SiO_2 case. So, the VOPc molecular orientation on ITO substrate also favored good charge carrier transport [13]. **Figure 4.16 (a)** and **4.16(b)** shows a schematic presentation of VOPc molecular packing on SiO_2 and ITO substrate. For both cases, the peak at 2θ=7.5° for more than 28-nm-thick film reveals the crystalline nature of the VOPc film. The diffraction peak intensity shows higher intensity when the substrate temperature is high due to improvement of molecular packing.

It is noticeable that several intense diffraction peaks appear in **Fig. 4.15(a)** and **4.15(b)** in the range of 2θ= 20-40° due to bare ITO glass. In the XRD pattern for VOPc thin film with the thickness of 65 nm, the intensity of the (010) peak position at 2θ=7.5° is significantly weaker at room temperature than that of VOPc thin film with equivalent thickness (see Fig. 5c) at higher substrate temperature (>170°C). At elevated substrate temperature, the molecules filled the voids and improve the crystallinity of molecular thin films during deposition resulting in the intense peak. It can be noted that beyond certain film thickness (~65 nm) and at elevated substrate temperature (~170°C), VOPc film show more crystalline signature on both

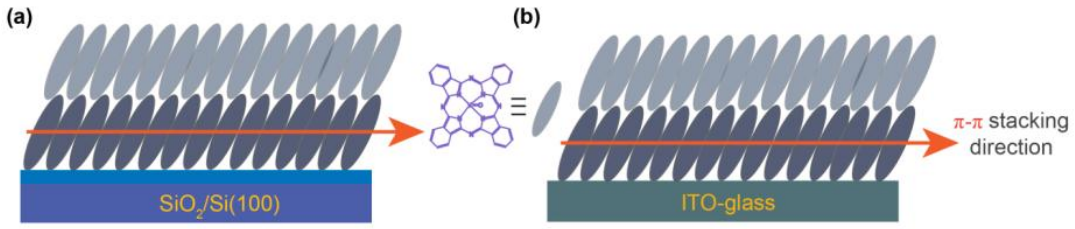

Figure 4.16: Schematic of the molecular packing of VOPc thin-film grown on two different substrates: (a)SiO_2/Si, and (b) ITO-glass substrate. The arrow shows the π-π stacking direction along (010) plane for both cases.

substrates SiO_2 and ITO glass, which are highly desirable for organic optoelectronic device fabrication. It is worth noting that titanyl phthalocyanine (TiOPc) based non-planar molecule give no predominant diffraction peak from any molecular plane as reported by Kim *et al.* [29]. In contrast VOPc film shows strong diffraction peaks (see **Fig. 4.15(a)-(b)**) with ordered arrangement on both SiO_2 and ITO substrates, although it is an intrinsically anisotropic-pyramidal (non-planar) structure, and it may prevent it from crystallizing on both ITO-glass as well as SiO_2 substrate. A more detailed study is needed in order to clarify this issue. In molecular crystalline thin films, molecules tend to stack in order to maximize their intermolecular interactions. The crystalline nature of VOPc thin films on both ITO and SiO_2 cannot be rationalized by only the step-edge barrier. Thus, the other factors related to substrate-induced growth kinetics can play a crucial role at molecule-substrate interface. In particular, small β value (0.17±0.06) reported are due to amorphous characteristics of thin

films for CuPc/PTCDA heterostructure [43]. In our case, this explanation is highly unlikely as VOPc film gives crystalline signature for both systems. It is worth noting that for organic molecular materials, there are several issues that may occur in growth behavior [15]: (i) organic molecules have internal degrees of freedom: vibrational, conformational, orientational; (ii) van der Waals force (vdW) dominated interaction between molecule-molecule (face to face stacking) and between molecule-substrate, and (iii) molecule size larger than the inorganic unit cell. So, it is likely that these issues might have some role on different growth modes, as observed for two different substrates: SiO_2 and ITO-glass.

4.4 Conclusions

In conclusion, we addressed the substrate dependent structural evolution of VOPc thin films on SiO_2 and ITO-glass substrates. The growth dynamics of VOPc thin films has been studied using AFM and HHCF analysis. Analyzing the scaling behavior and 2D fast Fourier transforms, it is concluded that the morphological evolution of the deposited VOPc molecules follows mound like formation, which suggests that the VOPc crystallites grow upward through the mound growth mechanism as the film thickness increases on ITO-glass as well as on SiO_2 substrates, which may be due to the high potential barrier or step-edge barrier. One of the important findings is that the β value for VOPc thin film on SiO_2 substrate is comparable to that predicted by the random deposition model, while for ITO substrate it is comparatively small and it signifies a small step-edge barrier. We have observed that the diffusion activation energy is almost equal for molecules grown on both substrates. VOPc film shows crystalline behavior on both SiO_2 and ITO-glass substrate, although they have significant differences in the β value. It is concluded that ITO glass is superiority for device fabrication over SiO_2 substrate for different applications.

References

[1] S. Fang, H. Hoshi, K. Kohama, Y. Maruyama, Nonlinear Optical Characteristics of Vanadyl Phthalocyanine Thin Film Grown by the Molecular Beam Epitaxial Method. *J. Phys. Chem.* **100**, 4104 (1996).

[2] A. Miller, E. Abrahams, Impurity Conduction at Low Concentrations. *Phys. Rev.* **120**, 745 (1960).

[3] S.M. Obaidulla, P.K. Giri, Low operating voltage and low bias stress in top-contact SnCl2Pc/CuPc heterostructure-based bilayer ambipolar organic field-effect transistors. *J. Mater. Chem. C* **3**, 7118 (2015).

[4] Y. Li, S. Chen, Q. Liu, Y. Li, Y. Shi, X. Wang, J. Ma, Z. Hu, Influence of Deposition Pressure on the Film Morphologies, Structures, and Mobilities for Different-Shaped Organic Semiconductors. *J. Phys. Chem. C* **118**, 14218 (2014).

[5] K. Vasseur, C. Rolin, S. Vandezande, K. Temst, L. Froyen, P. Heremans, A Growth and Morphology Study of Organic Vapor Phase Deposited Perylene Diimide Thin Films for Transistor Applications. *J. Phys. Chem. C* **114**, 2730 (2010).

[6] H.W. Donghang Yan, Baoxun Du, *Introduction to Organic Semiconductor Heterojunctions* (2010).

[7] W. Brütting, *Physics of Organic Semiconductors*, (2005).

[8] X.J. Yu, J.B. Xu, W.Y. Cheung, N. Ke, Optimizing the growth of vanadyl-phthalocyanine thin films for high-mobility organic thin-film transistors. *J. Appl. Phys.* **102**, 103711 (2007).

[9] L. Wang, G. Liu, F. Zhu, F. Pan, D. Yan, Electrical instability in vanadyl-phthalocyanine thin-film transistors. *Appl. Phys. Lett.* **93**, 173303 (2008).

[10] Y.-l. Pan, X.-d. Liao, Y.-j. Wu, L.-b. Chen, Z. You-yuan, Y.-h. Shen, F.-m. Li, S.-y. Shen, D.-y. Huang, Steady-state photovoltaic and electroreflective spectra in Al/vanadyl phthalocyanine (VOPc, in phase II)/indium–tin–oxide (ITO) sandwich cell. *Thin Solid Films* **324**, 209 (1998).

[11] C.H. Griffiths, M.S. Walker, P. Goldstein, Polymorphism in Vanadyl Phthalocyanine. *Molecular Crystals and Liquid Crystals* **33**, 149 (1976).

[12] T.V. Basova, V.G. Kiselev, I.S. Dubkov, F. Latteyer, S.A. Gromilov, H. Peisert, T. Chassè, Optical Spectroscopy and XRD Study of Molecular Orientation, Polymorphism, and Phase Transitions in Fluorinated Vanadyl Phthalocyanine Thin Films. *J. Phys. Chem. C* **117**, 7097 (2013).

[13] C. Nanjo, T. Fujimoto, M.M. Matsushita, K. Awaga, Ambipolar Transport in Phase-Separated Thin Films of p- and n-Type Vanadylporphyrazines with Two-Dimensional Percolation. *J. Phys. Chem. C* **118**, 14142 (2014).

[14] X. Zhang, E. Barrena, D. Goswami, D.G. de Oteyza, C. Weis, H. Dosch, Evidence for a Layer-Dependent Ehrlich-Schwobel Barrier in Organic Thin Film Growth. *Phys. Rev. Lett.* **103**, 136101 (2009).

[15] F. Schreiber, Organic molecular beam deposition: Growth studies beyond the first monolayer. *Phys. Status Solidi A* **201**, 1037 (2004).

[16] H. Ohta, T. Kambayashi, M. Hirano, H. Hoshi, K. Ishikawa, H. Takezoe, H. Hosono, Application of a Transparent Conductive Substrate with an Atomically Flat and Stepped Surface to Lateral Growth of an Organic Molecule: Vanadyl Phthalocyanine. *Adv. Mater.* **15**, 1258 (2003).

[17] F. Family, T. Vicsek, Dynamics of fractal surfaces (1991).
[18] A.-L. Barabasi, H.E. Stanley, Fractal concepts in surface growth, (1995).
[19] Y. Zhao, G.-C. Wang, a.T.-M. Lu, Characterization of Amorphous and Crystalline Rough Surface: Principles and Applications, ACADEMIC PRESS, (2001).
[20] G. Palasantzas, J. Krim, Scanning Tunneling Microscopy Study of the Thick Film Limit of Kinetic Roughening. *Phys. Rev. Lett.* **73**, 3564 (1994).
[21] A.C. Dürr, F. Schreiber, K.A. Ritley, V. Kruppa, J. Krug, H. Dosch, B. Struth, Rapid Roughening in Thin Film Growth of an Organic Semiconductor (Diindenoperylene). *Phys. Rev. Lett.* **90**, 016104 (2003).
[22] M. Pelliccione, T.-M. Lu, Evolution of Thin Film Morphology:Modeling and Simulations (2008).
[23] R. Chiarello, V. Panella, J. Krim, C. Thompson, X-ray reflectivity and adsorption isotherm study of fractal scaling in vapor-deposited films. *Phys. Rev. Lett.* **67**, 3408 (1991).
[24] M. Fendrich, J. Krug, Ehrlich-Schwoebel effect for organic molecules: Direct calculation of the step-edge barrier using empirical potentials. *Phys. Rev. B* **76**, 121302 (2007).
[25] J. Yang, S. Yim, T.S. Jones, Molecular-Orientation-Induced Rapid Roughening and Morphology Transition in Organic Semiconductor Thin-Film Growth. *Scientific Reports* **5**, 9441 (2015).
[26] S. Yim, T.S. Jones, Anomalous scaling behavior and surface roughening in molecular thin-film deposition. *Phys. Rev. B* **73**, 161305 (2006).
[27] S. Zorba, Y. Shapir, Y. Gao, Fractal-mound growth of pentacene thin films. *Phys. Rev. B* **74**, 245410 (2006).
[28] Y.P. Zhao, J.B. Fortin, G. Bonvallet, G.C. Wang, T.M. Lu, Kinetic Roughening in Polymer Film Growth by Vapor Deposition. *Phys. Rev. Lett.* **85**, 3229 (2000).
[29] J. Kim, N. Lim, C.R. Park, S. Yim, Growth dynamics of ZnPc and TiOPc thin films: Effect of crystallinity on anomalous scaling behavior. *Surface Science* **604**, 1143 (2010).
[30] J.L. Yang, S. Schumann, T.S. Jones, Morphology and Structure Transitions of Copper Hexadecafluorophthalocyanine (F16CuPc) Thin Films. *J. Phys. Chem. C* **114**, 1057 (2010).
[31] S.M. Obaidulla, P.K. Giri, Surface roughening and scaling behavior of vacuum-deposited SnCl2Pc organic thin films on different substrates. *Appl. Phys. Lett.* **107**, 221910 (2015).
[32] H. Peisert, T. Schwieger, J.M. Auerhammer, M. Knupfer, M.S. Golden, J. Fink, P.R. Bressler, M. Mast, Order on disorder: Copper phthalocyanine thin films on technical substrates. *J. Appl. Phys.* **90**, 466 (2001).
[33] M. Nakamura, Y. Morita, Y. Mori, A. Ishitani, H. Tokumoto, Molecular arrangement of copper phthalocyanine on hydrogen-terminated Si(111): Influence of surface roughness. *Journal of Vacuum Science & Technology B* **14**, 1109 (1996).
[34] S. Yim, K.i. Kim, T.S. Jones, Growth Morphology of Perylene-3,4,9,10-tetracarboxylic Dianhydride (PTCDA) Thin Films: Influence of Intermolecular Interactions and Step-Edge Barriers. *J. Phys. Chem. C* **111**, 10993 (2007).
[35] D. Tsamouras, G. Palasantzas, Temperature dependence of the growth front roughening of oligomer films. *Appl. Phys. Lett.* **80**, 4528 (2002).

[36] F. Biscarini, R. Zamboni, P. Samorí, P. Ostoja, C. Taliani, Growth of conjugated oligomer thin films studied by atomic-force microscopy. *Phys. Rev. B* **52**, 14868 (1995).

[37] R. Ruiz, D. Choudhary, B. Nickel, T. Toccoli, K.-C. Chang, A.C. Mayer, P. Clancy, J.M. Blakely, R.L. Headrick, S. Iannotta, G.G. Malliaras, Pentacene Thin Film Growth. *Chem. Mater.* **16**, 4497 (2004).

[38] Y. Zhang, E. Barrena, X. Zhang, A. Turak, F. Maye, H. Dosch, New Insight into the Role of the Interfacial Molecular Structure on Growth and Scaling in Organic Heterostructures. *J. Phys. Chem. C* **114**, 13752 (2010).

[39] D. Tsamouras, G. Palasantzas, J.T.M. De Hosson, Growth front roughening of room-temperature deposited oligomer films. *Appl. Phys. Lett.* **79**, 1801 (2001).

[40] H. Ohta, T. Kambayashi, K. Nomura, M. Hirano, K. Ishikawa, H. Takezoe, H. Hosono, Transparent Organic Thin-Film Transistor with a Laterally Grown Non-Planar Phthalocyanine Channel. *Adv. Mater.* **16**, 312 (2004).

[41] R.F. Ziolo, C.H. Griffiths, J.M. Troup, Crystal structure of vanadyl phthalocyanine, phase II. *J. Chem. Soc., Dalton Trans.*, 2300 (1980).

[42] L. Li, Q. Tang, H. Li, W. Hu, Molecular Orientation and Interface Compatibility for High Performance Organic Thin Film Transistor Based on Vanadyl Phthalocyanine. *J. Phys. Chem. B* **112**, 10405 (2008).

[43] D. Hong, Y.R. Do, H.T. Kwak, S. Yim, Structural templating and growth behavior of copper phthalocyanine thin films deposited on a polycrystalline perylenetetracarboxylic dianhydride layer. *J. Appl. Phys.* **109**, 063507 (2011).

This Page is Left Blank Intentionally

Chapter 5

Low Bias Stress and Reduced Operating Voltage in $SnCl_2Pc$ Based n-type Organic Field-Effect Transistors

In this chapter, we have studied vacuum deposited tin (IV) phthalocyanine dichloride ($SnCl_2Pc$) organic field-effect transistors fabricated on polymethylmethacrylate/ aluminum oxide (PMMA/Al_2O_3) bilayer gate dielectric, with reduced operating voltage and low contact resistance. We demonstrated the electrical performance and bias stress stability effect of Al and Ag top-contact as source and drain (*S/D*) electrodes. We show that the Ag-contact gives better performance of the OFET in all respect. We show that the devices with top contact Ag electrodes exhibit excellent n-channel behavior with electron mobility values of 0.01 cm^2/Vs, low threshold voltages ~4 V, current on/off ratio ~10^4 with an operating voltage of 10 V. We find that the amount of bias stress on $SnCl_2Pc$ based thin film transistor using PMMA gate dielectric is extremely small with high characteristic relaxation time >10^5 s obtained using stretched exponential model as compared to that of SiO_2 gate dielectric. Stressing the $SnCl_2Pc$ devices by applying 10 V to the gate for half an hour results in a decrease of the source drain current, I_{DS} of only ~ 10% under low vacuum. These devices show highly stable electrical behavior under multiple scans and low threshold voltage instability under electrical dc bias stress even after 40 days. We have investigated by different contact metals Ag, Al and the bias stress performance results show that the Al contact based OFET suffers significant bias stress instability as compared to that of the Ag-contact based OFET. The overall performances of the device with Ag contact shows superiority over the Al contact based devices.

5.1 Introduction

Over the last few years, high-quality, air stable, n-type transistors based on organic semiconductors has been demonstrated with performance close to that of the best p-type materials [1-4]. However, most research efforts have focused on the development of materials with high field-effect mobility and good environmental stability; as a result the mobility of n-channel organic field-effect transistors (OFETs) exceeds that of the amorphous silicon field-effect transistor (a-Si FETs). On the other hand, very limited studies have been performed on the bias-stress stability of n-channel organic field-effect transistor, though this is of paramount importance to realize the full commercial potential of OFETs. In such experiments, a defined constant bias voltage is applied to the gate, source, and drain electrodes for a prolonged period of time and the OFET performance usually degrades as a function of operating time. Such degradation commonly manifests itself as a shift of threshold voltage (ΔV_{Th}), an increase in sub threshold voltage, a reduction in mobility, an increase in off current and, or increase in hysteresis between subsequent measurements of the transfer characteristics with increase/ decrease of gate voltage etc. In some systems, the dominant signature of degradation observed is a shift of ΔV_{Th} when a prolonged gate bias-stress is in 'ON' and /or 'OFF' state. In general, for most of the systems this is caused by the trapping of charge carriers in localized states in the organic semiconductor, in the gate dielectric, or at the interface between the organic/dielectric interface [5-8]. There are two major approaches for suppressing the bias-stress effects: one is to reduce the trap sites in the semiconductor layer, such as by physically eliminating them with thermal annealing, and the other is to improve the semiconductor/dielectric interface, e.g., by reducing roughness at the interface, forming self-assembled monolayer modifications on the dielectric surfaces, or using hydroxyl-free or water-repellent amorphous fluoro-polymers as gate dielectric layer [9]. In a previous report, $SnCl_2Pc$ based transistors with high charge mobility and good dynamic response have been demonstrated and it was found to be comparable to a-Si FETs [10]. However, the bias stress stability on $SnCl_2Pc$ based n-type OFET has not been reported earlier.

In this chapter, we investigated the device performance and the electrical instability of $SnCl_2Pc/PMMA/Al_2O_3$ OFET's through the bias-stress process. We explore the bias stress effect in electron transporting $SnCl_2Pc$ thin film transistors fabricated with bilayer $PMMA/Al_2O_3$ as the gate dielectrics, which allows a low voltage operation. PMMA, a polymer dielectric was chosen since no chemical groups (-OH) are present at its surface that may act as electron traps, and previous work on pentacene and perylene derivative based OFETs has shown very small bias stress effect [3]. We observe that upon the application of a large gate voltage (up to 8V), the decrease in source drain current as a function of time, $I_{DS}(t)$, is very small in low vacuum even when the measurements were performed after one month. Fitting the data using a commonly used stretched exponential dependence enables the extraction of the characteristic time scale in seconds, which we find to exceed 10^5 s, remarkably almost of the orders of magnitude reported in pentacene based p-type devices [11]. We demonstrated that the $SnCl_2Pc$ based FETs on $PMMA/Al_2O_3$ reported here have significantly improved bias-stress characteristics as compared to other organic transistors investigated in the past.

The degradation of the performance of OFET during operation is reflected by changes of its current-voltage characteristics that result from changes of mobility (μ_{FE}), of threshold voltage (V_{Th}), or variations of the capacitance density (C_{in}) of the gate dielectric. The dynamics of the physical and/or chemical mechanisms producing these changes, intrinsic or extrinsic, affect the performance of a FET on different time scales. The stability of a FET is determined by the total effects produced by several physical and/or chemical processes, but in general, one tends to dominate over the others. This has caused current approaches to improve the stability to focus on mitigating individual processes.

5.2 Experiment Details

To form the control gate, a 150 nm thick layer of aluminum (Al) (Alfa Aesar, 99.9% pure) layer was vacuum deposited at a rate 30 $Å s^{-1}$ on to clean glass substrates. The Al layer is anodized by immersing in citric acid solution prepared with ultra-pure (18.2 MΩ.cm) de-ionized water as a solvent, $1mML^{-1}$. A constant current density of 0.3 mA/cm^2 is maintained

until the voltage reaches 10 V, and the voltage is then maintained at 10 V until the current density drops to 0.015 mA/cm^2. The thickness of the Al_2O_3 is estimated to be ~13 nm, given the anodization ratio ($c_{Al} \approx 1.3$ nm/V) [12,13].

The electrical characteristics including the voltage–current relationship and capacitance are measured with a semiconductor parameter analyzer (Keithley 4200-SCS) at room temperature in a probe station under low vacuum. The morphological analysis is carried out with an atomic force microscopy (AFM, Agilent-5500) in the tapping mode. PMMA can provide a high-quality hydroxyl free (-OH) interface to the organic semiconductor with high dielectric breakdown strength (~1 MV/cm) and it decrease the roughness as well as surface energy and thus it improves the flow of charges with reduced trap states. The thin buffer layer, PMMA (Sigma Aldrich, M_W = 550 000 kg/mol, 25 mg/ml in anisole) was used to deposit a very thin and uniform layer on Al_2O_3 surface at 5000 rpm for 60 s and annealed at 80°C for 30 minutes in reduced vacuum. The thickness of PMMA layer was 100 nm, as measured by surface profilometer (Veeco Dektak-150). The root-mean-square (RMS) roughness (σ_{rms}) of PMMA is less than 1 nm, the anodized Al_2O_3 layer (~6 nm) even lower than SiO_2 (~0.22nm) as measured by AFM (see **Fig 5.1**).

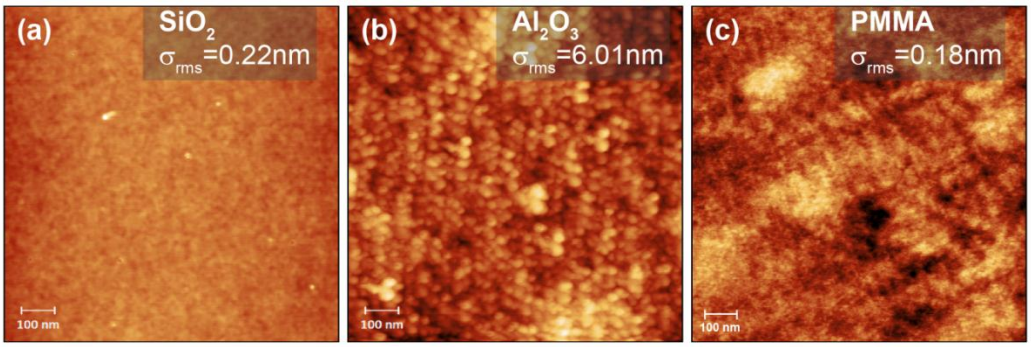

Figure 5.1: AFM topography images of different dielectric thin films: (a) SiO_2, (b) Al_2O_3, and (c) PMMA.

Root-mean-square surface roughness of various dielectric substrates is summarized in **Table 5.1**.

Table 5.1: Root-mean-square (RMS) roughness of different dielectric surface

Dielectric surface	SiO_2	Al_2O_3	PMMA
RMS roughness(σ_{rms})	0.22 nm	6.01 nm	0.18 nm

A 60-nm-thick $SnCl_2Pc$ (Alfa Aesar) film was deposited on PMMA/Al_2O_3 dielectrics and on SiO_2 under identical conditions at a rate 0.8 Å/s and at constant pressure 3×10^{-6} mbars, to act as the n-type active layer. The substrate were kept at various temperature 25 (RT), 60, 100 and 140 °C for PMMA/Al_2O_3 and 60 °C for SiO_2 substrate while the remaining deposition parameters were kept constant. The surface morphology of the organic thin films was characterized in air by AFM in the tapping mode is shown in **Fig. 5.2(a)** and **5.2(b)-(f)** on SiO_2 at substrate temperature 60°C and on PMMA at different substrate temperatures from 25-140°C, respectively.

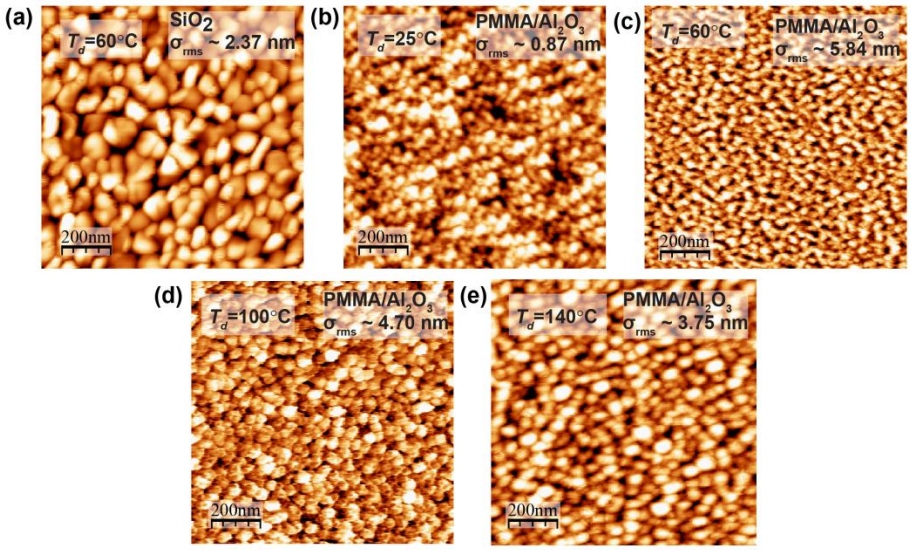

Figure 5.2: AFM topography images (scan size: 1 μm ×1 μm) of 60 nm thick $SnCl_2Pc$ thin films deposited on: **(a)** SiO_2 at substrate temperature (T_d) 60 °C and (b)-(e) on PMMA at different substrate temperature (T_d) 25, 60, 100 and 140 °C, respectively. The rms roughness, σ_{rms} is indicated in each case.

Finally, in thermal deposition vacuum chamber, a >50 nm silver (Ag) (Alfa Aesar, 99.9%) top electrode source/ drain (*S/D*) was deposited and patterned through a shadow mask on

both type of substrates, where the device channel length (L) and channel width (W) are defined as 30 μm and 780 μm, respectively, as shown in **Fig. 5.3(a)**. Ideally, the work function of the source/drain electrodes should match the lowest unoccupied molecular orbital LUMO level of an electron transporting in organic semiconductor to provide a low injection barrier for electrons [14]. Thus, a high work function of 4.26 eV Ag was chosen for *S/D* electrodes to facilitate electron injection into the lowest unoccupied molecular orbital (LUMO) (4.0 eV) level of $SnCl_2Pc$, since the barrier (φ_B) is nearly 0.26 eV between the $SnCl_2Pc$ LUMO level and the Ag Fermi level (E_F) according to the Mott- Shottky model, as shown in **Fig. 5.3(b)**. In this case, a lower barrier height of 0.26 eV is present for electron

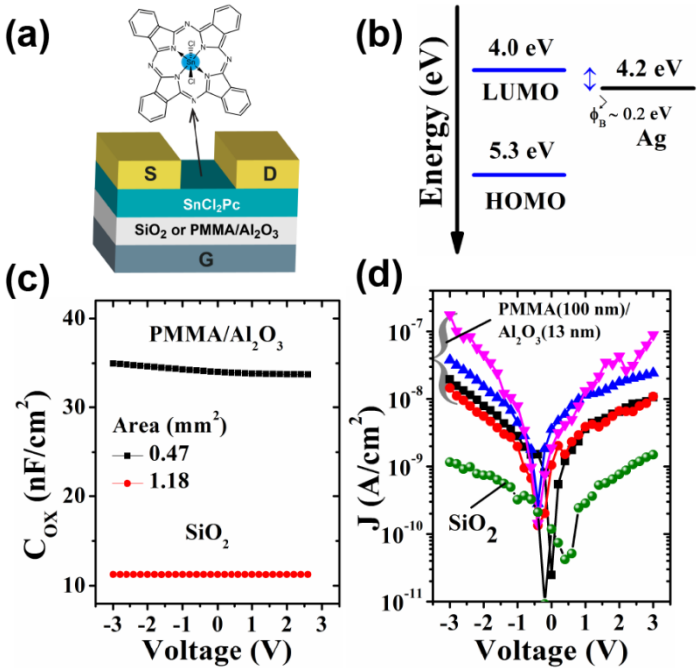

Figure 5.3: (a) A schematic diagram of the device cross-sectional of a top contact OFET along with the molecular structure of $SnCl_2Pc$. **(b)** Simplified energy level diagram of $SnCl_2Pc$ OFET (no bias applied), Shottky-contact formed with barrier height φ_B ~0.2 eV. **(c)** Capacitance of SiO_2 (300 nm) and PMMA (100 nm)/Al_2O_3 (13 nm) gate insulators as a function of voltage at 100 kHz. **(d)** Leakage current density, J (A/cm^2) vs. bias voltage (V) characteristics of MIM structure (Al/Al_2O_3 (13 nm)/PMMA (100 nm)/Ag (50 nm)) and SiO_2 (300 nm).

injection due to the higher work function of 4.26 eV of Ag. To compare electric instabilities, we fabricated $SnCl_2Pc$ top-contact OFET's on heavily n-doped Si substrates with a 300 nm

SiO_2 layer (C_{ox} = 11.2 nF/cm^2). The capacitance density C_{ox} (nF/cm^2) was measured from a metal-insulator-metal structure of parallel plate capacitors with 11 contact areas. The buffer layer PMMA on Al_2O_3 reduced the C_{ox} from 681 to 31 nF/cm^2 and while to 11.2 nF/cm^2 for SiO_2 (300 nm) measured with 4 contact areas (see **Fig. 5.3(c)**. The leakage current density, J (A/cm^2) through the gate dielectrics was negligible (below 10^{-7} A/cm^2) under an applied field ~ 1 MV/cm, as shown in **Fig. 5.3(d)**.

5.3 Results and Discussion

5.3.1 Electrical Characterization and Device Performance

The electrical characterization including the bias stress measurement was carried out at room temperature in dark conditions under a vacuum probe station (Lake Shore, <10^{-2} mbars) and with a semiconductor characterization (Keithley 4200-SCS) system. Output I_{DS} versus V_{DS} and transfer I_{DS} versus V_{GS} characteristics were measured for devices with channel length 30 μm. Field-effect mobility (μ_{FE}) values and threshold voltages (V_{Th}) were measured in the saturation regime from the highest slope of $|I_{DS}|^{1/2}$ versus V_{GS} plot using the saturation current equation,

$$I_{DS} = \frac{W}{2L}\mu_{FE}C_{in}\left(V_{GS} - V_{Th}\right)^2, \tag{5.1}$$

where C_{in} is the capacitance per unit area of the gate dielectrics (F/cm^2), W is the width and L is the length of the semiconductor channel defined by the source and drain electrodes of the transistor. We also investigate the stability of these devices under multiple transfer characteristics scans and under continuous electrical bias stress. Note that most of the fabrication steps have been performed under ambient conditions, while the characterizations were performed under vacuum condition. All the transistors, for which data are reported here, underwent the same fabrication process, measurement, and analysis steps.

Table 5.2: Summary of the electrical parameters and stretched exponential decay parameters for $SnCl_2Pc$ transistors fabricated on PMMA/Al_2O_3 at different temperatures and on SiO_2 at 60 °C. (Symbols are defined in the text.)

Dielectric	*Contact*	T_d [a] *(°C)*	μ *(cm^2/Vs)*	V_{Th} *(V)*	I_{on}/I_{off}	β	τ *(s)*
PMMA/Al_2O_3	Ag	25	0.0067	4.7	10^4	0.56	1.1×10^4
PMMA/Al_2O_3	Ag	60	0.0099	4	10^3	0.32	3.2×10^5
PMMA/Al_2O_3	Ag	100	0.0104	5	10^2	0.36	1.0×10^5
PMMA/Al_2O_3	Ag	140	0.0068	3.8	10^3	0.37	4.3×10^4
SiO_2(bare)	Ag	60	0.0010	20	10^3	0.46	2.6×10^2

[a] T_d is the substrate temperature

Devices with W = 780 μm and channel lengths L = 30 μm having electrode of Ag on a single substrate were characterized to obtain the μ_{FE}, V_{Th} and current on/off ratio (I_{on}/I_{off}). **Table 5.2** summarizes the performance parameters for all of the devices with μ_{FE} and V_{Th} averaged over several devices and I_{on}/I_{off} reported for one representative device. We fabricated $SnCl_2Pc$ based OFET's at different substrate temperatures ranging from 25 °C (RT) to 140 °C on PMMA/Al_2O_3 and at 60 °C on SiO_2 substrate. **Figure 5.4(a, c, e),** and **Fig. 5.5(a)** shows the typical output characteristics and **Fig. 5.4** (**b**, **d**, **f**) and **Fig. 5.5(b)** shows the transfer characteristics of the OFETs prepared on PMMA/Al_2O_3 at different substrate temperature (T_d) ranging from 25-140°C. **Figure 5.5(c)** and **Fig. 5.5(d)** show the output and transfer characteristics on SiO_2 at substrate temperature of 60 °C. The devices on SiO_2 with W/L = 780 μm/30 μm (6 devices) exhibited an average electron mobility of ~ 0.001 cm^2/V s with current on-off ratio ~ 10^3 and low threshold voltage ~ 20V. **Figures 5.4(c)** and **5.4(d)** show the performance of devices on PMMA/Al_2O_3 with substrate temperatures 60 °C (5 devices) and it exhibited an average electron mobility of ~ 0.01 cm^2/Vs. Note that our devices have shorter channel lengths W/L =

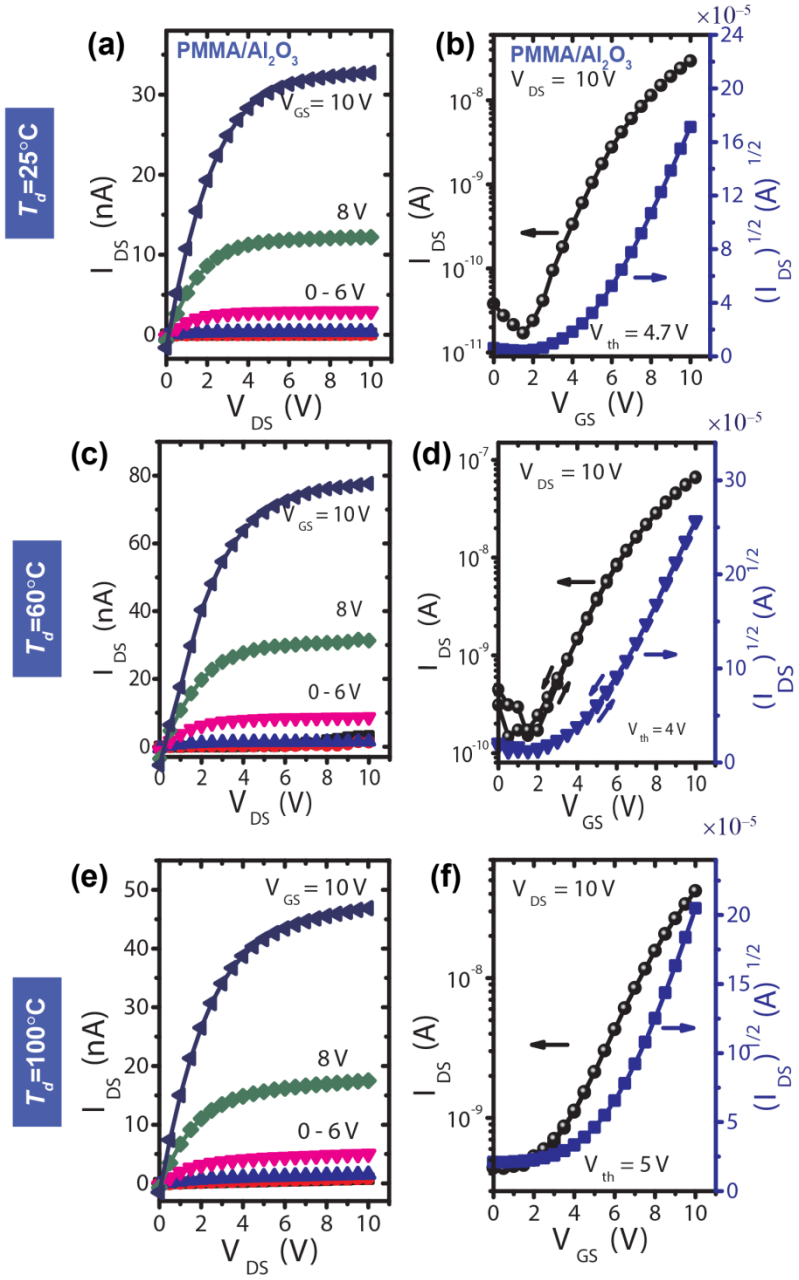

Figure 5.4: Output (I_{DS} vs. V_{DS}) [**a, c, e**] and transfer curves (I_{DS} vs.V_{GS}) [**b, d, f**] at constant V_{DS} of $SnCl_2Pc$ OFETs using $PMMA/Al_2O_3$ bilayer dielectrics layer at different substrate temperature 25, 60, and 100°C, as indicated in the left .

780 μm/30 μm, though the parameters obtained here with SiO_2 are similar to the reported values [15]. In $PMMA/Al_2O_3$ device, we obtained a low operating voltage (V_{op}) of 10V and low threshold voltage (V_{Th}) of 4V, compared to the high V_{op}=40V and V_{Th} =20V. It is

noticeable that the reported V_{Th} was ~ 27V (with V_{op}=100V) for SiO_2, which is ~7 times higher for the PMMA/Al_2O_3 fabricated devices reported here.

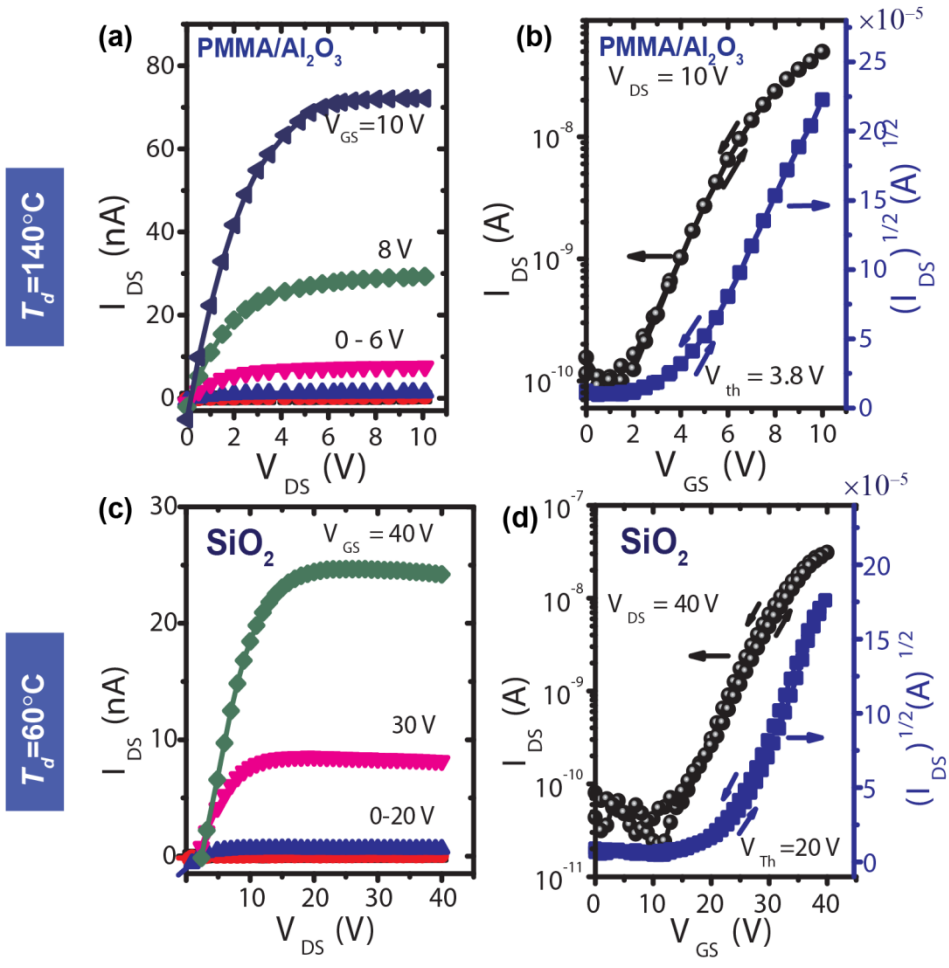

Figure 5.5: (Output (I_{DS} vs. V_{DS}), and transfer curves (I_{DS} vs.V_{GS}) at constant V_{DS} of $SnCl_2Pc$ OFET using (a, b) PMMA/Al_2O_3 bilayer dielectrics (c, d) SiO_2 layer, deposited at substrate temperature (T_d's) 140 and 60°C, respectively, as indicated in the left .

All the devices showed excellent n-channel behavior having no hysteresis in the transfer characteristics. In addition, the absence of contact effect reveals a low interface trap density. With PMMA/Al_2O_3 device, the output characteristics, i.e., I_{DS} vs. V_{DS} at constant V_{GS} show no hysteresis, good Ohmic contact (drain current increases linearly with initial bias voltage) and saturation behavior at a bias voltage of 10V, while hysteresis is noticeable in transfer

curves of SiO_2 devices. Such improved characteristics in PMMA/Al_2O_3 device is primarily due to low trap density at the $SnCl_2Pc$/PMMA interface. Trap density N_t ($C_i \Delta V_{Th}/q$, ΔV_{Th} = shift of threshold voltage, C_i is capacitance per unit area) is estimated to be 4.0×10^{11} cm^{-2} at the $SnCl_2Pc$/PMMA interface, compared to the value of 5.34×10^{11} cm^{-2} calculated at the interface $SnCl_2Pc/SiO_2$ interface (as estimated from **Figs. 5.4(d)** and **5.5(d)**).

The operational stability is of critical importance for circuit design and overall device lifetime. The mechanism of degradation under continuous operation is related to the dynamics of dipolar groups and charge trapping/de-trapping events at all of the critical interfaces in an OFET and in the bulk of the semiconductor and gate dielectric. One of the ways the operation stability can be evaluated is by applying a constant direct current (dc) bias stress. **Figure 5.6** shows the time-dependent decay of I_{DS} under a dc bias stress with V_{GS} = V_{DS} = 10 V over 30 min for all four types of devices with PMMA/Al_2O_3 and V_{GS} = V_{DS} = 30 V over 30 min for SiO_2. The current decay in this experiment exhibited typical features of bias stress instability showing an exponential decay behavior with only 15%-20% decay in case of PMMA/Al_2O_3 and in contrast more than 80% steep decay in case of SiO_2 after 30 min, where the degradation rate slows down with stressing time.

5.3.2 Bias Stress Stability

The bias stress instability can be modeled by a stretched exponential function fitted to either the threshold voltage shift V_{Th} or the drain-source channel current decay. A stretched-exponential decay is given by [16]

$$\Delta V_{Th}(t) = V_0 \left\{ 1 - \exp\left[-\left(\frac{t}{\tau} \right)^{\beta} \right] \right\} \tag{5.2}$$

Where, $V_0 = V_{GS} - V_{Th,0.}$ with $V_{Th,0}$ is the initial threshold voltage at time t = 0 s. The dispersion parameter β is the trap distribution parameters, and the constant τ represents the characteristic relaxation time of the carriers. If the term V_{GS} is replaced with V_{Th} in the

Equation (5.2), it is more appropriate for OFETs stressed for a very long time; however, for a shorter stressing time of 1h, both versions of this equation with V_{GS} or V_{Th} seem equally appropriate to use. This model can be extended to fit the decay of I_{DS} over time under a dc bias stress. Using the decay of I_{DS} instead of the threshold voltage shift to estimate stability can avoid the error and inaccuracy caused by the measurement and extraction of threshold voltage. In order to quantitatively compare the bias stress in our $SnCl_2Pc$ based transistors in vacuum, based on **Eq. (5.2)** for the saturation current $I_{DS}(t)$ curves recorded during 30 min operation were fitted with a stretched exponential model [17]

$$I_{DS}(t) = I_0 \exp\left[-\left(\frac{t}{\tau}\right)^{\beta}\right] \tag{5.3}$$

This model is extensively used to quantify the bias stress effect in both organic and inorganic transistors, where τ is a characteristic time associated with the rate of charge trapping/relaxation and dispersion parameter β ($0 < \beta \leq 1$) is the stretched exponential factor involving the width of the trap distribution/ the barrier energy height for charge trapping below the conduction edge (as $SnCl_2Pc$ is n-type), and I_0 is the initial drain current measured at the beginning of stressing. A stretching parameter close to 1 indicates a *narrow distribution* of time constants (the limit β = 1 being the exponential function with a single time constant), while a smaller stretching parameter *(β < 1)* implies a *broader distribution* of time constants. The bias stress in our experiment was applied in the saturation regime (V_{GS} = V_{DS}) and μ_{FE} was constant during bias stress. Under these conditions, the I_{DS} decay was fitted with **Eq. (5.3)** (solid line) for all the devices. **Figure 5.6** shows the decay characteristics for devices made at four different substrate temperatures (T_d). The fitted data using τ and β as the fitting parameters are shown with solid lines and the extracted parameters are listed in **Table 5.2**. These allow us to compare our results with those reported by others using bias stress experiment. The dispersion parameter β, reflecting the width of the involved trap distribution (at room temperature in this case) was 0.56, 0.32, 0.36 and 0.37 for the devices made on Al_2O_3/PMMA at 25, 60, 100 and 140 °C respectively, while β =0.46 on SiO_2 deposited at 60 °C. After applying V_{GS} = 10 V and V_{DS} = 10 V for 30 min, I_{DS} decreased only by 10% for the best device made at a substrate temperature 60 °C and the value of τ for PMMA was found to

be 3 orders of magnitude higher than that of SiO_2 case, which signifies the small magnitude of bias stress in our devices. For comparison purpose, similar low β values are found for OFET's with solution-processed P3HT OFET's (~β= 0.47) [18], vacuum evaporated TIPS pentacene on various dielectrics (~β =0.37) [7] at room temperature.

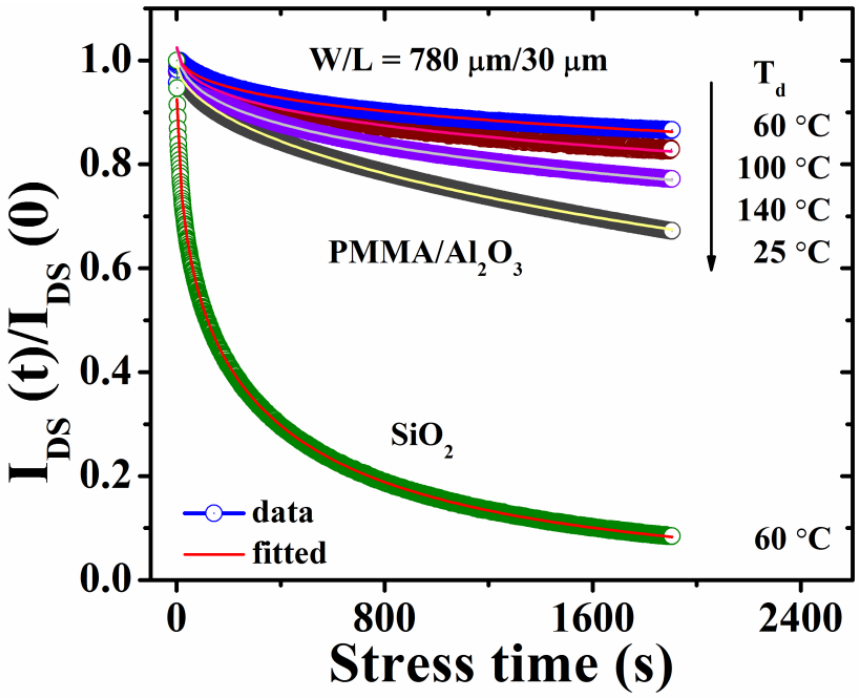

Figure 5.6: Time dependence of the normalized drain current, $I_{DS}(t)/I_{DS}(0)$ of $SnCl_2Pc$ thin film transistors that are gated with PMMA(100 nm) / Al_2O_3 (13 nm) at different substrate temperatures (T_d's) and with SiO_2 (300 nm) at 60 °C. Symbol is for experimental data and the solid line is the corresponding fit in each case using **Eq. (5.3).**

The extracted characteristics time, τ values for PMMA/Al_2O_3 based devices were in between 10^4 and 10^5 (1.1×10^4, 1.0×10^4 and 4.3×10^4 s for substrate temperatures of 25, 60, 100 and 140 °C, respectively) and 2.6×10^2 s for bare SiO_2. The highest value of $\tau = 3.2 \times 10^5$ s for $SnCl_2Pc$ OFET in this work, is two orders of magnitude higher than the value reported in vapor-deposited PDI-8 and one order higher than that reported in PDI-8CN_2 [19]. Interestingly, our τ value is quite comparable to 8-3NTCDI based n-type organic transistors in 'ON' state reported by Jung *et al* [20]. It is also comparable with that of the vacuum deposited pentacene [21] and TIPS-Pentacene based p-type single crystal field-effect organic transistor

reported by Lee *et al* [7]. It is significant that such a high τ value of 10^5 s is achieved in $SnCl_2Pc$ OFET with PMMA/Al_2O_3 bilayer gate dielectrics, as n-type devices traditionally suffer from the trapping effects due to the presence of hydroxyl (-OH) groups, oxygen and water and as a result a low τ value is observed. **Fig. 5.7** displays the range of time constants τ reported for different organic semiconductor based devices in. It is evident that τ value found in this work is quite comparable with other well-known semiconductors reported in the literature [22].

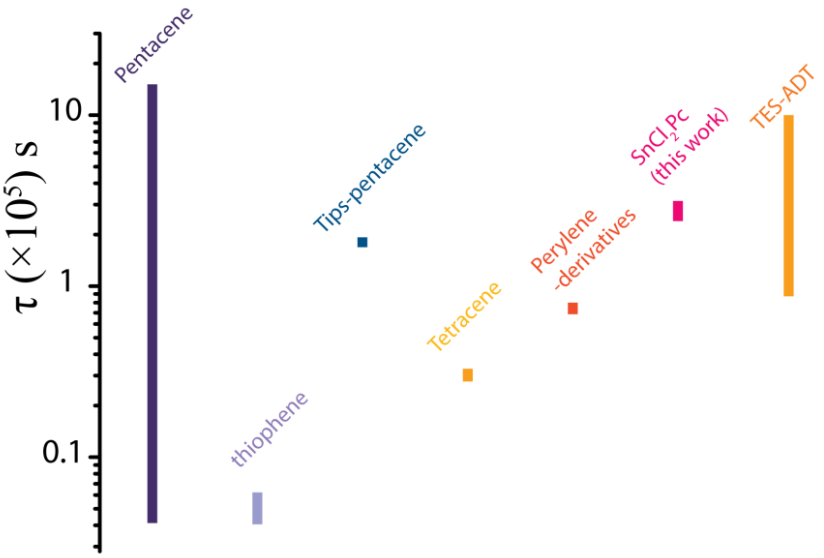

Figure 5.7: Comparison of relaxation time constant (τ) of different well known small molecules with that of our $SnCl_2Pc$ molecule [22]. This data may vary due to implementation of different dielectric interface, contact electrodes and environment condition.

We believe that the PMMA, a hydroxyl (-OH)-free polymer used with $SnCl_2Pc$ as gate dielectrics significantly improve the device stability. It is believed that the low interface trap density (4.0×10^{11} cm^{-2}) at the $SnCl_2Pc$/PMMA is primarily responsible for the improved device characteristics with low bias stress effect. Despite the fact that fabrication was not carried out in clean room environment and without a globe box, the observed characteristics show sufficient robustness of the adopted approach and this is important for commercial applications. Our interpretations are consistent with the report by Chua *et al*. that hydroxyl silanol (Si-OH) group can lead to the electrochemical trapping of electrons that results in

shift of threshold voltage when the transistor is under continuous bias [22]. Mathijssen *et al*. proposed that charge trapping in stressed devices does not occur in the semiconductor, but in gate dielectric [23]. Choi *et al.* suggested that the performance of OFET's degrades over time because of trap formation in the polymer gate-dielectrics under continuous bias stress [11]. However, PMMA is free of aromatic ring, which may induce slow charge trapping from semiconductor to the dielectric during bias stress; such a possibility is unlikely, since we observed very small degradation of the device performance over prolonged biasing [3].

5.3.3 Long-term Stability

To study the long term stability of devices upon exposure to ambient, we had taken the best performing devices with T_d= 60 °C; stress was measured as function of time at room temperature (25 °C). As a typical example, linear transfer curves are presented in **Fig. 5.8(a)** as a function of bias-stress time. The applied gate bias during stress was 10 V for PMMA/Al_2O_3 and 30 V for bare SiO_2. The transfer curves were measured by sweeping the gate bias after measuring every 3 min bias stress up to 2h shown in the inset of **Fig. 5.8(a)**. Arrow indicates that the transfer curves shift with stress time in the direction of applied bias to the right. It shows that there is hardly a small shift of threshold voltage (ΔV_{Th}) ~ 0.3 V for PMMA/Al_2O_3 based devices, while the shift is more than 4 V for SiO_2 based device measured under similar conditions up to 40 days (**Figures 5.8(b)** and **Fig. 5.8(c)**). These results show that these OFET's have relatively high operational and electrical bias stability compared to the device made on SiO_2, which is very important for the reliable operation of organic devices and circuits.

te of Technolo

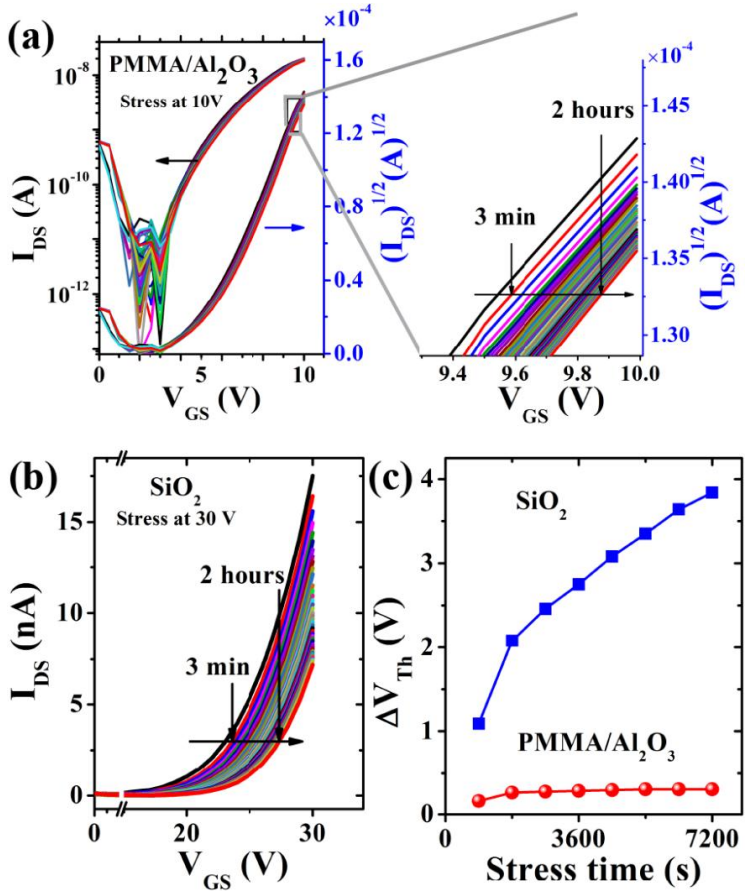

Figure 5.8: **(a)** and **(b)** Transfer curves of $SnCl_2Pc$ transistors as a function of stress time on PMMA/Al_2O_3 and SiO_2 dielectrics, respectively. The gate bias during the bias stress was V_{DS} = 10 V for PMMA/Al_2O_3 and while it was V_{DS} = 30 V for SiO_2; zoomed view of transfer curves for PMMA/Al_2O_3 measured at room temperature after 40 days at an interval of 3 min up to 2 hours is shown in the right panel. **(c)** Corresponding comparison of the threshold voltage shift (ΔV_{Th}) as a function of stress time.

5.4 Effect of Contact Metals in $SnCl_2Pc$ based OFETs

We have approached a long-time bias stress stability of $SnCl_2Pc$-based n-type organic field-effect transistors (OFETs), in bottom gate, top contacts configuration, with aluminum (Al), silver (Ag) source–drain (*S/D*) contacts. The results clearly shows that the bias stress effects in $SnCl_2Pc$-based n-type OFETs is similar to p-type OFETs and it can be reduced by choosing an appropriate metal for the source–drain contacts. During the bias stress time, the

threshold voltage shift and an increase in the contacts resistance have also been measured. On the basis of the stability of the device parameters, we show that the Ag source–drain contact-based devices give better stability as compared to the devices with Al source–drain contacts. It is shown that the bias stress-induced threshold voltage shift is due to the trapping of charges in the channel region and in the vicinity of the source–drain contacts.

OFETs are promising for numerous potential applications but suffer from poor charge injection, such that their performance is severely limited. Recent efforts in lowering contact resistance have led to significantly improved field-effect mobility of OFETs, many times higher, as a results of careful choice of contact materials and/or chemical treatment of contact electrodes. Here we investigated the innovative developments of contact engineering and focus on the mechanism behind the improved performance. Further improvement towards *Ohmic contact* can be expected along with the rapid advances in material research, which will also benefit other organic and electronic devices. The interface between the source and drain contact and organic semiconductor requires low contact resistance, which is a function of both parasitic resistance and the energy barrier at the contact/semiconductor interface. In practice, the actual resistance is rather high. Low energy barrier necessitate matching the electrode work function (Φ_M) with the semiconductor ionization potential (IPs).

5.4.1 Material Processing and Device Fabrication

The vacuum-deposited $SnCl_2Pc$ based OFET (W=780 μm, L=30 μm) was fabricated using PMMA/Al_2O_3 gate dielectrics. A schematic of cross section of device structure with $SnCl_2Pc$ molecule is shown in **Fig. 5.9(a)**. **Figure 5.9(b)** shows the energy schematic at the metal contact/semiconductor interface, where the work function of Ag (~4.26 eV) and Al (~4.28 eV) closely match with the LUMO level (~4.0 eV) of $SnCl_2Pc$. From this stand point, we have chosen Al and Ag as contact electrodes for efficient electron injection [24]. A hydroxyl (-OH) free PMMA dielectric material was spin coated on Al_2O_3, after the coated Al_2O_3 was prepared with standard anodization process. The PMMA-buffer layer yields low-leakage

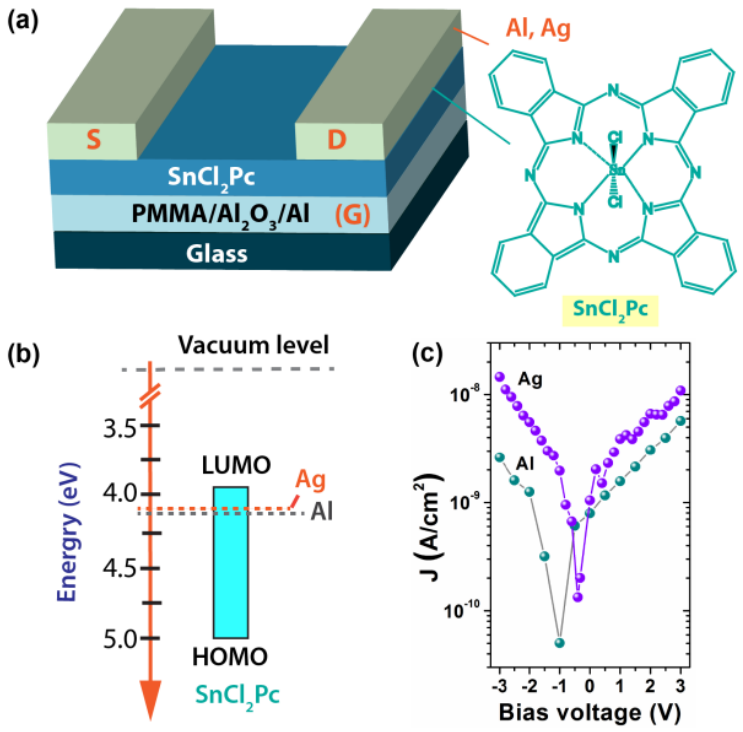

Figure 5.9: **(a)** Schematic diagram of a top-contact OFET along with the molecular structure of $SnCl_2Pc$. **(b)** Simplified energy band diagram of $SnCl_2Pc$ OFET (no bias applied), Shottky-contact formed with barrier height φ_B ~0.2-0.4 eV. Energy level diagram of metal contacts Ag, Al with $SnCl_2Pc$ molecule, and **(c)** leakage current density for Ag and Al contacts.

current density (~10^{-9} A/cm^2) [see **Fig. 5.9(c)**]. Al or Ag as a contact metal was finally deposited to complete the fabrication after $SnCl_2Pc$ (~60 nm) deposition.

Note that all the processes related to device fabrication were performed under identical conditions. The electrical characterization including the bias stress measurements were carried out at room temperature in dark at low vacuum (10^{-2} mbars) in a probe station.

5.4.2 Device Performance: Electrical Characterization

Figure 5.10(a) and **5.10(b)** shows the typical output characteristics of OFETs prepared using Al and Ag contact based top contact OFET with common PMMA/Al_2O_3 gate dielectric. It has reported that bottom gate-top contact based devices results the contact resistance is approximately one order of magnitude higher than the contact resistance of transistors with top contacts, so the top contact devices gives the better performances compared to that

bottom contact [25]. $SnCl_2Pc$ based OFET exhibited n-type characteristics with Al and Ag contact electrodes. The transfer characteristic (I_{DS} vs. V_{GS}) of devices operated in electron enhancement mode are shown in **Fig. 5.10 (c)** and **5.10(d)**. The field-effect mobilities (μ) and threshold voltages V_{Th} were calculated in the saturation regime defined by standard metal-oxide semiconductor field-effect transistor models by fitting the $\sqrt{I_{DS}}$ vs. V_{GS} data to the square law from **Eq. (5.1)**. We extracted on/off current ratio $I_{on/off}$ from the transfer characteristics from **Figs. 5.10 (c)** and **5.10(d)**. In both operational modes, the highest electron currents are larger in Ag contact based OFETs as compared to that of Al contact devices. The field-effect electron mobility is 0.004 cm^2/Vs for Al-contact and 0.01 cm^2 /Vs for Ag-contact based OFET, respectively.

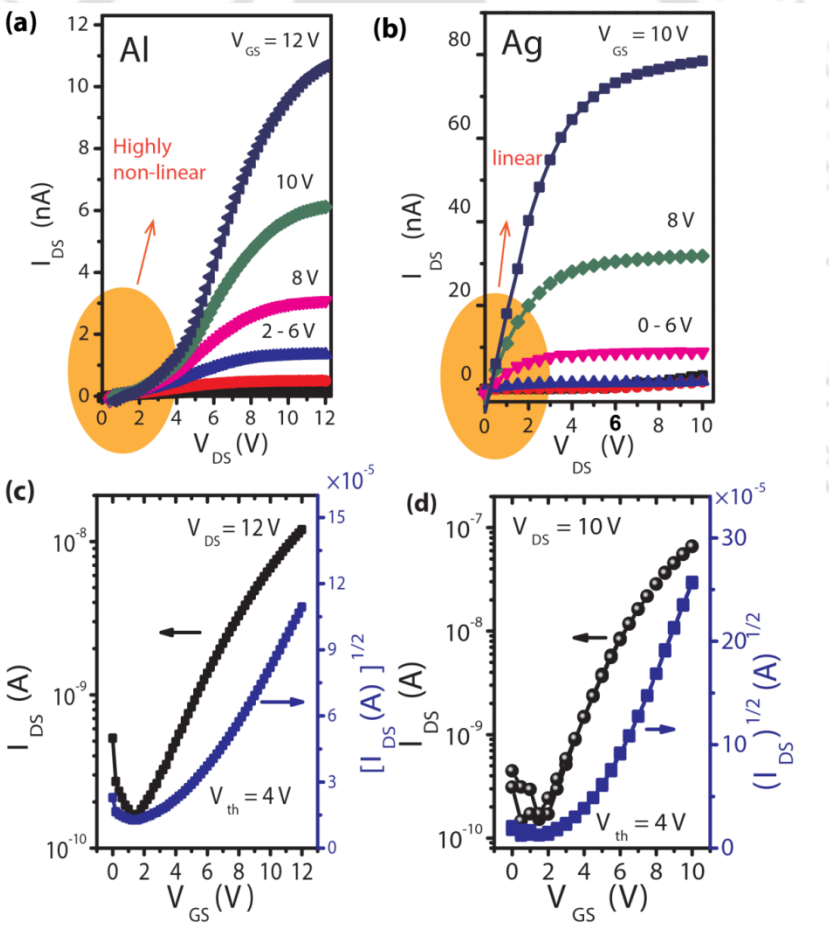

Figure 5.10: Output (I_{DS} vs. V_{DS}) and transfer characteristics (I_{DS} vs. V_{GS}) with Al contact [**(a)** and **(c)**], and Ag contact [**(b)** and **(d)**]. Arrows in output curves indicate the *non-linear/non-Ohmic* or *linear/Ohmic* region for Al and Ag contact, respectively.

Table 5.3 summarizes the performance parameters for μ and V_{Th} of devices reported for one representative device. At very low drain-source voltage (up to 5 V), the output curves clearly show *non Ohmic* behavior (curves are highly nonlinear) for Al-contact, while it is *Ohmic* in nature for Ag contact, though their work function (~4.3 eV) closely match with the LUMO level (4.2 eV) of $SnCl_2Pc$. It has been reported that their energy level alignment can be changes due to a number of physical and chemical processes: (a) charge transfer across the interface, (b) image potential induced polarization of the organic material, (c) pushing back of the electron cloud tail out of the metal surface by the organic material, (d) chemical reactions, (e) formation of interface state, and (f) alignment of the permanent dipole of the organic material [26,27]. The effects are schematically shown in **Fig. 5.6**.

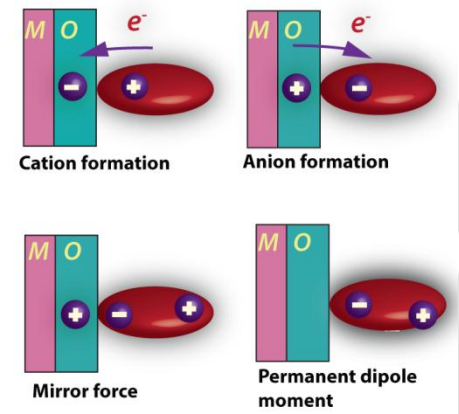

Figure 5.11: Possible factors behind forming and affecting the interfacial dipole layer: (a) Charge transfer across the interface, (b) Concentration of electrons in the adsorbate leading to positive charging of the vacuum side, (c) Existence of interface state serving as a buffer of charge carriers, and (f) Orientation of polar molecules or functional groups.

Here, one of the plausible explanation for the *Ohmic contact* is that it can carry current with a relatively negligible voltage drop at the metal-semiconductor (Ag-$SnCl_2Pc$) interface, since the interface is more conductive than the bulk, while the current due to charge carrier may be trapped or leaked at Al-$SnCl_2Pc$ interface and thus giving rise to a *non Ohmic* contact. It has been proposed that Ag is the noble metal and deposited metal atoms penetrate through large molecule layer without reacting and the penetration depth is approximately 8 nm. Further the band bending takes place due to charge transfer occurring from Ag to the $SnCl_2Pc$ layer, as it

was evidenced by other tetrafluorophthalocyanine ($CuPcF_4$) molecule [28]. So, the noble metal Ag form a unreacted interface and it show the *Ohmic* behavior while Al make a reactive interface with $SnCl_2Pc$ results highly *non-Ohmic* behavior.

Table 5.3: Summary of the electrical parameters and the stretched-exponential decay parameters for $SnCl_2Pc$ OFETs.

Contact	Dielectric	Channel	μ ($cm^2V^{-1}s^{-1}$)	V_{th} (V)	β	τ (s)
Ag	PMMA/Al_2O_3	$SnCl_2Pc$	0.01	4	0.46	1.2×10^5
Al	PMMA/Al_2O_3	$SnCl_2Pc$	4×10^{-3}	3.8	0.39	3.5×10^3

5.4.3 Contact Metal Dependent Bias Stress Stability

In order to quantitatively compare the bias stress stability in our $SnCl_2Pc$ based transistors with different electrode Ag and Al under continuous dc voltage biases of V_{GS}= V_{DS}=8 V in low vacuum, $I_{DS}(t)$ curves recorded during 30 min operation are shown in **Fig. 5.10**. The normalized drain currents are fitted with the stretched exponential **Eq. (5.3)**.

The $SnCl_2Pc$ OFETs with Ag contact show negligible degradation with 10% decrease in I_{DS}, while, device with Al contact show a steep decay with a 60% decrease in I_{DS}, after bias stressing. The stretched exponential fitting **Eq. (5.3**) empirically gives characteristics time constant τ= 10^5 s and β= 0.46 for devices with Ag contact, while τ=10^3 s and β= 0.39 for devices with Al contact, respectively. The bias-stress fitting parameters for each case is summarized in the **Table 5.3**. The values of τ is very large for devices with Ag conact, which is a result of the very small magnitude of bias stress in our devices. On the other hand, devices with Al contact yield very high amount of bias stress during operation. It is commonly believed that charge carrier trapping in OFETs is caused by the trap states at the semiconductor dielectric interface, or/and in bulk semiconductor or in the gate dielectric [9]. In our experiments, charge trapping due to PMMA/Al_2O_3 gate dielectric should be same for

both the devices, as the channel $SnCl_2Pc$, and gate dielectric layers–during processing and deposition conditions were same. However, for the Al and Ag devices with the same $SnCl_2Pc$ thickness, a large difference in the bias stress effect was observed, as shown in **Fig. 5.12**. Primarily, the very low bias stress in the devices with Ag contact can be noticeable due

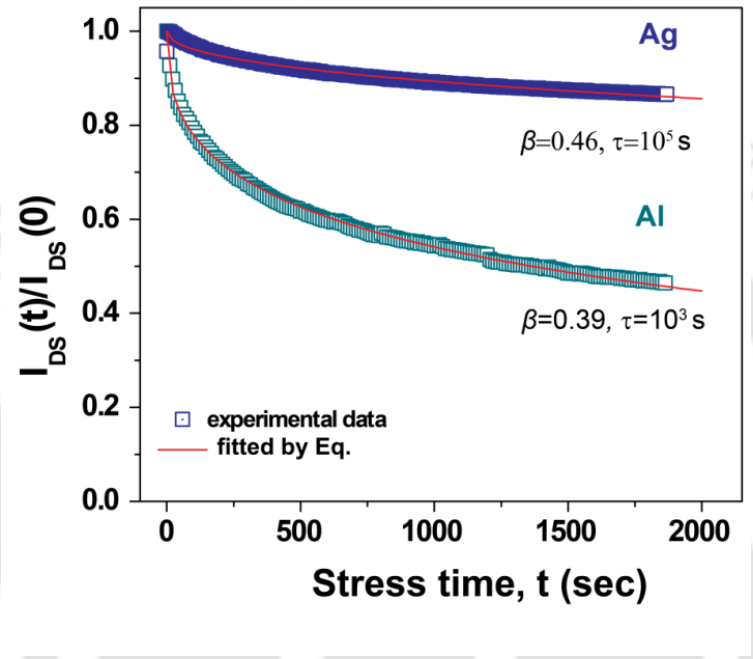

Figure 5.12: Time dependence of the normalized drain current, $I_{DS}(t)/I_{DS}(0)$ of $SnCl_2Pc$ thin film transistors. Symbol is for the experimental data and the solid line is the corresponding best fit to the stretched exponential model in each case.

to deep trap creates at the grain boundary. Again π-group free PMMA dielectric OFETs with high operational stability can be achieved for both cases [3]. These facts indicate that the trap states at the semiconductor/dielectric interface in the channel region are not the only factor that causes carrier trapping rather in the contact region also [29]. So, the effects of the contact should also be considered and it has significant role on device stability. It has been reported that the time-dependent charge trapping into the deep trap states in both the contact and channel regions is responsible for the bias stress effect in organic field-effect transistors [30]. However, the microscopic mechanism of the gate bias stress effect in organic semiconductors

based OFET has not been conclusively determined, but interfacial incident can be summarized in the following way:

(i) When the metal is deposited on an organic layer by evaporation, the high reactivity of the vaporized hot metal atom often leads to a chemical reaction at the interface. Also it is known that metal atoms may diffuse into the organic layer. In such cases, the interface cannot be regarded as a simple contact between the metal and the organic layer. This is important since the metal-on-organic system is used in the actual devices. Sometimes, it should be considered as a third layer which is resulting from reaction and/or diffusion [26].

This explanation is further confirmed by Hiroyuki Yoshida group that the redox reaction occurs between the *n*-type semiconductor and the Al metal contact [31]. The electron transfer reaction is driven by the oxidation of a reactive metal, like Al [32].

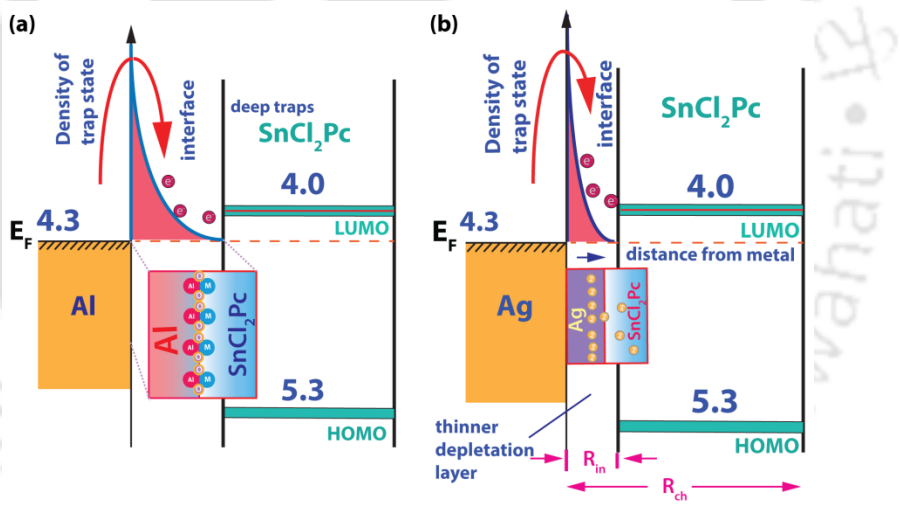

Figure 5.13: Schematic representations of metal-organic interface: **(a)** Al-$SnCl_2Pc$ and **(b)** Ag-$SnCl_2Pc$

(iii) It has been reported that Al atom will bond directly to oxygen atoms with organic molecules and results a strong Al-O interaction. The relatively poor performance of Al for electron injection into organic semiconductor is probably due to the formation of this reacted layer (leads to high injection barrier, see **Fig. 5.13(a)** and **5.3(b)**) in the device fabrication [31]. Because of the large size of the organic molecule, 0.2–0.4 nm of deposited Al could

produce a reacted layer of more than 10 nm and significantly modify the charge injection properties of the interface.

It should be noted that the bias stress effects are also caused by extrinsic factors, such as oxidation, presence of moisture, or chemical impurities, or whether the intrinsic structural and energetic disorder of the organic semiconductor and/or specific structural defects are responsible for charge trapping cannot be ruled out here as they are classified by Sirringhaus, although the experiment are carried out in low vacuum condition [5].

5.5 Conclusions

In conclusion, the electrical performances and operation stability of vacuum-deposited $SnCl_2Pc$ thin film based n-channel organic field-effect transistors was studied in top contact bottom gate configuration using Ag source/drain electrodes and PMMA/Al_2O_3 as a bilayer gate dielectric layer. The devices of $SnCl_2Pc$ and Ag *S/D* metal electrodes exhibited excellent n-channel behavior with average field-effect electron mobility of 0.01 cm^2/Vs and low threshold voltage 4 V (for $L = 30\ \mu m$ and $W = 780\ \mu m$). These OFET's showed current on-off ratio ~10^4 and high operational stability of electrical behavior with no hysteresis when tested under low vacuum condition. On the other hand, multiple transfer characteristics scans and bias stress indicates that these OFET's exhibit extremely low threshold voltage instability when tested in low vacuum and long term operation stability even after a month. This extremely small bias stress effect results in very long characteristics time constant ~10^5 s which is 3 orders of magnitude higher than the commonly used SiO_2 based devices and dispersion parameter, β ~0.32 in low vacuum is significant, since n-type organic devices are considered to be more sensitive to trapping and ambient oxidants than the p-type counterparts [33-35]. So, it is remarkable that not only the mobility but also the threshold voltage is very stable in low vacuum in n-channel OFETs using PMMA/Al_2O_3 as a gate dielectric and Ag contact electrode. We have investigated the effect of contact electrodes on the electrical performances of $SnCl_2Pc$ based n-channel organic field-effect transistors. The bias stress

performance results on the Al contact based OFET suffers significant bias stress instability as compared to that of the Ag-contact based OFET. Hence, we can conclude that the overall performances of the device with Ag contact is superior to that of the Al contact based devices. We believe that detailed analysis of charge-trapping mechanism can reveal the origin of bias stress instability and that will reduce bias instability, and this work allow practical applications namely OFETs based flexible flat panel displays for better performance.

References

[1] R. Schmidt, J.H. Oh, Y.S. Sun, M. Deppisch, A.M. Krause, K. Radacki, H. Braunschweig, M. Konemann, P. Erk, Z.A. Bao, F. Wurthner, High-Performance Air-Stable n-Channel Organic Thin Film Transistors Based on Halogenated Perylene Bisimide Semiconductors. *J. Am. Chem. Soc* **131**, 6215 (2009).

[2] B.A. Jones, M.J. Ahrens, M.H. Yoon, A. Facchetti, T.J. Marks, M.R. Wasielewski, High-mobility air-stable n-type semiconductors with processing versatility: Dicyanoperylene-3,4 : 9,10-bis(dicarboximides). *Angew. Chem. Int. Ed.* **43**, 6363 (2004).

[3] X.J. She, J. Liu, J.Y. Zhang, X. Gao, S.D. Wang, Operational stability enhancement of low-voltage organic field-effect transistors based on bilayer polymer dielectrics. *Appl. Phys. Lett.* **103** (2013).

[4] M.P. Walser, W.L. Kalb, T. Mathis, B. Batlogg, Low-voltage organic transistors and inverters with ultrathin fluoropolymer gate dielectric. *Appl. Phys. Lett.* **95** (2009).

[5] H. Sirringhaus, Reliability of Organic Field-Effect Transistors. *Adv. Mater.* **21**, 3859 (2009).

[6] P.A. Bobbert, A. Sharma, S.G.J. Mathijssen, M. Kemerink, D.M. de Leeuw, Operational Stability of Organic Field-Effect Transistors. *Adv. Mater.* **24**, 1146 (2012).

[7] B. Lee, A. Wan, D. Mastrogiovanni, J.E. Anthony, E. Garfunkel, V. Podzorov, Origin of the bias stress instability in single-crystal organic field-effect transistors. *Phys. Rev. B* **82** (2010).

[8] X.H. Zhang, B. Kippelen, High-performance C-60 n-channel organic field-effect transistors through optimization of interfaces. *J. Appl. Phys.* **104**, 104504 (2008).

[9] D.K. Hwang, C. Fuentes-Hernandez, J. Kim, W.J. Potscavage, S.-J. Kim, B. Kippelen, Top-Gate Organic Field-Effect Transistors with High Environmental and Operational Stability. *Adv. Mater.* **23**, 1293 (2011).

[10] D. Song, H. Wang, F. Zhu, J. Yang, H. Tian, Y. Geng, D. Yan, Phthalocyanato Tin(IV) Dichloride: An Air-Stable, High-Performance, n-Type Organic Semiconductor with a High Field-Effect Electron Mobility. *Adv. Mater.* **20**, 2142 (2008).

[11] H.H. Choi, W.H. Lee, K. Cho, Bias-Stress-Induced Charge Trapping at Polymer Chain Ends of Polymer Gate-Dielectrics in Organic Transistors. *Adv. Funct. Mater.* **22**, 4833 (2012).

[12] M. Kaltenbrunner, P. Stadler, R. Schwödiauer, A.W. Hassel, N.S. Sariciftci, S. Bauer, Anodized Aluminum Oxide Thin Films for Room-Temperature-Processed, Flexible, Low-Voltage Organic Non-Volatile Memory Elements with Excellent Charge Retention. *Adv. Mater.* **23**, 4892 (2011).

[13] L.A. Majewski, R. Schroeder, M. Grell, Flexible high capacitance gate insulators for organic field effect transistors. *J. Phys. D: Appl. Phys.* **37**, 21 (2004).

[14] S.P. Tiwari, X.H. Zhang, W.J. Potscavage, B. Kippelen, Study of electrical performance and stability of solution-processed n-channel organic field-effect transistors. *J. Appl. Phys.* **106** (2009).

[15] D. Song, H.B. Wang, F. Zhu, J.L. Yang, H.K. Tian, Y.H. Geng, D.H. Yan, Phthalocyanato tin(IV) dichloride: An air-stable, high-performance, n-type organic semiconductor with a high field-effect electron mobility. *Adv. Mater.* **20**, 2142 (2008).

[16] F.R. Libsch, J. Kanicki, Bias-stress-induced stretched-exponential time dependence of charge injection and trapping in amorphous thin-film transistors. *Appl. Phys. Lett.* **62**, 1286 (1993).

[17] M.H. Zhang, S.P. Tiwari, B. Kippelen, Pentacene organic field-effect transistors with polymeric dielectric interfaces: Performance and stability. *Org Electron* **10**, 1133 (2009).

[18] H.H. Choi, M.S. Kang, M. Kim, H. Kim, J.H. Cho, K. Cho, Decoupling the Bias-Stress-Induced Charge Trapping in Semiconductors and Gate-Dielectrics of Organic Transistors Using a Double Stretched-Exponential Formula. *Advanced Functional Materials* **23**, 690 (2013).

[19] M. Barra, F.V. Di Girolamo, F. Chiarella, M. Salluzzo, Z. Chen, A. Facchetti, L. Anderson, A. Cassinese, Transport Property and Charge Trap Comparison for N-Channel Perylene Diimide Transistors with Different Air-Stability. *J. Phys. Chem. C* **114**, 20387 (2010).

[20] B.J. Jung, K. Lee, J. Sun, A.G. Andreou, H.E. Katz, Air-Operable, High-Mobility Organic Transistors with Semifluorinated Side Chains and Unsubstituted Naphthalenetetracarboxylic Diimide Cores: High Mobility and Environmental and Bias Stress Stability from the Perfluorooctylpropyl Side Chain. *Adv. Funct. Mater.* **20**, 2930 (2010).

[21] T. Miyadera, S.D. Wang, T. Minari, K. Tsukagoshi, Y. Aoyagi, Charge trapping induced current instability in pentacene thin film transistors: Trapping barrier and effect of surface treatment. *Appl. Phys. Lett.* **93** (2008).

[22] L.L. Chua, J. Zaumseil, J.F. Chang, E.C.W. Ou, P.K.H. Ho, H. Sirringhaus, R.H. Friend, General observation of n-type field-effect behaviour in organic semiconductors. *Nature* **434**, 194 (2005).

[23] S.G.J. Mathijssen, M.J. Spijkman, A.M. Andringa, P.A. van Hal, I. McCulloch, M. Kemerink, R.A.J. Janssen, D.M. de Leeuw, Revealing Buried Interfaces to Understand the Origins of Threshold Voltage Shifts in Organic Field-Effect Transistors. *Adv. Mater.* **22**, 5105 (2010).

[24] H.B. Michaelson, The work function of the elements and its periodicity. *J. Appl. Phys.* **48**, 4729 (1977).

[25] M. Marinkovic, D. Belaineh, V. Wagner, D. Knipp, On the Origin of Contact Resistances of Organic Thin Film Transistors. *Adv. Mater.* **24**, 4005 (2012).

[26] H. Ishii, K. Sugiyama, E. Ito, K. Seki, Energy Level Alignment and Interfacial Electronic Structures at Organic/Metal and Organic/Organic Interfaces. *Adv. Mater.* **11**, 605 (1999).

[27] Y. Gao, Surface analytical studies of interfaces in organic semiconductor devices. *Materials Science and Engineering: R: Reports* **68**, 39 (2010).

[28] T. Schwieger, H. Peisert, M. Knupfer, Direct observation of interfacial charge transfer from silver to organic semiconductors. *Chem. Phys. Lett.* **384**, 197 (2004).

[29] Y. Liang, H.-C. Chang, P. Paul Ruden, C. Daniel Frisbie, Examination of Au, Cu, and Al contacts in organic field-effect transistors via displacement current measurements. *Journal of Applied Physics* **110**, 064514 (2011).

[30] S.D. Wang, T. Minari, T. Miyadera, Y. Aoyagi, K. Tsukagoshi, Bias stress instability in pentacene thin film transistors: Contact resistance change and channel threshold voltage shift. *Appl. Phys. Lett.* **92**, 063305 (2008).

[31] H. Yoshida, N. Sato, Aluminum diffusion and reaction in thin films of perylene-3,4,9,10-tetracarboxylic dianhydride: Depth profiles and time-dependent diffusion coefficients. *Appl. Phys. Lett.* **91**, 141915 (2007).

[32] S. Schols, L. Van Willigenburg, R. Müller, D. Bode, M. Debucquoy, S. De Jonge, J. Genoe, P. Heremans, S. Lu, A. Facchetti, Influence of the contact metal on the performance of n-type carbonyl-functionalized quaterthiophene organic thin-film transistors. *Appl. Phys. Lett.* **93**, 263303 (2008).

[33] B.A. Jones, A. Facchetti, M.R. Wasielewski, T.J. Marks, Tuning orbital energetics in arylene diimide semiconductors. Materials design for ambient stability of n-type charge transport. *J. Am. Chem. Soc* **129**, 15259 (2007).

[34] D.M. de Leeuw, M.M.J. Simenon, A.R. Brown, R.E.F. Einerhand, Stability of n-type doped conducting polymers and consequences for polymeric microelectronic devices. *Synthetic Metals* **87**, 53 (1997).

[35] R.J. Chesterfield, J.C. McKeen, C.R. Newman, C.D. Frisbie, P.C. Ewbank, K.R. Mann, L.L. Miller, Variable temperature film and contact resistance measurements on operating n-channel organic thin film transistors. *J. Appl. Phys.* **95**, 6396 (2004).

Chapter 6

High Bias Stress Stability and Low Threshold Voltage Shift in VOPc Based p-channel Organic Field-Effect Transistors Operated Under Ambient Condition

In this chapter, we have studied the vacuum deposited vanadium (IV) oxide phthalocyanine (VOPc) field-effect transistors, which were fabricated on bare SiO_2 and hexamethyledisilazane (HMDS) monolayer passivated SiO_2 layer. The devices with top contact *Au* metal electrodes exhibit excellent p-channel behavior with high hole mobility of ~0.01 cm^2/Vs for HMDS-treated device, as compared to the extremely low mobility of ~0.00023 cm^2/Vs for bare SiO_2 case. We performed bias stress stability studies on both systems under ambient condition, since it is of utmost importantance for real life application of the devices. We demonstrate that the time dependent on-current decay, and threshold voltage shift can be effectively controlled by using self-assembled mono layers of HMDS. Bias stress stability study shows stretchehed expoential decay during long term operation with constant bias voltage under ambient conditions with resulting decay of drain current by <15% for the HMDS-treated case, while it shows a very sharp decay of >70% for the devices with bare SiO_2 layer. The corresponding characteric decay time constant is ~10000 s for HMDS treated case, while that of the bare SiO_2 case is only 480 s. The poor performance of the device with bare SiO_2 layer may be due to the charge trapping at the voids in the inter-grain region of the films, while it is almost negligible for HMDS-treated case, as confirmed from AFM and XRD analyses. Thus, the HMDS treatment provides a very viable approach for attaining the long term stability and low threshold voltage shift for the VOPc based OFET devices.

6.1 Introduction

Organic field-effect transistors (OFETs) are the fundamental building blocks of integrated circuits; they allow the fabrication of complex and useful integrated devices such as active matrix displays [1,2], chemical or biological sensors [3,4], and radio-frequency identification (RFID) tags[5] etc. Further, high performance OFETs are essential for various optoelectronic applications. The bulk and interface properties of the dielectrics are very crucial for the electrical performance of the final device, since charge carriers are restricted to the first few nanometers away from the dielectric interface [6,7]. Engineering the surface chemistry of the dielectric is a key parameter to tune the electrical performance of organic semiconductor based OFETs. It has been reported that the passivation of self-assembled monolayers (SAMs) on the inorganic oxide dielectric (specifically on SiO_2) can increase the surface conductivity for π-conjugated organic semiconducting materials [8-10]. So, controling the chemical species of the insulator surface and/or tailoring the surface energy are the most popular methods for altering the characteristics of semiconductor/insulator interface to improve the thershold voltage, carrier mobility and on/off ratio of the device. Note that the magnitude of the effect depends upon the chemical structure of alkyl tail of SAMs [8,11]. In addition, it is believed that the density and order of the SAM strongly affect the semiconductor nucleation mechanism and grain size; the nucleation has been identified as the most important stage of film growth for controlling the bulk film morphology and is highly dependent on the chemical and topological composition of the substrate [12-14]. The growth studies of organic thin film have experimentally and theoretically proven that the grain size and density of grain boundaries directly affect the field-effect mobility carriers in OFETs.

In addition, the stability of OFETs is a critical issue that must be addressed before their commercialization. First, long-term environmental stability is of utmost importantance. For example, the display devices need very long operating times. The gate-bias stress instability, which decreases the current in a channel and shifts the threshold voltage V_{th} (and correspondigly drain-source current, I_{DS} changes), under a constant applied bias is a major concern. As a consequence of instability, the brightness of an organic light emitting diode (OLED), organic light emitting field effect transistors (OLFET), liquid crystal display (LCD) driven by an OFET will vary inhomogeneously with time because the on-current varies with stress time in the presence of prolonged gate bias. Further, the device might not turn on/off

appropriately when the threshold voltage shift exceeds the operating voltage of the devices [15].

For quantitative analysis, time dependent drian current decay can be analyzed using a stretched exponential function [16,17]. This method is better than the determination of the changes in transfer curves, since there is no recovered charges during the measurement. However, it is only applicable to "ON-state" bias stress and the field-effect mobility must be assumed to be constant. Although the OFET instability behavior can be satisfactorily fitted to a stretched exponential function, the detailed mechanisms underlying the behavior are still elusive. It is worth pointing out that some of the original high mobility organic semiconductors that are throughout cited as a constant reference, such as pentacene and Poly(3-hexylthiophene) (P3HT) suffers from chemical instabilities when exposed to ambient conditions during gate bias stress [18-20]. The primary reason may be the relatively low ionization potential (~4.8 eV), which leads to the poor performance under ambient conditions.

In most systems, the instability is caused by trapping of charge carriers through the following pathways: (1) in the organic semiconductors [21-23] (in the bulk, disordered areas, regions in-between crystalline grains), (2) in the gate dielectric due to varrious chemical species [18] (e.g., humidity, ionic conduction, chemical species), or/and (3) at the interface [19,24-28] (induced polarization) between the two layers due to charge transfer/doping. Among these, charge trapping is significant at semiconductor-dielectric interface, as reported by most of the literatures. In many cases the microscopic, molecular-level nature of these defects and whether they are related to intrinsic structural defects or extrinsic chemical impurities or a combination thereof are not well understood. However, metal contacts and its degradation can also play a crucial role on the long term stabilitty of OFETs [29,30].

Vacuum deposition of organic semiconductors attempts to lower the fabrication complexity due to in-situ chemical purification of materials by sublimation, low un-intensional doping, lack of solvent use, and precise control of deposition conditions in terms of film quality (smoothness) and thickness. These devices are quite reproducible as compared to the solution process based OFET devices. Several metal phthalocyanine (M-Pc) derivatives, the predominant vacuum processed organic semiconductor, have been researched for many years

to understand the growth modes as a function of substrate composition and resultant performance in field-effect transistors. The devices made with M-Pcs are usually stable, both thermally and chemically and they are widely used for solar cells, optical limiters, and photoconductors [31]. In ideal conditions, a field-effect hole mobility of higher than 1 cm^2/Vs can be achieved in case of VOPc transistors, as demonstrated by Wang et al.[32]. A good dynamic response has also been reported for VOPc transistors, which is comparable to a-Si:H TFTs. These devices were fabricated using ordered para-hexaphenyl (p-6P) layer and it showed very good bias stress sability and very low threshold voltage under vacuum as well as dark conditions. It was proposed that the traps occured near the semiconductor/dielectric interface rather than in the dielectric or bulk semiconductor [33]. However, under ambient conditions, using silicon nitride as gate dielectric, the stability decreased [34].

In this chapter, we have studied the performances of VOPc based OFETs under ambient condition with HMDS treated SiO_2 layer and bare SiO_2 layer, which has not been reported earlier. We also present the influence of the chemical species on the insulator surface on the shift in V_{th} that is induced by the gate bias stress in top contact transistors with VOPc as an active layer. It is shown that strong bias stress instability found for non-treated SiO_2 layer is likely to be caused by the inter-grain voids present in the active channel. In case of HMDS treated surface, the devices exhibited very low bias stress and low threshold voltage shift. The bias stress stability data obey the stretched-exponential decay with charactersitis time constat >20 times higher than that of the untreated SiO_2 case.

6.2 Experimental Details

A heavily p^{++}-doped silicon wafer covered with 200 nm SiO_2 layer served as a common gate dielectric. Prior to the device fabrication, the substrates were cleaned thoroughly in deionized water, acetone and finally in 2-propanol, 15 minute each and subsequently dried using the N_2 gas. Next, the surface of the SiO_2 layer was exposed to a hexamethyldisilazane (HMDS) self-assembled monolayers (short-chain length, high purity, and stable against moisture) (Alfa Aesar, 97%) vapor, which was heated at 120°C for 1 hour in order to reduce the surface energy and it served as a

buffer layer. Thermogravimetric analysis (TGA) (NETZSCH) was carried out in Ar gas up to 1000 °C at a heating rate of 10 °C/min and it shows (**Fig. 6.1**) that the VOPc

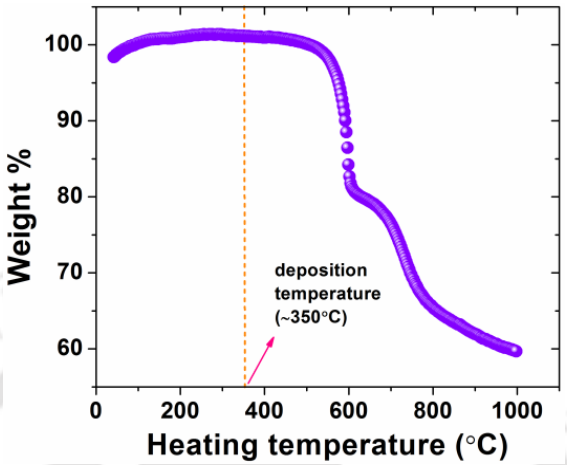

Figure 6.1: TGA plot for VOPc molecule (heating rate: 10°C/min with Ar gas).

molecules (Alfa Aesar, 97%) are stable up to a temperature of 450°C. The VOPc organic molecules were sublimed at ~350 °C to deposit thin-films of thickness ~60 nm on various substrates susing effusion cell based thermal evaporator (BESTEC, Germany) at a chamber preassure of ~10^{-7} mbar with a constant growth rate of 0.4 Å/s. Thickness of the film was measured using a digital thickness monitor. As sublimation temperature of VOPc molecules is about 350 °C in this case, we believe that the molecules are not fragmented during the deposition on various substrates. The substrate temperature was kept constant at 120 °C (lower than the HMDS fragmentation temperature) to improve the device performance. Finally, to complete the device structure, gold (Au) source/drain electrodes, a high work function (~5.3 eV) metal of ~60 nm thickness that act as an ohmic contact, was deposited through a stainless steel shadow mask, on the top of the VOPc coated thin films (HOMO level ~ 5.5 eV) by thermal vapor deposition at a vacuum level of 2×10^{-6} mbar. Contact electrodes were defined in a top-contact device configuration (see **Fig. 6.2**) with a channel width (W) and length (L) of 2050 μm and 50 μm, respectively.

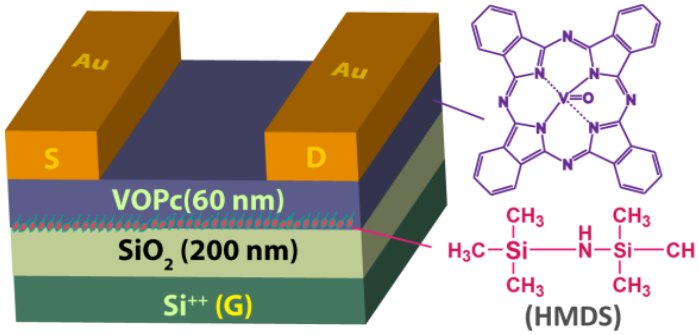

Figure 6.2: A schematic of the cross-section of bottom gate top contact VOPc based OFET along with the molecular structure of VOPc and HMDS.

The surface morphology of the deposited VOPc thin film was examined by atomic force microscopy (AFM) in the tapping mode with an Agilent-5500 AFM in ambient condition. X-ray diffraction (XRD) (Rigaku) pattern was measured with a Cu-K_α source (λ= 1.54056 Å). Before applying bias stress to the devices, at first all transfer and output curves were measured by Keithley 2602A in air ambient. After this reference measurement, the OFETs were stressed in enhancement mode at a high constant drain-source and gate-source voltage under ambient conditions. V_{th} and charge carrier mobility, μ, were extracted from the transfer characteristic in the saturation region of the drain current I_{DS} on the basis of the relation,

$$I_{DS} = \frac{\mu W C_i}{2L}(V_{GS} - V_{th})^2 \qquad (6.1)$$

where, V_{GS} is the gate-source voltage, L is the channel length, W is the channel width, and C_i is the dielectric capacitance per unit area.

6.3 Results and Discussion

6.3.1 Thin Film Morphology

To study the surface morphology, the VOPc-films were characterized by AFM in tapping mode. **Figure 6.3** shows the AFM images for two 60-nm-thick films of VOPc grown at 120°C. The images were recorded over an area of 1 µm × 1 µm for both HMDS-treated and

non-treated cases, as shown in **Fig. 6.3(a)** and **6.3(b)**. To calculate different parameters statistically related with the

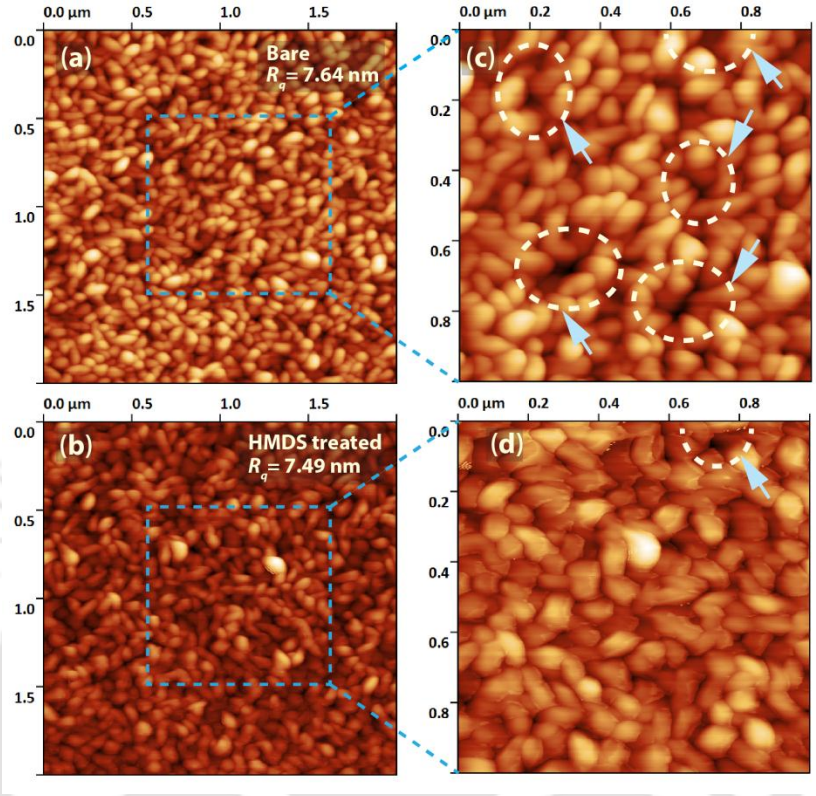

Figure 6.3: Tapping mode AFM images (1µm×1µm) of ~60 nm-thick VOPc thin film grown on: **(a)** untreated SiO_2 and **(b)** HMDS-treated SiO_2 layers. The magnified view of the corresponding images are shown in **(c)** and **(d)**. Dotted circular zones show the voids created in-between the inter-grain regions in the VOPc layer. The RMS roughness, R_q of the surfaces is indicated in each case.

grains, such as grain volume and grain area, we also have taken AFM images over 2µm×2µm area. The morphology for VOPc film deposited on bare SiO_2 and HMDS treated SiO_2 are almost similar with uniform granular structure. It is noticeable that some voids in between grains are present on the VOPc film shown in **Fig. 6.3(a)** for non-treated SiO_2 substrate (arrows indicate voids location). In contrast, the void-free morphology can clearly be observed in the films on the HMDS-passivated SiO_2 substrate, as shown in **Fig. 6.3(b)**. Grain size calculated using Gwyddion software (watershed programme) are ~17.9 nm and ~18.3 nm for thin films on HMDS-treated SiO_2 and bare SiO_2 substrates, respectively. Note that the

rms roughness of the film is 7.49 nm in HMDS treated case, which is slightly lower than the bare SiO2 case (7.64 nm) due to low surface energy.

In order to investigate the crystalline quality of the VOPc films, we carried out XRD analysis. The XRD pattern of the VOPc thin film with a thickness of 60-nm grown on HMDS-treated and non-treated cases is shown in **Fig. 6.4**. The VOPc layer shows a distinct XRD peak at 2θ≈7.5° corresponding to the crystalline (010) planes of VOPc with inter planar spacing ≈11.77 Å (phaseII, triclinic, spacegroup $P\bar{1}$, a =12.027 Å,

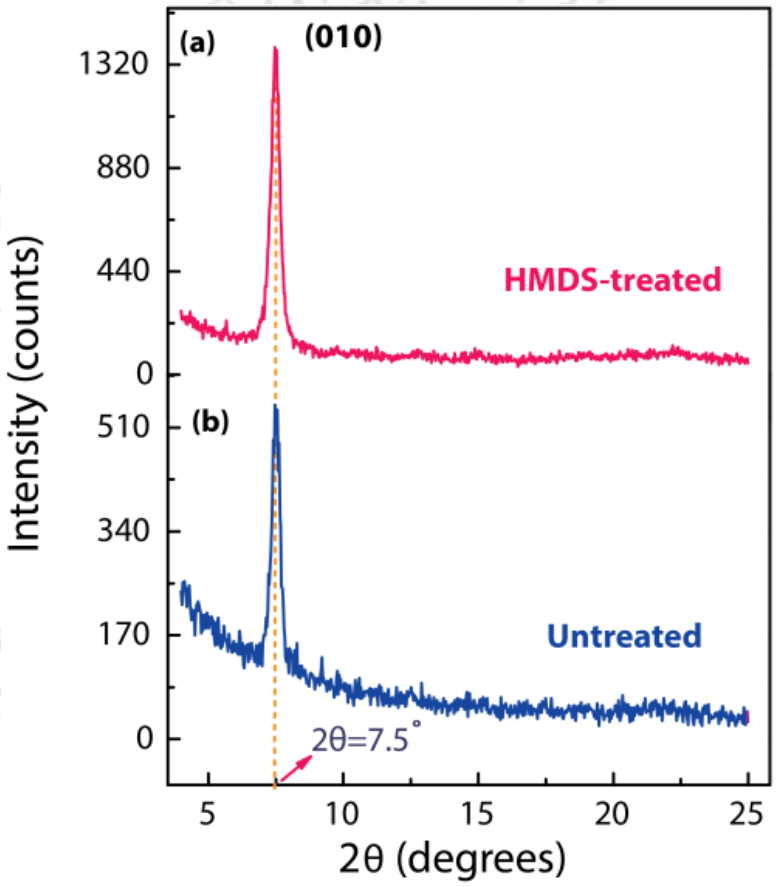

Figure: 6.4 XRD-patterns of 60-nm thick VOPc thin film deposited at a substrate-temperature of 120°C on SiO_2 substrate for: **(a)** non-treated SiO_2 and **(b)** HMDS-treated SiO_2.

b=12.571 Å, c =8.690 Å, α=96.04°, β=94.80°, and γ=68.20°) [35,36]. We noticed that the intensity of the first order diffraction peak increased significantly (about 2.5 times) for film on HMDS treated substrate as compared to the film on bare SiO_2 substrate. However, no measurable shift in peak position is observed indicating no change in

inter planar spacing in two cases. It is worth noting that XRD pattern provides information on the intermolecular ordering perpendicular to the substrate. Our result reveals that the ordering of VOPc molecules is improved highly with HMDS treatment and it can be hypothesized that the VOPc-molecules are arranged vertically on HMDS treated substrate with lower suface energy than the case of bare SiO_2. The presence of distinct peaks in the XRD pattern of the VOPc film implies the formation of the crystalline film and intermolecular π–π stacking direction (herring-bone pattern) parallel to the substrate. This feature implies that the crystalline quality of thin film is appropriate to expect good transport of charge carriers in the OFET geometry.

The schematic of device structure (widh W=2050 μm, length L=45 μm) of bottom gate top contact OFET based on VOPc along with the chemical structure of VOPc and HMDS is shown in **Fig. 6.2**. Here, VOPc acts as a p-channel and the hydrophobic HMDS thin buffer layer (~2 nm) serves as a surface modification agent for the SiO_2 dielectric.

6.3.2 Electrical Characterization and Device Performance

A series of bottom gate top contact devices were fabricated by using SiO_2 and HMDS-modified SiO_2 substrates. HMDS treated devices exhibit very good p-type field-effect characteristics. **Figure 6.5(a)-(b)** shows the output characteristics curves (I_{DS}-V_{DS}, with V_{GS}=constant) of HMDS-treated and non-treated devices, respectively. The drain-source saturation current I_{DS} for HMDS-treated devices exibits one order of magnitude higher value than the non-treated (bare) SiO_2 devices. The output curves show excellent linearity (Ohmic) in the region with low V_{DS}, demonstrating good contact between Au and VOPc layer. The saturation mobility μ and threshold voltage V_{th} are extracted from the linear fitting of the square-root of I_{DS} versus V_{GS} curves (data not shown) for a drain-source voltage V_{DS}= −40 V. The transfer characteristic of I_{DS} versus V_{GS} for V_{DS} = −40 V exhibits a two orders of magnitude increase in the on/off current ratio for the HMDS treated OFETs as compared to the devices with untreated gate oxide case.

It is also apparent that the devices based on HMDS terated substrate exhibited much improved field-effect characteristics (**Fig. 5a**) than those devices on bare SiO_2 substrates (**Fig. 6.5b)**. For example, the hole mobility of the devices on bare SiO_2 is calculated as 0.23×10^{-3} cm^2 V^{-1} s^{-1} and on/off ratio is 10^1-10^2, while the devices on HMDS-modified SiO_2

substrates exhibited mobility of ~0.10×10^{-1} cm^2 $V^{-1}s^{-1}$ and on/off ratio of 10^3. Thus, the mobility of the devices on HMDS-modified SiO_2 substrates is nearly two orders of

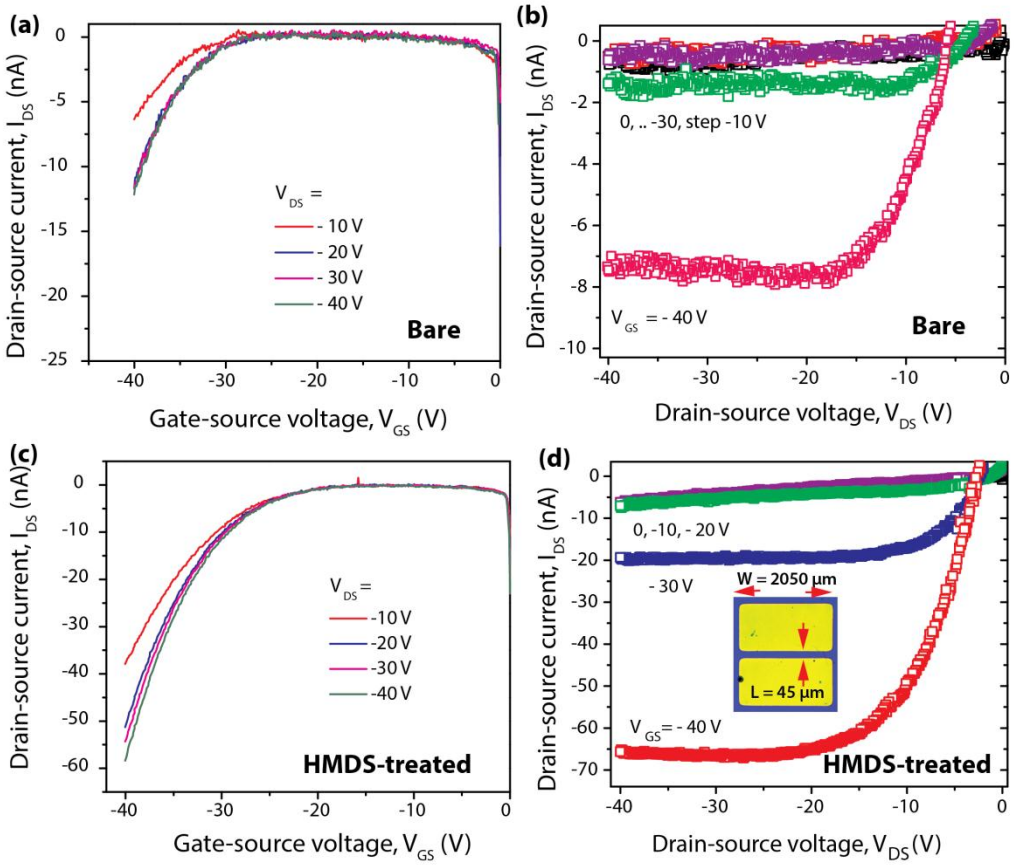

Fig. 6.5 (a, c) Transfer characteristic (I_{DS}-V_{GS}) and **(b, d)** Output characteristics (I_{DS}–V_{DS}) of VOPc OFETs with HMDS treated SiO_2 and bare SiO_2 layers. The inset shows a schematic of the device structure.

magnitude higher than that of the devices on non-treated SiO_2.The summary of the performance parameters of the devices on HMDS-modified SiO_2 substrates and bare sunstrate is listed in **Table 6.1**. Previous reports suggest that the off-current can significantly be supressed due to reduced density of interfacial trap states caused by the HMDS treatment; consequently it improves the device performances [37]. It is commonly acknowledged that the structure (crystal phase composition, molecular ordering, and molecular orientation) and morphology (grain, boundary, and interconnection) of semiconductor film play important roles on the carrier mobility in organic thin film transistor (OTFT). Therefore, characterization of the structure and morphology of VOPc film prior to

Table 6.1 Summary of the electrical and stretched-exponential fitting parameters for the VOPc based OFETs.

Device	$\lvert\Delta V_{th}\rvert$ (V)	$\mu^{\dagger}$ ($cm^2V^{-1}s^{-1}$)	β	τ (s)
Untreated SiO_2	~ 5	0.23×10^{-3}	0.73	480
HMDS-treated SiO_2	~ 2	$\sim0.10\times10^{-1}$	0.67	10000

†hole mobility

device fabrication was necessary to understand the mechanism behind the improvement in performance after HMDS treatment. One of the possible explanation that emerges from the AFM analysis of Fig. 6.3 is that several inhomogeneous voids or charge trapping centers (indicated by circles with arrow heads) are created on the film on bare SiO_2 substrate, which is consistent with other reports, despite the fact that the grain features are almost identical in both cases [22]. Based on the report by Kalb et.al, the structural defects associated with grain boundaries are the primary cause of "fast" hole traps in OTFT's made with vacuum-evaporated pentacene [38].

The major improvement in device characteristics with HMDS treatment may be due to the following factors. Firstly, HMDS may be covalently attached with the inorganic dielectric and bridges linking with organic semiconductor. It optimizes the surface energy of SiO_2, which increases the adhesion of the organic semiconductor on the substrate and improve the π-π stacking structures in the herringbone of VOPc film. Thus, the mobility is also improved as π-π stacking structures control the strong intermolecular interaction that enhances the stacking. From the AFM images of VOPc films shown in **Fig. 6.3**, a large number of closed grains and smooth surface can be observed. One explanation for the apparent disparity between grain size and mobility is due to creation of voids between disconnected grains in two dimensional growth on high energy surface, reducing the effective channel width of the transistor, and the voids are efficiently filled when 3D growth is favoured on low energy surface [12,14,39]. The correlation between morphology (grain size/degree of crystallinity) and TFT mobility is a key point that has been studied extensively, though unfortunately the exact relationship remains unclear. Secondly, HMDS behaves as a silent coupling reactant, the chemical action of which changes OH-terminated SiO_2 to a $(CH_3)_3$-Si surfaces [37].

Thus, the introduction of HMDS reduces the water molecules, OH-group and at the same time the HMDS hydrophobic surface also makes it less dipolar, which improves the electrical properties. In essence, it provides an excellent interface with low traps and passivate the dangling bonds, which improve the charge transportation. However, several groups also reported on negative results of passivation by the self-assembled monolayers [40,41]. Thus, there is an ongoing debate regarding the performance of devices with the insertation of SAM.

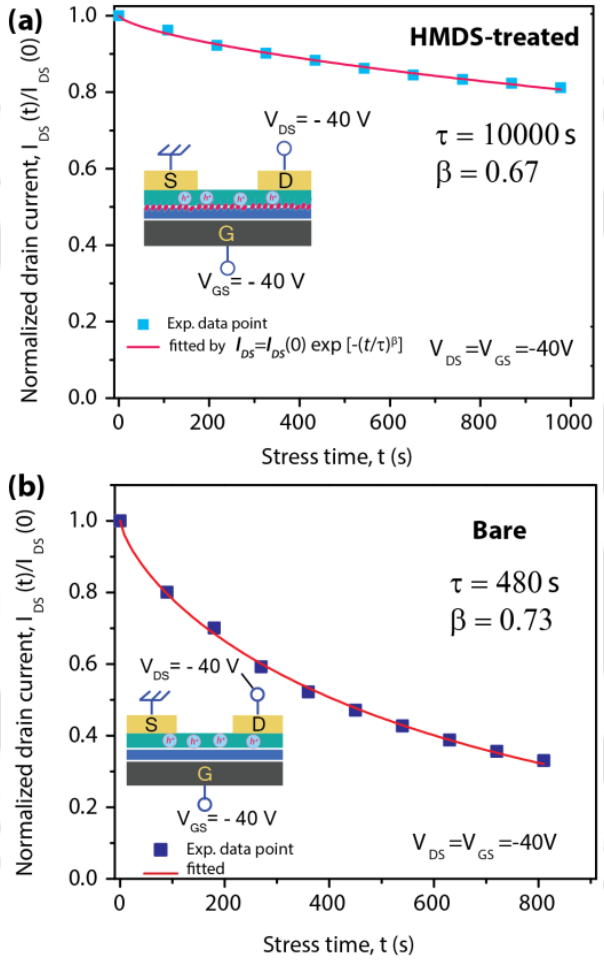

Figure 6.6: Normalized drain-source current $I_{DS}(t)/I_{DS}(0)$ as a function of bias-stress time (t) under ambient condition for: (a) HMDS treated SiO_2, and (b) untreated SiO_2 layers.

6.3.3 Bias Stress Stability

After the standard dc characterization, the electrical response of VOPc based devices both for bare and HMDS treated cases has been investigated with respect to bias stress effect. The bias stress phenomenon is analyzed by monitoring the time decay of I_{DS}

upon static voltage polarization (fixed V_{DS} and V_{GS}). Bias stress effect has been investigated by recording the I_{DS} with stress time under an applied gate bias V_{GS} of -40 V. The drain-source voltage V_{DS} has been fixed at -40 V for VOPc. The experimental curves have been fitted with stretched exponential decay functions. If the OFET mobilities are approximately constant under bias stress, the decay of drain current $I_{DS}(t)$ can be given by a stretched exponential function [16],

$$I_{DS}(t) = I_{DS}(0)\exp\left[-\left(\frac{t}{\tau}\right)^{\beta}\right], \quad (6.2)$$

where β is the stretching parameter (temperature dependent) related to the barrier energy height for charge trapping ($0 < \beta \leq 1$), τ is the relaxation time, and $I_{DS}(0)$ is the initial maximum drain–source current measured at the beginning of stressing. Although the stretched-exponential model was originally developed to describe the bias stress effect in amorphous silicon transistors considering the time-dependent evolution of trap states due to hydrogen migration,[42] we employ the formalism here to describe a dispersive trapping process in OFETs. Stretched exponential function (**Eq. (6.2)**) provides a perfect fit (coefficient of determination $R^2 \rightarrow 1$ represents better fit) to the data in both bare and HMDS treated systems. **Figure 6.6** (**a** and **b**) shows the data points (symbols) as well as fitted lines using Eqn (2). Fitting parameters τ and β are listed in **Table 6.1**. The values of τ at room temperature extracted from the fitting are ~10000 s and ~480 s in HMDS treated and nontreated devices, respectively. The corresponding exponent values are β = 0.67 and 0.73, respectively. The large τ value in HMDS treated case implies a long-term stability of the device, which is very much desirable for practical applications. It should be pointed out that our results for HMDS treated systems is quite comparable to that of earlier reported p-type semiconductors, where τ value on tetracene based single crystal OFET was $\tau = 3.1\times10^4$ s, one order less compared to TIPS-pentacene systems ($\tau \approx 1.8\times10^5$ s) reported by Lee et al. [24].This analysis reveals that VOPc-OFETs based on bare SiO_2 substrate are much more sensitive to the bias stress than the HMDS treated devices. Indeed, for the HMDS-treated devices the current decreases by only <15% after 900 s of constant V_{GS} application, while for the non-treated /bare devices the current reduction is as large as >70%. For HMDS case, τ is about twenty times higher than the untreated device. This is a significant improvement from the application point of view.

The mechanism behind the charge trapping is under debate. Sharma et al. proposed a proton migration mechanism involving water [25], while Lee et al. assumed direct drift/diffusion of holes into the dielectric [24]. Long term charge trapping in devices with SiO_2 is known to be due to trapping in the SiO_2 layer as reported by Mathijssen et al [26]. One of the other possiblities that can not be ignored is the *Au* top contact, which can create deep traps. Previous works have shown that carrier trapping in the long channel of the Au devices was indirectly caused by the deep trap states at the pentacene-dielectric interface in the contact region generated by *Au* penetration [43].

Squre-root of linear transfer characteristics with V_{DS}= −40V as a function of bias stress time (before and after 15 min bias stress) under ambient conditions are shown in **Fig. 6.7(a)** and 6.**7(b)** for HMDS treated and bare case. The relative threshold voltage shifts ($|\Delta V_{th}|$) for HMDS-treated device is much smaller ($\Delta V_{th}\approx$2V) than the device with bare SiO_2 layer (ΔV_{th} >5V), as summarized in **Table 6.1.** If we assume that ΔV_{th} originated from trapped charges at active layer-insulator interface, the density of interface-traps N_t ($N_t \approx C_i|\Delta V_{th}|/q$, C_i is the capacitance per unit area of dielectric insulator and q is the elementary charge) [44] is calculated as 2.12×10^{11} cm^{-2} in HMDS treated-devices, which is much smaller than the bare case ($5.31\times10^{11}cm^{-2}$). With stress time the transfer curves shift in the direction of the applied gate bias to more negative voltages, as shown in **Fig. 6.7.** It clearly shows that the shift in V_{th} is smaller in the HMDS treated devices than that of untreated devices. The V_{th} shift is indicative of the charge trapping instabilities in transistors. These results are very significant and it is believed that the water-related charge traps are reduced by passivation with HMDS on SiO_2 [45]. The main effect of gate bias stress is a shift in the threshold voltage, a typical for organic transistors, which can thus be avoided by simple HMDS treatment of the dielectric layer.

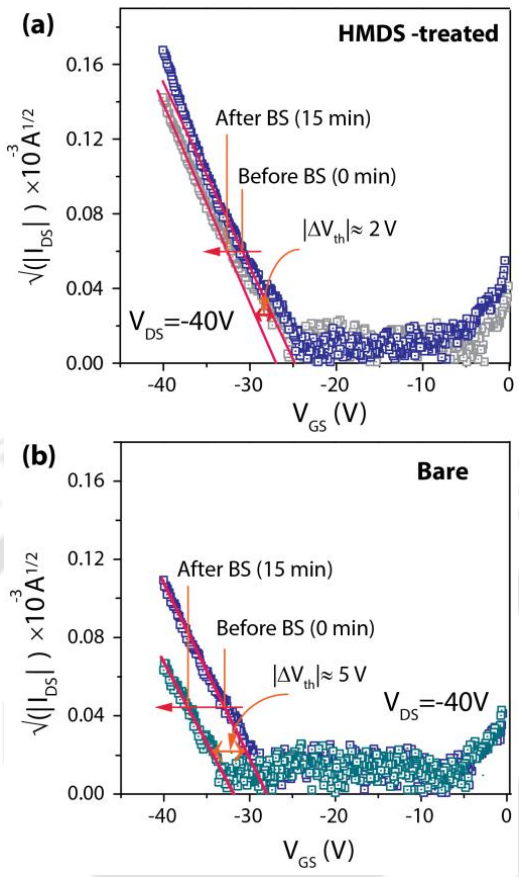

Figure 6.7: Threshold voltage shift before and after 15 min bias stress (BS) for: **(a)** HMDS-treated and **(b)** untreated devices operated in an ambient condition.

6.4 Conclusions

In conclusion, we demonstrate that the VOPc based OFET devices with HMDS passivation of SiO_2 dielectric layer shows high performances and better air stability than the devices with non-treated SiO_2 layer. The devices with top contact *Au* electrodes exhibit excellent p-channel behavior with high hole mobility value of ~0.01 cm^2/Vs for HMDS-treated devices. Bias stress stability study shows stretchehed expoential decay of drain current during long term operation under constant bias voltage in ambient conditions with resulting decay of current by <15% for the HMDS-treated case and a very sharp fall by >70% for the devices with bare SiO_2 layer. The corresponding characteric time constant (τ) is calculated as 10000 s for HMDS-treated case, while it is very low (~480 s) for bare/non-treated devices. Thus, HMDS treated VOPC based OFETs with long term stability are suitable for practical applications. For low performance devices based on bare SiO_2, it is believed that the charge

trapping occurs primarily at the voids in the inter grain regions of the VOPc film, while it is almost negligible for HMDS-treated SiO_2 case.

References

[1] G.H. Gelinck, H.E.A. Huitema, E. van Veenendaal, E. Cantatore, L. Schrijnemakers, J.B.P.H. van der Putten, T.C.T. Geuns, M. Beenhakkers, J.B. Giesbers, B.-H. Huisman, E.J. Meijer, E.M. Benito, F.J. Touwslager, A.W. Marsman, B.J.E. van Rens, D.M. de Leeuw, Flexible active-matrix displays and shift registers based on solution-processed organic transistors. *Nat. Mater.* **3**, 106 (2004).

[2] H. Sirringhaus, 25th Anniversary Article: Organic Field-Effect Transistors: The Path Beyond Amorphous Silicon. *Adv. Mater.* **26**, 1319 (2014).

[3] R.D. Yang, J. Park, C.N. Colesniuc, I.K. Schuller, J.E. Royer, W.C. Trogler, A.C. Kummel, Analyte chemisorption and sensing on n- and p-channel copper phthalocyanine thin-film transistors. *J. Chem. Phys.* **130**, 164703 (2009).

[4] D. Khim, G.-S. Ryu, W.-T. Park, H. Kim, M. Lee, Y.-Y. Noh, Precisely Controlled Ultrathin Conjugated Polymer Films for Large Area Transparent Transistors and Highly Sensitive Chemical Sensors. *Adv. Mater.* **28**, 2752 (2016).

[5] P.F. Baude, D.A. Ender, M.A. Haase, T.W. Kelley, D.V. Muyres, S.D. Theiss, Pentacene-based radio-frequency identification circuitry. *Appl. Phys. Lett.* **82**, 3964 (2003).

[6] A. Dodabalapur, L. Torsi, H.E. Katz, Organic Transistors: Two-Dimensional Transport and Improved Electrical Characteristics. *Science* **268**, 270 (1995).

[7] H. Klauk, Organic Electronics: Materials, Manufacturing and Applications, Wiley-VCH Verlag, (2006).

[8] S. Kobayashi, T. Nishikawa, T. Takenobu, S. Mori, T. Shimoda, T. Mitani, H. Shimotani, N. Yoshimoto, S. Ogawa, Y. Iwasa, Control of carrier density by self-assembled monolayers in organic field-effect transistors. *Nat. Mater.* **3**, 317 (2004).

[9] M. Shtein, J. Mapel, J.B. Benziger, S.R. Forrest, Effects of film morphology and gate dielectric surface preparation on the electrical characteristics of organic-vapor-phase-deposited pentacene thin-film transistors. *Appl. Phys. Lett.* **81**, 268 (2002).

[10] L. Miozzo, A. Yassar, G. Horowitz, Surface engineering for high performance organic electronic devices: the chemical approach. *J. Mater. Chem.* **20**, 2513 (2010).

[11] K. Suemori, S. Uemura, M. Yoshida, S. Hoshino, N. Takada, T. Kodzasa, T. Kamata, Threshold voltage stability of organic field-effect transistors for various chemical species in the insulator surface. *Appl. Phys. Lett.* **91**, 192112 (2007).

[12] W. Kalb, P. Lang, M. Mottaghi, H. Aubin, G. Horowitz, M. Wuttig, Structure–performance relationship in pentacene/Al2O3 thin-film transistors. *Synthetic Metals* **146**, 279 (2004).

[13] P. Prisawong, P. Zalar, A. Reuveny, N. Matsuhisa, W. Lee, T. Yokota, T. Someya, Vacuum Ultraviolet Treatment of Self-Assembled Monolayers: A Tool for Understanding Growth and Tuning Charge Transport in Organic Field-Effect Transistors. *Adv. Mater.* **28**, 2049 (2016).

[14] Y.W. Park, Editorial for the Conducting Polymers for Carbon Electronics themed issue. *Chem. Soc. Rev.* **39**, 2352 (2010).

[15] W.H. Lee, H.H. Choi, D.H. Kim, K. Cho, 25th Anniversary Article: Microstructure Dependent Bias Stability of Organic Transistors. *Adv. Mater.* **26**, 1660 (2014).

[16] X.-H. Zhang, S.P. Tiwari, B. Kippelen, Pentacene organic field-effect transistors with polymeric dielectric interfaces: Performance and stability. *Organic Electronics* **10**, 1133 (2009).

[17] S. Md. Obaidulla, D.K. Goswami, P.K. Giri, Low bias stress and reduced operating voltage in SnCl2Pc based n-type organic field-effect transistors. *Appl. Phys. Lett.* **104**, 213302 (2014).

[18] D. Kumaki, T. Umeda, S. Tokito, Influence of H2O and O2 on threshold voltage shift in organic thin-film transistors: Deprotonation of SiOH on SiO2 gate-insulator surface. *Appl. Phys. Lett.* **92**, 093309 (2008).

[19] T. Miyadera, S.D. Wang, T. Minari, K. Tsukagoshi, Y. Aoyagi, Charge trapping induced current instability in pentacene thin film transistors: Trapping barrier and effect of surface treatment. *Appl. Phys. Lett.* **93**, 033304 (2008).

[20] J. Sprogies, S. Scheinert, I. Hörselmann, Analyzing the influence of negative gate bias stress on the transconductance of solution-processed, organic thin-film transistors. *J. Appl. Phys.* **116**, 074507 (2014).

[21] A. Salleo, F. Endicott, R.A. Street, Reversible and irreversible trapping at room temperature in poly(thiophene) thin-film transistors. *Appl. Phys. Lett.* **86**, 263505 (2005).

[22] M. Tello, M. Chiesa, C.M. Duffy, H. Sirringhaus, Charge Trapping in Intergrain Regions of Pentacene Thin Film Transistors. *Adv. Funct. Mater.* **18**, 3907 (2008).

[23] J.B. Chang, V. Subramanian, Effect of active layer thickness on bias stress effect in pentacene thin-film transistors. *Appl. Phys. Lett.* **88**, 233513 (2006).

[24] B. Lee, A. Wan, D. Mastrogiovanni, J.E. Anthony, E. Garfunkel, V. Podzorov, Origin of the bias stress instability in single-crystal organic field-effect transistors. *Phys. Rev. B* **82**, 085302 (2010).

[25] A. Sharma, S.G.J. Mathijssen, M. Kemerink, D.M. de Leeuw, P.A. Bobbert, Proton migration mechanism for the instability of organic field-effect transistors. *Appl. Phys. Lett.* **95**, 253305 (2009).

[26] S.G.J. Mathijssen, M.-J. Spijkman, A.-M. Andringa, P.A. van Hal, I. McCulloch, M. Kemerink, R.A.J. Janssen, D.M. de Leeuw, Revealing Buried Interfaces to Understand the Origins of Threshold Voltage Shifts in Organic Field-Effect Transistors. *Adv. Mater.* **22**, 5105 (2010).

[27] K. Fukuda, T. Suzuki, T. Kobayashi, D. Kumaki, S. Tokito, Suppression of threshold voltage shifts in organic thin-film transistors with bilayer gate dielectrics. *Phys. Status Solidi A* **210**, 839 (2013).

[28] J. Kim, J. Jang, K. Kim, H. Kim, S.H. Kim, C.E. Park, The Origin of Excellent Gate-Bias Stress Stability in Organic Field-Effect Transistors Employing Fluorinated-Polymer Gate Dielectrics. *Adv. Mater.* **26**, 7241 (2014).

[29] S.D. Wang, T. Minari, T. Miyadera, Y. Aoyagi, K. Tsukagoshi, Bias stress instability in pentacene thin film transistors: Contact resistance change and channel threshold voltage shift. *Appl. Phys. Lett.* **92**, 063305 (2008).

[30] S. Yim, T.S. Jones, Growth dynamics of C60 thin films: Effect of molecular structure. *Applied Physics Letters* **94**, 021911 (2009).

[31] Y. Sun, Y. Liu, D. Zhu, Advances in organic field-effect transistors. *J. Mater. Chem.* **15**, 53 (2005).

[32] H. Wang, D. Song, J. Yang, B. Yu, Y. Geng, D. Yan, High mobility vanadyl-phthalocyanine polycrystalline films for organic field-effect transistors. *Appl. Phys. Lett.* **90**, 253510 (2007).

[33] L. Wang, G. Liu, F. Zhu, F. Pan, D. Yan, Electrical instability in vanadyl-phthalocyanine thin-film transistors. *Appl. Phys. Lett.* **93**, 173303 (2008).

[34] L. Wang, H. Qin, W. Zhang, L. Zhang, D. Yan, High reliability of vanadyl-phthalocyanine thin-film transistors using silicon nitride gate insulator. *Thin Solid Films* **545**, 514 (2013).

[35] C.H. Griffiths, M.S. Walker, P. Goldstein, Polymorphism in Vanadyl Phthalocyanine. *Molecular Crystals and Liquid Crystals* **33**, 149 (1976).

[36] H. Ohta, T. Kambayashi, K. Nomura, M. Hirano, K. Ishikawa, H. Takezoe, H. Hosono, Transparent Organic Thin-Film Transistor with a Laterally Grown Non-Planar Phthalocyanine Channel. *Adv. Mater.* **16**, 312 (2004).

[37] I. Yagi, K. Tsukagoshi, Y. Aoyagi, Modification of the electric conduction at the pentacene/SiO2 interface by surface termination of SiO2. *Appl. Phys. Lett.* **86**, 103502 (2005).

[38] W.L. Kalb, S. Haas, C. Krellner, T. Mathis, B. Batlogg, Trap density of states in small-molecule organic semiconductors: A quantitative comparison of thin-film transistors with single crystals. *Phys. Rev. B* **81**, 155315 (2010).

[39] S.Y. Yang, K. Shin, C.E. Park, The Effect of Gate-Dielectric Surface Energy on Pentacene Morphology and Organic Field-Effect Transistor Characteristics. *Adv. Funct. Mater.* **15**, 1806 (2005).

[40] F. Gholamrezaie, A.-M. Andringa, W.S.C. Roelofs, A. Neuhold, M. Kemerink, P.W.M. Blom, D.M. de Leeuw, Charge Trapping by Self-Assembled Monolayers as the Origin of the Threshold Voltage Shift in Organic Field-Effect Transistors. *Small* **8**, 241 (2012).

[41] S.K. Possanner, K. Zojer, P. Pacher, E. Zojer, F. Schürrer, Threshold Voltage Shifts in Organic Thin-Film Transistors Due to Self-Assembled Monolayers at the Dielectric Surface. *Adv. Funct. Mater.* **19**, 958 (2009).

[42] J. Kakalios, R.A. Street, W.B. Jackson, Stretched-exponential relaxation arising from dispersive diffusion of hydrogen in amorphous silicon. *Phys. Rev. Lett.* **59**, 1037 (1987).

[43] Y. Liang, H.-C. Chang, P. Paul Ruden, C. Daniel Frisbie, Examination of Au, Cu, and Al contacts in organic field-effect transistors via displacement current measurements. *J. Appl. Phys.* **110**, 064514 (2011).

[44] J. Zhou, R. Chen, A low voltage and small hysteresis C 60 thin film transistor. *Journal of Semiconductors* **32**, 024006 (2011).

[45] S.G.J. Mathijssen, M. Kemerink, A. Sharma, M. Cölle, P.A. Bobbert, R.A.J. Janssen, D.M. de Leeuw, Charge Trapping at the Dielectric of Organic Transistors Visualized in Real Time and Space. *Adv. Mater.* **20**, 975 (2008).

This Page is Left Blank Intentionally

Chapter 7

Low Operating Voltage and Low Bias Stress in Top-Contact $SnCl_2Pc$/ CuPc Heterostructure Based Bilayer Ambipolar Organic Field-Effect Transistors

In this chapter, a symmetrical Ag top contact- bottom gate (TC-BG) bilayer ambipolar organic field-effect transistor based on heterojunction of vacuum-deposited small molecules, tin(IV) phthalocyanine dichloride ($SnCl_2Pc$) (n-channel) and copper phthalocyanine (CuPc) (p-channel), has been fabricated and studied. A hydroxyl(-OH)-free poly (methyl methacrylate) (PMMA) with aluminum oxide (Al_2O_3) bilayer dielectric exhibits low operating voltage (~10 V) and low bias stress (relaxation time $\tau \sim 10^5$s) for both n-channel and p-channel cases. The optimized $SnCl_2Pc$/CuPc heterostructure exhibits balanced carrier mobility and both type of charge carriers, electron and holes, are facilitated through the same low work function Ag contacts (depending on the bias conditions) from the TC-BG architecture. The Ag contact also exhibits Ohmic injection of charge carriers with low contact resistance in the n-channel region under optimal heterostructure configuration. The contact resistances for electron and hole-injection are strongly dependent on the thickness of the $SnCl_2Pc$ and CuPc layers, respectively. The bias stress stability is modeled using stretched exponential fitting. Our results demonstrate that the ambipolar device characteristics and performance can be controlled by adjusting the thickness of the molecular layer, which is highly desirable. Such a simple heterostructure engineering with utilization of organic molecular semiconductors can truly enable the promising low-cost and flexible organic electronics for extensive applications.

7.1 Introduction

Ambipolar organic field-effect transistors (OFETs) have attracted enormous attention due to their unique operation, which allows both electrons and holes to be injected and transported in the same devices, i.e., the device can operate in unipolar mode as well as in an ambipolar mode [1-4]. These devices find active applications in organic complementary logic

circuits, double carrier devices, like light emitting field-effect transistors for organic active matrix displays, organic photovoltaic cells (OPVs), sensors, radio frequency identification components, e-papers, and inverters [5-9] etc. High-performance inverters are the building blocks of the integrated circuits (ICs). Complementary metal-oxide semiconductor (CMOS) technology is desirable for the preparation of Ics, because it provides straightforward circuit design, good noise margins, low power consumption, and robust operation. Organic CMOS technology requires the use of p- and n-type transistors on the same substrate [10,11]. In addition, both hole and electron can transport within the same device (depending upon the bias conditions) and recombination of opposite charge carriers within the transistor channel can result in light emission, light emitting field-effect transistor, which has a potential to be at the heart of the next generation of light emitting devices [12-14]. For these, there is needed to inject efficient balanced chage carriers (both types, electon and hole) in the channel of the device. To achieve this goal, different groups have followed different approaches: (i) ambipolar OTFTs featuring symmetric or asymmetric source and drain electrodes for single or double channel organic semiconductors [15-17], (ii) bilayer heterojunction structures consisting of electron- and hole-transporting organic layers [18-20], and (iii) blending two organic semiconductors with different charge carriers [21-23]. They all have particular characteristics and advantages as well as challenges to overcome.

In a single semiconductor, the main difficulty to achieve ambipolar transistor operation is the injection of holes and electrons into a single semiconductor from the same electrode. This electrode needs to have a work function that allows injection of holes in the highest occupied molecular orbital (HOMO) of the semiconductor, and the injection of electrons in the lowest unoccupied molecular orbital (LUMO). Consequently, this will result in an injection barrier of at least half of the band gap energy for one of the carriers (either electron or hole as most of the standard semiconductors have band gap of ~2-3 eV). To overcome the injection problems due to this barrier, in double-carrier devices, such as light emitting diodes and photovoltaic cells, two dissimilar, i.e. high- and low-work-function metal electrodes are used to enable injection or collection of holes and electrons [15]. Unfortunately, this approach makes circuit fabrication complex and potentially expensive. Alternatively, a single low-cost electrode material can be used in combination with two different semiconductors, where one

has its HOMO level and the other its LUMO level aligned with the metal work function. Recently, Long *et al.* reported a mixed contact interlayer of transition-metal oxides that control the efficient charge injection in ambipolar diketopyrrolopyrrole-thieno[3,2-b]thiophene copolymer (DPPT-TT) organic transistors with using low-cost molybdenum (Mo)-source/drain electrodes [24]. To optimize the contact effect, one can introduce a self-assembled monolayer (SAM) to lessen injection barrier, and it results into the efficient injection of electrons and holes [25,26]. Another important challenge is the trapping of one or both type of carriers in the defects/impurities. In particular, the electrons are likely to be trapped by impurities at certain chemical moieties at the semiconductor-dielectric interfaces and/or semiconductor surfaces. We have found that the particular choice of hydroxyl-free low-cost PMMA buffer polymer dielectric layers (as compared to fluorinated polymer dielectric layer, CYTOP) and low work function Ag electrodes can exhibit superior performances in terms of low gate-bias stress and efficient injection [27]. Takahashi *et al*. reported rubrene single crystal ambipolar OFETS with Ag paste electrode to inject charge carriers and PMMA buffer layer to terminate the interfacial electrons traps [17]. Most of the ambipolar characteristics reported in the literature are based on bottom contact SiO_2 gate dielectric and heavily doped Si wafer serving as a gate electrode. Such a rigid substrate requirement limits the flexibility of the composed circuits. Further, SiO_2 layer may contain of high density of hydroxyl-groups known as electron traps which significantly suppress n-type device characteristics. Therefore, the majority of the OFETs have reported p-type transistors with high work function Au- electrodes that serve as a hole injection layer and these devices are highly gate-bias stress sensitive (i.e., decay of drain source current I_{DS} under prolonged biased condition).

Among all organic semiconductors, vacuum deposited small molecules exhibit certain advantages over polymeric-thin film in terms of morphology, as demonstrated in this study, A solution processed field-effect transistor (FET) is of interest because of its potential contributions to low-cost fabrication of circuits thorough manufacturing roll-to-roll processes using conventional coating and printing techniques. Recently, Cheng *et al.* reported balance carrier mobilities in 2-(4-n-octylphenyl) benzo[*d,d'*] thieno[3,2-b;4,5-b'] dithiophene (OP-BTDT)-based fused-thiophene derivative with small-molecule, fullerene (C_{60}) bulk

heterojunction ambipolar transistors [22]. Further, due to molecular weight distribution (polydispersity), regio- and stereo- irregularity, and end-group contaminations of polymeric materials, performance of polymer-based OTFTs could exhibit relatively large batch-to-batch variations. The lack of ambipolar transport in binary blends of polymers for most of the compositions is due to the fact that controlling the thin film morphology is crucial for obtaining continuous path for both type of charge carriers. Further, a limited number of polymer blend is available due to lack of high performing solution processable n-type polymers. On the other hand, small molecule materials are easier to synthesize and high chemical purity can be achieved using techniques, such as vacuum sublimation. Therefore impurities are low, which can be considered as intrinsic semiconductor and can greatly improve reproducibility of fabricated devices as compared to that of polymeric materials. Small molecules can easily be purified by various methods of chromatography, sublimation, and recrystallization, while polymers can only be purified by recrystallization.

Therefore, bilayer heterojunction structure appears to be one of the very promising approaches for device fabrication, as they are readily deposited using the same substrates without breaking vacuum. Unfortunately, carrier mobility in these devices rarely exceeds the order of 10^{-3} cm^2 V^{-1} s^{-1}, because of poor control over molecular packing. In general, organic-based large electronic circuit may need >1800 transistors and as the number of transistors per circuit increases there is an increasing need for circuits characterized by low power dissipation, high noise margin, and greater operation stability [6]. So, the high operating voltage and environmental stability of ambipolar OFETs are still major challenges for their commercial applications. To reduce the operating voltage, herein, we used an anodized Al_2O_3 modified with PMMA, as a buffer gate dielectric layer instead of the commonly used SiO_2 layer. The optimized $SnCl_2Pc$/CuPc heterostructure ambipolar OFETs with operating voltages down to 10 V and carrier mobilities of 1.8×10^{-4} cm^2 V^{-1} s^{-1} and 2.1×10^{-4} cm^2 V^{-1} s^{-1} for hole, and electron, respectively are demonstrated here. The heterojunction OFET's consisting of p-type CuPc and n-type $SnCl_2Pc$ have been chosen for the following reasons: (i) they possess almost identical molecular shapes, and very similar crystal packing structures and grain sizes under the same deposition conditions, so it may be convenient to produce a heterojunction with perfect crystalline interface, (ii) the field-effect

mobility (μ_{FE}) of carriers in these two materials is very similar at a level of 10^{-1} $cm^2 V^{-1} s^{-1}$ in unipolar case [28,29]. So, it may be easier to obtain a balanced ambipolar characteristics with engineering of small molecules. Several groups have reported that low band gap organic semiconductors, especially small molecules based semiconductors are promising candidates for ambipolar OFETs [18,30,31] . Most studies reported on ambipolar OFETs focus on the hole and electron field-effect mobilities (μ_h and μ_e, respectively), while the issues of the bias stress effect (i.e., drain current (I_{DS}) instability with prolonged operation time) and contact resistance (R_C) effect have been addressed rarely, except in a few reports [19,24,32], especially for bilayer heterostructure ambipolar OFETs. As gate-bias stress effect and R_C effect can be critical factors to limit the practical applications of ambipolar OFETs, it is essential to investigate the contact resistance as well as gate-bias stress effects for both holes and electrons in the organic bilayer structures [19,33,34].

7.2 Experimental Details

A. Materials

Tin (IV) phthalocyanine dichloride ($SnCl_2Pc$) ($C_{32}H_{16}Cl_2N_8Sn$) and copper phthalocyanine (CuPc) ($C_{32}H_{16}CuN_8$) that served as organic semiconductors in all devices are purchased from Alfa Aesar. Poly (methyl methacrylate) (Alfa Aesar, PMMA, M_w~550000 kg/mol, 25 mg/ml in anisole) was used as polymer gate dielectric. A silver (Ag) wire (Alfa Aesar, 97%) is used for evaporation of source/drain (*S/D*) contact. All materials were used as received without any further purification.

B. Heterostructure Device Fabrication

To form the control gate, about 150 nm-thick layer of aluminum (Al) (Alfa Aesar, 99.9% pure) was vacuum deposited at a rate 30 $Å s^{-1}$ on to clean glass substrates. The Al layer is anodized by immersing in citric acid solution prepared with ultra-pure (18.2 MΩ.cm) de-ionized water as a solvent, $1mML^{-1}$. A constant current density of 0.3 mA cm^{-2} is maintained until the voltage reaches 10 V, and the voltage is then maintained at 10 V until the current density drops to 0.015 mA cm^{-2}. The thickness of the Al_2O_3 is estimated to be 13 nm, given the anodization ratio (c_{Al} ≈1.3 nm/V) [27]. A thin buffer layer of PMMA was coated at 5000

rpm for 60 s to deposit a very thin and uniform layer on Al_2O_3 surface and annealed at 80°C for 30 minutes in reduced vacuum to remove residual solvents. The morphological analysis is carried out with an AFM (Agilent-5500) in the tapping mode as shown in **Fig. 7.1(a).** PMMA can provide a high-quality hydroxyl free (-OH) interface to the organic semiconductor with

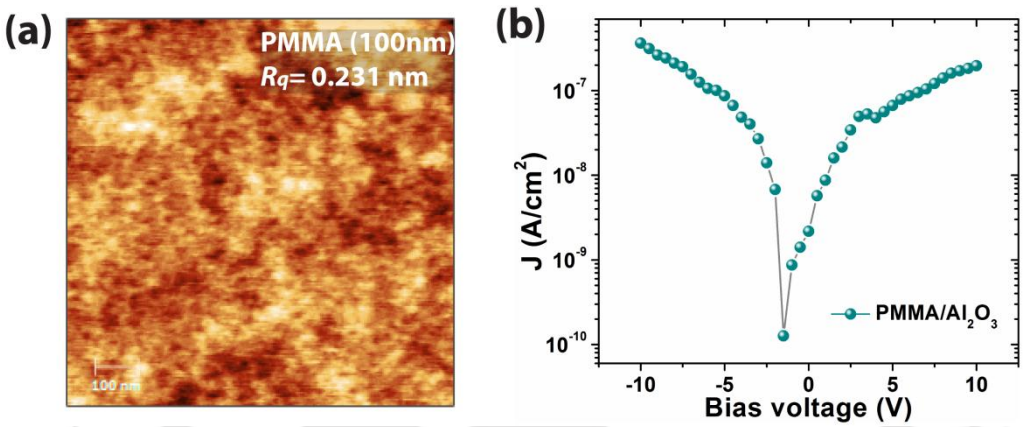

Figure 7.1: (a) AFM image of PMMA layer. Surface roughness (*Rq*) is shown as inset. **(b)** Leakage current density (J) as function of bias voltage for PMMA (100 nm)/Al_2O_3 (15 nm) bilayer gate dielectric.

high dielectric breakdown strength (~1 MV/cm). The optimized thickness of PMMA layer was 100 nm, as measured by surface profilometer (Veeco Dektak-150). The surface morphology of PMMA and leakage current density of PMMA/Al_2O_3 bilayer dielectric layer are shown in **Fig. 7.1 (a)** and **Fig. 7.1(b),** respectively. The root-mean-square (RMS) surface roughness (R_q) of PMMA layer was 0.231 nm, as measured using an AFM, which is much lower than the thickness of the anodized Al_2O_3 layer (≈5 nm), as measured by AFM. A 60-nm-thick $SnCl_2Pc$ film was deposited on CuPc layer with different thicknesses made on to the PMMA/Al_2O_3 dielectrics under identical conditions at a rate 0.8 Å/s using thermal evaporation at a pressure ~10^{-6} mbar, to act as the n-channel and p-channel, respectively. The thickness of top $SnCl_2Pc$ layer is kept constant while thickness of CuPc layer was varied. The substrate temperature was kept at 60 °C during all depositions. Finally, using a thermal vacuum deposition chamber, a >50 nm thick silver (Ag) top electrode drain/source (*S/D*) were deposited and patterned through a shadow mask on the substrate to complete the device structure, where the device channel length (*L*) and channel width (*W*) are defined as 30 µm and 780 µm, respectively. The surface morphology of the organic thin films was characterized by AFM in tapping mode to avoid any damage to the film.

C. Device Characterization

We fabricated $SnCl_2Pc$ top-contact OFET's on PMMA/Al_2O_3 substrates. The capacitance density C_i (nF/cm^2) was measured from a metal-insulator-metal structure of parallel plate capacitors with different contact areas. The buffer layer PMMA on Al_2O_3 gives the capacitance density C_i ~ 31 nF cm^{-2}. The leakage current density, J (A/cm^2) through the gate dielectrics was very small (~10^{-7} A/cm^2) [see **Fig.7.1 (b)**]. The electrical characteristics including the voltage-current relationship and capacitance are measured with a Keithley 4200-SCS system at room temperature in a probe station (Lake shore, USA) under low vacuum (~10^{-3} mbar). The field-effect mobility (μ_{FE}) and threshold voltage (V_{Th}) were calculated in the saturation regime using equation, $|I_{DS}| = (WC_i/2L)\mu_e(V_{GS} - V_{Th,e})^2$ and $|I_{DS}| = (WC_i/2L)\mu_h [V_{DS} - (V_{GS} - V_{Th,e})]^2$ for electron and hole transport, respectively (where W is channel width (780 µm) and L is channel length (30 µm), C_i is the capacitance of PMMA/Al_2O_3 gate dielectrics (~ 31 nF cm^{-2}).

7.3 Results and Discussion

In bilayer heterostructure, depending on the device configuration and on the materials used, charge accumulation and transport of electrons and holes can occur in different layers. However, at least one of the two accumulation zones will form at the interface and therefore charge transport will depend on the quality of interface. Consequently, an accurate control of the growth conditions of the evaporated film is necessary. The top contact-bottom gate (TC-BG) ambipolar bilayer device structure with silver (Ag) as source/drain (S/D) electrodes and the chemical structures of small band-gap molecules tin(IV) phthalocyanine ($SnCl_2Pc$) and copper phthalocyanine (CuPc) are shown in **Fig. 7.2(a)**. In general, top contact OFETs exhibit the lowest contact resistance, at least two orders of magnitude lower, because of the increased metal-semiconductor contact area in this configuration [35]. Details of fabrication procedures for devices are provided in the experimental section. CuPc was deposited as the first active layer on the top of the insulator, PMMA/Al_2O_3, and $SnCl_2Pc$ was deposited as a second active layer on the top of CuPc layer. The bilayer dielectrics PMMA/Al_2O_3 enable low voltage operation. PMMA as a polymer dielectric is chosen, since no chemical groups (-OH) are present at its surface that may act as electron traps, and it shows very low bias stress

effect, low contact resistance and is of low cost compared to other hydroxyl-free flouro polymer, like CYTOP [27,36] . The same device structure is reported to show the low bias stress and low operating voltage of 10^5 s, and 10 V, respectively. Herein, we used Ag electrodes as a top-contact source/drain (*S/D*) electrodes, instead of the usual gold electrodes, which facilitate the electron injection due to their low work function. In addition, top contact-bottom gate (TC-BG)-OFET behaves as inverted-staggered, and TC-BG transistor is affected by current crowding effect, in which contact resistance R_c, is lower than the channel sheet resistance, R_{ch} [37]. The schematic of energy level diagram of $SnCl_2Pc$ and CuPc – heterostructure with symmetric Ag-contact is shown in **Fig. 7.2(b)** (under zero bias condition). The lowest unoccupied molecular orbital (LUMO) level of $SnCl_2Pc$ is 4.0 eV [38], which has a very small difference with Fermi energy level (E_F) of silver (Ag) (work function $\Phi \approx$ - 4.3 eV), and it results in an Ohmic electron injection (i.e., an output drain-source current initially increase and finally saturated) into the LUMO level of $SnCl_2Pc$ layer. It is known that a good Ohmic contact can be achieved when the work function of metal is closely aligned with the LUMO or HOMO energy level of the semiconductor. On the other hand, the difference between HOMO level of CuPc and Fermi energy of Ag is quite large (≈

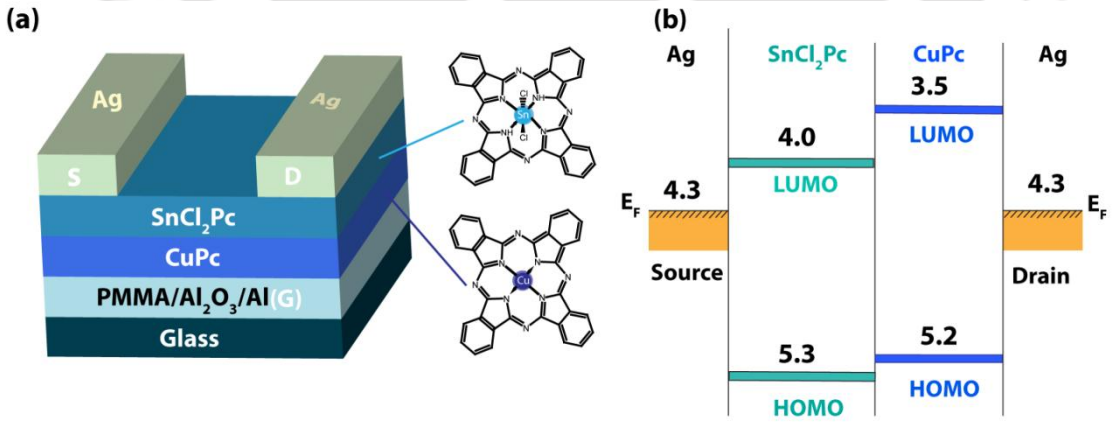

Figure 7.2: (a) A schematic of the top-contact ambipolar device configuration employed in this study, with chemical structures of the small molecules $SnCl_2Pc$ and CuPc. **(b)** A schematic of the energy band diagram of $SnCl_2Pc$/CuPc heterostructures with Ag electrodes without any external bias.

0.9 eV). When the gate bias is applied, the band-bending occurs at the metal/semiconductor interface and reduce the energy barriers and will allow tunneling of charge carriers from the

electrode to the semiconductor. However, we did not find any ambipolar signature for CuPc/$SnCl_2Pc$ (top/bottom) configuration of the bilayer heterostructures. Therefore, $SnCl_2Pc$/CuPc (top/bottom) heterostructure pair is an excellent choice for obtaining ambipolar characteristics.

7.3.1 Morphological and Structural Analysis

The performance of electronic devices depends crucially on depletion width, film thickness, and in particular the spatial location of trap states, either in organic/organic or organic/dielectric interface. In addition, an energy land scape at organic-organic interface is complicated due to several electrostatic phenomena such as charge transfer, dipole generation and/or dipole orientation, and doping, which are related to the feature of molecular structure (orientation), crystallinity, inter-diffusion, and domain size. Therefore, it is necessary to track the evolution of device characteristics with film thickness [30,39].

In order to investigate the crystalline quality of the $SnCl_2Pc$/CuPc heterostructure, we carried out X-ray diffraction (XRD) analysis with Cu-K_α radiation (λ= 1.54056Å). The XRD pattern of $SnCl_2Pc$ thin film of thickness 60 nm grown on different thickness (4, 12 and 16 nm) of CuPc layer is shown in **Fig.7.3.** The $SnCl_2Pc$ layer without the CuPc layer has XRD peaks at 2θ= 10.48˚ and 12.18˚ corresponding to (010) and (100) planes, respectively. With increasing thickness of CuPc layer, the intensity of the peaks related to $SnCl_2Pc$ decreases and a new peak appears at 2θ = 6.84˚ for the 12 nm and 16 nm CuPc thin films. The peak at 2θ = 6.84˚ results from (200) lattice planes of CuPc, where the inter-stacking distance is $d \approx$ 12.9Å. It implies that the trace of herring bone pattern is parallel to the substrate [18]. The presence of distinct peaks in the XRD pattern of $SnCl_2Pc$ film implies the formation of the crystalline films and inter molecular π- π stacking direction parallel to the substrate. This feature implies that the crystalline quality of the thin film is appropriate to expect good transport of charge carriers in the OFET geometry [29].

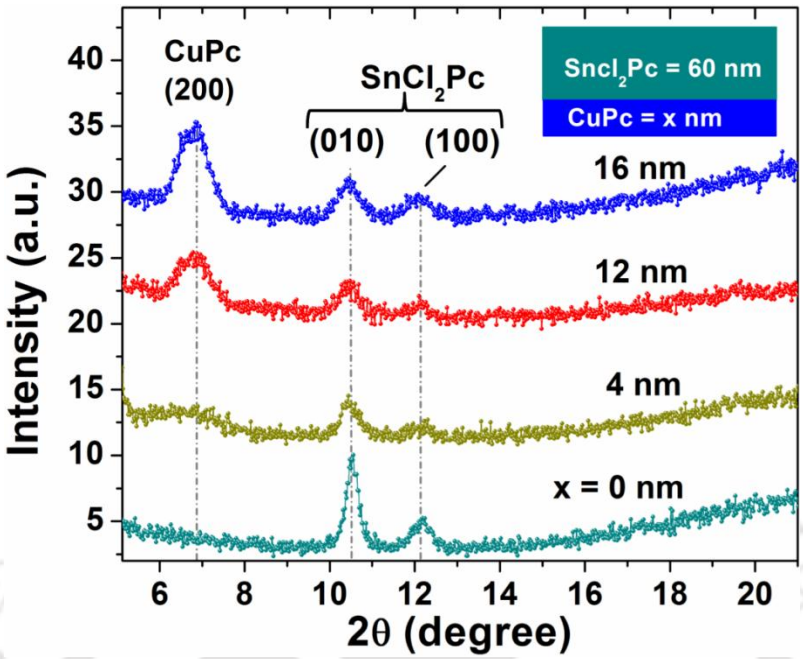

Figure 7.3: X-ray diffraction (XRD) patterns of $SnCl_2Pc$ (60 nm) deposited on different thicknesses of CuPc layer at a substrate temperature, T_d = 60 ºC. Inset shows a schematic of the layer configuration (60 nm $SnCl_2Pc$ as top layer and CuPc with varying thickness (x) as bottom layer) used for the XRD measurement.

We used an atomic force microscope (AFM) to study the surface features of the as-deposited films that influence the ambipolar behavior of the fabricated transistors, and to investigate whether the CuPc to $SnCl_2Pc$ thickness variation have any influence on the phase-separated network. **Figure 7.4(a-d)** shows the AFM images in tapping mode of the $SnCl_2Pc$ thin film (~60 nm) grown over the CuPc layer with different thicknesses (0, 4, 12 and 16 nm) at a substrate temperature 60 ºC. It is noticeable that the root-mean-square roughness (R_q) of $SnCl_2Pc$ thin film becomes higher with increasing CuPc thickness ($R_q \approx$ 1.7 to 2.2 nm). The thickness of the CuPc film is controlled by building up of separate single layers. At a very low thickness of CuPc deposited at 60 ºC, voids may appear in the film, since all grains are not fully connected with each other, and it provides the location upon which the second layer can grow. Thus, the $SnCl_2Pc$/CuPc heterojunction interface is smooth with the ultra-thin CuPc layer, but it may become little rougher with increasing CuPc thickness.

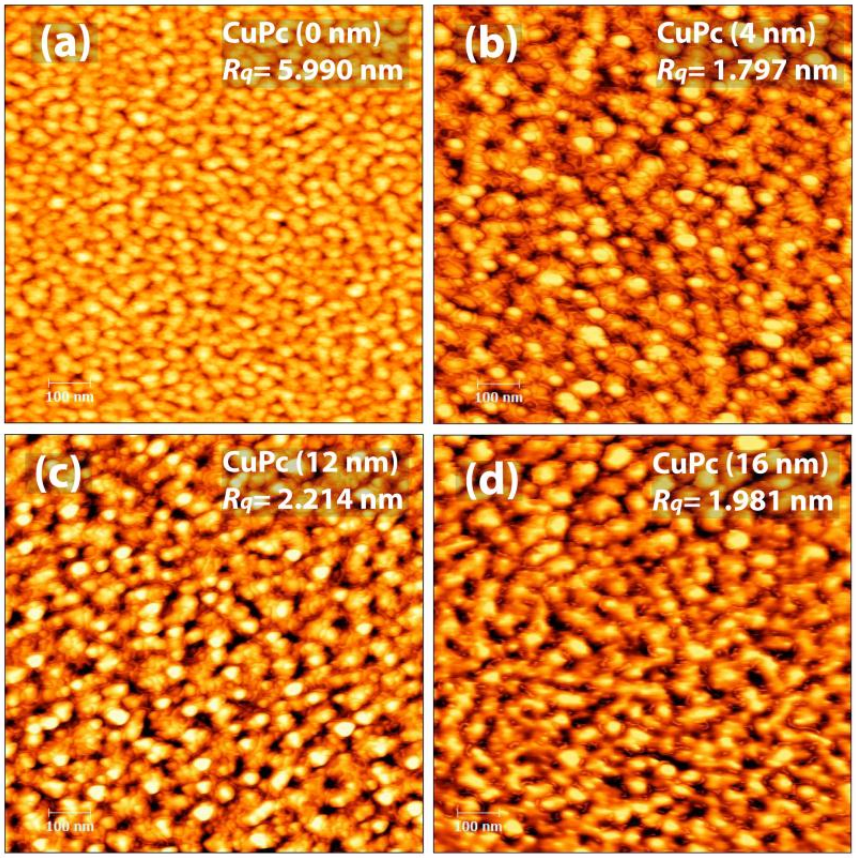

Figure 7.4: Tapping-mode AFM images (1 μm × 1 μm) of 60-nm-thick $SnCl_2Pc$: **(a)** without CuPc layer, and 60-nm-thick $SnCl_2Pc$ film grown on CuPc layer with different thicknesses: **(b)** 4 nm, **(c)** 12 nm, and **(d)** 16 nm. The measured RMS roughness (R_q) of the $SnCl_2Pc$ surface is indicated in each case.

7.3.2 Electrical Characterization and Device Performance

A typical unipolar OFET based on vacuum-deposited $SnCl_2Pc$ exhibited carrier mobility of 0.01 $cm^2\ V^{-1}\ s^{-1}$ [27]. The bilayer heterostructure ambipolar OFET device charateristics are shown in **Fig. 7.5(a-f)** and in **Fig. 7.6 (a-c)** with optimal 60-nm thick $SnCl_2Pc$ and x-nm (x = 4, 12, and 16 nm) thick CuPc bilayer heterostructure. **Figures 7.5(a), 7.5(d)** and **7.6(a)** shows the output characteristics (I_{DS} -V_{DS}), **Figs. 7.5(b-c), 7.6 (e-f)** are the transfer characteristics in p-channel and n-

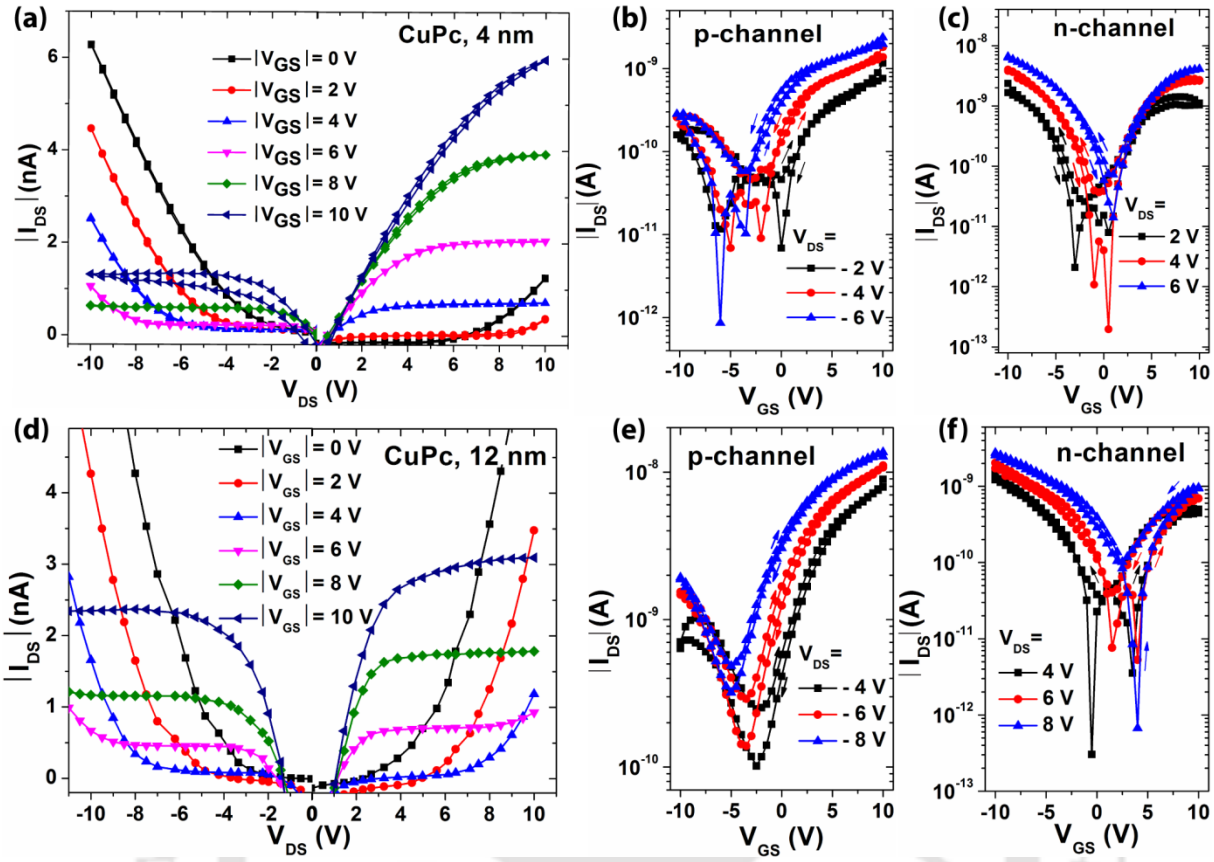

Figure 7.5: **(a)** Output characteristics (I_{DS}-V_{DS}), and **(b)-(c)** transfer characteristics (I_{DS}-V_{GS}) (for p-channel and n-channel, respectively) of the heterostructure ambipolar OFET for CuPc thickness of 4 nm. **(d)** Output characteristics (I_{DS}-V_{DS}), and **(e)-(f)** transfer characteristics (I_{DS}-V_{GS}) for p-channel and n-channel, respectively, of the heterostructure ambipolar OFET for CuPc thickness 12 nm (L= 30 µm, W = 780 µm). Note that the thickness of $SnCl_2Pc$ was kept constant (60 nm) for both the cases.

channel regime for two different CuPc-thicknesses (4 nm and 12 nm), respectively. The bilayer heterostructure OFETs show V-shape transfer characteristics of typical ambipolar transistors of n-channel and p-channel ambipolar OFET under low vacuum (~10^{-3} mbar) and in dark condition with electron and hole mobility of 5×10^{-4} and 3×10^{-4} cm^2 V^{-1} s^{-1} for n-channel and p-channel regime, repectively. In the case of thick CuPc with corresponding rough heterojunction interface, hole- current dominates I_{DS}, while the electron-dominant I_{DS} is supressed. We have noticed that at V_{DS}=0 V, electrons and holes contributed equally to eletron current and hole-current, as shown in **Fig 7.7**.

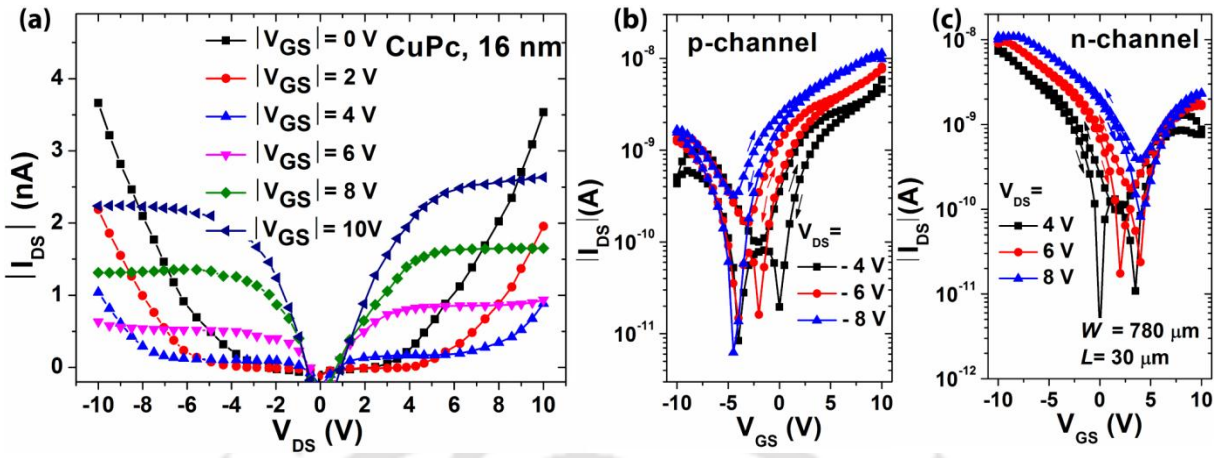

Figure 7.6: (a) Output characteristics (I_{DS} - V_{DS}), and **(b)-(c)** transfer characteristics (I_{DS}-V_{GS}) for p-channel and n-channel, respectively, of the heterostructure ambipolar OFET for CuPc thickness 16 nm, while the thickness of $SnCl_2Pc$ was 60 nm (L= 30 μm, W = 780 μm).

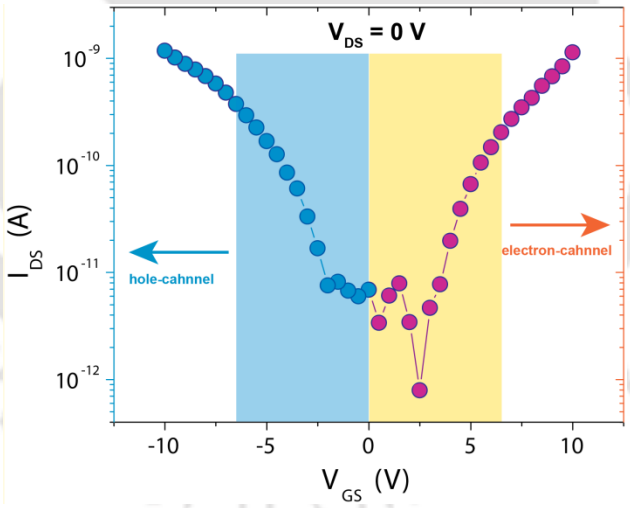

Figure 7.7: Transfer characteristics of heterostructure OFETs at V_{DS}=0 V, which shows equal electron and hole-current.

In **Fig. 7.8**, Mobility (μ) distribution of representative devices for different thicknesses of CuPc layers for p-channel (left panel) and n-channel (right panel). Average μ and its standard deviation are mentioned in each case at the top of the plots.

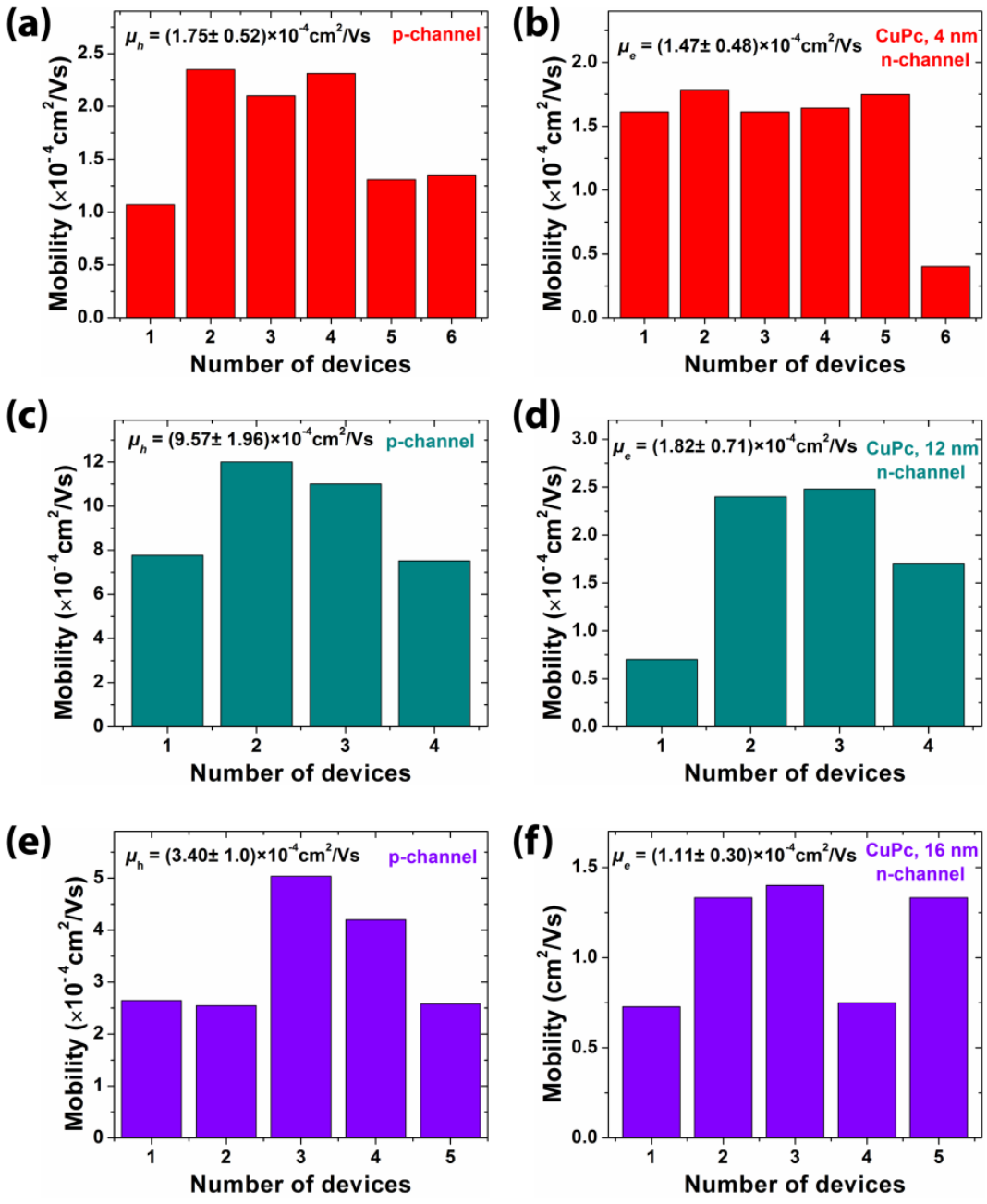

Figure 7.8: The mobility (μ) distribution of representative devices for different thicknesses of CuPc layers for p-channel (left panel) and n-channel (right panel). Average μ and its standard deviation are mentioned in each case.

The device parameters are summarized in **Table 7.1**, $V_{Th,e}$, and $V_{Th,h}$ are threshold voltages for the top n-channel and bottom p-channel, respectively.

Table 7.1. Electrical parameters for the TC/BG OFET (Ag-contact) with SnCl2Pc/CuPc heterostructures for different CuPc thicknesses grown at a substrate temperature of 60°C.

$SnCl_2Pc$-thickness[a)] [nm]	CuPc-thickness[b] [nm]	n-channel OFET			p-channel OFET		
		μ_e [$cm^2 V^{-1}s^{-1}$]	$V_{Th,e}$ [V]	$R_{c,e}$ [$\times 10^9$ Ω-cm]	μ_h [$cm^2 V^{-1}s^{-1}$]	$V_{Th,h}$ [V]	$R_{c,h}$ [$\times 10^9$ Ω-cm]
60	4	1.8×10^{-4}	2.53	1.60	2.1×10^{-4}	-6.84	7.19
	12	2.4×10^{-4}	4.22	15.6	1.2×10^{-3}	-2.88	9.78
	16	1.4×10^{-4}	3.40	115.15	4.2×10^{-4}	-3.41	10.70

a) active layer (n-channel), b) active layer (p-channel)

A noticieable hysteresis in the output characteristics of p-channel regime may be due to hole scattering and/or trapping at CuPc/PMMA interface (as the thin CuPc layer may have formed as interconnected grains, not fully covered on the dielectric surface). As the growth of heterostructures was sequential and was performed under vacuum conditions, the measurement of the surface roughness of only the CuPc layer was not possible. The mechanism of charge carrier transport in the present heterostructure ($SnCl_2Pc/CuPc$) transistor is schematically illustrated in **Figs. 7.9(a)** and **7.9(b)** for n-channel and p-channel cases, respectively. With $V_{DS}> 0$ and $V_{GS}> 0$, electron conduction takes place from the source to the drain mainly through the $SnCl_2Pc$ layer due to the particular positions of the Fermi and LUMO levels, as explained in **Fig. 7.2(b)**. Similarly, under $V_{DS}<0$ and $V_{GS}<0$, the hole conduction takes place through the CuPc layer only. In this way, an ambipolar characteristic is obtained in the hererostructure device.

Note that at higher thickness of CuPc, μ_e is reduced marginally (see **Fig.7.10(a)**) that may be due to the enhanced electron scattering and/or electron trapping owing to the increased roughness of heterojunction at the $SnCl_2Pc/CuPc$ interface. It is evident that the ambipolar OFETs can work well with the CuPc layer as thin as 4 nm and gives almost balanced electron and hole mobilities (~ 2×10^{-4} cm^2 V^{-1} s^{-1}), which is an interesting feature and it is crucial for

applications in electronic circuits and light emitting OFET. μ_h and μ_e in this devices are ~10^{-4} cm^2 V^{-1} s^{-1}, which is comparable to the literature reports on other CuPc based ambipolar devices [18,30]. Note that the commonly reported mobility for unipolar devices is comparatively higher (~10^{-2} cm^2 V^{-1} s^{-1}) than that of the ambipolar devices. It has been generally attributed to low conductivity of evaporated CuPc and $SnCl_2Pc$ that exhibit disorder of dipole at the heterojunction interface [31]. At low values of V_{GS}, the bilayer heterojunction ambipolar transistors exhibited diode-like (super-linear) curves, which are frequently observed for typical ambipolar transistors, due to the presence of both charge carriers (electron and hole) in the active channel of the device. We attribute this behaviour to the highly negative threshold voltage, $V_{Th,h}$, for p-channel operation and /or the positive threshold voltage for n-channel operation. The relatively high threshold voltages imply electron and hole trapping at the interface between the p- and n- channel materials in the phase separated network (see **Table 7.1**).

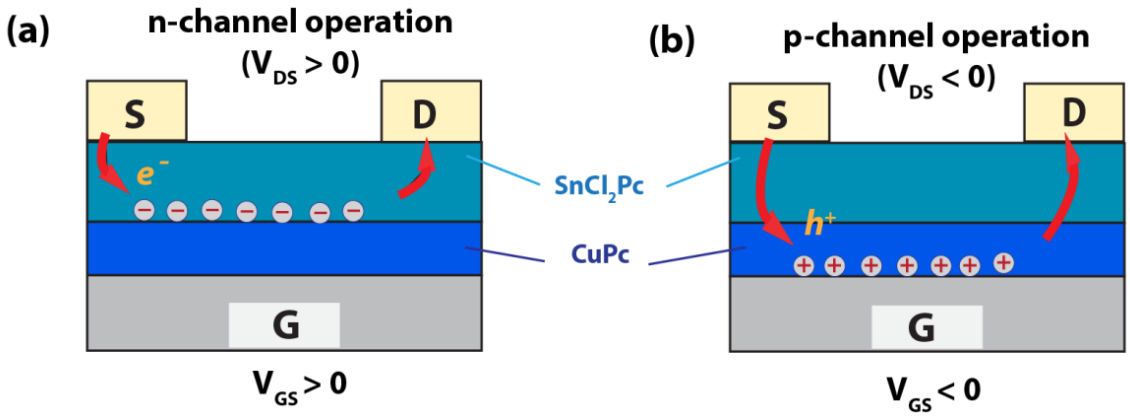

Figure 7.9: Schematic of the conduction process in the TC-BG $SnCl_2Pc$/CuPc heterostructure transistor for **(a)** n-channel, and **(b)** p-channel operations under different bias conditions. The flow of electrons and holes is indicated with arrows in the respective cases.

Table 7.1 shows that the threshold voltages, $V_{Th,e}$ and $V_{Th,h}$, shifts oppositely towards negative and positive sides, respectively, with the increase of the heterojunction roughness. A possible mechanism of the shift in $V_{Th,e}$ and $V_{Th,h}$ may be due to charge transfer to some extent (a possible mechanism may be electrons from CuPc HOMO to $SnCl_2PC$ LUMO) at the $SnCl_2Pc$/CuPc interface, which could be facilitated by rough interface due to an increased interfacial area [19]. With increasing thickness of CuPc layer, both the electron and the hole threshold voltages shift oppositely to more negative and positive values, respectively. In an

n-channel device, threshold voltage shows a less shift $\Delta V_{Th,e} \approx 0.87$ V when the CuPc thickness is changed from 4 nm to 16 nm, and consequently the p- channel threshold shows a larger shift $\Delta V_{Th,h} \approx 3.43$ V to more positive voltages ($V_{Th,h}$ down from - 6.84 V to - 3.41 V). Thus, the shift of threshold voltage in n-channel is much smaller compared to that of p-channel device. This may occur due to the larger contact area of Ag with CuPc-thin film with high thickness. At higher thickness of the CuPc layer, the diffusion of noble metals Ag is high in organic semiconductor. These diffused Ag impurity can create deep trap centers in $SnCl_2Pc$/CuPc layers, which may affect the long term trap states. Note that most of the deep trap states are located directly under the contact layer. However, some trap states may extend to the underneath of semiconductor layer [37,40].

To further investigate the degree of charge trapping, we extracted the density of traps for CuPc (4nm), N_{tr} (= $C_i \Delta V_{Th}/q$, where, C_i capacitance per unit area, ΔV_{Th} is shift of threshold voltage). The trap density derived from the trans-conductance curves are 6.31×10^{11} cm^{-2} and 9.69×10^{10} cm^{-2} at $|V_{DS}| = \pm 4$V, in p-channel and n-channel, respectively. It has been proposed that deep traps are usually responsible for the shift of threshold voltage and its density is higher in CuPc/PMMA interface than at the $SnCl_2Pc$/CuPc interface. The deep trap states may be generated at both interfaces in the contact region due to the diffusion of Ag atoms [40]. To further confirm the modulated charge injection, we analyzed the contact resistance. **Figure 7.10(b)** shows the channel width (W)- normalized contact resistance (R_c) as a function of CuPc thickness, in the *n*-channel regime (for electrons) as well as p-channel regime (for holes) of the OFETs. In an n-channel regime, the normalized contact resistance is 1.60×10^9 Ω cm for $SnCl_2Pc$ (60 nm)/CuPc (4 nm), which is smallest, as compared to that with larger thickness of CuPc layer. Note that the R_c is extracted by the Y-function method (YFM) for individual $SnCl_2Pc$/CuPc OFETs (channel width/ channel length (W/L) of 780 µm/30 µm) using the following equation [41],

$$R_c = \frac{V_{DS}}{I_{DS}} - \frac{1}{G_m\left(V_{GS} - V_{Th}\right)}, \tag{7.1}$$

where $G_m=(W/L)\mu_0 C_i$, is the trans conductance parameters. This is in contrast to the transfer line method (TLM) used to estimate contact resistance for the amorphous silicon transistors, where one can only obtain an average R_c, from the set of different channel lengths of transistors. This leads to the scattering of data in the plot, as R_c varies from transistor to transistor. Again, this method cannot be used if contact resistance is nonlinear (i.e. departs from Ohms law), as it is applicable in linear regime. The YFM offers a straightforward way to obtain the R_c in a single transistor and thereby it accesses the evolution of charge injection induced by different combination of heterostructures with same channel length, L. In devices with different thickness combination, the R_cW ($R_{c,e}$) for electron injection systematically increases from 1.6 $\times 10^9$ Ω-cm to 115$\times 10^9$ Ω-cm, while the R_cW ($R_{c,h}$) for hole injection does not change significantly. This is due to the importance of diffusion at the contact. As the thickness of CuPc increases, diffusion is no longer sufficient to derive the current through the bulk of the semiconductor, since for a given number of charges induced by the gate voltage, a sizeable concentration gradient can only be maintained over a finite distance and this results in the increase in contact resistance, $R_{c,e}$ for electron conduction. Furthermore, the V_{GS} dependence of normalized R_c shown in **Fig. 7.10(c)** and **7.10(d)** supports the above analysis. It is noticeable that the contact resistance R_c of hole is one order of magnitude higher than that of electrons for $SnCl_2Pc/CuPc$ heterostructure reflecting a finite Schottky barrier at Ag/CuPc interface. It is clear that R_c decreases with increasing V_{GS} for both hole and electron injection, and it is due to the fact that higher V_{GS} induces more accumulated charges, which will increase the conductivity of contact region and follow the current crowding model [42]. In staggered TC-BG OFETs (where contact and accumulation layer are formed at opposite sides of the semiconducting layer), the gate-voltage dependent R_c has been observed to mainly arise from current crowding. At a small gate bias, the bulk semiconductor between contacts and channel would be highly resistive if the injected charges are limited, and the injection is confined in a small contact area close to the channel. At higher gate bias, charges accumulate in the channel and also spread far from the channel interface and thus increase the bulk conductivity at contacts. Moreover, charge injection extends to larger contact area, as injection current gets more and more crowded and consequently R_c decreases. It has also been found that in staggered devices, R_c does not change significantly. Thus, the optimized

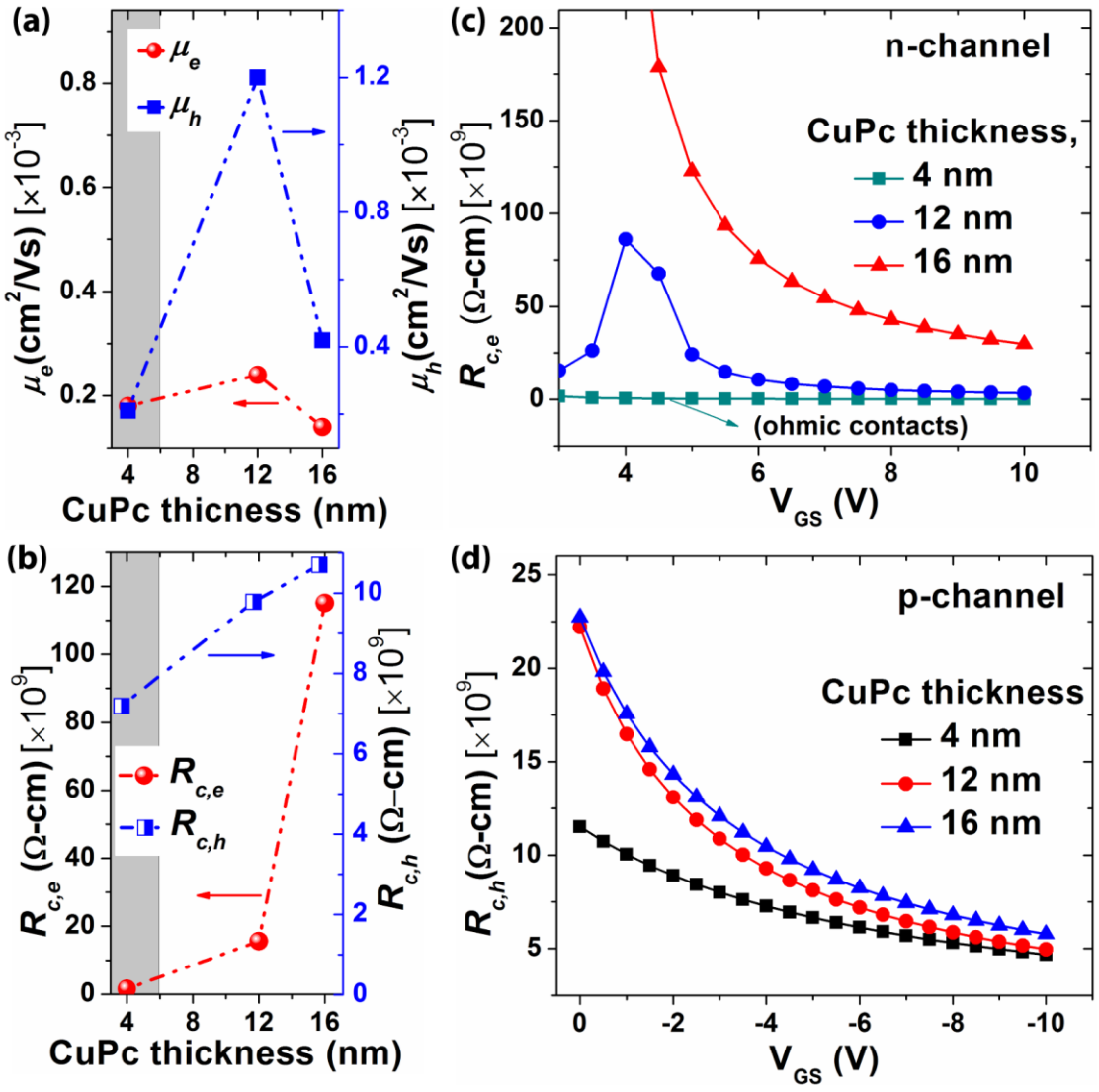

Figure 7.10: (a) Electron (μ_e), and hole-mobility (μ_h) of SnCl$_2$Pc/CuPc bilayer heterostructure OFETs at the saturation region (V_{DS} = ± 10 V) using Ag electrodes for different thickness (4, 12 and 16 nm) of CuPc layer with a fixed thickness (60 nm) of SnCl$_2$Pc layer. **(b)** Contact resistance for n-channel regime ($R_{c,e}$) and p-channel regime ($R_{c,h}$) of the corresponding devices extracted from the Y-function method. **(c)-(d)** Gate bias dependence of channel width normalized contact resistance for the top contact- bottom gate (TC-BG) devices based on SnCl$_2$Pc (60 nm)/CuPc (x nm, x = 4, 12 and 16) for n-channel and p-channel regime, respectively.

SnCl$_2$Pc/CuPc heterostructures results in gate-voltage independent R_c and signifies Ohmic contact.

7.3.3 Device Reliability

Besides the static device characteristics, the dynamic device characteristics are correlated significantly to the $SnCl_2Pc/CuPc$ heterojunction. **Figure 7.11(a)** shows the bias stress results at positive V_{GS} and V_{DS} (V_{GS} = V_{DS} = 8 V) in the ambipolar OFETs, i.e., the operational instability of electron-dominant drain-source current, $I_{DS}(t)$ normalized by its initial maximum value $I_{DS}(0$, initial source-drain current established right after the transistor is on (in n-channel and p-channel regime) for $SnCl_2Pc$ (60 nm)/CuPc(4 nm). In $SnCl_2Pc/CuPc$ bilayer heterojunction OFETs, the dark bias stress effect is very small; the current decreases by only 5–7 % after a continuous bias-stressing for 1 h at V_{GS} = V_{DS} = 8 V for n-channel (**Fig. 7.11(a)**) and in p-channel regime (V_{GS} = V_{DS} = -8V) it shows very similar small decay (<10%, see **Fig. 7.11(b)**). It is noticeable that initially (t<50 s) I_{DS} increases to some extend and then it decays at longer times for both n-channel and p-channel devices. It is believed to be caused by dipoles that can be oriented at the $PMMA/Al_2O_3$ interface or at Al_2O_3 bulk[43]. Although the $SnCl_2Pc$-based unipolar OFETs show good bias stress stability, the bias stress effect for electron-dominant I_{DS} in the ambipolar OFETs is generally significant.

The bias stress-induced drain-source current, I_{DS} decay in OFETs can be described by stretched-exponential time (t) dependent formula applicable to wide variety of disordered system and can be written as (when field effect mobility, μ_{FE}, is almost constant) [44,45],

$$I_{DS}(t) = I_{DS}(0)\exp\left[-\left(\frac{t}{\tau}\right)^{\beta}\right], \qquad (7.2)$$

where β is the stretching parameter (temperature dependent) related to the barrier energy height for charge trapping ($0 < \beta \leq 1$), τ is the relaxation time at room temperature, and $I_{DS}(0)$ is the initial maximum drain-source current measured at the beginning of stressing. Although this expression was originally developed to describe the bias-stress effect in amorphous silicon transistors considering the time-dependent evolution of trap states due to hydrogen migration, we employ similar formalism to describe dispersive trapping process in OFETs. A stretched exponential function (**Equation 7.2**) provides a perfect fit to both systems in n-channel and p-channels. **Figure 7.11(a)** and **(b)**, shows the data points (symbols) as well as fitted line using **Eq. (7.2)**. The values of τ at room temperature, extracted from the fitting are 4.28×10^5 s and 1.58×10^5 s in n-channel and p-channel device, respectively. The exponent

values are β=0.57 and 0.67, respectively. The large τ values imply a long-term stability of the device, which is very much desirable for practical applications. Considering that the interfacial chemistry at the heterojunction remains identical, the bias stress effect is primarily attributed to structural defects at the SnCl$_2$Pc/CuPc interface, which may generate deep traps for electron in the n-channel. It has been proposed that the time-dependent charge trapping in deep traps is responsible for the bias stress effect in OFETs and thus, charge traps at organic heterojunction can be the origin of the small bias-stress instability in the n-channel device[46].

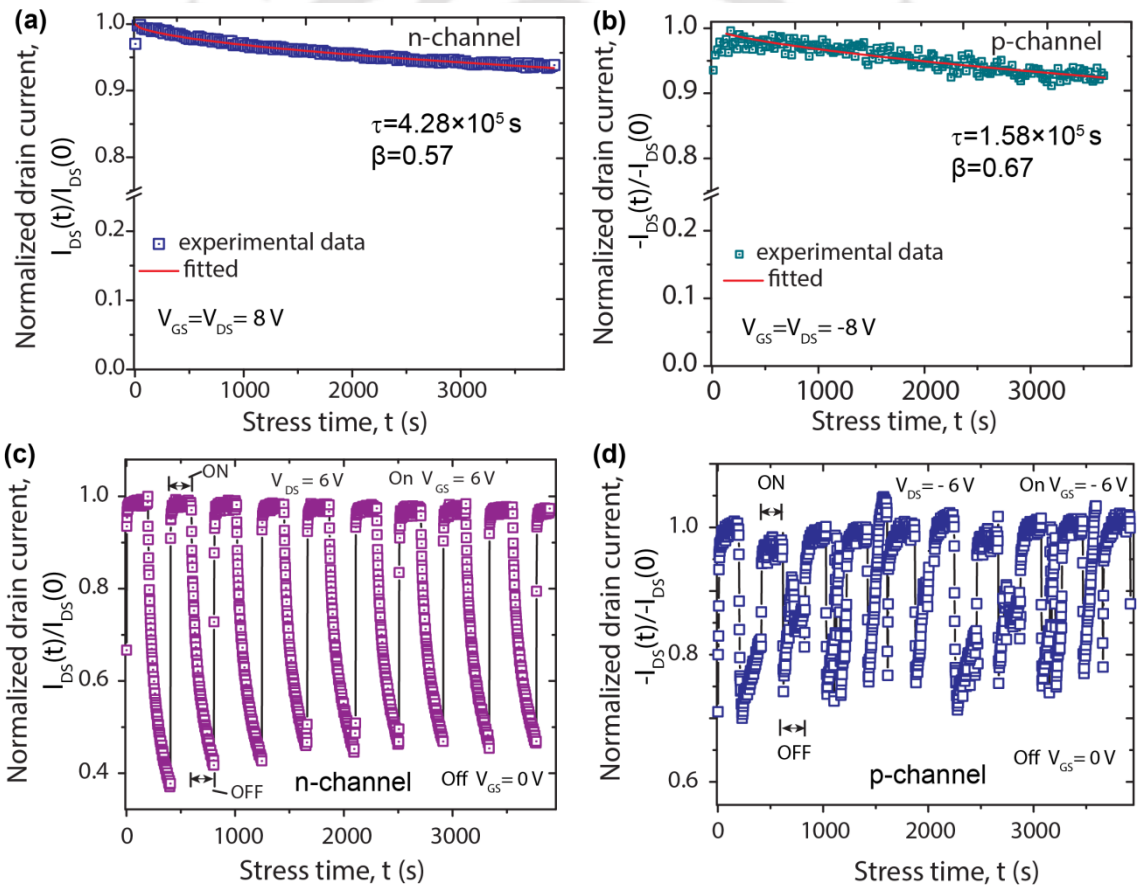

Figure 7.11: (a)-(b) Normalized drain-source current decay $I_{DS}(t)/I_{DS}(0)$ as a function of time in n-channel (SnCl$_2$Pc) at electron accumulation state and in p-channel (CuPc) at hole accumulation state. Cyclic stability with the "ON" and "OFF" cycles up to 3600 s for TC-BG heterostructure ambipolar OFET device based on SnCl$_2$Pc (60 nm)/CuPc (4 nm) (c) n-channel, and (d) p-channel.

As for the bias stress effect in the p-channel shown in **Fig. 7.11(b)**, it has less dependence on the $SnCl_2Pc$/CuPc heterointerface. It is in agreement with the argument that the p-channel is close to the CuPc/PMMA dielectric interface rather than to the $SnCl_2Pc$/CuPc heterointerface. Therefore, both the organic/dielectric and organic/organic interfaces influence the bias stress effect in the bilayer ambipolar OFETs [1,46].

To study the influence of gate bias on the cyclic bias stress behavior, we measured the drain-source current, I_{DS} of bilayer ambipolar OFET applying gate-source voltage V_{DS} of 6 V while varying V_{GS} of 6V results in "ON" state (for 180 s) and V_{GS} 0 V shows "OFF" state (for 180 s). It is plotted as function of time in **Fig. 7.11(c)**. During "OFF" state the drain current slowly decreases with time and in "ON" state it sharply raises to its maximum value. It is noticeable from **Fig. 7.11(c)-(d)** that negligible decay of drain current occurs after repeated ON and OFF states during 3600 s of operation at room temperature under low vacuum for

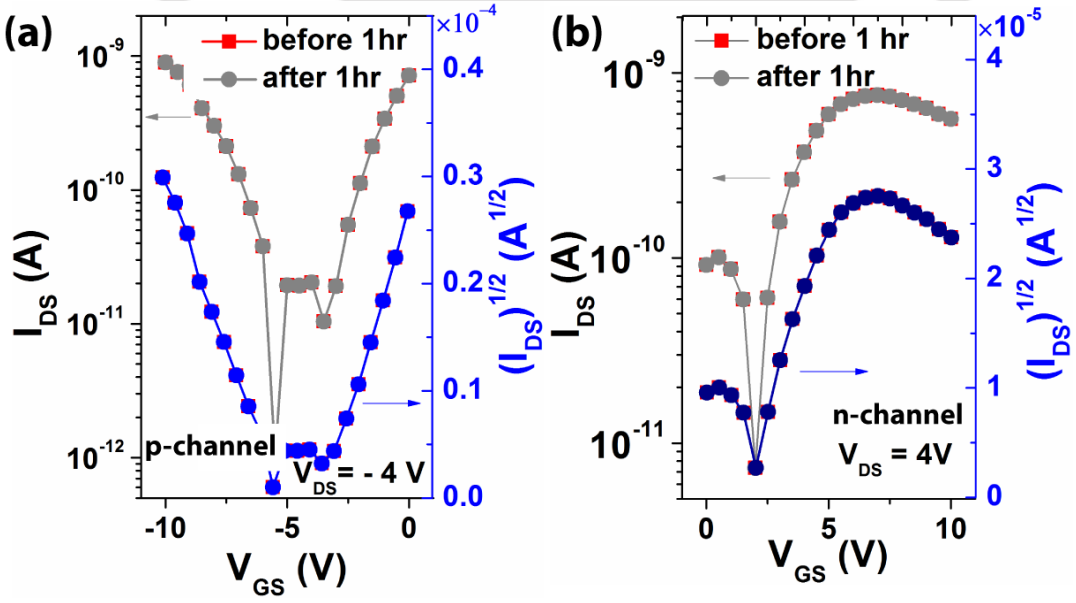

Figure 7.12: Transfer characteristics of top-contact OFET with PMMA/Al_2O_3 bilayer dielectric at room temperature before and after an applied cyclic gate-bias stress (BS) for 1 hr in **(a)** p-channel of V_{GS} = -10 V(V_{DS} = - 4V) and **(b)** n-channel of V_{GS} = 10 V (V_{DS} = 4 V) devices.

both n-channel and p-channel case. The time constant for "OFF" state is ~333 s. We acquired the transconductance curves before and after cyclic bias stress of 1h for both channels and it shows no shift of threshold voltage (see **Fig. 7.12(a)** and **(b)**). Thus the devices are very stable under low vacuum conditions.

7.4 Conclusions

In conclusion, we have demonstrated an ambipolar OFET based on low band gap $SnCl_2Pc$ and CuPc small molecules heterojunction that exhibits ambipolar conduction depending on the applied gate bias, either an accumulation layer of holes (negative gate bias) is formed in the CuPc layer or an accumulation layer of electrons (positive gate bias) is formed in the $SnCl_2Pc$ layer of the heterostructure device. The change in operation mode was attributed to the appropriate choice of the organic/organic heterojunction and the contact electrode metal work function. The change in the layer thickness resulted in evolution of the field-effect mobility values and an optimized thickness $SnCl_2Pc$/CuPc heterostructure yielded a balanced carrier mobility (~10^{-4} cm^2 V^{-1} s^{-1}). The bias stress effect and contact behavior in the bilayer ambipolar OFETs have been investigated. For the top $SnCl_2Pc$ n-channel, a smooth and continuous organic heterojunction enabled not only high bias stress stability (τ ~10^5 s) but also optimal contact resistance (R_C) for efficient carrier injection. For the bottom CuPc p-channel, the hole injection may be realized by the Ag penetration into $SnCl_2Pc$ to form local direct contact to CuPc, and the bias stress stability is dependent on the CuPc/dielectric interface rather than on the organic heterojunction. Using low work function Ag as a top contacts and a hydroxyl-free PMMA gate dielectric, the electron injection is greatly enhanced, leading to an improvement of both the electron and hole currents at the saturation regime. We believe that the present results are significant to develop better understanding on the carrier transportation process in organic-organic (p-n) heterojunction, and will be helpful to develop the fabrication of stable, ambipolar OFETs, which will be superior candidate for organic complementary circuits, organic light emitting field-effect transistors and organic lasers.

References

[1] J. Zaumseil, H. Sirringhaus, Electron and Ambipolar Transport in Organic Field-Effect Transistors. *Chem. Rev.* **107**, 1296 (2007).

[2] A. Dodabalapur, H.E. Katz, L. Torsi, R.C. Haddon, Organic field‐effect bipolar transistors. *Appl. Phys. Lett.* **68**, 1108 (1996).

[3] M.S. Kang, C.D. Frisbie, A Pedagogical Perspective on Ambipolar FETs. *ChemPhysChem* **14**, 1547 (2013).

[4] M.-H. Yoon, C. Kim, A. Facchetti, T.J. Marks, Gate Dielectric Chemical Structure−Organic Field-Effect Transistor Performance Correlations for Electron, Hole, and Ambipolar Organic Semiconductors. *J. Am. Chem. Soc.* **128**, 12851 (2006).

[5] J. Cornil, J.L. Brédas, J. Zaumseil, H. Sirringhaus, Ambipolar Transport in Organic Conjugated Materials. *Adv. Mater.* **19**, 1791 (2007).

[6] G.H. Gelinck, H.E.A. Huitema, E. van Veenendaal, E. Cantatore, L. Schrijnemakers, J.B.P.H. van der Putten, T.C.T. Geuns, M. Beenhakkers, J.B. Giesbers, B.-H. Huisman, E.J. Meijer, E.M. Benito, F.J. Touwslager, A.W. Marsman, B.J.E. van Rens, D.M. de Leeuw, Flexible active-matrix displays and shift registers based on solution-processed organic transistors. *Nat. Mater.* **3**, 106 (2004).

[7] G.A. Chamberlain, Organic solar cells: A review. *Solar Cells* **8**, 47 (1983).

[8] F. Eder, H. Klauk, M. Halik, U. Zschieschang, G. Schmid, C. Dehm, Organic electronics on paper. *Appl. Phys. Lett.* **84**, 2673 (2004).

[9] G. Gelinck, P. Heremans, K. Nomoto, T.D. Anthopoulos, Organic Transistors in Optical Displays and Microelectronic Applications. *Adv. Mater.* **22**, 3778 (2010).

[10] B. Crone, A. Dodabalapur, Y.Y. Lin, R.W. Filas, Z. Bao, A. LaDuca, R. Sarpeshkar, H.E. Katz, W. Li, Large-scale complementary integrated circuits based on organic transistors. *Nature* **403**, 521 (2000).

[11] D. Khim, K.-J. Baeg, M. Caironi, C. Liu, Y. Xu, D.-Y. Kim, Y.-Y. Noh, Control of Ambipolar and Unipolar Transport in Organic Transistors by Selective Inkjet-Printed Chemical Doping for High Performance Complementary Circuits. *Adv. Funct. Mater.* **24**, 6252 (2014).

[12] C. Rost, S. Karg, W. Riess, M.A. Loi, M. Murgia, M. Muccini, Ambipolar light-emitting organic field-effect transistor. *Appl. Phys. Lett.* **85**, 1613 (2004).

[13] J. Zaumseil, R.H. Friend, H. Sirringhaus, Spatial control of the recombination zone in an ambipolar light-emitting organic transistor. *Nat. Mater.* **5**, 69 (2006).

[14] M. Ullah, K. Tandy, S.D. Yambem, K. Muhieddine, W.J. Ong, Z. Shi, P.L. Burn, P. Meredith, J. Li, E.B. Namdas, Efficient and bright polymer light emitting field effect transistors. *Org. Electron.* **17**, 371 (2015).

[15] T. Lindner, G. Paasch, S. Scheinert, Operation and properties of ambipolar organic heterostructure field-effect transistors. *J. Appl. Phys.* **101**, 014502 (2007).

[16] E.C.P. Smits, T.D. Anthopoulos, S. Setayesh, E. van Veenendaal, R. Coehoorn, P.W.M. Blom, B. de Boer, D.M. de Leeuw, Ambipolar charge transport in organic field-effect transistors. *Phys. Rev. B* **73**, 205316 (2006).

[17] T. Takahashi, T. Takenobu, J. Takeya, Y. Iwasa, Ambipolar organic field-effect transistors based on rubrene single crystals. *Appl. Phys. Lett.* **88**, 033505 (2006).

[18] J. Wang, H. Wang, X. Yan, H. Huang, D. Jin, J. Shi, Y. Tang, D. Yan, *Adv. Funct. Mater. Adv. Funct. Mater.* **16**, 824 (2006).

[19] Y. Yan, Q.-J. Sun, X. Gao, P. Deng, Q. Zhang, S.-D. Wang, Probing bias stress effect and contact resistance in bilayer ambipolar organic field-effect transistors. *Appl. Phys. Lett.* **103**, 073303 (2013).

[20] F. Dinelli, R. Capelli, M.A. Loi, M. Murgia, M. Muccini, A. Facchetti, T.J. Marks, High-Mobility Ambipolar Transport in Organic Light-Emitting Transistors. *Adv. Mater.* **18**, 1416 (2006).

[21] M. Bronner, A. Opitz, W. Brütting, Ambipolar charge carrier transport in organic semiconductor blends of phthalocyanine and fullerene. *phys. stat. sol. (a)* **205**, 549 (2008).

[22] S.-S. Cheng, P.-Y. Huang, M. Ramesh, H.-C. Chang, L.-M. Chen, C.-M. Yeh, C.-L. Fung, M.-C. Wu, C.-C. Liu, C. Kim, H.-C. Lin, M.-C. Chen, C.-W. Chu, Solution-Processed Small-Molecule Bulk Heterojunction Ambipolar Transistors. *Adv. Funct. Mater.* **24**, 2057 (2014).

[23] T.P.I. Saragi, J. Salbeck, Organic heterostructure field-effect transistors using C60 and amorphous spirolinked compound. *Appl. Phys. Lett.* **89**, 253516 (2006).

[24] D.X. Long, K.-J. Baeg, Y. Xu, S.-J. Kang, M.-G. Kim, G.-W. Lee, Y.-Y. Noh, Gradual Controlling the Work Function of Metal Electrodes by Solution-Processed Mixed Interlayers for Ambipolar Polymer Field-Effect Transistors and Circuits. *Adv. Funct. Mater.* **24**, 6484 (2014).

[25] S.R. I. H. Campbell, T. A. Zawodzinski, J. D. Kress, R. L. Martin, and D. L. Smith, Controlling Schottky energy barriers in organic electronic devices using self-assembled monolayers. *Phys. Rev. B* **54**, R14321 (1996).

[26] X. Cheng, Y.-Y. Noh, J. Wang, M. Tello, J. Frisch, R.-P. Blum, A. Vollmer, J.P. Rabe, N. Koch, H. Sirringhaus, Controlling Electron and Hole Charge Injection in Ambipolar Organic Field-Effect Transistors by Self-Assembled Monolayers. *Adv. Funct. Mater.* **19**, 2407 (2009).

[27] S. Md. Obaidulla, D.K. Goswami, P.K. Giri, Low bias stress and reduced operating voltage in SnCl2Pc based n-type organic field-effect transistors. *Appl. Phys. Lett.* **104**, 213302 (2014).

[28] Z. Bao, A.J. Lovinger, A. Dodabalapur, Organic field‐effect transistors with high mobility based on copper phthalocyanine. *Appl. Phys. Lett.* **69**, 3066 (1996).

[29] D. Song, H. Wang, F. Zhu, J. Yang, H. Tian, Y. Geng, D. Yan, Phthalocyanato Tin(IV) Dichloride: An Air-Stable, High-Performance, n-Type Organic Semiconductor with a High Field-Effect Electron Mobility. *Adv. Mater.* **20**, 2142 (2008).

[30] S. Yadav, A. Sharma, S. Ghosh, Organic transistor and inverter based on assembly of organic nanowires achieved by optimizing surface morphology. *Appl. Phys. Lett.* **102**, 093303 (2013).

[31] H.W. Jun Wang, Xuanjun Yan, Haichao Huang, and Donghang Yan, Organic heterojunction and its application for double channel field-effect transistors. *Appl. Phys. Lett.* **87**, 093507 (2005).

[32] H.-J. Yun, S.-J. Kang, Y. Xu, S.O. Kim, Y.-H. Kim, Y.-Y. Noh, S.-K. Kwon, Dramatic Inversion of Charge Polarity in Diketopyrrolopyrrole-Based Organic Field-

Effect Transistors via a Simple Nitrile Group Substitution. *Adv. Mater.* **26**, 7300 (2014).

[33] G. Horowitz, R. Hajlaoui, D. Fichou, A. El Kassmi, Gate voltage dependent mobility of oligothiophene field-effect transistors. *J. Appl. Phys.* **85**, 3202 (1999).

[34] Y.X. Chuan Liu, and Yong-Young Noh, Contact engineering in organic field-effect transistors. *Materials Today* **00**, 00 (2014).

[35] Z. Bao, J. Locklin, *Organic Field-Effect Transistors*, CRC Press, Boca Raton, FL, USA, (2007).

[36] Y.X. Chuan Liu, Yun Li, William Scheideler, and Takeo Minari, Critical Impact of Gate Dielectric Interfaces on the Contact Resistance of High-Performance Organic Field-Effect Transistors. *J. Phys. Chem. C* **117**, 12337 (2013).

[37] D. Natali, M. Caironi, Charge Injection in Solution-Processed Organic Field-Effect Transistors: Physics, Models and Characterization Methods. *Adv. Mater.* **24**, 1357 (2012).

[38] H. Wang, Z. Liu, T.W. Ng, M.F. Lo, C.-S. Lee, D. Yan, S.-T. Lee, Interfacial electronic structure of copper hexadecafluorophthalocyanine and phthalocyanatotin (IV) dichloride studied by photoemission spectroscopy. *Appl. Phys. Lett.* **96**, 173303 (2010).

[39] S.J. Noever, S. Fischer, B. Nickel, Dual Channel Operation Upon n-Channel Percolation in a Pentacene-C60 Ambipolar Organic Thin Film Transistor. *Adv. Mater.* **25**, 2147 (2013).

[40] Y. Liang, H.-C. Chang, P. Paul Ruden, C. Daniel Frisbie, Examination of Au, Cu, and Al contacts in organic field-effect transistors via displacement current measurements. *J. Appl. Phys.* **110**, 064514 (2011).

[41] Y. Xu, T. Minari, K. Tsukagoshi, J.A. Chroboczek, G. Ghibaudo, Direct evaluation of low-field mobility and access resistance in pentacene field-effect transistors. *J. Appl. Phys.* **107**, 114507 (2010).

[42] T.J. Richards, H. Sirringhaus, Analysis of the contact resistance in staggered, top-gate organic field-effect transistors. *J. Appl. Phys.* **102**, 094510 (2007).

[43] D.K. Hwang, C. Fuentes-Hernandez, J. Kim, W.J. Potscavage, S.-J. Kim, B. Kippelen, Top-Gate Organic Field-Effect Transistors with High Environmental and Operational Stability. *Adv. Mater.* **23**, 1293 (2011).

[44] X.-H. Zhang, S.P. Tiwari, B. Kippelen, Pentacene organic field-effect transistors with polymeric dielectric interfaces: Performance and stability. *Org. Electron.* **10**, 1133 (2009).

[45] B. Lee, A. Wan, D. Mastrogiovanni, J.E. Anthony, E. Garfunkel, V. Podzorov, Origin of the bias stress instability in single-crystal organic field-effect transistors. *Phys. Rev. B* **82**, 085302 (2010).

[46] S.D. Wang, T. Minari, T. Miyadera, Y. Aoyagi, K. Tsukagoshi, Bias stress instability in pentacene thin film transistors: Contact resistance change and channel threshold voltage shift. *Appl. Phys. Lett.* **92**, 063305 (2008).

Chapter 8

Summary and Outlook

The summary of the original contributions of the thesis and important conclusions of the present thesis are presented in this chapter. New findings on the surface roughening and growth dynamics of organic thin films on various substrates, fabrication and characterization of top contact organic field-effect transistors with different dielectric materials, treated and non-treated, different contact electrodes and their stability, ambipolar organic filed-effect transistors with performance and stability studies are summarized here. Outlooks and scope for future work are also presented at the end.

8.1 Summary of The Thesis

In this thesis work, we studied the substrate dependent growth dynamics of a non-planar (bi-pyramidal), disc-like $SnCl_2Pc$. We addressed the evolution of surface morphology and scaling behavior of $SnCl_2Pc$ thin films grown on Si(100) and glass substrates. We observed the crystalline nature of the $SnCl_2Pc$ thin film on glass substrate, while no crystallographic ordering is present for the film grown on Si substrate. From scaling analysis, we found an upward dominant growth on glass substrate during thin film growth due to high step-edge barrier presents in glasss substatre, while lying down geometry without proper arrangement of molecules on the Si substrate. We described the possible analogy of surface evolution to a closely mound like growth mode (*Chapter 3*). Thin films changes their morphology at different deposition parameters and results into substrate induced growth/roughening behavior. We discussed the growth dynamics of non-planar (pyramidal) VOPc molecules on both ITO-glass and SiO_2 substrate that shows crystalline nature. From scaling analysis and thin film morphology, it was explained most possible analogy that the surface diffusion and step-edge barrier are responsible for the overall surface evolution. However, a molecular level understanding is necessary to provide further explanation (*Chapter* 4). The observed growth exponents for $SnCl_2Pc$ and VOPc organic thin films on different substrates do not match with the reported conserved growth models available for inorganic material and it belongs to a different new universality class. Next, we studied the vacuum deposited

$SnCl_2Pc$ organic field-effect transistors. Devices were fabricated on PMMA/Al_2O_3 bilayer gate dielectric and SiO_2 gate dielectrics insulator and it results in a low operating voltage and a low contact resistance device. It exhibits excellent n-channel behavior with high electron mobility, low threshold voltages, large current on/off ratio for PMMA/Al_2O_3, while devices with SiO_2 gate insulator shows poor performance. Further, we observed that the amount of bias stress for $SnCl_2Pc$ based thin film transistor is extremely small with large characteristic relaxation time obtained using a stretched exponential model. These devices show highly stable electrical behavior under multiple scans and low threshold voltage shift under electrical dc bias stress even after 40 days of operation. We have addressed the contact electrode Al, Ag dependent devices performance and concluded that Ag contact based OFET shows overall good performance as compared to that of Al contact device (*Chapter 5*). High bias stress stability and low threshold voltage shift under ambient condition are highly desirable for practical applications of organic field-effect transistors (OFETs). We demonstrated a 20-fold enhancement in the bias-stress stability for hexamethyledisilazane (HMDS) treated VOPc based OFETs as compared to the bare VOPc case under ambient condition. VOPc based OFETs were fabricated on bare SiO_2 and HMDS monolayer passivated SiO_2 layer. The devices with top contact Au electrodes exhibit excellent p-channel behavior with a high hole mobility for HMDS-treated device as compared to that non-treated case. We observed a very small decay of drain current during long term operation under ambient conditions for the HMDS-treated case, while it shows a large decay for the nontreated devices (*Chapter 6*). We have investigated a symmetrical Ag top contact-bottom gate (TC-BG) bilayer ambipolar organic field-effect transistor based on the bilayer heterojunction of vacuum-deposited small molecules $SnCl_2Pc$ (n-channel) and CuPc (p-channel). A hydroxyl (-OH) free poly(methyl methacrylate) (PMMA) with aluminum oxide (Al_2O_3) bilayer dielectric exhibits low operating voltage and low bias stress for both n-channel and p-channel cases. The optimized $SnCl_2Pc$/CuPc heterostructure exhibits balanced carrier mobility and both types of charge carriers, electrons and holes, are facilitated by the same low work function Ag contact, depending on the bias conditions. The Ag contact also exhibits Ohmic injection of charge carriers with low contact resistance in the n-channel region under an optimal heterostructure configuration. The contact resistance for electron and hole-injection is strongly dependent on the thickness of the $SnCl_2Pc$ and CuPc layers,

respectively. The bias stress stability is modeled using a stretched exponential decay function and it shows that the devices are highly bias stress stable during prolonged operation (*Chapter 7*).

The major contributions and new findings of the present thesis is presented below.

8.2 Highlights of the Thesis Contribution

A. Substrate-induced Surface Roughening and Scaling behavior of Non-planar Bipyramidal $SnCl_2Pc$ Organic Thin Films and Mound Growth Scenario

The structural evolution of vacuum deposited $SnCl_2Pc$ thin films on Si(100) and glass substrates has been studied systematically. The growth dynamics of $SnCl_2Pc$ thin films has been studied using AFM and HHCF analysis. It may be noted that there has been no report on the scaling behavior and growth dynamics of $SnCl_2Pc$ on different substrates that are most relevant for device applications. By analyzing the scaling behavior, it has been found that the growth exponent β is be much larger for the film on glass substrate as compared to that on Si substrate, which suggests that the $SnCl_2Pc$ crystallites grow in the upward direction as the film thickness increases on glass substrate, which may be due to the high potential barrier or step-edge barrier. Small β value for Si substrate may be attributed to small step-edge barrier at edge of the molecular layer and consequent decrease in the crystallographic ordering of the films. One of the important findings is that the growth exponent β value for $SnCl_2Pc$ thin film on glass substrate is comparable to that predicted by the random deposition model, while for Si substrate it is very small and results in "smoothening"-a lying down geometry without proper molecular arrangement, which may be due to the small step-edge barrier. This different growth modes observed on two different substrates can be understood partly in terms of molecule-substrate interactions, since molecule-molecule interaction strength is nearly the same for all investigated films. Here, the molecule-substrate interaction strength may be stronger for Si substrate than the glass substrate. Our XPS analysis supports the above explanation. XPS investigation on ~5 nm thin $SnCl_2Pc$ film on Si and glass substrate shows different oxygen concentrations in the film. Thus, the nature of molecular interactions in two different substrates are likely to be different, giving rise to different molecular structures. So, the adsorption of the molecule

occurs in a lying geometry of $SnCl_2Pc$ molecules on Si substrate. $SnCl_2Pc$ films grown here on glass substrate exhibited crystalline behavior, which is suitable for device fabrication. The derived growth exponents (α, β, $1/z$) are quite close to the exponents predicted by the model of mound formation, which is reported for both organic and inorganic materials. Note that the asymptotic value of roughness exponent satisfy the condition for mound formation. We have plotted two dimensional (2D) fast Fourier transform (FFT) of the surfaces from the AFM images on Si and glass substrates, which shows a ring like behavior, supporting the mound growth morphology. $SnCl_2Pc$ films grown here on glass substrate exhibited crystalline behavior, which is suitable for device fabrication.

B. Effect of Growth Parameters on Surface Roughening and Scaling behavior of non-planar, Pyramidal VOPc Organic Thin Films

The structural evolution of VOPc thin films for different deposition parameters such as substrate temperature and film thickness on SiO_2 and ITO-glass substrates has been studied. At elevated substrate temperature, VOPc film shows different surface morphology on two different substrates, as confirmed from the AFM images. The growth dynamics of VOPc thin films has been studied using AFM and HHCF analysis. It may be noted that growth dynamics of VOPc thin films has not been reported earlier, to our knowledge. Analyzing the scaling behavior and 2D fast Fourier transform, it is concluded that the morphological evolution of the deposited VOPc molecules follows mound like formation, which suggests that the VOPc crystallites grow in the upward direction and closely follows mound growth mechanism as the film thickness increases on ITO-glass as well as on SiO_2 substrates, which may be due to the high potential barrier or step-edge barrier. X-ray diffraction measurement confirms the crystalline nature of the VOPc thin film grown on both substrates, SiO_2 and ITO-glass. From the scaling analysis, the growth exponent β is found to be much larger for the film on SiO_2 substrate as compared to that on ITO-glass substrate, which may be due to the high step-edge barrier resulting in the upward dominant growth with rapid roughening on SiO_2 substrate. One of the important findings is that the β value for VOPc thin film on SiO_2 substrates is large, while for ITO substrate it is comparatively small and signifies the small step-edge barrier. We observed that the diffusion activation energy is almost equal for molecules grown on both substrates. VOPc film shows crystalline behavior on both SiO_2 and ITO-glass

substrate although they have significant differences in the growth exponent β value. The other non planar disc/pyramidal phthalocyanine molecules are reported to have amorphous nature, while VOPc non planar pyramidal molecules exhibits crystalline behavior on two different substrates, SiO_2 and ITO. This observation is not rationalized by step-edge barrier or simply by molecular diffusion, rather it opens further questions for which more indepth study is required at the molecular level.

C. Effect of Gate Dielectrics and Contact Electrodes on the $SnCl_2Pc$ based n-Channel OFET

The electrical performances and stability of vacuum-deposited thin film based n-channel organic field-effect transistors with $SnCl_2Pc$ were demonstrated in top contact bottom gate configuration using Ag source/drain electrodes, and PMMA/Al_2O_3 and SiO_2 as a gate dielectrics. We observed that the devices of $SnCl_2Pc$ with PMMA/Al_2O_3 bilayer dielectric exhibited excellent n-channel behavior with high field-effect electron mobility and low operating voltage, while devices with SiO_2 gate dielectric exhibits poor performance and high operating voltage. We estimated that a lower trap density occurs at the hydroxyl (-OH) free PMMA/Al_2O_3 dielectric interface as compared to that of SiO_2 interface. These OFET's showed high current on-off ratio and high operational stable electrical behavior with no hysteresis when tested under low vacuum condition as compared to the devices with SiO_2 gate dieletric. Further, multiple transfer characteristics scans and bias stress results indicate that these OFET's exhibit extremely low threshold voltage instability when tested in low vacuum and long term operation stability even after a month. In contrast, the devices with SiO_2 gate dielectric exhibit poor operation stability. The mechanism of degradation under continuous operation is related to the dynamics of dipolar groups and charge trapping and detrapping events at all of the critical interfaces in the OFET and in the bulk of the semiconductor and gate dielectric. However, the exact mechanism is still unknown and is under debate. This extremely small bias stress effect results in very long characteristics time constant, which is three orders of magnitude higher than the commonly used SiO_2 based devices, which is significant, since n-type organic devices are considered to be more sensitive to trapping and ambient oxidants than the p-type counterparts. We arrive at the conclusion that the nature of the gate dielectric layer is more important than the chemistry of the organic semiconductor in order to obtain transistors with a high electrical stability.

This results is very much useful to make CMOS integrated circuits, organic light emitting field-effect transistors, organic inverters where both p-channel as well as n-channel active layer is necessary.

We also studied the electrical performance and bias stress stability of Al and Ag top-contact as source and drain electrodes. We show that the Ag-contact yields a better performance in all respect. We have investigated the bias stress effect by using different contact metals Ag, Al. The Al contact based OFET suffers significant bias stress instability as compared to that of the Ag-contact based OFET. It was also observed that Al contact devices results in non-ohmic (nonlinear in output characteristics at low bias) behavior at metal-semiconductor interface, while Ag contact devices shows Ohmic (linear in output characteristics at low bias) nature. We find the characteristics time constant is two order of magnitude higher in case of Ag contact devices as compared to the Al contact devices. It is likely that the Al atom will bond directly to oxygen atoms with organic molecules and results in a strong Al-O interaction. In contrast, Ag is noble metal and the atoms will directly penetrate at organic layer without reaction. So, the relatively poor performance of Al for electron injection into organic semiconductor is probably due to the formation of this reacted layer that leads to a high injection barrier at the interface, while for Ag, there is no injection barrier at metal-semiconductor interface. It may be noted that there are only a limited number of low operating voltage and low bias stress (high operation stable) n-channel OFET reported till date. In addition, choice of Ag electrode is more superior for optoelectronic applications, as solution processable Ag-paste is readily available in the market. So, these results are of paramount important to make device for real life applications.

D. Effect of HMDS monolayers on SiO_2 and its Influence on the Performance of VOPc p-channel OFETs

We have demonstrated the beneficial role of HMDS passivation of SiO_2 dielectric layer as compared to non treated SiO_2 layer on the performance of VOPc based OFET under ambient condition. It may be noted that HMDS treated VOPc OFET has not been reported in literature. We observed that HMDS treated devices shows high performance and better air stability than the devices with non-treated SiO_2 layer. All the devices with top contact Au electrodes exhibit excellent p-channel behavior with high hole mobility for HMDS-treated

devices. Bias stress stability study shows stretchehed expoential decay behavior during the long term operation under constant bias voltage in ambient conditions with a very low decay of drain current for the HMDS-treated case and very sharp fall for the devices with bare SiO_2 layer. The corresponding characteric time constant is large for HMDS-treated case, while it is very low for bare/non-treated devices. Thus, HMDS treated devices with long term stability are suitable for practical applications. For low performance devices based on bare SiO_2, it is believed that the charge trapping occurs primarily at the voids in the inter grain regions of the film, while it is almost negligible for HMDS-treated SiO_2 case as it has been observed from the morphological analysis of VOPc tin films using AFM analysis. It should be noted that the insatbility due to molecular grains which has a significant contribution is rarely addressed in the literature. This work will lead to the better performance devices, by controlling the thin film morphology.

E. Fabrication of Low Operating Voltage and High Bias Stress Stable $SnCl_2Pc$/CuPc based Ambipolar OFET

We have investigated an ambipolar OFET based on the heterojunction of low band gap $SnCl_2Pc$ and CuPc small molecules that exhibit ambipolar conduction depending on the applied gate bias, either an accumulation layer of holes is formed in the CuPc layer or an accumulation layer of electrons is formed in the $SnCl_2Pc$ layer of the heterostructure device. We have shown that the change in operation mode was attributed to the appropriate choice of the organic/organic heterojunction and the contact electrode metal work function. The change in the layer thickness resulted in evolution of the field-effect mobility values and an optimized thickness $SnCl_2Pc$/CuPc heterostructure yielded a balanced carrier mobility. The bias stress effect and contact behavior in the bilayer ambipolar OFETs have been studied. For the top $SnCl_2Pc$ n-channel, a smooth and continuous organic heterojunction enabled not only high bias stress stability but also optimal contact resistance for efficient carrier injection. For the bottom CuPc p-channel, the hole injection may be realized by the Ag penetration into $SnCl_2Pc$ to form a local direct contact with CuPc, and the bias stress stability is dependent on the CuPc/dielectric interface rather than on the organic-organic heterojunction. Using a low work function Ag as a top contact and a hydroxyl-free PMMA gate dielectric, the electron injection is greatly enhanced, leading to an improvement of both

the electron and hole currents in the saturation region. We believe that the present results are significant to develop further understanding of the carrier transportation process in organic–organic (p–n) heterojunction, and will be helpful to develop the fabrication of stable ambipolar OFETs, which are superior candidates for organic complementary circuits, organic light emitting field-effect transistors and organic lasers.

8.3 Outlooks and Scope for Future Work

We believe that the comprehensive study presented in this thesis on the growth dynamics of organic thin films on commonly used substrates and fabrication of low power consumption and high air stable organic unipolar/ambipolar field-effect transistors-based research and development efforts will stimulate further investigations for real life applications. We are quite affirmative about the real life applications of the phthalocyanine based promising organic thin films and its devices with superior performances, since the properties are being improved continuously through the newer findings. However, there are several unresolved issues on the growth study of growth study of organic thin films and long term operational stability of organic thin film based field-effect transistors. Thus, there is enormous scope to extend the present work for the study of growth kinetics and developing high performance organic field-effect transistors to address the challenges of the real life applications, as discussed below:

1. Studies of the growth dynamics of organic thin films opened up new avenues on the growth of organic-organic heterostructure, which is more complex than single layer growth and it very essential for photovoltaic, light emitting diode where two or more active layers are needed. In this context, one can investigate the growth dynamics of $SnCl_2Pc$/VOPc (n-type/p-type) heterostructure and make theoretical framework based on continuous modeling of height fluctuations of growing film.

2. Organic thin film deposition and consequently surface evolution occurs at far from euilibrium condition. So, the growth dynamics does not follow the commonly conserved growth model or does not fall into any known universality classes, which are reported for inorganic systems. So, there is a need for new model or new universality class for particular organic thin film system.

3. The bias stress stability as well as cyclic stability can be performed under different gas environment such as NH_3, Ar, N_2, O_2 for the development of organic based gas sensors.

4. Low operating voltage OFET may be achieved by using high k-dielectric material such as $BaTiO_3$, $SrTiO_3$ and their combination. These are room temperature processable and low cost method and should be implemented for OFET fabrication.

5. A more detailed understanding of the physics of charge transport behavior in single crystal organic field-effect transistor based $SnCl_2Pc$, VOPc and CuPc molecules should be developed.

6. Specific role of doping of SAM layer on organic active layer need to be studied, since SAM can improve the device performance. It has been found that device performances and stability also sometimes suffer instability due to SAM treatment.

7. The tuning of the thickness of the active layer of bilayer heterostructure ($SnCl_2Pc$/CuPc) may result the balance ambipolar charge transport. There are several factors taken care to enable into better ambipolar charge carrier transport: a trap-free dielectric-semiconductor interface, a trap-free semiconductor and sufficiently low injection barriers for both charge carrier types. The influence of gate dielectric layer, active layer thickness, contact materials, grain size and substrate temperature on the charge carrier transport has been investigated. This works shows the way for the fabrication light emitting transistors, which has significant potential for the next generation light emitting devices.

8. Charge transport physics between organic-inorganic heterostructure can be studied using stretched exponential model. In this systems a modified stretched exponential function may be needed, which may lead to a new bias stress model. The physical significance of stretched exponential parameters is still illusive, which calls for an indepth study in this context.